Award Number: W81XWH-15-1-0271

TITLE: Low-Cost, High-Throughput 3D Pulmonary Imager Using Hyperpolarized Contrast Agents and Low-Field MRI

PRINCIPAL INVESTIGATOR: Eduard Y. Chekmenev, Ph.D.

CONTRACTING ORGANIZATION: Wayne State University, Detroit, MI 48202

REPORT DATE: October 2019

TYPE OF REPORT: Annual

PREPARED FOR: U.S. Army Medical Research and Materiel Command
Fort Detrick, Maryland, 21702-5012

REPORT DOCUMENTATION PAGE

Form Approved
OMB No. 0704-0188

1. REPORT DATE	2. REPORT TYPE	3. DATES COVERED
OCT 2019	ANNUAL	09/30/2018–09/29/2019

4. TITLE AND SUBTITLE
LOW-Cost, High-Throughput 3D Pulmonary Imager Using Hyperpolarized Contrast Agents and Low-Field MRI

5a. CONTRACT NUMBER
W81XWH–15–1–0271

5b. GRANT NUMBER

5c. PROGRAM ELEMENT NUMBER

6. AUTHOR(S)
Eduard Y. Chekmenev, Ph.D.

E-Mail: chekmenev@wayne.edu

5d. PROJECT NUMBER

5e. TASK NUMBER

5f. WORK UNIT NUMBER

7. PERFORMING ORGANIZATION NAME(S) AND ADDRESS(ES)
Wayne State University
5101 Cass Ave
DETROIT, MI, 48202

8. PERFORMING ORGANIZATION REPORT NUMBER

9. SPONSORING / MONITORING AGENCY NAME(S) AND ADDRESS(ES)

U.S. Army Medical Research and Materiel Command
Fort Detrick, Maryland 21702-5012

10. SPONSOR/MONITOR'S ACRONYM(S)

11. SPONSOR/MONITOR'S REPORT NUMBER(S)

12. DISTRIBUTION / AVAILABILITY STATEMENT

Approved for Public Release; Distribution Unlimited

13. SUPPLEMENTARY NOTES

14. ABSTRACT
This report covers the first year of the no-cost extension period. Overall, this is the fourth year of the project performance. During the indicated period of performance, we have focused our activities on all three specific aims. With regards to Aim #1 (^{129}Xe polarizer development), we have been working on testing the ^{129}Xe automated hyperpolarizer: to that goal, we have performed extensive tests of all key components of this device as we reported earlier and also focused on automation and integration completion. With regards to propane hyperpolarization, we have focused our efforts on additional tests and investigating the approaches to improve the quality of hyperpolarized propane gas. The remaining efforts will primarily focus on testing this device with the 0.35 T MRI scanner. With respect to the delivery and installation of 0.35 T MRI scanner, we have been engaged with the vendor to ensure that the delivered MRI scanner will be customized to our needs to meet the specifications for scan speed and resolution.

15. SUBJECT TERMS
low-field MRI; pulmonary imaging, high-throughput; low cost

16. SECURITY CLASSIFICATION OF:			17. LIMITATION OF ABSTRACT	18. NUMBER OF PAGES	19a. NAME OF RESPONSIBLE PERSON
a. REPORT	b. ABSTRACT	c. THIS PAGE			USAMRMC
Unclassified	Unclassified	Unclassified	Unclassified	96	19b. TELEPHONE NUMBER *(include area code)*

Standard Form 298 (Rev. 8-98)
Prescribed by ANSI Std. Z39.18

Table of Contents

Page

1. Introduction

We are developing clinical scale production of two gaseous hyperpolarized contrast agents and hyperpolarized MRI allowing for ultrafast (potentially sub-second) and high-throughput molecular imaging of lung function. The key additional focus of this project is on significantly lower cost of our imaging technology of low-field MRI compared to conventional high-field MRI (1.5 T and beyond) due to much higher patient throughput/much faster exams and the use of low field = low cost MRI. We focus our research effort on the high-risk critical challenges that must be solved to enable clinical implementation of hyperpolarized gases for pulmonary imaging.

Specifically, the research efforts during Year 4 have focused on three specific aims as described in the Statement of Work (Appendix 1):

Aim 1: Develop and construct a fully automated high-pressure low-cost stand-alone ^{129}Xe hyperpolarizer

During Year 3 the original laser of the ^{129}Xe hyperpolarizer failed (due to a design flaw), and it was replaced by a different laser (from the same vendor) during Year 4 of the project performance. Our team at Wayne State University has installed the laser, and performed tests. While this new laser has met the required specifications, its performance has deteriorated within 4 months after the installation (as a reference, a similar laser previously installed in the PI lab has been operated for a period of 5 years without a noticeable changes in performance). During this period of time our team has performed exhaustive tests on this hyperpolarizer device, identifying areas of improvement of the hyperpolarization process. The performed work is described in the accomplishments. Once the laser deterioration was noticed and characterized, the laser was sent back to the vendor for repairs. We expect the laser to be fixed by vendor, and the device to be operational for integration with the low-field MRI scanner.

Aim 2: Develop a large-scale hyperpolarization method for HP propane

As noted in the previous reports, we have developed and installed clinical-scale hyperpolarizer. The activities during Year 4 have focused in improving the relaxation properties of hyperpolarized propane and researching other biomedically suitable hydrocarbons as inhalable proton-hyperpolarized contrast agents.

Aim 3: Develop and construct a 0.35 T MRI scanner

As descried in the previous reports, we have placed the order for a custom 0.35 T clinical MRI scanner from Time-Medical, which will provide FDA-approved proton imaging capability and clinical research ^{129}Xe imaging capabilities. This report describes our activities during Year 4 and the estimated time line for device installation at Wayne State University.

2. Keywords

Low-field MRI, lung imaging, molecular imaging, functional imaging; propane; xenon-129; NMR; MRI; hyperpolarization.

3. ACCOMPLISHMENTS

Please, refer to Appendix 1 for the statement of work of the entire project. The following sections describe the specific areas/tasks of the project conducted during Year 4 of this project.

Aim 1.

Task 1.6 Final Testing of the ^{129}Xe Hyperpolarizer

The key challenge that our team has faced with the new hyperpolarizer device is the failure of the laser module during Y3 of the project. A new laser was received during Year 4. Unfortunately, it has failed after only four months of moderate use. The laser was sent back to the vendor for repairs. We expect the repairs to be finished during Year 5 of the project and the ^{129}Xe hyperpolarizer to be ready for integration with the 0.35 T MRI scanner. During the four-month period, we have performed extensive testing of the hyperpolarizer, detailing the quality and the production rates of this stand-alone device. The results of these tests are now summarized in a manuscript, which is being submitted for publication in a peer-reviewed journal. We found that indeed the new hyperpolarizer device offers advantages over the previous-generation device primarily from the perspective of significantly faster production of HP ^{129}Xe gas (not to mention simpler device operation).

During this period of performance, we have also performed studies to investigate the utility of helium-rich ^{129}Xe gas mixtures versus the previously employed N_2-rich mixtures for our hyperpolarization process. He has much better thermal conductivity than N_2, and therefore it was hypothesized that He may render better thermal management of the spin-exchange optical pumping process of ^{129}Xe gas hyperpolarization. Indeed, our results confirmed this hypothesis. While the gains seen are modest (5-10%), they positively impact the process of hyperpolarization, and we aim to employ them in our future studies. From the data presented in Figure 1a and Figure 1b, we draw three primary conclusions. The first of these is that SEOP in the ^{4}He-rich gas mixture resulted in a slight increase in maximum achievable P_{Xe} (55.9 ± 0.9% at a jacket temperature of 64 °C), relative to the N_2-rich mixture (49.3 ± 3.3% at a jacket temperature of 70 °C). Secondly, near-identical ^{129}Xe polarization build-up rates were achieved in the ^{4}He-rich gas-mixture at substantially lower jacket temperatures (ΔT ~ 8 °C) for rapid polarization build-up with γ_{SEOP} ~ 0.1 min^{-1}. Lastly, cells with ^{4}He-rich SEOP experienced a significantly more stable maximum P_{Xe} as a function of changing jacket temperature, with a flatter plateau--illustrating ^{129}Xe polarization values between 50% and 60% being achieved over a range of temperatures from 58 °C to 67 °C. By contrast, the N_2-rich gas mixture began to show a steady reduction in P_{Xe} when performing SEOP above 69 °C. This result is of practical importance, because it means that the polarizer operation is easier to automate (because of more stable operation over a wider temperature range), with a quicker cool-down cycle (resulting in reduced dead time and increased duty cycle). As an aside, we note that there is an additional benefit for using helium in the gas mixture: the less-dense gas mixture is easier to inhale, particularly for subjects with impaired lung function.

Selected results of this work are summarized below in Figure 1, and will soon be submitted for peer-reviewed publication in Year 5.

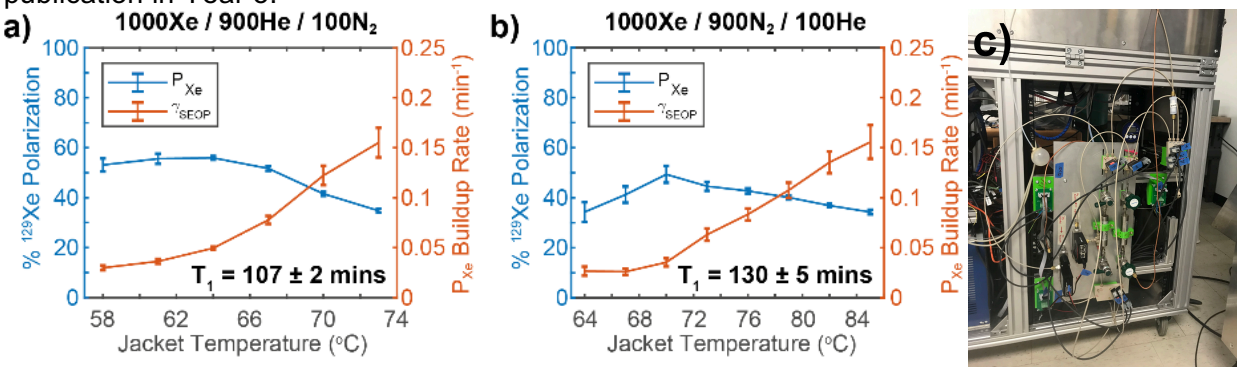

Figure 1. Steady state $\%P_{Xe}$ and γ_{SEOP} measurements following rapid-buildup, high T_1 SEOP in both He-rich (1000 Torr Xe / 900 Torr He / 100 Torr N_2, (a) and N_2-rich (1000 Torr Xe / 900 Torr N_2 / 100 Torr He, (b)) gas mixtures as a function of optical cell jacket temperature. Note the higher polarization achieved in (a) over a wider temperature range, despite the somewhat shorter ^{129}Xe T_1 relaxation time constant.

While performing the extensive tests during Y4 of the project, we discovered that although the existing gas-loading manifold of the ^{129}Xe hyperpolarizer allows for reloading of the optical pumping cell with a new batch of ^{129}Xe gas, the quality of the cell deteriorates in approximately 10 refills. During trouble-shooting we concluded that the likely failure is caused by the solenoid valves employed. We note that the vendor of these valves rates

them for the vacuum use, but we clearly experienced challenges likely due to oxygen contamination pointing to the valves. As a result of these findings, we have redesigned the gas-loading manifold of the ^{129}Xe hyperpolarizer device using a different type of solenoid valves (which we have tested for vacuum and pressure performance in our laboratory). A new manifold has been constructed during Year 4 of the project performance, and it has passed initial pressure testing. During Year 5, we will perform a quality assurance study to demonstrate that the SEOP cell can be refilled many times. Our metrics of success: successful refill of more than 200 times (monitored by P_{Xe} (a change of no more than a factor of 2) and by ^{129}Xe T_1 (more than 60 minutes)). We plan on testing the new gas-loading manifold with our previously constructed hyperpolarizer when the laser module will be repaired by the vendor. The photograph of the new manifold installed in the polarizer for testing is shown in Figure 1c.

We have also installed a glove box and other auxiliary equipment, which allows the team at Wayne State University to fill Rb metal in spin-exchange optical pumping cells. This new equipment allows us to place Rb in the SEOP cell, and then remove the SEOP cell from the glove box. The next step is applying vacuum and spreading Rb metal on the walls of the SEOP cell. The final step is filling the SEOP cell with the custom Xe mixture. Overall, we have already filled over 10 SEOP cells using this setup.

Aim 2. Following the success of clinical production demonstration reported in the previous report, the activities during Year 4 of the project were focused around Task 2.4. The activities for task 2.6 will be performed after the installation of the MRI scanner as described under the progress of Aim 3.

Task 2.4 Prototype Optimization

Our previous reports have demonstrated the clinical-scale propane hyperpolarizer. The corresponding publication has been published during Year 4 of the project (peer-reviewed paper #6). Moreover, we have also previously reported on the study of the relaxation properties in the clinically relevant conditions, and the corresponding results have been published during Year 4 (peer-reviewed paper #2).

During this project, we have also investigated (and reported in previous reports) the feasibility of parahydrogen (pH_2) addition to cyclopropane yielding more symmetric and potentially ultra-long-lived spin states (ULLSS) of propane**.** We have recently employed a Rh/TiO_2 heterogeneous catalyst to perform pairwise addition to cyclopropane despite the lack of a double bond in the cyclopropane molecular structure (Salnikov OG, Kovtunov KV, Nikolaou P, Kovtunova LM, Bukhtiyarov VI, Koptyug IV, Chekmenev EY. Heterogeneous Parahydrogen Pairwise Addition to Cyclopropane. ChemPhysChem. 2018;19(20):2621-2626). Unlike the case of propylene substrate (yielding one major spin isomer product), pairwise pH_2 addition to cyclopropane leads to formation of three spin isomers based on the proposed reaction mechanism (Figure 2a). Only one of the three HP spin-isomers is NMR visible. Because the HP states produced by route 2 and 3 (Figure 2) are NMR invisible, we have employed deuteration of cyclopropane to provide more mechanistic insights. In case of propylene, the deuteration primarily proceeds in accord to route 1 (Figure 2c), whereas in case of cyclopropane, deuteration happens via all three routes (Figure 2c). The comparison of thermal proton NMR spectra of the produced propane is shown in Figure 2d (note the NMR lines are complex due to convoluted multiplets): indeed, NMR spectra of cyclopropane-derived deuterated products reveal additional spectral intensity (green trace) compared to that of propylene-derived deuterated products (blue trace). Depending on the experimental conditions the contribution of route 1 varied from 15% to 30% in case of cyclopropane. This finding is important, because it confirms that deuterium addition to cyclopropane indeed undergoes hydrogenation via all three routes (Figure 2)—indicating that route

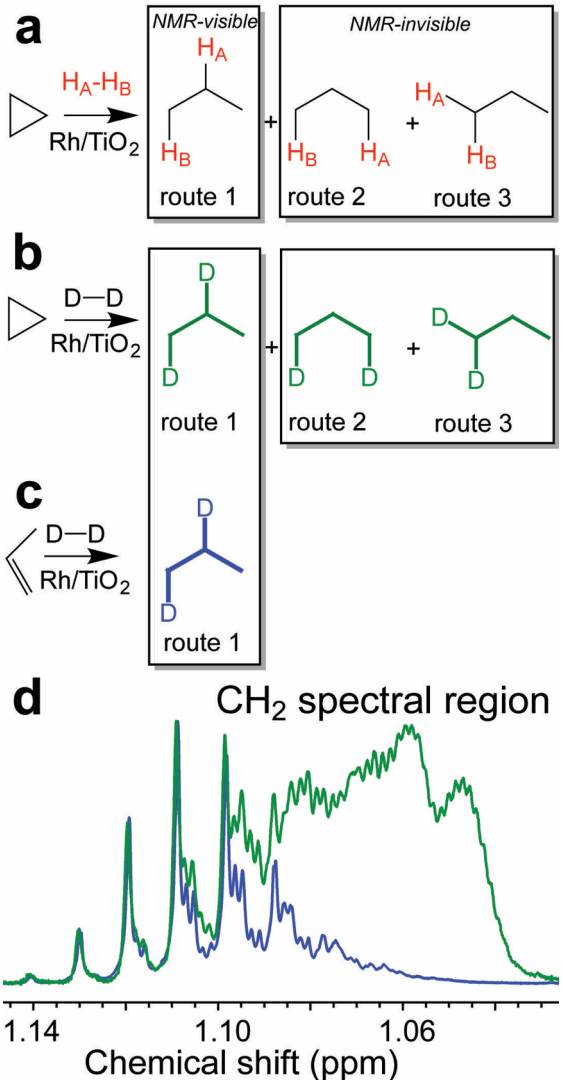

Figure 2. (a) diagram of pairwise pH_2 addition to cyclopropane; (b) diagram of D_2 addition to cyclopropane; (c) diagram of D_2 addition to propylene; (d) ^{1}H NMR spectroscopy (700 MHz) of reaction products via reaction processes shown in b (green trace) and c (blue trace).

2 and 3 dominate over route 1 in case of pH_2 addition, even if the products are NMR invisible—as in the case of parahydrogen addition to cyclopropane.

The products produced by routes 2 and 3 have a higher degree of symmetry, because both pH_2-derived protons are in the same type of chemical group ($-CH_3$), versus $-CH_2$ and $-CH_3$ in case of route 1. The enhanced symmetry offers two advantages. First of all, different and more symmetric spin states may be populated and the lifetime of the produced HP state can be enhanced significantly. In favorable cases, the exponential decay constant T_{LLSS} can exceed T_1 by 50-fold and more, corresponding to up to 1000 seconds in favorable cases of symmetric gases. Therefore, ***we hypothesize that more symmetric spin isomers of HP propane may indeed render ultra-long-lived spin states (ULLSS) with decay time constants on the order of one minute—and potentially up to 15 minutes***. The second advantage of these more symmetric spin states is a minute frequency difference (δ_A-δ_B) of less than 0.02 ppm, *i.e*. the condition of strong coupling $J_{AB}>(\delta_A-\delta_B)$ is met at any clinically relevant magnetic field (up to 3 T). As a result, these ULLSS may potentially remain long-lived on any clinical MRI scanner. This study was accomplished during Year 4 of the project, and we submitted funding application to DOD for the extension mechanism to continue this project with the goal of developing an ultra-long lived HP propane gas contrast agent.

Although our propane hyperpolarizer employs heterogeneous catalysis, during project performance, we have investigated the possibility of employing homogeneous catalysis for hyperpolarization of propane (Salnikov OG, Barskiy DA, Coffey AM, Kovtunov KV, Koptyug IV, Chekmenev EY. Efficient Batch-Mode Parahydrogen-Induced Polarization of Propane. ChemPhysChem. 2016;17(24):3395–3398). Although this process is relatively efficient, propane has unfavorable properties for homogeneous catalysis. Specifically, the boiling point is below -40 °C, which leads to unwanted evaporation of HP propane during the hyperpolarization process in our setup (Figure 3), which employs the process of parahydrogen bubbling via solution of catalyst and to-be-hyperpolarized substrate. During Year 4, we have investigated the feasibility of hyperpolarization of diethyl ether. Diethyl ether has a boiling point of +35 °C, and it is therefore less susceptible to evaporation under high pressure (typically 6-7 atm is employed). Figure 4 shows the feasibility study for such process. Approximately 12% proton polarization is demonstrated (Figure 3b) demonstrating the possibility of preparation of highly concentrated and highly polarized diethyl ether. This is very promising, because high levels of polarization (*i.e*. significantly exceeding 1% for HP propane) can be obtained.

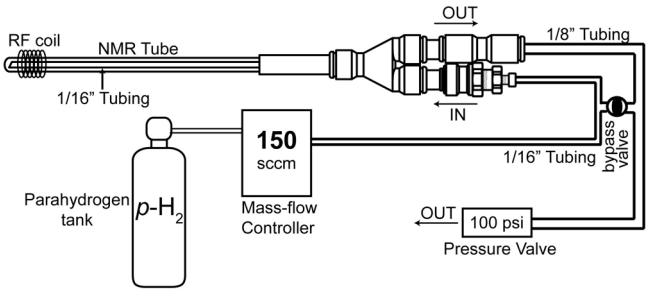

Figure 3. **Schematic of polarizer setup** for homogeneous PHIP hyperpolarization.

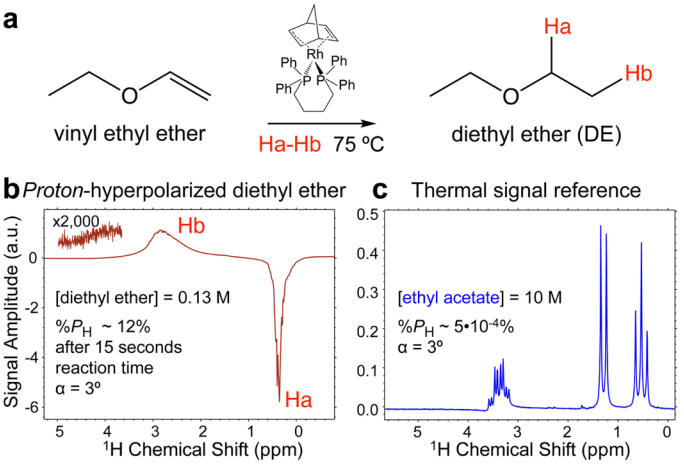

Figure 4. **PHIP of diethyl ether (DE) in methanol-d_4**. (a) Reaction scheme of molecular addition of parahydrogen to vinyl ethyl ether resulting in HP diethyl ether, (b) high-resolution NMR spectroscopy of HP diethyl ether in methanol-d_4 at 1.4 T (NMR spectrum is acquired 10 seconds after production. (c) corresponding signal reference spectrum of thermally polarized neat ethyl acetate-1-^{13}C.

Aim 3. Develop and construct a 0.05 T MRI scanner

Task 3.1. Design low-field MRI system with commercial vendors

We have described our plan for acquisition of a 0.35 T MRI system from Time Medical previously. As a part of transition to Wayne State University (WSU), WSU has made the commitment for space and infrastructure (up to $1.1M) of the 0.35 T MRI system to support this funded project. No space option was found at VUMC (previous institution).

The order to Time-Medical has been placed during Year 4 of the project for the MRI scanner and its delivery. The space renovation to suit the needs of the proposed research has been approved and began during Year 4 of the project. The completion of the space renovation is expected by the end of February. The delivery and installation of the magnet and the patient bed is scheduled for January 8-10 (2020) time frame and the installation of the MRI scanner console is scheduled for March 2020.

The MRI scanner will be installed in ~850 sq. ft. facility consisting of four major areas:

(1) chemistry space for production of parahydrogen and hyperpolarized ^{129}Xe. The ^{129}Xe hyperpolarizer developed under this project will be installed in this facility. This space will also be equipped with dual channel ^{129}Xe/^{1}H benchtop NMR spectrometer for quality assurance of hyperpolarized ^{129}Xe gas and *proton*-hyperpolarized hydrocarbons;
(2) control room equipped with computer stations for MRI image acquisition and image processing;
(3) shield room that contains the 0.35 T MRI magnet equipped with patient bed. This area will also contain the clinical-scale propane hyperpolarizer.
(4) equipment room, which will house the remaining equipment including the MRI scanner console.

The vendor (Time-Medical) plans to deliver the MRI system in Year 5; the scanner is FDA-approved in the USA. This scanner will have a significant benefit in terms of the potential clinical translation of propane MRI scan as the hardware is already FDA approved. Once the HP agent is approved, the entire scan can be easily translated to clinical setting. During Year 4, we worked with the vendor on the logistics of the ^{129}Xe hardware/software frame, and also worked extensively on the siting preparation (of note our first siting option on campus did not meet our collective requirements to bring together MRI and novel chemistries of HP contrast agent production, but luckily this problem was remedied with the second siting option).

Time Medical (the vendor of the MRI scanner) agreed to develop the ^{129}Xe hardware/software, which we discussed extensively during Year 4 of the project. Specifically, the following listed items have been thoroughly discussed with the vendor:

1) Additional RF excitation volume coil built and integrated in the body frame of the MRI scanner. This coil will provide uniform RF excitation for ^{129}Xe scans;
2) Additional electronic board to enable ^{129}Xe transmit and receive; This board will be switchable: *i.e*. if the board is physically powered off, the device will remain FDA compliant (for scanning of *proton*-hyperpolarized contrast agents);
3) Ecoplanar imaging (EPI) sequence will be available on this MRI scanner for the purpose of ultrafast MRI scans on ^{1}H and ^{129}Xe channels;
4) Custom chest RF coil will be developed to provide simultaneous acquisition of optimized ^{129}Xe images and coarse (for co-registration purposes) of anatomical proton scans;
5) Vendor will provide co-registration software for seamless co-registration of anatomical and 129Xe gas images.

We expect the vendor to deliver all of these components by the end of the funding period 06/06/2020.

Task 3.2. Low-field MRI system construction by Vendors

The magnet construction and the construction of other components has started by the vendor. The delivery, installation and training timelines have been provided by the vendor (during Year 5 of the project).

Task 3.4. RF coils (^{129}Xe and ^{1}H) construction for pulmonary imaging

The RF coil design has been discussed with the vendor extensively during Year 4. The coil will be dual tuned with the sensitivity optimized for ^{129}Xe, while proton detection (in this RF coil) will have significantly reduced sensitivity – primarily for the purposes of anatomy co-registration. The vendor will also provide their standard suite of RF imaging coils for proton MRI.

Task 3.5. Pulse-sequence development and installation

Two sequences have been discussed with the vendor: gradient echo imaging and eco-planar imaging (2D and 3D). The vendor is aware of the requirement that the HP gas scan is to be completed on a single breath hold of a large animal or a human.

What opportunities for training and professional development has the project provided?

Several trainees from the partnering site (SIUC) attended the 60th Experimental Nuclear Magnetic Resonance conference

How were the results disseminated to communities of interest?

Several oral presentations (see below).

4. IMPACT

What was the impact on the development of the principal discipline(s) of the project?

Nothing to Report.

What was the impact on other disciplines?

Nothing to Report.

What was the impact on technology transfer?

Nothing to Report.

What was the impact on society beyond science and technology?

Nothing to Report.

5. CHANGES / PROBLEMS

We have fixed the issue with our laser diode array (LDA) during Year 4 by replacing LDA with the older (and supposedly more reliable) model. Unfortunately, the new LDA has deteriorated very quickly (in 4 months of relatively light use: less than 200h of total run time). The LDA has been shipped back to vendor. Repairs are in progress.

6. PRODUCTS

Oral Presentations

1) Chekmenev EY. Parahydrogen Derived Polarization for Metabolic Imaging. The Fifth International Workshop on Metabolic Imaging; October 18-20; University of Pennsylvania, Philadelphia, PA, USA 2018.
2) Goodson BM. New Approaches in SABRE: Cleavable Metabolic / pH-Sensing "Double Agents", and Preparation of Purified Agents via Heterogeneous Catalysis and Catalyst Immobilization. The Fifth International Workshop on Metabolic Imaging; October 18-20; University of Pennsylvania, Philadelphia, PA, USA 2018.
3) Chekmenev EY. Parahydrogen Derived Polarization for Metabolic Imaging. Department of Chemistry Seminar Series; April 23; Texas A&M University, College Station, TX, USA 2019.
4) Salnikov OG, Ariyasingha NM, Nikolaou P, Goodson BM, Kovtunov KV, Koptyug IV, Chekmenev EY. Hyperpolarized Propane: Clinical-scale Production of Long Lived Spin States, Condensation, and Imaging. The 2019 International Workshop on Pulmonary Imaging; February 28-March 2; University of Pennsylvania, Philadelphia, PA, USA 2019.
5) Chekmenev EY. Long-lived hyperpolarized spin state enabled by low magnetic fields. Workshop on Low Field Magnetic Resonance; August 11-13; NIST, Boulder, CO, USA 2019.
6) Goodson BM. New Developments in 129Xe and 131Xe Hyperpolarization via Clinical-Scale Stopped-Flow Spin-Exchange Optical Pumping. The 2019 International Workshop on Pulmonary Imaging; February 28-March 2; University of Pennsylvania, Philadelphia, PA, USA 2019.
7) Salnikov OG, Kovtunov KV, Ariyasingha NM, Nikolaou P, Chekmenev EY, Koptyug IV. New developments in production of proton-hyperpolarized propane gas for MRI. EUROISMAR 2019; August 25-30; Berlin, Germany 2019.
8) Shchepin R, Birchall J, Chukanov N, Kovtunov K, Koptyug I, Theis T, Warren W, Gelovani J, Goodson B, Rosen M, Yen Y-F, Pham W, Chekmenev EY. Efficient Spin-Relayed Heteronuclear Long-Range Signal Amplification by Reversible Exchange. 60th Experimental NMR Conference; April 7-12; Asilomar, CA, USA2019.

Conference Abstracts

9) Bales L, Basler D, Albin K, Islam S, Barlow MJ, Chekmenev EY, Goodson BM. Developing Hyperpolarized 131Xe as a Potential Target for Neutron Optics Searches for Time-Reversal Invariance Violation. 60th Experimental NMR Conference; April 7-12; Asilomar, CA, USA 2019.
10) Limbach MN, Gemeinhardt ME, Gebhardt TR, Senanayake I, Mashni JA, Kidd BE, Chekmenev EY, Hou Y, Goodson BM. Towards Synthesis of a Family of Novel Cleavable “Double Agents” for SABRE Hyperpolarization. 60th Experimental NMR Conference; April 7-12; Asilomar, CA, USA 2019.
11) Porter J, Basler D, Plummer JW, Russell G, Kidd BE, Chekmenev EY, Barlow MJ, Goodson BM. 85Rb / 133Cs Optically Detected Electron Spin Resonance in “Hybrid” Spin-Exchange Optical Pumping Cells in Clinically Relevant Regimes. 60th Experimental NMR Conference; April 7-12; Asilomar, CA, USA 2019.

Peer-Reviewed Manuscripts, Dissertation & Book Chapters

1) Ariyasingha NM, Lindale JR, Eriksson SL, Clark GP, Theis T, Shchepin RV, Chukanov NV, Kovtunov KV, Koptyug IV, Warren WS, Chekmenev EY. Quasi-Resonance Fluorine-19 Signal Amplification by Reversible Exchange. The Journal of Physical Chemistry Letters. 2019;10:4229-4236.
2) Ariyasingha NM, Salnikov OG, Kovtunov KV, Kovtunova LM, Bukhtiyarov VI, Goodson BM, Rosen MS, Koptyug IV, Gelovani JG, Chekmenev EY. Relaxation Dynamics of Nuclear Long-Lived Spin States in Propane and Propane-d6 Hyperpolarized by Parahydrogen. The Journal of Physical Chemistry C. 2019;18(123):11734–11744.
3) Chukanov NV, Kidd BM, Kovtunova LM, Bukhtiyarov VI, Shchepin RV, Chekmenev EY, Goodson BM, Kovtunov KV, Koptyug IV. A versatile synthetic route to the preparation of ^{15}N heterocycles. Journal of Labelled Compounds and Radiopharmaceuticals. 2019:doi:10.1002/jlcr.3699.

4) Lindale JR, Eriksson SL, Tanner CPN, Zhou Z, Colell JFP, Zhang G, Bae J, Chekmenev EY, Theis T, Warren WS. Unveiling coherently driven hyperpolarization dynamics in signal amplification by reversible exchange. Nature Communications. 2019;10(1):395.
5) Salnikov OG, Chukanov NV, Shchepin RV, Manzanera Esteve IV, Kovtunov KV, Koptyug IV, Chekmenev EY. Parahydrogen-Induced Polarization of 1-^{13}C-Acetates and 1-^{13}C-Pyruvates Using Side-Arm Hydrogenation of Vinyl, Allyl and Propargyl Esters. The Journal of Physical Chemistry C. 2019;123(20):12827-12840.
6) Salnikov OG, Nikolaou P, Ariyasingha NM, Kovtunov KV, Koptyug IV, Chekmenev EY. Clinical-Scale Batch-Mode Production of Hyperpolarized Propane Gas for MRI. Analytical Chemistry. 2019;91(7):4741–4746.
7) Shchepin RV, Birchall JR, Chukanov NV, Kovtunov KV, Koptyug IV, Theis T, Warren WS, Gelovani JG, Goodson BM, Shokouhi S, Rosen MS, Yen Y-F, Pham W, Chekmenev EY. Hyperpolarizing Concentrated Metronidazole $^{15}NO_2$ Group Over Six Chemical Bonds with More Than 15% Polarization and 20 Minute Lifetime. Chemistry – A European Journal. 2019;25:8829-8836.

Inventions, patent applications and licenses:

Nothing to Report.

Funding applied for based on work supported by this award

1. Title "**Ultra-Long-Lived Hyperpolarized Propane Gas for 3D Pulmonary Imaging**"
   Eduard Y Chekmenev, Wayne State University, PI
   Boyd M. Goodson, Southern Illinois University Carbondale (SIUC), co-investigator
   Time Commitment: PI (35% effort; 4.2 calendar months)
   Supporting agency: DOD
   Program Contact Name: not yet available
   Program Contact Phone: not yet available
   Program Contact Email: not yet available
   Performance period: 4/1/2020 to 3/31/2023
   Level of funding: $ 1,741,808 (total award including IDC) at
   We have worked to develop an alternative to hyperpolarized noble gases for MRI imaging applications. We recently demonstrated that hydrogen nuclei of gaseous propane can be hyperpolarized using parahydrogen induced polarization (PHIP) to a sufficiently high level to enable high-resolution 2D and 3D MRI. Although early efforts with HP propane at high magnetic field revealed a very short exponential decay constant of the HP state T_1 of ~1 s, our recent research demonstrated the existence of long-lived spin states (LLSS) in HP propane gas at lower magnetic fields. The LLSS of HP propane decays exponentially with the constant T_{LLSS} of ~3 s at 1 atm (and more than 13 s at elevated pressure). Although it may be possible to perform *in vivo* imaging using this rapidly decaying LLSS, this approach will require significant image correction to account for rapid signal decay during an MRI scan, and it will require very fast HP propane administration work flow. Moreover, the propane LLSS requires a low magnetic field of 0.35 T and below, and MRI detection requires application of specialized pulse sequences. Here, we propose to develop ultra-long-lived spin states (ULLSS) of HP propane by employing deuterated cyclopropane as a precursor for parahydrogen addition (the source of hyperpolarization), which renders creation of more symmetric and therefore potentially longer-lived spin states (*i.e*. higher decay constant T_{ULLSS}) than those in HP propane LLSS prepared by hydrogenation of propylene. ***We hypothesize that the ULLSS lifetime of HP propane can be enhanced significantly – potentially by an order of magnitude, and these more symmetric ULLSS can exist at any clinically relevant magnetic fields, and can be readily detected using conventional MRI pulse sequences with 3D sub-second scan speed***. These advances should enable the clinical use of HP propane gas, which can be mass-produced at significantly higher production rates (one dose every 5 seconds) at a small fraction of the cost (<$1) of hyperpolarized ^{129}Xe.
   Specific Aims:
   Aim 1. Develop a facile synthesis of deuterated cyclopropane: we will employ a deuterium exchange process between D_2O and cyclopropane on zeolites to prepare deuterated cyclopropane from cyclopropane.
   Aim 2. Hyperpolarize ultra-long-lived spin states of propane by pairwise parahydrogen addition of deuterated cyclopropane. We hypothesize that each of the many possible spin states will have a characteristic decay constant. Here, we will study the lifetime of the HP state as a function of the level

of deuteration, reactants' temperature, and partial pressures. We will also investigate the possibility of tuning the reaction conditions to predominantly prepare a spin isomer of interest.
Aim 3. Optimize the hyperpolarization process of parahydrogen induced polarization (PHIP) of ULLSS of propane for efficient clinical scale production and MRI. In parallel to Aim 2, we will study the process of clinical-scale production (0.5 L dose in ≤ 5 seconds) of ULLSS of hyperpolarized propane by investigating the effects of temperature, reactant's mixture partial pressure, and particle size of the Rh/TiO_2 heterogeneous catalyst.

2. Title "**Low-Cost, High-Throughput 3D Pulmonary Imaging Using Hyperpolarized Propane Gas**"
Eduard Y Chekmenev, Wayne State University, initiating PI
Boyd M. Goodson, Southern Illinois University Carbondale (SIUC), partnering PI
Time Commitment: PI (35% effort; 4.2 calendar months)
Supporting agency: DOD
Program Contact Name: not yet available
Program Contact Phone: not yet available
Program Contact Email: not yet available
Performance period: 4/1/2020 to 3/31/2023
Level of funding: $ 1,732,500 (total award including IDC)
We have worked to develop an alternative to hyperpolarized noble gases for MRI imaging applications. We recently demonstrated that hydrogen nuclei of gaseous propane can be hyperpolarized using parahydrogen induced polarization (PHIP) to a sufficiently high level suitable for 2D and 3D MRI. Our early efforts with HP propane at high magnetic field revealed a very short relaxation constant for the exponential decay of the propane gas hyperpolarized state of ~1 s. Importantly, our research recently demonstrated the existence of longer-lived spin states in hyperpolarized propane gas in lower magnetic fields (0.35 T and below). These spin states allow significantly extending the lifetime of hyperpolarized propane (e.g. increasing the decay constant of up to >13 s) making it suitably long-lived for administration as an inhalable contrast agent. Moreover, our research clearly demonstrates that the low-field MRI detection of hyperpolarized contrast agents in general offers the same or even better detection sensitivity as that of high-field MRI scanners. These two developments--long-lived proton-hyperpolarized propane gas and low-field MRI on conventional FDA-approved MRI scanners—should enable the clinical use of HP propane gas, which can be mass-produced at significantly higher production rates (one dose every 2-5 seconds) at a fraction of the cost of hyperpolarized ^{129}Xe.
In 2014, Chekmenev and Goodson received a partnering PI CDMRP award. This award enabled the development of our human-scale hyperpolarizer device (successfully completed). Here, we propose taking the next significant step to develop and test a hyperpolarized propane production technology device under the following **Specific Aims:**
Aim 1. Develop a clinical low-cost and high-throughput biomedical device for production of hyperpolarized propane contrast agent: the future propane hyperpolarizer will be developed to enable its Good Manufacturing Practices (GMP), mass-production, and robust use;
Aim 2. Develop a safe method for HP propane gas administration and utilization, and test the purity and safety of the HP contrast agent produced by our device;
Aim 3. Assess the feasibility of MRI using HP propane gas for *in vivo* functional imaging of normal lungs and in a bleomycin-induced COPD model in sheep. We will compare the effectiveness of hyperpolarized propane MRI to that using a more established contrast agent (hyperpolarized ^{129}Xe gas—created using a polarizer we developed in our previous DOD-funded work), and also to the standards of care: computed tomography and spirometry. Furthermore, we will also investigate the effectiveness of hyperpolarized propane gas MRI to monitor the progression of bleomycin-induced lung injury in the sheep animal model.

3. Title "**Sub-second Functional Lung Proton MRI Using Hyperpolarized Propane Gas in a Clinical Scanner**"
Eduard Y Chekmenev, Wayne State University, PI
Boyd M. Goodson, Southern Illinois University Carbondale (SIUC), co-investigator
Time Commitment: PI (35% effort; 4.2 calendar months)
Supporting agency: NIH
RHL152027A
Program Contact Name: not yet available
Program Contact Phone: not yet available

Program Contact Email: not yet available
Performance period: 4/1/2020 to 3/31/2024
Level of funding: $ 3,074,142 (total award including IDC)
We propose in vivo validation of hyperpolarized propane gas as an inhalable contrast agent to perform a sub-second functional 3D lung MRI scan using conventional FDA-approved low-field (0.35 T) non-cryogenic MRI scanners already available in the US and around the world. The proposed technology will employ no ionizing radiation, and it can be used for population screening, staging, and also for monitoring the response to treatment. It will be superior to spirometry and chest X-ray methods practiced today in a number of important ways, including early disease detection and characterization, which can be difficult to accomplish with these conventional methods.
Specific Aims:
Aim 1. Develop a clinical, low-cost, high-throughput device for production and administration of HP propane contrast agent for ultimate research use in human volunteers: the future propane hyperpolarizer will be developed to enable its Good Manufacturing Practices (GMP), mass-production, and robust use.
Aim 2. Develop a safe method for HP propane gas administration and utilization, and test the purity and safety of the HP contrast agent produced by our device.
Aim 3. Assess the feasibility of ultrafast ^{1}H MRI using HP propane gas for *in vivo* functional imaging of normal lungs and in a bleomycin-induced lung injury model in sheep. As part of this effort, we will compare the effectiveness of hyperpolarized propane MRI to that using a more established contrast agent (hyperpolarized ^{129}Xe gas—created using a hyperpolarizer we developed in our previously funded work, and also to the standards of care: computed tomography and spirometry. Furthermore, we will also investigate the effectiveness of hyperpolarized propane gas MRI to monitor the progression of bleomycin-induced lung injury in the sheep animal model. We hypothesize that HP propane gas MRI will provide similar predictive power for detection of lung injury compare to that of HP ^{129}Xe MRI.

4. Title "**Hyperpolarized Diethyl Ether for Sub-second Pulmonary MRI**"
Eduard Y Chekmenev, Wayne State University, PI
Time Commitment: PI (35% effort; 4.2 calendar months)
Supporting agency: NIH
Program Contact Name: not yet available
Program Contact Phone: not yet available
Program Contact Email: not yet available
Performance period: 4/1/2020 to 3/31/2024
Level of funding: $418,864 (total award including IDC)
We propose developing highly magnetized diethyl ether gas via pairwise addition of parahydrogen gas to vinyl ether. The proposed low-cost and high-throughput technology for clinical-scale production of hyperpolarized diethyl ether can be employed for sub-second gas pulmonary MRI, which we envision as a novel inhalable contrast agent for functional regional mapping of lung function in a wide range of lung diseases without the use of ionizing radiation.
Specific Aims:
Aim 1. Develop clinical-scale production of pure HP diethyl ether gas and optimize the production process to maximize the degree of polarization. Specifically, we will perform optimization of the hydrogenation catalyst, temperature and other reaction conditions. The metrics of success will be production of ~100 cubic centimeters (cc) corresponding to 0.3 grams of diethyl ether gas with 40% proton spin polarization.
Aim 2. Perform characterization of the lifetime of HP state of diethyl ether. Parallel to Aim 1, we will systematically study the T1 relaxation decay of HP state in several magnetic fields, partial pressures and in liquid and gaseous phases.
Aim 3. Investigate the feasibility of sub-second 3D MRI in phantoms and excised animal lungs. We will perform imaging studies on clinical FDA-approved MRI scanner with the goals of demonstrating the overall feasibility of future clinical MRI scan and investigating the limits of spatial resolution. The metrics of success will be a sub-second 3D scan speed on clinical MRI scanner with high in-plane spatial resolution of 2´2 mm2 pixel size over 320´320 mm2 field of view with pixel signal-to-noise ratio over 100 at physiologically-relevant contrast agent concentration of 0.5 mM.

7. PARTICIPANTS & OTHER COLLABORATING ORGANIZATIONS

Individuals worked on the project

The following personnel worked on the project

Name:	Eduard Chekmenev
Project Role:	Initiating PI (Vanderbilt)
Researcher Identifier (ORCID ID):	orcid.org/0000-0002-8745-8801
Nearest person month worked:	1
Contribution to Project:	Dr. Chekmenev was responsible for the overall progress of the project, performing some experiments with hyperpolarized propane and hyperpolarized xenon-129, developing RF coils, analyzing some of the data for the above-mentioned experiments, preparing the manuscripts.
Funding Support:	DOD W81XWH-12-1-0159/BC112431; NSF CHE-1416268;

Name:	Nuwandi M. Ariyasingha
Project Role:	PhD student
Researcher Identifier (ORCID ID):	
Nearest person month worked:	1
Contribution to Project:	Nuwandi M. Ariyasingha worked on many of the experiments concerning hyperpolarized clinical-scale propane hyperpolarization. She also analyzed the data, prepared figures, and manuscripts.
Funding Support:	DOD W81XWH-12-1-0159/BC112431

Name:	Boyd M. Goodson
Project Role:	Partnering PI (SIUC)
Researcher Identifier (ORCID ID):	orcid.org/0000-0001-6079-5077
Nearest person month worked:	1
Contribution to Project:	Prof. Goodson was responsible for the overall progress of the project at the partnering site, performing some experiments with hyperpolarized xenon-129, xenon-131, and ODESR polarization measurements, analyzing some of the data for the above-mentioned experiments, preparing manuscripts and presentations.
Funding Support:	SIUC DOD PRMRP W81XWH-15-1-0272 NSF-CHE-1905341 NSF DMR-1757954

Name:	Liana Bales
Project Role:	MS chemistry graduate student
Researcher Identifier (ORCID ID):	
Nearest person month worked:	2
Contribution to Project:	Led xenon-129 and xenon-131 spin-exchange optical pumping experiments, until she defended her MS thesis this summer. Processed and analyzed data, wrote up contents for presentations and manuscripts.
Funding Support:	SIUC / NMR Facility

Name:	Dustin Basler
Project Role:	Undergraduate student researcher
Researcher Identifier (ORCID ID):	Now leads xenon-129 and xenon-131 spin-exchange optical pumping experiments; participates in some optically detected ESR polarization measurements. Processes and analyzes data. Prepared conference presentations.
Nearest person month worked:	2
Contribution to Project:	
Funding Support:	DOD PRMRP W81XWH-15-1-0272 SIUC Chemistry Alumni Foundation Research Corporation Cottrell SEED Award

Name:	Justin Porter
Project Role:	Undergraduate student researcher
Researcher Identifier (ORCID ID):	
Nearest person month worked:	2
Contribution to Project:	Performed xenon-129 spin-exchange optical pumping experiments, led use of optically detected ESR efforts to characterize spin polarization during optical pumping. Analyzed data, prepared conference presentions.
Funding Support:	DOD PRMRP W81XWH-15-1-0272 Research Corporation Cottrell SEED Award

Name:	Kierstyn Albin
Project Role:	Undergraduate student researcher
Researcher Identifier (ORCID ID):	
Nearest person month worked:	1
Contribution to Project:	Assisted with some xenon-129 spin-exchange optical pumping experiments and laser characterization experiments, analyzed data.
Funding Support:	DOD PRMRP W81XWH-15-1-0272 NSF DMR-1757954 Research Corporation Cottrell SEED Award

Has there been a change in the active other support of the PD/PI(s) or senior/key personnel since the last reporting period?

Yes, new NSF grant was awarded. Provided bellow, please see the detailed information.

Title "Collaborative Research: Exploiting Spin Networks and Efficient Catalyst/Substrate Separations for NMR "SABRE" Enhancement of Complex Systems"

CHE-1904780 (Chekmenev, PI; Goodson, collaborative PI)

Time Commitment: Principal Investigator (8.3% effort; 1.0 summer month)

Supporting agency: National Science Foundation

Program Contact Name: Kelsey D. Cook

Program Contact Phone: (703) 292-7490

Program Contact Email: kcook@nsf.gov

Performance period: 08/01/2019-07/31/2022

Level of funding: $282,000 (total award including IDC)

With support from the Chemical Measurement and Imaging Program in the Division of Chemistry, Professors Boyd Goodson at Southern Illinois University (SIU) and Eduard Chekmenev at Wayne State University (WSU) are working to improve the sensitivity of nuclear magnetic resonance (NMR), an important method of chemical analysis which underlies the well-known clinical imaging modality, magnetic resonance imaging (MRI). The Goodson/Chekmenev team is developing new, inexpensive, and easy-to-make means of enhancing nuclear magnetization - a sensitivity-limiting factor in many NMR and MRI applications, including diagnostic tests for a host of diseases. Anticipated cost savings can also make these methods more available for other lab settings, particularly those that have more limited research infrastructure and/or that feature undergraduate research. Several students are involved, gaining exposure to highly interdisciplinary training. The team is also engaged in efforts to recruit undergraduate students and match them with a variety of mentored research opportunities on both campuses, with a goal of increasing the numbers and diversity of undergraduate students seeking STEM careers.

The NMR/MRI approaches being used are based on Signal Amplification by Reversible Exchange, or SABRE. In SABRE, an organometallic catalyst is used to co-locate parahydrogen and a target molecule (substrate) within a transient complex; with properly matched external magnetic fields, nuclear spin order can transfer spontaneously and efficiently from parahydrogen to the substrate, giving rise to NMR and MRI signals that are increased by several orders of magnitude. Work by the Goodson/Chekmenev team seeks to: (1) improve the understanding and utility of long-range SABRE polarization transfer via spin-relay networks in model systems, for both homonuclear and heteronuclear cases; (2) develop and characterize new heterogeneous catalysts for SABRE ("HET-SABRE"), as well as approaches for catalyst recovery; and (3) broaden the range of substances amenable to SABRE through improved understanding of the fundamental quantum mechanics of complex spin behavior in model extended networks.

What other organizations were involved as partners?

In addition to the two performing sites (and consultant listed on the original application), we have been collaborating with scientists engaged in this project for Aim 2.

Organization Name: International Tomography Center

Location of Organization: Novosibirsk, Russia

Partner's contribution to the project:

In-kind support: Our collaborators provided catalyst materials for propane hyperpolarizer development work as well as for the final polarizer design;

Collaboration: We have enjoyed a planned two-month visit with two collaborators visiting us at Wayne State University site in the fall of 2018. We have performed collaborative experiments, analyzed the data. The work during this period has focused on preparing manuscripts for peer-reviewed publications. A new visit with the collaborators is underway in the fall of 2019, and the results of this visit will be reported in the next (final) progress report.

Personnel exchanges: see above.

Moreover, we have been collaborating with scientists engaged in this project for Aim 1 and Aim 3.

Organization Name: University of Nottingham

Location of Organization: Nottingham, UK

Partner's contribution to the project:

In-kind support: Our collaborators provided their insights in the design and installation of 0.35 T MRI scanner, and their input in the improvement of 129Xe hyperpolarizer.

Collaboration: We have enjoyed regular (monthly to weekly) teleconferences with the Nottingham team (lead PI: Michael J. Barlow). Moreover, we hosted a six-week long exchange visit with PhD student Robert Irwin, who visited Wayne State University site in the fall of 2019; two additional trainees from Nottingham, James Ball and Eleanor Sparling, performed capstone experiments for their MSC degrees at the partnering site (SIUC) for over 2 months.

Personnel exchanges:

See above.

8. SPECIAL REPORTING REQUIREMENTS

Collaborative Award

This is a collaborative award with two partnering PIs.

9. APPENDICES

Appendix 1: Original Statement of work, Years 1-3

STATEMENT OF WORK – 10/10/2014
PROPOSED START DATE September 1, 2015

Site 1:	Vanderbilt University		Site 2:	Southern Illinois University
	1161 21st Ave South MCN AA-1105 Nashville, TN 37232-2310			900 SOUTH NORMAL AVENUE CARBONDALE, IL 62901
	PI: Chekmenev			Partnering PI: Goodson

Specific Aim 1	Timeline	Site 1 (Vanderbilt)	Site 2 (SIU)
Develop and construct a fully automated high-pressure low-cost stand-alone ^{129}Xe hyperpolarizer	Months		
1.1. Design	1-5	80%	20%
1.2. Prototyping	6-10	75%	25%
1.3. Prototype construction and testing	11-15	90%	10%
Milestone Achieved	Prototype ^{129}Xe polarizer constructed		
1.4. Final Design	16-20	80%	20%
1.5. Final Construction	21-24	90%	10%
1.6. Final Testing	25-30	75%	25%
1.7. Polarizer Integration with MRI scanner	31-34	90%	10%
Milestone Achieved	Final ^{129}Xe polarizer constructed		
1.8. Replica Polarizer Construction and Testing	31-36	50%	50%
Milestone Achieved	Replica ^{129}Xe polarizer constructed		

Specific Aim 2	**Timeline**	**Site 1 (Vanderbilt)**	**Site 2 (SIU)**
Develop a large-scale hyperpolarization method for HP propane			
2.1. Chemistry of Large Scale PHIP of propane	1-6	75%	25%
Milestone Achieved:	Clinical Scale Production of HP Propane is developed		
2.2. Initial Polarizer Design	7-12	100%	0%
2.3. Polarizer Prototyping	13-18	100%	0%
Milestone Achieved:	Prototype Polarizer Constructed		
2.4. Prototype Optimization	19-24	100%	0%
2.5. Final Polarizer Construction	25-30	100%	0%
2.6. Final Polarizer Testing and Integration with low-field MRI system	31-36	75%	25%
Milestone(s) Achieved:	Final Propane Polarizer Constructed		
Specific Aim 3	**Timeline**	**Site 1 (Vanderbilt)**	**Site 2 (SIU)**
Develop and construct a 0.05 T MRI scanner	Months		
3.1. Design low-field MRI system with commercial vendors	1-6	50%	50%
3.2. Low-field MRI system construction by Vendors	7-12	50%	50%
3.3. Low-field MRI system installation and fine-tuning at site 1 (Vanderbilt)	13-18	100%	0%

Milestone Achieved:	Clinical low-field MRI system for high-throughout pulmonary imaging is installed		
3.4. RF coils (^{129}Xe and ^{1}H) construction for pulmonary imaging	19-24	100%	0%
3.5. Pulse-sequence development and installation	25-30	50%	50%
Milestone Achieved:	Low-field MRI system is ready for use with contrast agents		
3.6. MRI system integration with Propane Hyperpolarizer	31-36	100%	0%
3.7. MRI system integration with Propane Hyperpolarizer	31-34	90%	10%
3.8. Demonstration of high-speed MRI and high-speed contrast agent production/ imaging scan	35-36	90%	10%
Milestones Achieved:	Functional high-speed MRI of hyperpolarized propane and ^{129}Xe; System ready for clinical trial.		

Appendix 2: Abstracts Presented and Manuscripts Published and Accepted

9 abstracts and 7 published peer-reviewed publications are reported. PDF files of these materials are provided below in the Appendix 2.

THE JOURNAL OF PHYSICAL CHEMISTRY C

Article

Cite This: J. Phys. Chem. C 2019, 123, 11734−11744

pubs.acs.org/JPCC

Relaxation Dynamics of Nuclear Long-Lived Spin States in Propane and Propane-d_6 Hyperpolarized by Parahydrogen

Nuwandi M. Ariyasingha,[†] Oleg G. Salnikov,[‡,§] Kirill V. Kovtunov,[‡,§] Larisa M. Kovtunova,[§,∥] Valerii I. Bukhtiyarov,[§,∥] Boyd M. Goodson,[⊥] Matthew S. Rosen,[#] Igor V. Koptyug,[‡,§] Juri G. Gelovani,[†] and Eduard Y. Chekmenev*[,†,¶]

[†]Department of Chemistry, Integrative Biosciences (Ibio), Wayne State University, Karmanos Cancer Institute (KCI), Detroit, Michigan 48202, United States

[‡]International Tomography Center SB RAS, 3A Institutskaya Street, Novosibirsk 630090, Russia

[§]Novosibirsk State University, 2 Pirogova Street, Novosibirsk 630090, Russia

[∥]Boreskov Institute of Catalysis SB RAS, 5 Acad. Lavrentiev Pr., Novosibirsk 630090, Russia

[⊥]Department of Chemistry and Biochemistry and Materials Technology Center, Southern Illinois University, Carbondale, Illinois 62901, United States

[#]Massachusetts General Hospital, Athinoula A. Martinos Center for Biomedical Imaging, Boston, Massachusetts 02129, United States

[¶]Russian Academy of Sciences, Leninskiy Prospekt 14, Moscow 119991, Russia

Supporting Information

ABSTRACT: We report a systematic study of relaxation dynamics of hyperpolarized (HP) propane and HP propane-d_6 prepared by heterogeneous pairwise parahydrogen (pH_2) addition to propylene and propylene-d_6, respectively. Long-lived spin states (LLSs) created for these molecules at a low magnetic field of 0.0475 T were employed for this study. The parahydrogen-induced overpopulation of a HP propane LLS decays exponentially with a time constant (T_{LLS}) approximately threefold greater than the corresponding T_1 values. Both T_{LLS} and T_1 increase linearly with propane pressure in the range of 1 atm (the most biomedically relevant conditions for pulmonary MRI) to 5 atm. The T_{LLS} value of HP propane gas at 1 atm is ∼3 s. Deuteration of the substrate (propylene-d_6) yields HP propane-d_6 gas with T_{LLS} values approximately 20% shorter than those of HP fully protonated propane gas, indicating that deuteration does not benefit the lifetime of the LLS HP state. The use of pH_2 or Xe/N_2 buffering gas during heterogeneous hydrogenation reaction [leading to production of pure HP propane (100:0, i.e., no buffering gas) versus a 43:57 mixture of HP propane gas with buffering gas] results in (i) no significant changes in T_1, (ii) decrease of T_{LLS} values (by 35 ± 7 and 8 ± 7%, respectively); and (iii) an increase of the polarization levels of HP propane gas with a propane concentration decrease (by 1.6 ± 0.1-fold and 1.4 ± 0.1-fold, respectively, despite the decrease in T_{LLS}, which leads to disproportionately greater polarization losses during HP gas transport). Moreover, we demonstrate the feasibility of HP propane cryocollection (which can be potentially useful for preparing larger amounts of concentrated HP propane, when buffering gas is employed), and T_{LLS} of liquefied HP propane reaches 14.7 s, which is greater than the T_{LLS} value of HP propane gas at any pressure studied. Finally, we have explored the utility of using a partial spin-lock induced crossing (SLIC) radio-frequency (RF) pulse sequence for converting the overpopulated LLS into observable ^1H nuclear magnetization at a low magnetic field. We find that (i) the bulk of the overpopulated LLS is retained even when the optimal or near-optimal values of SLIC pulse duration are employed, and (ii) the overpopulated LLS of propane is also relatively immune to strong RF pulses, thereby indicating that LLS is highly suitable as a spin-polarization reservoir in the context of NMR/MRI detection applications. The presented findings may be useful for improving the levels of polarization of HP propane produced by HET-PHIP via the use of an inert buffer gas; increasing the lifetime of the HP state during preparation and storage; and developing efficient approaches for ultrafast MR imaging of HP propane in the context of biomedical applications of HP propane gas, including its potential use as an inhalable contrast agent.

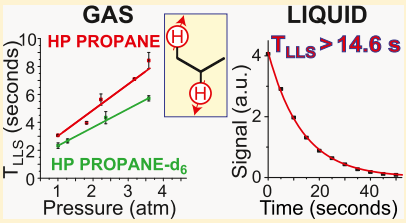

INTRODUCTION

Hyperpolarization increases the nuclear spin polarization by several orders of magnitude over its thermal equilibrium value.[1,2] This dramatic polarization increase results in corresponding gains in NMR and MRI signals.[3,4] The biomedical

Received: February 17, 2019
Revised: April 9, 2019
Published: April 11, 2019

DOI: 10.1021/acs.jpcc.9b01538
J. Phys. Chem. C 2019, 123, 11734−11744

Scheme 1. HET-PHIP Polarizer Apparatus and Low-Field NMR Setup[a]

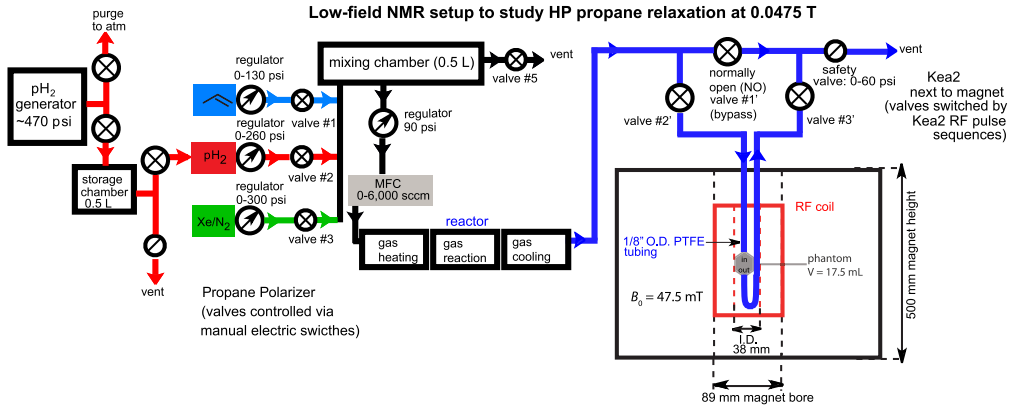

[a]This setup consists of three major components (outlined by dashed lines): parahydrogen generator, propane hyperpolarizer, and the 0.0475 T NMR spectrometer/pulse-programmable automated gas manifold controlled by a Kea2 NMR spectrometer with a pressurized phantom (~17.5 mL).

use of hyperpolarized (HP) spin states enables a variety of new applications, such as probing metabolism and organ function on the time scale of tens of seconds.[1,5,6] In the case of gases and lung MRI, the potential of HP noble gases like ^{3}He and ^{129}Xe for such applications was demonstrated over 20 years ago,[7−10] and they have been shown to be safe in clinical trials (e.g., ref 11). Although HP ^{3}He MRI was demonstrated before ^{129}Xe,[12−14] the supply of ^{3}He is limited (it is a product of tritium decay), thus presenting a significant obstacle for a sustainable widespread clinical use. As a consequence, ^{129}Xe is the leading HP noble gas for prospective use as an inhalable contrast agent for imaging COPD,[15] emphysema,[16,17] brown fat,[18] and other applications.[19−21] However, while progress has been made, the clinical-scale hyperpolarization hardware for HP ^{129}Xe preparation remains relatively complex and costly.[12,22−27] More importantly, clinical MRI scanners are not equipped with the hardware or software required for HP ^{129}Xe imaging, because they are designed to image the ^{1}H spins from water and lipids in the body, whereas ^{129}Xe resonates at a frequency that is several-fold lower than that of ^{1}H. Because of the above limitations of HP ^{129}Xe production and imaging technologies, the search for biomedically useful inhalable HP contrast agents remains an active area of basic and translational research.

HP gaseous hydrocarbons potentially obviate the shortcomings of HP ^{129}Xe in the context of biomedical applications, because protons of hydrocarbons can be hyperpolarized quickly and cheaply via the parahydrogen utilization.[28−30] Using heterogeneous catalysts, gaseous hydrocarbons can be hyperpolarized via the pairwise addition of parahydrogen (pH_2)[6,31−35] to a suitable unsaturated substrate via a process termed heterogeneous parahydrogen-induced polarization (HET-PHIP). Although gas-phase proton T_1 values are generally short—ca. 1 s at 1 atm[36]—a number of approaches have been developed to extend the lifetime of HP states in hydrocarbons, including the use of high operating pressure[36] and reversible dissolution.[37] Most importantly, the pioneering works of Levitt,[38−41] Bodenhausen,[42,43] Warren,[44,45] and others[46−49] have demonstrated that the relaxation decay of the HP state can be significantly prolonged when two HP nuclear spins are entangled in a singlet state. More broadly in spin systems with three[50] and more spins,[41] long-lived spin states (LLSs) can exist because of the symmetry properties of the spin Hamiltonian. The exponential decay constant of LLS T_{LLS} can significantly (by up to several orders of magnitude) exceed T_1.

HP propane has garnered our attention because it is relatively inert,[51,52] has low in vivo toxicity,[53] and it is approved by the FDA for its use in the food industry as a propellant and for food storage.[54] More broadly, it is used as a food additive (E944). Therefore, we envision its potential use as an inhalable HP gas in a manner similar to that of HP ^{129}Xe. However, unlike HP ^{129}Xe, HP propane can be produced using relatively simple, low-cost, and high-throughput hyperpolarization hardware,[55] and HP propane can be readily imaged using conventional clinical MRI scanners which can readily detect HP protons of propane gas,[56−59] representing the clear advantages for biomedical use. Recently, we have demonstrated a clinical-scale hyperpolarization process for production of pure (from catalyst) HP propane gas capable of producing ~0.3 standard liters of HP hydrocarbon gas in ~2 s.[55] As a result, access to HP propane for potential use in humans and large animals is enabled. The work presented here is focused on systematic relaxation studies of HP propane in the gas and liquid states with the key focus on the biomedical application of this potential inhalable contrast agent and extending the lifetime of the HP state as much as possible for potential bioimaging applications.

METHODS

Parahydrogen Generation and Experimental Setup. Two different NMR spectrometer systems were used in this study: one setup used a dual-channel Kea-2 low-field NMR spectrometer (Magritek, New Zealand) to study HP propane at 0.0475 T (Scheme 1) with a previously built radio frequency (RF) coil.[60] The other setup employed a bench-top 1.4 T NMR spectrometer (NMRPro 60, Nanalysis, Canada) (Scheme S1).

Parahydrogen was prepared using a custom-made pH_2 generator using 99.9995% hydrogen (Airgas), producing a pH_2 enrichment fraction of ~87%. During operation, pH_2 is produced continuously and collected in a storage chamber (0.5 L size) prior to its use in the experiments. pH_2 was combined with propylene (Sigma-Aldrich 295663-300G) or propylene-d_6

DOI: 10.1021/acs.jpcc.9b01538
J. Phys. Chem. C 2019, 123, 11734−11744

(99% atom D, Sigma-Aldrich 455687) gas in a mixing chamber[55] to achieve a given desired ratio of the reagents. In some experiments, an additional cylinder containing a buffering gas was used (extra pH_2 was added or a 3:1 Xe/N_2 mixture was added in parallel, Scheme 1). The prepared reaction mixture was then sent through a mass flow controller (MFC) set to approximately 2000 standard cubic centimeters per minute (sccm) flow rate (unless otherwise stated), and then into the reactor.[36] The catalytic reactor (44 cm-long copper tubing with 1/4 in. outer diameter, o.d.) contains ~280 mg of 1% (by weight) Rh/TiO_2 catalyst mixed with 12 g of copper particles (10−40 mesh size, >99.90% purity, Sigma-Aldrich) in the gas-reaction section, Scheme 1. The gas heating and gas cooling sections of the reactor were also filled with 12 g of the copper particles in each section (with Cu particles added for even heat distribution), giving a total of ~36 g of copper particles in this copper tube; the three sections were separated by glass wool. In the first section, the gas mixture is heated using cartridge heaters connected to a PID temperature controller. The second reactor section is heated similarly but contains the catalyst (with Cu particles added for even heat distribution) to perform substrate hydrogenation with pH_2 (Scheme 2a,d). The third/final section of the reactor is for gas cooling, where a third PID temperature controller/heater/cooling fan combination is employed to regulate the cooling of the gas, which is facilitated by passing it through another ~12 g of Cu particles (Scheme 1). The gas mixture exiting the reactor is then directed to either the 0.0475 T or the 1.4 T NMR system to collect enhanced ^{1}H NMR spectra of HP propane or propane-d_6. The following scheme was used for the 0.0475 T system. The HP gas exiting the reactor was sent through a valve (#2′) into the small phantom (17.5 mL) located within the RF coil of the 0.0475 T magnet. The flow of the gas is then directed through another valve (#3′), after which the gas is vented to the atmosphere (i.e. within a hood) via a safety valve operating at 0−60 psi overpressure. The gas inlet and outlet are also connected via a normally open valve (#1′) through a bypass connection to enable the gas flow, when the phantom is closed for the gas flow—this way, the production of HP gas remains uninterrupted.

The details of the 1.4 T apparatus are provided in Scheme S1 in Supporting Information. For these experiments, the HP propane gas exiting the reactor system was directed to the bench-top NMR spectrometer. The inlet was connected to the bottom of a standard 5 mm NMR tube. This NMR tube was cut at the bottom and glued with epoxy to 1/8 in. o.d. polyethylene tubing. The NMR tube designed in this fashion was placed inside the NMR spectrometer. The top of the NMR tube was connected to a manual valve (via 1/4 in. o.d. Teflon tubing), which was then vented via two manual valves and a safety valve. Here, we also employed a bypass between the inlet and the outlet lines of the NMR tube. A receiver gain of 4 dB was used for all the spectra recorded using this 1.4 T NMR spectrometer system. The 1.4 T bench-top NMR spectrometer arrangement was used to directly measure the polarization enhancement values and chemical conversion of HP propane (Figure 1a) under the following experimental conditions: a 1.2:1 mixture of pH_2/propylene was used at a gas flow rate of 2000 sccm at variable reactor temperatures. NMR spectra of HP propane were acquired in two flow regimes: continuous-flow (Figure 1b, under continuous flow) and stopped-flow (Figure 1d, when the flow was terminated). The overpressure was measured using a pressure gauge connected downstream

Scheme 2. (a) Diagram of the Pairwise Addition of pH_2 to Propylene Over the Rh/TiO_2 Catalyst; (b) The Sequential Steps of the Signal Acquisition Method Using the 0.0475 T Setup for the Measurement of HP Propane T_{LLS} (Achieved by Varying the Relaxation Delay τ_R), Optimization of the Chamber-Refill Time τ_{CR}, and Optimization of SLIC Transformation (Varying RF Amplitude, Power, and Frequency Offset); (c) Corresponding Pulse Sequence Used for HP Propane T_1 Measurements Using 90° RF Pulse (to Create z-Magnetization) after SLIC Irradiation Followed by a Small Angle (α) RF Pulse; Note the SLIC Pulse and Chamber Refill Are Performed Once in the Sequence Shown in (c) vs Multiple Refills Employed in the Sequence Shown in (b); (d) Diagram of the Pairwise Addition of pH_2 to Propylene-d_6 Over the Rh/TiO_2 Catalyst; (e) Pulse Sequence Used for the Measurement of HP Propane-d_6 T_{LLS}. Note the pH_2 Symmetry Breaking is Achieved by the Chemical Reaction, with Nascent Protons H_A and H_B Placed in Methylene and Methyl Chemical Groups in (a,d)

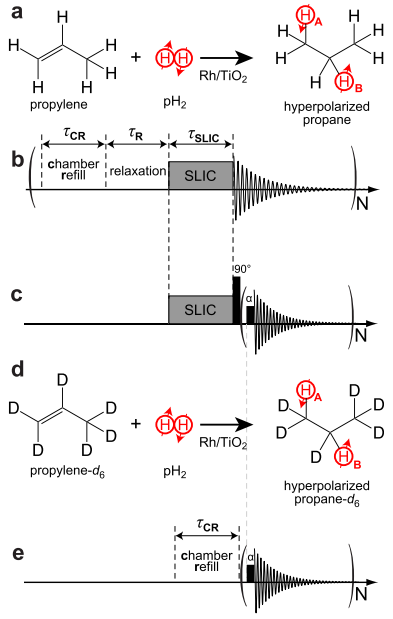

of the NMR tube setup (Scheme S1). These experiments were performed by flowing the HP gas mixture from the exit of the catalytic reactor into the 5 mm NMR tube via the bottom side of the bench-top NMR spectrometer (Scheme S1). The gas exiting at the top of the NMR tube was then flowed through the manual valves (#1″ and #2″) to the vent, and the spectrum was recorded under continuous-flow conditions. In the stopped-flow condition, after flowing the gas for at least 20−40 s the gas flow was stopped by setting the MFC to zero sccm flow rate and closing the manual valve #2″, so the HP propane gas would be trapped (and stopped) throughout the duration of the NMR spectrum acquisition (Figure 1d). The time delay between stopping the gas flow and the NMR acquisition was 0.5−1 s. After the relaxation of hyperpolarization, NMR spectra of stopped-flow thermally polarized propane gas were recorded (an example is shown in Figure 1c). Although the stopped-flow mode exhibited a better spectral resolution because the gas-flow artifacts were eliminated, we generally used the continuous-flow mode for data acquisition owing to

DOI: 10.1021/acs.jpcc.9b01538
J. Phys. Chem. C 2019, 123, 11734−11744

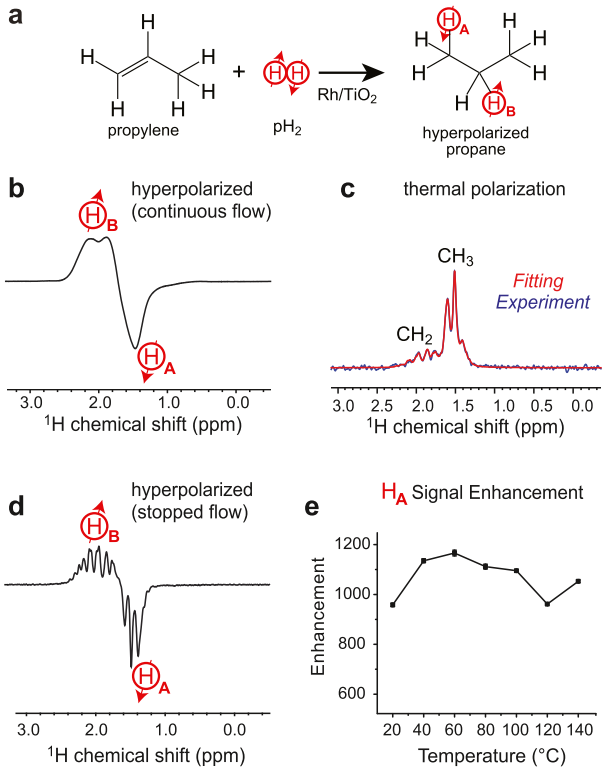

Figure 1. ^{1}H NMR single-scan spectroscopy of HP propane gas using the 1.4 T setup (see Scheme S1 for details). (a) Schematic of heterogeneous pairwise pH_2 addition. (b) ^{1}H NMR spectrum of HP propane acquired with the apparatus in the continuous-flow mode. (c) ^{1}H NMR spectrum of the thermally polarized propane (blue) and spectral fitting (red) using the Bruker Daisy software package. (d) ^{1}H NMR spectrum of HP propane acquired in the stopped-flow mode. (e) Plot of NMR signal enhancement values of the HP methyl proton (H_A) at different operating temperatures obtained via a continuous-flow operation (reactor prepared by mixing ~62 mg of the Rh/TiO_2 catalyst and 6.6 g of Cu in the 2nd section of the hyperpolarizer). Connecting lines in display (e) are meant only to guide the eye.

the less complicated experimental procedure, more reproducible data, and greater HP signals.

For the HP propane condensation, a slightly modified version of the setup shown in Scheme 1 was employed: the phantom inside the RF coil was replaced by a 5 mm NMR tube via a Wye-connector in which the reaction mixture was cryocooled inside a dry ice/ethanol bath at a flow rate of 1300 sccm for ~20 s in the Earth's magnetic field. Then, the NMR tube was rapidly placed inside the 0.0475 T magnet, and spectra were collected using a RF spin-lock induced crossing (SLIC) pulse (200 ms).

NMR Pulse Sequences. Both the filling of the pressurized phantom and the acquisition of NMR spectra were fully automated in Prospa software (Magritek, New Zealand) using a custom-made pulse program and hardware of the pulse-programmable polarizer described previously.[61] This setup was used for most of the experiments reported here to study the effects of varying the refill duration, SLIC[62] pulse duration, etc. All experiments were conducted by first filling the phantom with HP gas, terminating the flow by closing valves #2′ and 3′, and then applying the sequence of RF pulses of interest on the static HP gas mixture (i.e., under stopped-flow conditions, in contrast with our previous work on HP propane, where RF pulses were applied to continuously flowing HP gas[63]) and finally collecting the FID as shown in Scheme 2b,c,e.

The exponential decay of the LLS in HP propane is characterized by the exponential decay constant T_{LLS},[57] which was measured by varying the relaxation delay time period as shown in Scheme 2b. The corresponding NMR spectrum of HP propane after SLIC is shown in Figure 2a. After the SLIC

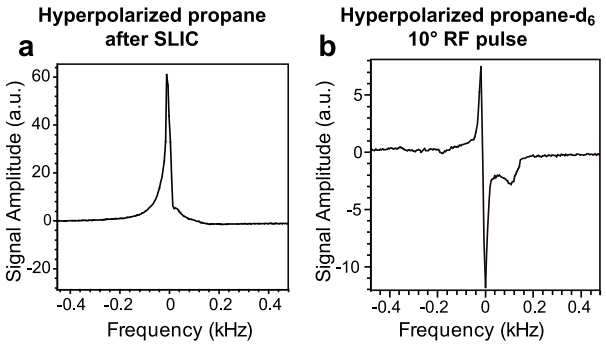

Figure 2. (a) ^{1}H 0.0475 T NMR spectrum of HP propane after SLIC transformation (as shown in Scheme 2b). (b) ^{1}H 0.0475 T NMR spectrum of HP propane-d_6 acquired using a small-angle (~10°) hard RF pulse (as shown in Scheme 2e).

transformation of the pH_2-induced overpopulation of the LLS the observable magnetization is aligned along the axis of the SLIC irradiation (i.e. x or y axis of the rotating frame, which is a typical approach employed in NMR to describe the effect of RF pulses), and a 90° pulse is applied to align the magnetization of HP propane along the z-axis (i.e. along the applied static magnetic field referred to as the z-axis of the rotating frame, Scheme 2c. Although the LLS is denoted schematically as a singlet in Figure 3a, it should be noted that the spin eigenstates of protonated propane have eight protons, and therefore the resulting spin system is different from the prototypical "singlet" and "triplet" states—after pairwise addition of the pH_2 singlet (as the two protons belonging to the CH_2 and CH_3 groups, respectively), many collective states of the proton spin system can be populated, and some of these states can be long-lived because of the symmetry properties of the spin Hamiltonian. Therefore, strictly speaking, LLS of propane cannot be called a "singlet" state. After these RF-induced transformations, the resulting z-magnetization decays exponentially according to the spin-lattice decay time constant T_1, which is measured by applying a small-angle excitation pulse α (~10°) followed by FID detection, applied several (N) times to observe the decay (as shown in Scheme 2c). Although LLS exists for HP propane-d_6, the application of a SLIC pulse for transformation of the LLS into observable magnetization is not required because of the spin−spin coupling of nascent protons with deuterons—see ref 58 for details. As a result, T_{LLS} can be conveniently measured by applying a small-angle excitation pulse (~10°) followed by FID detection, repeated several times to observe the decay (Scheme 2e). The corresponding NMR spectrum of HP propane-d_6 is shown in Figure 2b.

RESULTS AND DISCUSSION

Optimization of SLIC RF Pulse Sequence and Reaction Temperature, and Tests of Reproducibility.

DOI: 10.1021/acs.jpcc.9b01538
J. Phys. Chem. C 2019, 123, 11734−11744

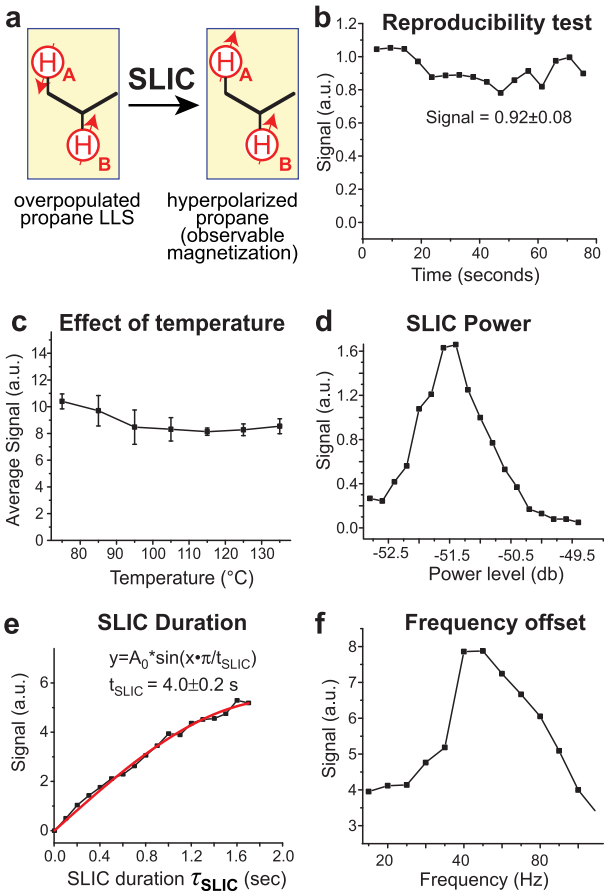

Figure 3. Results from SLIC pulse optimization with HP propane data acquired using the 0.0475 T NMR spectrometer setup shown in Scheme 1 at a production/reactor/reaction temperature of 60 ± 1 °C (except for display (c) where the temperature was varied). (a) Diagram showing the transformation of LLS of HP propane (denoted schematically as a singlet) into observable magnetization achieved using a SLIC pulse. (b) Results from a test of the shot-to-shot reproducibility of the intensity of the HP propane signal. (c) Temperature dependence of the average (over three data points) HP propane SLIC-induced signal using a 1:1 gas mixture of pH_2 and propylene. (d) Optimization of RF power of the SLIC pulse (note the *x*-axis is provided in db units of the Kea NMR spectrometer due to the nonlinearity of the RF amplifier at low power levels; the maximum is expected at the B_1 RF strength between 10 and 30 Hz[63]). (e) The dependence of the HP propane signal on the SLIC pulse duration (experimental data: black points; a fit using a sinusoidal function is shown by the solid red curve). (f) The dependence of the HP propane signal on the SLIC pulse frequency offset. Note a SLIC pulse duration of 500 ms was employed for the data acquisition in panels (b–d,f). Connecting lines in displays (b–d,f) are meant only to guide the eye.

The effects of different experimental conditions toward the HP propane signal intensity induced by the SLIC pulse were tested in order to optimize the pulse parameters and thereby maximize the HP propane signal (Figure 3). All the data were recorded using the 0.0475 T experimental setup (Scheme 1) via the sequence shown in Scheme 2b. A 1:1 gas mixture of pH_2 and propylene was used for the temperature variation experiments in order to determine the optimal temperature for the reactor, particularly in the second section of the hyperpolarizer setup. The gas flow rate was 2000 sccm, and the refill time was 5 s for each run. For refilling the phantom, first the gas was allowed to flow through the phantom for ∼5 s with valve #1′ closed and valves #2′ and #3′ open, and after ∼5 s of gas flow valves #2′ and 3′ were closed, and the bypass valve #1′ was opened. First, the consistency of the HP propane signal was tested (Figure 3b) using a SLIC pulse duration of 500 ms; over numerous scans a standard deviation of ∼9% was found, indicating good shot-to-shot reproducibility for the hyperpolarizer. Next, the SLIC sequence was used for the experiment, and three HP propane spectra were collected at each reaction temperature (recorded as the temperature of the reactor's aluminum jacket). The average signal value and the corresponding standard deviation are plotted for each temperature in Figure 3c. The strength of the SLIC RF pulse also has a negligible effect on the signal, as identified in previous studies.[63] The results from SLIC pulse power optimization are shown in Figure 3d; from this SLIC power plot, the highest SLIC signal corresponds to a power setting of −51.25 dB (this value likely corresponds to 20−30 Hz of B_1 power[63]), and this optimal power was used for the remaining studies using the SLIC sequence. The SLIC pulse duration was varied from 2 to 1802 ms, and the signal was found to increase with the SLIC pulse duration and was well-reproduced by a sinusoidal function (in a manner similar to the B_1 nutation curve, which is predicted by the similar works of Rosen and co-workers,[62] and the previous study of the HP propane system;[63] note that data acquisition at long SLIC times is impractical because of the T_2 relaxation effects[63]) (Figure 3e), yielding a SLIC period (t_{SLIC}) of 4.0 ± 0.2 s.[62] The last parameter optimized was the SLIC pulse frequency offset.[63] The offset was swept from ∼10 to 80 Hz while monitoring the signal strength, and the resulting signal intensity data indicated an optimal offset of ∼45 Hz for the system under study (Figure 3f) using the experimental setup presented here.

^{1}H Relaxation Dynamics of HP Propane at 0.0475 T.

First, we measured T_1 and T_{LLS} values for HP propane gas in the pressure range between 1 and 4.6 atm, formed using a 1:1 mixture of pH_2 and propylene at 75 °C and 2000 sccm flow rate. As discussed below, the chemical conversion was ∼100% at these conditions, that is, yielding a nearly 100% propane gas product. We note that a previous T_1 and T_{LLS} study of HP propane[63] was performed within a significantly higher pressure regime (3−7.6 atm total pressure), whereas the present study is focused on a lower pressure regime relevant for future in vivo studies (wherein the gas would need to be imaged at 1 atm). In the overlapping range of the pressure values, the present results generally agree with those of the previous study:[63] although the T_1 and T_{LLS} values reported here are somewhat larger (by approximately 10%), this difference likely reflects the fact that the previous study employed reaction conditions where the chemical conversion of substrates was incomplete. Examples of the signal decay curves associated with T_1 and T_{LLS} of HP propane are shown in Figure 4a,c respectively. Figure 4b shows the dependence of HP propane T_1 time on the propane pressure, yielding values in the range of ∼1.05 s (at 1.6 atm) to 3.4 s (at 4.5 atm). Figure 4d shows the corresponding dependence of HP propane T_{LLS} time on the propane pressure, showing values in the range of ∼3.1 s (at 1.0 atm) to 9.4 s (at 4.5 atm). On average, the T_{LLS} values were approximately 3 times greater than the corresponding T_1 values, with nearly linear dependence on pressure, which is in accord with the previous report.[63] Such a linear T_1 dependence is consistent with the major contribution of the gas-phase nuclear spin

DOI: 10.1021/acs.jpcc.9b01538
J. Phys. Chem. C 2019, 123, 11734−11744

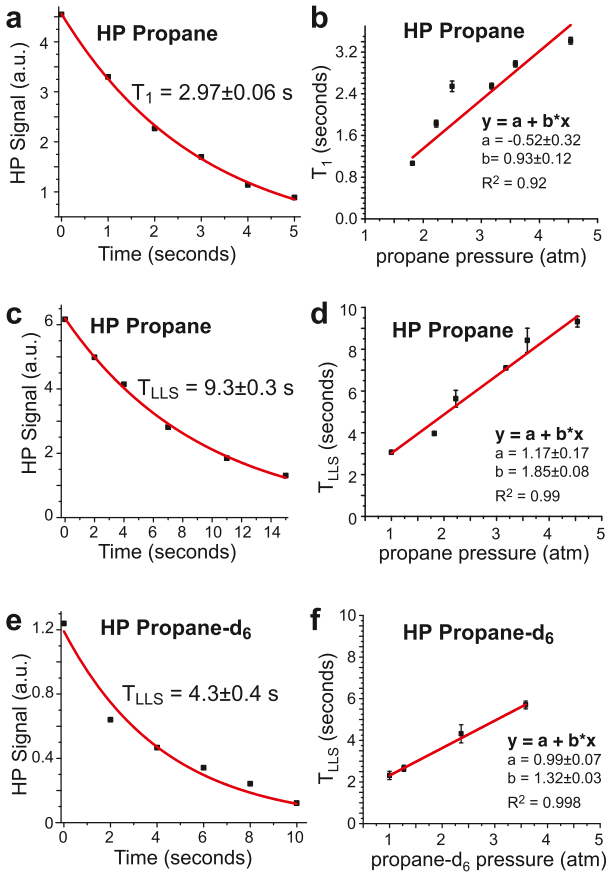

Figure 4. Examples of T_1 (at ∼3.6 atm pressure) and T_{LLS} (at ∼4.5 atm pressure) signal decays of HP propane and mono-exponential fitting are shown in (a,c); (e) corresponding example of LLS decay of HP propane-d_6. Dependences of T_1 (b) and T_{LLS} (d) of propane hyperpolarization on its pressure. (f) Dependence of T_{LLS} of propane-d_6 hyperpolarization on its pressure (an example of experimental data reporting on effective T_1 for HP propane-d_6 is shown in Figure S3). All data are acquired at 0.0475 T using production/reaction conditions of 75 °C and 2000 sccm flow rate with near-100% chemical conversion of pH_2 and unsaturated substrates. See Scheme 1 for additional details.

relaxation being from the spin-rotation mechanism in the intermediate-density (here, multi-amagat) regime.[64,65] Under such conditions, different relaxation times for T_1 and T_{LLS} (and slopes with respect to density) would not be surprising as spin states with different symmetries would likely couple to different rotational states.[64] Future theoretical studies are certainly warranted to provide a more-detailed understanding of the observed trends.

Effect of HP Propane Deuteration on LLS Decay at 0.0475 T. Because T_{LLS} is considerably greater than T_1 in HP propane, the LLS of HP propane may be better suited for in vivo experiments, which would likely require at least several seconds of HP gas handling for inhalation and MR imaging. Given the desire to further lengthen the lifetime of the non-equilibrium spin order endowed by hyperpolarization,[66,67] we also studied the effect of deuteration on T_{LLS} in HP propane-d_6 (the corresponding effective T_1 data are shown in Figure S3), acquiring data under conditions similar to the HP propane T_{LLS} measurements discussed above (Figure 4c). We note that the symmetry of nascent parahydrogen protons is broken in propane-d_6 in a way that the magnetization is already observable, even in the absence of significant chemical shift differences (Figure 2b) at 0.0475 T; for additional details the reader is referred to ref 58. Therefore, the data acquisition for HP propane-d_6 was performed differently from that for HP propane (i.e. using the sequence shown in Scheme 2e), and small tipping-angle (∼10°) RF excitation pulses followed by NMR signal detection were employed. An example of the LLS decay of HP propane-d_6 is shown in Figure 4e. Such T_{LLS} values were plotted against the gas pressure, and a linear fit was performed for the data obtained (Figure 4f). According to Figure 4f, T_{LLS} for propane-d_6 increases linearly with pressure, with T_{LLS} values being ∼20% lower (on average) than the corresponding T_{LLS} values of HP propane (Figure 4d). We note that this small difference is likely a combination of two effects: some depolarization losses due to RF excitation pulses (not taken into account) employed for data collection for HP propane-d_6, as well as the effect of deuterium labeling of the substrate; future theoretical studies are certainly warranted to provide the understanding of the observed trends. Taking into account the RF pulse excitation (which we did not perform because of concerns described by Kharkov and co-workers[68]) would lengthen T_{LLS} values by less than 8%, which is insufficient to account for the ∼20% difference between the T_{LLS} values of HP propane and HP propane-d_6. We also note a different slope of the curves shown in Figure 4d,f.

It should be noted that although HP propane-d_6 T_{LLS} values are generally lower than the corresponding values for HP propane, the detection of HP propane-d_6 offers the advantage of direct detection using a hard, short RF excitation pulse, whereas a long soft SLIC pulse is required to obtain observable magnetization in case of using HP propane at low magnetic fields. This advantage can be useful in the context of MRI applications, because RF excitation pulses can be very short (compared to SLIC RF pulses).

NMR Spectroscopy of HP Propane Gas at 1.4 T. We note that the methylene and methyl proton resonances still partially overlap at 1.4 T; the spectral appearance was well-reproduced by spectral simulation. No traces of unreacted propylene were seen (as evidenced by the lack of methine proton resonances after multiple averaging, data not shown), which is consistent with a full (i.e. near 100%) chemical conversion of the unsaturated substrate in the hydrogenation reaction with pH_2 under these experimental conditions: the corresponding NMR spectrum of thermally polarized propylene is provided in Figure S2.

We note that SLIC-based detection does not allow obtaining the true value of polarization enhancement of the over-populated LLS at 0.0475 T[63] because SLIC transformation does not offer a 100% conversion efficiency of the LLS into observable magnetization. On the other hand, direct detection of HP propane gas at 1.4 T was employed to measure polarization enhancement values. For this purpose, the integral values of the signals from H_A and H_B protons (the continuous-flow mode) (Figure 1, we note that the absolute values for H_A and H_B were similar) were compared to the corresponding integral values for thermally polarized propane under the same pressure and multiplied by a factor of 8 (to account for eight protons contributing to the NMR signal of thermally polarized propane). The enhancement values recorded in such a manner for the H_A proton were nearly unchanged (ε_{H_A} ranging from

DOI: 10.1021/acs.jpcc.9b01538
J. Phys. Chem. C 2019, 123, 11734−11744

950 to 1150, Figure 1e) over the range of the reactor temperatures studied (between 20 and 140 °C), which is in agreement with our similar studies using the 0.0475 T setup (Figure 3a). This trend is important for two reasons. First of all, it indicates that a robust catalyst performance in production of HP propane gas can indeed be obtained over a wide range of temperatures with effectively ∼100% chemical conversion (note: 20% excess pH_2 was employed for data collection in Figure 1e). Second, the highest levels of polarization enhancement were observed at 40−60 °C, suggesting that reactor temperatures near that of the human body (ca. 40 °C) can be readily employed without sacrificing polarization efficiency. This finding bodes well for future in vivo use of HP propane gas because the produced HP propane can be immediately inhaled by the subject without the need for significant additional cooling.

Effects of Buffering Gases on Propane Hyperpolarization Level and Decay. The effect of buffering gas on the relaxation constants and polarization values of HP propane was also studied using the 0.0475 T NMR spectrometer setup (Scheme 1). For these experiments, we used a flow rate of 2000 sccm, a reaction temperature of 75 °C, and 38 psi overpressure (total pressure of 3.6 atm); SLIC sequences were used for all acquisitions. The results obtained with pH_2 buffering gas and with variable propane concentrations are shown in Figure 5a−c, whereas those obtained with the Xe/N_2 mixture (3:1 ratio) as the buffering gas and with a variable propane concentration are shown in Figure 5d−f. The rationale for the mixture of Xe and N_2 was to test the effects of reduced gas diffusion by using a dense gas (indeed, we note that previous attempts employing pure Xe were challenging because of high gas viscosity). The results indicate that T_1 decay of HP propane is not significantly impacted by the presence of light (H_2) or heavy (Xe/N_2) buffering gases, as shown in Figure 5a,d, respectively. However, LLS decay of HP propane decreases significantly (by 35 ± 7% from 100 to 43% mixture) with the increased presence of a light buffering gas, H_2 (Figure 5b). Yet in the presence of a heavy buffering gas (Xe/N_2, 3/1), the observed decrease in T_{LLS} is far more modest (by 8 ± 7% from 100 to 43% mixture, Figure 5e). Note, if we consider polarization levels, pH_2 is not truly a buffering gas, because its concentration can influence the processes occurring on the catalyst surface including the percentage of pairwise hydrogen addition. On the other hand, the Xe/N_2 mixture is inert relative to the catalyst operation (except the dilution of the reactants leading to decrease of their partial pressures). The ^1H polarization values increase in the presence of the buffering gas by 1.6 ± 0.1 fold (100% propane mixture vs 43% propane mixture) in the case of H_2 buffering gas (in agreement with previous studies[36,69]), and by 1.4 ± 0.1 fold (100% propane mixture vs 43% propane mixture) in the case of Xe/N_2 (3:1) buffering gas, as shown in Figure 5c,f, respectively. We note that the actual increase in (initial) polarization of HP propane gas may be significantly greater because in the case of more dilute mixtures, HP propane has lower corresponding T_{LLS} values (see Figure 5c,f), and therefore, likely experiences disproportionately greater polarization losses during more than 5−10 s of transport time from the reactor to the detector.

The observation that the buffering gas boosts propane hyperpolarization in the HET-PHIP process is important in the context of biomedical applications with the goal of maximizing the levels of hyperpolarization. Although the produced HP gas is diluted with the buffering gas, it can potentially be separated by rapid cryocondensation of HP propane gas, as discussed below.

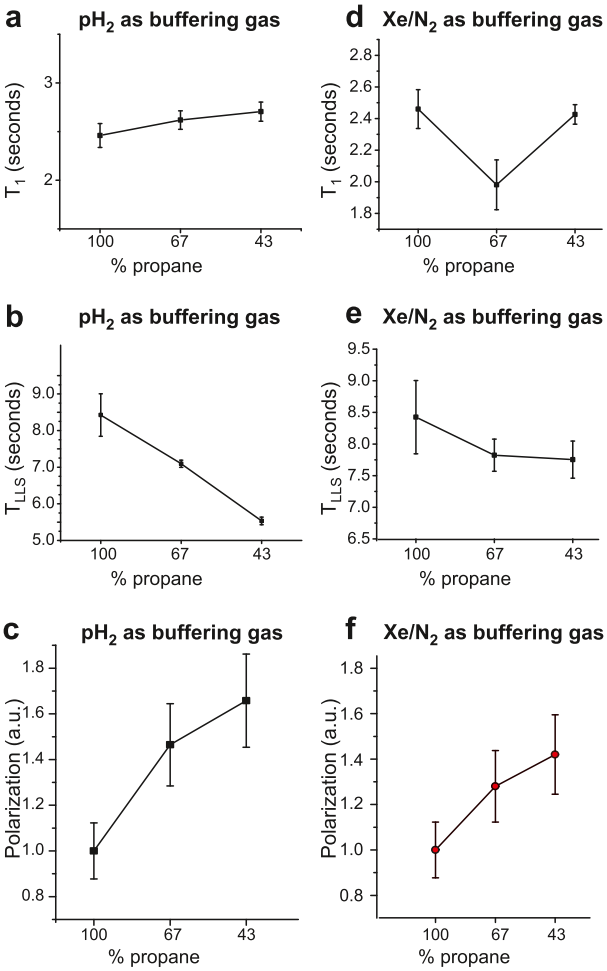

Figure 5. Effects of using different buffering gases on the hyperpolarization decay constants and polarization levels of HP propane determined using the 0.0475 T magnetic field NMR spectrometer setup (Scheme 1). T_1 (a) and T_{LLS} (b) dependence of HP propane on the propane fraction in the resultant gas mixtures with the use of pH_2 buffering gas. (c) Dependence of propane ^1H polarization (arbitrary units, a.u.) on the propane fraction in the resultant gas mixtures with the use of H_2 buffering gas. T_1 (d) and T_{LLS} (e) dependence of HP propane on the propane fraction in the resultant gas mixtures with the use of the Xe/N_2 (3:1) buffering gas mixture. (f) Dependence of propane ^1H polarization (arbitrary units, a.u.) on the propane fraction in the resultant gas mixtures with the use of the Xe/N_2 (3:1) buffering gas mixture. All data were obtained at 38 psi backpressure (∼3.6 atm total pressure), and the pH_2 to propylene ratio was 1:1 for the experiments shown in displays (d−f). Connecting lines are meant only to guide the eye.

Partial SLIC RF Excitation of HP Propane Gas at 0.0475 T. We carried out a series of experiments with a variable SLIC pulse duration on HP propane gas using the 0.0475 T spectrometer setup (Scheme 1) for a 1:1 reaction mixture of propylene and pH_2 at 38 psi overpressure (∼3.6 atm total pressure). Once the phantom was filled with fresh HP propane gas, the SLIC pulse was applied followed by immediate signal detection, and these two steps were repeated

DOI: 10.1021/acs.jpcc.9b01538
J. Phys. Chem. C 2019, 123, 11734−11744

N times on a single fill of HP propane (Figure 6a). The signal of HP propane obtained in this fashion falls exponentially as a result of a combination of LLS decay and the application of SLIC pulses. Several different SLIC RF pulse durations (varying between 50 and 1600 ms) were employed to record NMR spectra, the intensities of which are plotted against time in Figure 6b. We note that in the case of longer SLIC durations, the RF pulses were applied more sparsely, resulting in a longer repetition time (TR) but in greater signal intensities (Figure 6c). An effective T_{LLS} value was determined for each experimental series in Figure 6b, and these effective T_{LLS} values (detailed in Table S1) are plotted in Figure 6d. As expected, when the SLIC pulse duration is increased, the effective decay time constant decreases, indicating faster depletion of the HP state. All effective T_{LLS} values measured in this fashion were in the range of 4.7−8.1 s (due to decay and RF depletion), which is less than the corresponding T_{LLS} value (~8.4 s) obtained at otherwise identical conditions using the procedure described above (cf. Figure 4d). This finding indicates that partial SLIC can be applied to HP propane to convert only a fraction of the hyperpolarization pool at one time (prolonging the useful lifetime of the enhanced spin order). We note that even though near-optimal values of SLIC pulses are applied (i.e. 800−1600 ms durations, making an analogy with a 90° excitation pulse—note the corresponding signal produced by SLIC pulse increases with duration, Figures 3e and 6c), the overpopulated LLS remains largely intact, because subsequent RF excitation pulses produce comparable signal levels, Figure 6a. This finding is useful for several reasons. First, a short SLIC pulse (i.e., with the duration significantly shorter than the optimal value) can be employed in a manner similar to a small tipping-angle excitation pulse for applications ranging from measurements of relaxation of HP species to MRI encoding. In the case of MRI applications, we note that the resulting magnetization (after SLIC pulse) is in the x−y plane, and therefore, can be conveniently combined with the echo-planar imaging (EPI) readout. As a result, SLIC can provide both partial excitation of overpopulated LLS to record 2D slices, and also enable singlet order selection filtering[70] for selective excitation of the singlet states in the presence of proton background signal of tissues.

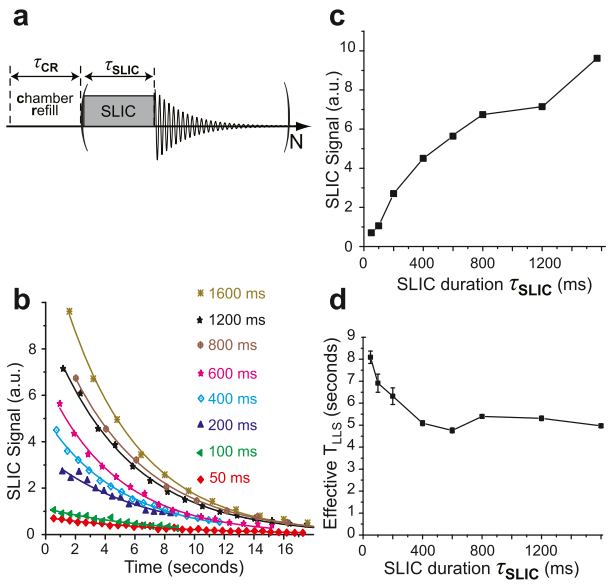

Figure 6. (a) Pulse sequence comprising a series of partial SLIC pulses with variable duration each followed by NMR signal acquisition; note the sequence is repeated N times on a single batch of static HP propane gas. (b) Decay of HP propane signals obtained using the partial SLIC excitation scheme (with variable SLIC duration); note the color coding of the SLIC pulse duration in the figure legend (see Table S1 for additional details). (c) Intensity of the first data point in display (b) plotted as a function of the SLIC pulse duration. Connecting lines in displays (c,d) are meant only to guide the eye.

There are at least two possible explanations for the observed retention of overpopulated LLS even after the application of a SLIC pulse of optimal duration (which in principle is designed to convert most of the singlet order into observable magnetization[62]). First, gas convection and B_1 inhomogeneities may lead to subpar performance of the SLIC pulse sequence, leaving the bulk of the HP LLS unaffected by the SLIC pulse sequence.[68] Second, the HP propane spin system cannot be, strictly speaking, treated as a true singlet[57,58,63] because there are eight spin−spin coupled protons, and therefore, the application of the SLIC sequence may indeed generate observable magnetization while retaining some overpopulated LLS in the spin system of HP propane gas. Future studies using stronger magnets and more homogeneous excitation RF coils are certainly warranted to delineate the relative contribution of these two effects.

We have also tested the immunity of the overpopulated LLS with respect to irradiation by hard RF pulses. The applied sequence is shown in Figure 7a, and the corresponding decay data are presented in Figure 7b (red curve). Specifically, we have employed a SLIC pulse duration of 200 ms, which was followed by signal acquisition. This partial SLIC detection was repeated four times. Next, 64 hard 90° RF pulses were applied back-to-back. This process was repeated three times, and the integral intensity of the HP signals (obtained via partial SLIC and shown as red squares in Figure 7b) is plotted versus time. The resulting data were fit to give an effective T_{LLS} constant of 5.3 ± 0.1 s. This value is close to a corresponding value obtained when no hard RF pulses were employed: effective T_{LLS} of 6.3 ± 0.4 s (Figure 7b, blue curve), indicating that the

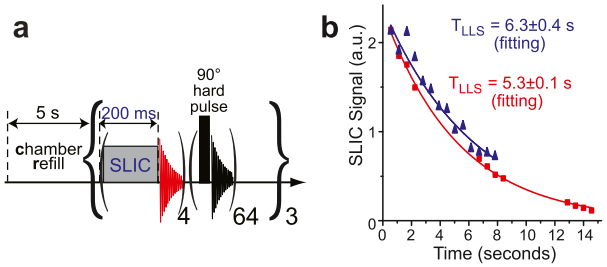

Figure 7. (a) Pulse sequence comprising a series of partial SLIC pulses with 200 ms duration followed by NMR signal acquisition. The 200 ms SLIC pulse is followed by NMR detection; this loop is repeated 4 times, and a train of sixty-four (equally spaced) hard 90° RF pulses is applied and the entire sequence is repeated three times. (b) The recorded SLIC NMR signal intensities (comprising 12 data points). The mono-exponential fitting (red) yielded an effective T_{LLS} constant of 5.3 ± 0.1 s. The corresponding decay curve without the use of hard RF pulses is shown by a blue trace with triangles. All experiments were performed at 38 psi of overpressure (~3.6 atm total pressure).

DOI: 10.1021/acs.jpcc.9b01538
J. Phys. Chem. C 2019, 123, 11734−11744

overpopulated LLS is relatively immune to the application of hard RF pulses. This observation is useful in the context of future MR imaging studies, where the application of strong RF pulses may be desirable for background signal suppression, while retaining the overpopulated LLS of HP propane gas.

Feasibility of Condensation of HP Propane Gas and LLS Decay of Liquefied HP Propane at 0.0475 T. Cryocollection of HP gas is a common practice in a continuous-flow production of HP noble gases, a practice that is designed to make the contrast agent more concentrated.[26,71,72] Because the addition of buffering gas increases the degree of propane hyperpolarization (Figure 5c,f), we have investigated the feasibility of HP propane cryocollection. A slight modification to the 0.0475 T experimental setup was made to perform HP propane condensation (Scheme 1 and Methods section for details). The phantom inside the RF coil was replaced by a 5 mm NMR tube, wherein the reaction mixture was cryocooled. The cryocooling was performed at a flow rate of 1300 sccm for ∼20 s inside a cooling bath with dry ice and ethanol (ca. −78 °C) outside the magnet, that is, at the Earth's magnetic field. Then the NMR tube containing liquid HP propane was carefully placed inside the magnet, and a series of NMR spectra were collected using partial SLIC excitation with 200 ms pulse duration. The typical NMR spectrum of the liquefied propane (Figure S1a) was similar to the one of HP propane gas (Figure 2a). The fitting to monoexponential decay (Figure S1b−d) revealed an effective T_{LLS} time constant of 14.7 ± 0.5 s. We note that this value is actually a lower-limit estimate, because the partial SLIC excitation reduces the pool of HP LLS (Table S1), and the effect of the RF pulse-associated losses was not taken into account in our data fitting. Nevertheless, this relatively long T_{LLS} value is significantly greater than any T_{LLS} value of HP propane in the gas phase measured here or elsewhere.[63] This lower-limit T_{LLS} value for liquid HP propane is somewhat lower than the T_1 value of HP propane dissolved in deuterated organic solvents (28−35 s).[37]

Because higher polarization values can be obtained via HET-PHIP using buffering gases, and because buffering gases can be potentially separated from cryocollected HP propane, this approach may be a viable option for future experimentations to boost propane hyperpolarization via HET-PHIP. Moreover, the relatively long T_{LLS} value of cryocollected HP propane may be a useful means for temporary storage of HP propane gas prior to its use as an inhalable contrast agent.

CONCLUSIONS

A systematic study of nuclear spin relaxation dynamics at 0.0475 T of HP propane prepared by HET-PHIP is reported using a clinical-scale hyperpolarizer device under conditions providing nearly 100% chemical conversion. We find that the HP propane T_{LLS} is ∼3 s at 1 atm, that is, under clinically relevant conditions. T_{LLS} and T_1 values generally exhibit a linear dependence on propane pressure. At the pressures studied, the T_{LLS} values are approximately 3 times greater than the corresponding T_1 values. The use of deuterated propylene as a HP propane precursor (i.e. production of HP propane-d_6) reduces T_{LLS} by as much as ∼20%, indicating that deuteration of the precursor maybe somewhat detrimental to the lifetime of the HP state. The use of light and heavy buffering gases (pH_2 and a 3:1 mixture of Xe/N_2) is found to have a negligible effect on T_1 and generally results in somewhat lower T_{LLS} values: the T_{LLS} reduction is concentration dependent. At the same time, the use of buffering gases increases the polarization levels of HP propane gas during HET-PHIP production, which is welcome in the context of biomedical applications. Although the buffering gas dilutes the HP propane gas, it can be separated through a process of HP propane cryocollection, the feasibility of which was demonstrated here. The added benefit of HP propane cryocollection is the increase of the T_{LLS} value to 14.7 s in the liquid state, which is significantly greater than any reported T_{LLS} value for HP propane gas at any pressure, and which can be useful for temporary storage of produced HP propane prior to its in vivo administration. We have also investigated the possibility of applying a partial SLIC pulse to HP propane LLS, and we find that most of the pool of the overpopulated LLS is retained even after application of an optimized SLIC pulse. The overpopulated LLS of propane is relatively immune to the application of hard RF pulses. This behavior of the HP propane spin system with respect to application of partial SLIC and strong RF pulses can be potentially useful for developing efficient ultrafast MR imaging approaches, especially those involving EPI readout. To summarize, the results presented in this study may be beneficial for guiding future work studying the preparation of highly polarized batches of HP propane and designing efficient MR imaging approaches.

ASSOCIATED CONTENT

Supporting Information

The Supporting Information is available free of charge on the ACS Publications website at DOI: 10.1021/acs.jpcc.9b01538.

Experimental setup for NMR spectroscopy at 1.4 T; ^1H spectrum of condensed HP propane; thermally equilibrated proton NMR spectrum; and exponential decay constants (PDF)

AUTHOR INFORMATION

Corresponding Author

*E-mail: chekmenev@wayne.edu.

ORCID

Oleg G. Salnikov: 0000-0003-2266-7335
Kirill V. Kovtunov: 0000-0001-7577-9619
Boyd M. Goodson: 0000-0001-6079-5077
Igor V. Koptyug: 0000-0003-3480-7649
Eduard Y. Chekmenev: 0000-0002-8745-8801

Notes

The authors declare no competing financial interest.

ACKNOWLEDGMENTS

This work was supported by NSF under grant CHE-1836308 and CHE-1416432, NIBIB under 1R21EB020323, DOD CDMRP under W81XWH-15-1-0271 and W81XWH-15-1-0272. The Russian team thanks RFBR (projects # 17-54-33037 OHKO_a, 18-43-543023) and the Russian Ministry of Science and Higher Education (AAAA-A16-116121510087-5) for the support.

REFERENCES

(1) Goodson, B. M. Nuclear Magnetic Resonance of Laser-Polarized Noble Gases in Molecules, Materials, and Organisms. *J. Magn. Reson.* **2002**, *155*, 157−216.

(2) Kovtunov, K. V.; Pokochueva, E. V.; Salnikov, O. G.; Cousin, S. F.; Kurzbach, D.; Vuichoud, B.; Jannin, S.; Chekmenev, E. Y.; Goodson, B. M.; Barskiy, D. A.; Koptyug, I. V. Hyperpolarized NMR

DOI: 10.1021/acs.jpcc.9b01538
J. Phys. Chem. C 2019, 123, 11734−11744

Spectroscopy: d -DNP, PHIP, and SABRE Techniques. *Chem.—Asian J.* **2018**, *13*, 1857−1871.
(3) Albert, M. S.; Cates, G. D.; Driehuys, B.; Happer, W.; Saam, B.; Springer, C. S.; Wishnia, A. Biological Magnetic-Resonance-Imaging Using Laser Polarized Xe-129. *Nature* **1994**, *370*, 199−201.
(4) Golman, K.; Axelsson, O.; Jóhannesson, H.; Månsson, S.; Olofsson, C.; Petersson, J. S. Parahydrogen-Induced Polarization in Imaging: Subsecond C-13 Angiography. *Magn. Reson. Med.* **2001**, *46*, 1−5.
(5) Kurhanewicz, J.; Vigneron, D. B.; Brindle, K.; Chekmenev, E. Y.; Comment, A.; Cunningham, C. H.; DeBerardinis, R. J.; Green, G. G.; Leach, M. O.; Rajan, S. S.; Rizi, R. R.; Ross, B. D.; Warren, W. S.; Malloy, C. R. Analysis of Cancer Metabolism by Imaging Hyperpolarized Nuclei: Prospects for Translation to Clinical Research. *Neoplasia* **2011**, *13*, 81−97.
(6) Hövener, J.-B.; Pravdivtsev, A. N.; Kidd, B.; Bowers, C. R.; Glöggler, S.; Kovtunov, K. V.; Plaumann, M.; Katz-Brull, R.; Buckenmaier, K.; Jerschow, A.; Reineri, F.; Theis, T.; Shchepin, R. V.; Wagner, S.; Bhattacharya, P.; Zacharias, N. M.; Chekmenev, E. Y. Parahydrogen-Based Hyperpolarization for Biomedicine. *Angew. Chem., Int. Ed.* **2018**, *57*, 11140−11162.
(7) Bhaskar, N. D.; Happer, W.; McClelland, T. Efficiency of Spin Exchange between Rubidium Spins and Xe-129 Nuclei in a Gas. *Phys. Rev. Lett.* **1982**, *49*, 25−28.
(8) Happer, W.; Miron, E.; Schaefer, S.; Schreiber, D.; van Wijngaarden, W. A.; Zeng, X. Polarization of the Nuclear Spins of Noble-Gas Atoms by Spin Exchange with Optically Pumped Alkali-Metal Atoms. *Phys. Rev. A: At., Mol., Opt. Phys.* **1984**, *29*, 3092−3110.
(9) Chupp, T. E.; Wagshul, M. E.; Coulter, K. P.; Mcdonald, A. B.; Happer, W. Polarized, high-density, gaseous He 3 targets. *Phys. Rev. C: Nucl. Phys.* **1987**, *36*, 2244−2251.
(10) Cates, G. D.; Benton, D. R.; Gatzke, M.; Happer, W.; Hasson, K. C.; Newbury, N. R. Laser Production of Large Nuclear-Spin Polarization in Frozen Xenon. *Phys. Rev. Lett.* **1990**, *65*, 2591−2594.
(11) Driehuys, B.; Martinez-Jimenez, S.; Cleveland, Z. I.; Metz, G. M.; Beaver, D. M.; Nouls, J. C.; Kaushik, S. S.; Firszt, R.; Willis, C.; Kelly, K. T.; Wolber, J.; Kraft, M.; McAdams, H. P. Chronic Obstructive Pulmonary Disease: Safety and Tolerability of Hyperpolarized Xe-129 MR Imaging in Healthy Volunteers and Patients. *Radiology* **2012**, *262*, 279−289.
(12) Walker, T. G.; Happer, W. Spin-Exchange Optical Pumping of Noble-Gas Nuclei. *Rev. Mod. Phys.* **1997**, *69*, 629−642.
(13) Ebert, M.; Grossmann, T.; Heil, W.; Otten, W. E.; Surkau, R.; Leduc, M.; Bachert, P.; Knopp, M. V.; Schad, L. R.; Thelen, M. Nuclear Magnetic Resonance Imaging with Hyperpolarised Helium-3. *Lancet* **1996**, *347*, 1297.
(14) Kauczor, H. U.; Hofmann, D.; Kreitner, K. F.; Nilgens, H.; Surkau, R.; Heil, W.; Potthast, A.; Knopp, M. V.; Otten, E. W.; Thelen, M. Normal and Abnormal Pulmonary Ventilation: Visualization at Hyperpolarized He-3 MR Imaging. *Radiology* **1996**, *201*, 564−568.
(15) Kaushik, S. S.; Cleveland, Z. I.; Cofer, G. P.; Metz, G.; Beaver, D.; Nouls, J.; Kraft, M.; Auffermann, W.; Wolber, J.; McAdams, H. P.; Driehuys, B. Diffusion-Weighted Hyperpolarized Xe-129 MRI in Healthy Volunteers and Subjects with Chronic Obstructive Pulmonary Disease. *Magn. Reson. Med.* **2011**, *65*, 1154−1165.
(16) Stephen, M. J.; Emami, K.; Woodburn, J. M.; Chia, E.; Kadlecek, S.; Zhu, J.; Pickup, S.; Ishii, M.; Rizi, R. R.; Rossman, M. Quantitative Assessment of Lung Ventilation and Microstructure in an Animal Model of Idiopathic Pulmonary Fibrosis Using Hyperpolarized Gas MRI. *Acad. Radiol.* **2010**, *17*, 1433−1443.
(17) Mugler, J. P.; Altes, T. A. Hyperpolarized ^{129}Xe MRI of the Human Lung. *J. Magn. Reson. Imaging* **2013**, *37*, 313−331.
(18) Branca, R. T.; He, T.; Zhang, L.; Floyd, C. S.; Freeman, M.; White, C.; Burant, A. Detection of Brown Adipose Tissue and Thermogenic Activity in Mice by Hyperpolarized Xenon MRI. *Proc. Natl. Acad. Sci. U.S.A.* **2014**, *111*, 18001−18006.
(19) Barskiy, D. A.; Coffey, A. M.; Nikolaou, P.; Mikhaylov, D. M.; Goodson, B. M.; Branca, R. T.; Lu, G. J.; Shapiro, M. G.; Telkki, V.-V.; Zhivonitko, V. V.; Koptyug, I. V.; Salnikov, O. G.; Kovtunov, K. V.; Bukhtiyarov, V. I.; Rosen, M. S.; Barlow, M. J.; Safavi, S.; Hall, I. P.; Schröder, L.; Chekmenev, E. Y. NMR Hyperpolarization Techniques of Gases. *Chem.—Eur. J.* **2017**, *23*, 725−751.
(20) Wild, J. M.; Marshall, H.; Xu, X.; Norquay, G.; Parnell, S. R.; Clemence, M.; Griffiths, P. D.; Parra-Robles, J. Simultaneous Imaging of Lung Structure and Function with Triple-Nuclear Hybrid MR Imaging. *Radiology* **2013**, *267*, 251−255.
(21) Butler, J. P.; Loring, S. H.; Patz, S.; Tsuda, A.; Yablonskiy, D. A.; Mentzer, S. J. Evidence for Adult Lung Growth in Humans. *N. Engl. J. Med.* **2012**, *367*, 244−247.
(22) Zook, A. L.; Adhyaru, B. B.; Bowers, C. R. High Capacity Production of > 65% Spin Polarized Xenon-129 for NMR Spectroscopy and Imaging. *J. Magn. Reson.* **2002**, *159*, 175−182.
(23) Ruset, I. C.; Ketel, S.; Hersman, F. W. Optical Pumping System Design for Large Production of Hyperpolarized Xe-129. *Phys. Rev. Lett.* **2006**, *96*, 053002.
(24) Freeman, M. S.; Emami, K.; Driehuys, B. Characterizing and Modeling the Efficiency Limits in Large-Scale Production of Hyperpolarized ^{129}Xe. *Phys. Rev. A: At., Mol., Opt. Phys.* **2014**, *90*, 023406.
(25) Nikolaou, P.; Coffey, A. M.; Walkup, L. L.; Gust, B. M.; Whiting, N.; Newton, H.; Muradyan, I.; Dabaghyan, M.; Ranta, K.; Moroz, G. D.; Rosen, M. S.; Patz, S.; Barlow, M. J.; Chekmenev, E. Y.; Goodson, B. M. Xena: An Automated "Open-Source" ^{129}Xe Hyperpolarizer for Clinical Use. *Magn. Reson. Imaging* **2014**, *32*, 541−550.
(26) Rosen, M. S.; Chupp, T. E.; Coulter, K. P.; Welsh, R. C.; Swanson, S. D. Polarized Xe-129 Optical Pumping/Spin Exchange and Delivery System for Magnetic Resonance Spectroscopy and Imaging Studies. *Rev. Sci. Instrum.* **1999**, *70*, 1546−1552.
(27) Walker, T. G. Fundamentals of Spin-Exchange Optical Pumping. *J. Phys.: Conf. Ser.* **2011**, *294*, 012001.
(28) Koptyug, I. V.; Kovtunov, K. V.; Burt, S. R.; Anwar, M. S.; Hilty, C.; Han, S.-I.; Pines, A.; Sagdeev, R. Z. Para-Hydrogen-Induced Polarization in Heterogeneous Hydrogenation Reactions. *J. Am. Chem. Soc.* **2007**, *129*, 5580−5586.
(29) Kovtunov, K. V.; Zhivonitko, V. V.; Skovpin, I. V.; Barskiy, D. A.; Koptyug, I. V. Parahydrogen-Induced Polarization in Heterogeneous Catalytic Processes. *Top. Curr. Chem.* **2012**, *338*, 123−180.
(30) Kovtunov, K. V.; Zhivonitko, V. V.; Skovpin, I. V.; Barskiy, D. A.; Salnikov, O. G.; Koptyug, I. V. Toward Continuous Production of Catalyst-Free Hyperpolarized Fluids Based on Biphasic and Heterogeneous Hydrogenations with Parahydrogen. *J. Phys. Chem. C* **2013**, *117*, 22887−22893.
(31) Bowers, C. R.; Weitekamp, D. P. Transformation of Symmetrization Order to Nuclear-Spin Magnetization by Chemical-Reaction and Nuclear-Magnetic-Resonance. *Phys. Rev. Lett.* **1986**, *57*, 2645−2648.
(32) Bowers, C. R.; Weitekamp, D. P. Para-Hydrogen and Synthesis Allow Dramatically Enhanced Nuclear Alignment. *J. Am. Chem. Soc.* **1987**, *109*, 5541−5542.
(33) Pravica, M. G.; Weitekamp, D. P. Net NMR Alighnment by Adiabatic Transport of Parahydrogen Addition Products to High Magnetic Field. *Chem. Phys. Lett.* **1988**, *145*, 255−258.
(34) Eisenschmid, T. C.; Kirss, R. U.; Deutsch, P. P.; Hommeltoft, S. I.; Eisenberg, R.; Bargon, J.; Lawler, R. G.; Balch, A. L. Para Hydrogen Induced Polarization in Hydrogenation Reactions. *J. Am. Chem. Soc.* **1987**, *109*, 8089−8091.
(35) Salnikov, O. G.; Kovtunov, K. V.; Nikolaou, P.; Kovtunova, L. M.; Bukhtiyarov, V. I.; Koptyug, I. V.; Chekmenev, E. Y. Heterogeneous Parahydrogen Pairwise Addition to Cyclopropane. *ChemPhysChem* **2018**, *19*, 2621−2626.
(36) Barskiy, D. A.; Kovtunov, K. V.; Gerasimov, E. Y.; Phipps, M. A.; Salnikov, O. G.; Coffey, A. M.; Kovtunova, L. M.; Prosvirin, I. P.; Bukhtiyarov, V. I.; Koptyug, I. V.; Chekmenev, E. Y. 2D Mapping of NMR Signal Enhancement and Relaxation for Heterogeneously Hyperpolarized Propane Gas. *J. Phys. Chem. C* **2017**, *121*, 10038−10046.

DOI: 10.1021/acs.jpcc.9b01538
J. Phys. Chem. C 2019, 123, 11734−11744

(37) Burueva, D. B.; Romanov, A. S.; Salnikov, O. G.; Zhivonitko, V. V.; Chen, Y.-W.; Barskiy, D. A.; Chekmenev, E. Y.; Hwang, D. W.; Kovtunov, K. V.; Koptyug, I. V. Extending the Lifetime of Hyperpolarized Propane Gas Via Reversible Dissolution. *J. Phys. Chem. C* **2017**, *121*, 4481−4487.
(38) Carravetta, M.; Johannessen, O. G.; Levitt, M. H. Beyond the T_1 Limit: Singlet Nuclear Spin States in Low Magnetic Fields. *Phys. Rev. Lett.* **2004**, *92*, 153003.
(39) Carravetta, M.; Levitt, M. H. Long-Lived Nuclear Spin States in High-Field Solution NMR. *J. Am. Chem. Soc.* **2004**, *126*, 6228−6229.
(40) Pileio, G.; Carravetta, M.; Levitt, M. H. Storage of Nuclear Magnetization as Long-Lived Singlet Order in Low Magnetic Field. *Proc. Natl. Acad. Sci. U.S.A.* **2010**, *107*, 17135−17139.
(41) Levitt, M. H. Symmetry Constraints on Spin Dynamics: Application to Hyperpolarized NMR. *J. Magn. Reson.* **2016**, *262*, 91−99.
(42) Vasos, P. R.; Comment, A.; Sarkar, R.; Ahuja, P.; Jannin, S.; Ansermet, J.-P.; Konter, J. A.; Hautle, P.; van den Brandt, B.; Bodenhausen, G. Long-Lived States to Sustain Hyperpolarized Magnetization. *Proc. Natl. Acad. Sci. U.S.A.* **2009**, *106*, 18469−18473.
(43) Ahuja, P.; Sarkar, R.; Jannin, S.; Vasos, P. R.; Bodenhausen, G. Proton Hyperpolarisation Preserved in Long-Lived States. *Chem. Commun.* **2010**, *46*, 8192−8194.
(44) Warren, W. S.; Jenista, E.; Branca, R. T.; Chen, X. Increasing Hyperpolarized Spin Lifetimes through True Singlet Eigenstates. *Science* **2009**, *323*, 1711−1714.
(45) Feng, Y.; Davis, R. M.; Warren, W. S. Accessing Long-Lived Nuclear Singlet States between Chemically Equivalent Spins without Breaking Symmetry. *Nat. Phys.* **2012**, *8*, 831−837.
(46) Franzoni, M. B.; Buljubasich, L.; Spiess, H. W.; Münnemann, K. Long-Lived H-1 Singlet Spin States Originating from Para-Hydrogen in Cs-Symmetric Molecules Stored for Minutes in High Magnetic Fields. *J. Am. Chem. Soc.* **2012**, *134*, 10393−10396.
(47) Roy, S. S.; Rayner, P. J.; Norcott, P.; Green, G. G. R.; Duckett, S. B. Long-Lived States to Sustain SABRE Hyperpolarised Magnetisation. *Phys. Chem. Chem. Phys.* **2016**, *18*, 24905−24911.
(48) Zhou, Z.; Yu, J.; Colell, J. F. P.; Laasner, R.; Logan, A.; Barskiy, D. A.; Shchepin, R. V.; Chekmenev, E. Y.; Blum, V.; Warren, W. S.; Theis, T. Long-Lived $^{13}C_2$ Nuclear Spin States Hyperpolarized by Parahydrogen in Reversible Exchange at Microtesla Fields. *J. Phys. Chem. Lett.* **2017**, *8*, 3008−3014.
(49) Theis, T.; Ortiz, G. X.; Logan, A. W. J.; Claytor, K. E.; Feng, Y.; Huhn, W. P.; Blum, V.; Malcolmson, S. J.; Chekmenev, E. Y.; Wang, Q.; Warren, W. S. Direct and Cost-Efficient Hyperpolarization of Long-Lived Nuclear Spin States on Universal $^{15}N_2$-Diazirine Molecular Tags. *Sci. Adv.* **2016**, *2*, No. e1501438.
(50) Dumez, J.-N.; Håkansson, P.; Mamone, S.; Meier, B.; Stevanato, G.; Hill-Cousins, J. T.; Roy, S. S.; Brown, R. C. D.; Pileio, G.; Levitt, M. H. Theory of Long-Lived Nuclear Spin States in Methyl Groups and Quantum-Rotor Induced Polarisation. *J. Chem. Phys.* **2015**, *142*, 044506.
(51) All-Gas-Inc. Propane Gas Properties. http://www.allgasinc.com/propane-gas-properties.php (accessed on February 17, 2019).
(52) Abdelkhalik, A.; Askar, E.; Markus, D.; Brandes, E.; El-sayed, I.; Hassan, M.; Nour, M.; Stolz, T. Explosion Regions of Propane, Isopropanol, Acetone, and Methyl Acetate/Inert Gas/Air Mixtures. *J. Loss Prev. Process Ind.* **2016**, *43*, 669−675.
(53) Stewart, R. D.; Newton, P. E.; Baretta, E. D.; Herrmann, A. A.; Forster, H. V.; Soto, R. J. Physiological Response to Aerosol Propellants. *Environ. Health Perspect.* **1978**, *26*, 275−285.
(54) Food and Drug Administration. *Code of Federal Regulations Title 21*; Office of the Federal Register: United States, 2018; p 21cfr184.1655.
(55) Salnikov, O. G.; Nikolaou, P.; Ariyasingha, N. M.; Kovtunov, K. V.; Koptyug, I. V.; Chekmenev, E. Y. Clinical-Scale Batch-Mode Production of Hyperpolarized Propane Gas for MRI. *Anal. Chem.* **2019**, *91*, 4741−4746.
(56) Kovtunov, K. V.; Barskiy, D. A.; Coffey, A. M.; Truong, M. L.; Salnikov, O. G.; Khudorozhkov, A. K.; Inozemtseva, E. A.; Prosvirin, I. P.; Bukhtiyarov, V. I.; Waddell, K. W.; Chekmenev, E. Y.; Koptyug, I. V. High-Resolution 3D Proton Hyperpolarized Gas MRI Enabled by Parahydrogen and Rh/TiO_2 Heterogeneous Catalyst. *Chem.—Eur. J.* **2014**, *20*, 11636−11639.
(57) Kovtunov, K. V.; Truong, M. L.; Barskiy, D. A.; Koptyug, I. V.; Coffey, A. M.; Waddell, K. W.; Chekmenev, E. Y. Long-Lived Spin States for Low-Field Hyperpolarized Gas MRI. *Chem.—Eur. J.* **2014**, *20*, 14629−14632.
(58) Kovtunov, K. V.; Truong, M. L.; Barskiy, D. A.; Salnikov, O. G.; Bukhtiyarov, V. I.; Coffey, A. M.; Waddell, K. W.; Koptyug, I. V.; Chekmenev, E. Y. Propane-D_6 Heterogeneously Hyperpolarized by Parahydrogen. *J. Phys. Chem. C* **2014**, *118*, 28234−28243.
(59) Bouchard, L.-S.; Burt, S. R.; Anwar, M. S.; Kovtunov, K. V.; Koptyug, I. V.; Pines, A. NMR Imaging of Catalytic Hydrogenation in Microreactors with the Use of Para-Hydrogen. *Science* **2008**, *319*, 442−445.
(60) Coffey, A. M.; Truong, M. L.; Chekmenev, E. Y. Low-Field MRI Can Be More Sensitive Than High-Field MRI. *J. Magn. Reson.* **2013**, *237*, 169−174.
(61) Coffey, A. M.; Shchepin, R. V.; Feng, B.; Colon, R. D.; Wilkens, K.; Waddell, K. W.; Chekmenev, E. Y. A Pulse Programmable Parahydrogen Polarizer Using a Tunable Electromagnet and Dual Channel NMR Spectrometer. *J. Magn. Reson.* **2017**, *284*, 115−124.
(62) DeVience, S. J.; Walsworth, R. L.; Rosen, M. S. Preparation of Nuclear Spin Singlet States Using Spin-Lock Induced Crossing. *Phys. Rev. Lett.* **2013**, *111*, 173002.
(63) Barskiy, D. A.; Salnikov, O. G.; Romanov, A. S.; Feldman, M. A.; Coffey, A. M.; Kovtunov, K. V.; Koptyug, I. V.; Chekmenev, E. Y. NMR Spin-Lock Induced Crossing (SLIC) Dispersion and Long-Lived Spin States of Gaseous Propane at Low Magnetic Field (0.05 T). *J. Magn. Reson.* **2017**, *276*, 78−85.
(64) Lemaire, C.; Armstrong, R. L. Proton Spin Longitudinal Relaxation Time in Gaseous Ammonia and Hydrogen Chloride. *J. Chem. Phys.* **1984**, *81*, 1626−1631.
(65) True, N. S. Gas Phase Applications of NMR Spectroscopy. In *Encyclopedia of Spectroscopy and Spectrometry*; Lindon, J. C., Ed.; Elsevier: Oxford, 1999; pp 660−667.
(66) Taglang, C.; Korenchan, D. E.; von Morze, C.; Yu, J.; Najac, C.; Wang, S.; Blecha, J. E.; Subramaniam, S.; Bok, R.; VanBrocklin, H. F.; Vigneron, D. B.; Ronen, S. M.; Sriram, R.; Kurhanewicz, J.; Wilson, D. M.; Flavell, R. R. Late-Stage Deuteration of ^{13}C-Enriched Substrates for T_1 Prolongation in Hyperpolarized ^{13}C MRI. *Chem. Commun.* **2018**, *54*, 5233−5236.
(67) Shchepin, R. V.; Coffey, A. M.; Waddell, K. W.; Chekmenev, E. Y. Parahydrogen Induced Polarization of 1-^{13}C-Phospholactate-D_2 for Biomedical Imaging with >30,000,000-Fold NMR Signal Enhancement in Water. *Anal. Chem.* **2014**, *86*, 5601−5605.
(68) Kharkov, B.; Duan, X.; Canary, J. W.; Jerschow, A. Effect of Convection and B_1 Inhomogeneity on Singlet Relaxation Experiments. *J. Magn. Reson.* **2017**, *284*, 1−7.
(69) Salnikov, O. G.; Kovtunov, K. V.; Barskiy, D. A.; Bukhtiyarov, V. I.; Kaptein, R.; Koptyug, I. V. Kinetic Study of Propylene Hydrogenation over Pt/Al_2O_3 by Parahydrogen-Induced Polarization. *Appl. Magn. Reson.* **2013**, *44*, 279−288.
(70) Kiryutin, A. S.; Pravdivtsev, A. N.; Yurkovskaya, A. V.; Vieth, H.-M.; Ivanov, K. L. Nuclear Spin Singlet Order Selection by Adiabatically Ramped RF Fields. *J. Phys. Chem. B* **2016**, *120*, 11978−11986.
(71) Driehuys, B.; Cates, G. D.; Miron, E.; Sauer, K.; Walter, D. K.; Happer, W. High-Volume Production of Laser-Polarized Xe-129. *Appl. Phys. Lett.* **1996**, *69*, 1668−1670.
(72) Ruth, U.; Hof, T.; Schmidt, J.; Fick, D.; Jänsch, H. J. Production of Nitrogen-Free, Hyperpolarized Xe-129 Gas. *Appl. Phys. B: Lasers Opt.* **1999**, *68*, 93−97.

DOI: 10.1021/acs.jpcc.9b01538
J. Phys. Chem. C 2019, 123, 11734−11744

THE JOURNAL OF PHYSICAL CHEMISTRY C

Article

Cite This: J. Phys. Chem. C 2019, 123, 12827−12840

pubs.acs.org/JPCC

Parahydrogen-Induced Polarization of 1-^{13}C-Acetates and 1-^{13}C-Pyruvates Using Sidearm Hydrogenation of Vinyl, Allyl, and Propargyl Esters

Oleg G. Salnikov,*[†,‡] Nikita V. Chukanov,[†,‡] Roman V. Shchepin,[§,∥] Isaac V. Manzanera Esteve,[§,∥] Kirill V. Kovtunov,[†,‡] Igor V. Koptyug,[†,‡] and Eduard Y. Chekmenev*[§,∥,⊥,#,∇,○]

[†]International Tomography Center SB RAS, Institutskaya Street 3A, Novosibirsk 630090, Russia

[‡]Novosibirsk State University, Pirogova Street 2, Novosibirsk 630090, Russia

[§]Vanderbilt University Institute of Imaging Science (VUIIS), [∥]Department of Radiology, [⊥]Department of Biomedical Engineering, and [#]Vanderbilt-Ingram Cancer Center (VICC), Vanderbilt University, Nashville, Tennessee 37232-2310, United States

[∇]Department of Chemistry, Integrative Biosciences (Ibio), Karmanos Cancer Institute (KCI), Wayne State University, Detroit, Michigan 48202, United States

[○]Russian Academy of Sciences, Leninskiy Prospekt 14, Moscow 119991, Russia

Supporting Information

ABSTRACT: ^{13}C-hyperpolarized carboxylates, such as pyruvate and acetate, are emerging molecular contrast agents for magnetic resonance imaging (MRI) visualization of various diseases, including cancer. Here, we present a systematic study of ^{1}H and ^{13}C parahydrogen-induced polarization of acetate and pyruvate esters with ethyl, propyl, and allyl alcoholic moieties. It was found that allyl pyruvate is the most efficiently hyperpolarized compound from those under study, yielding 21 and 5.4% polarization of ^{1}H and ^{13}C nuclei, respectively, in CD_3OD solutions. Allyl pyruvate and ethyl acetate were also hyperpolarized in the aqueous phase using homogeneous hydrogenation with parahydrogen over a water-soluble rhodium catalyst. ^{13}C polarization values of 0.82 and 2.1% were obtained for allyl pyruvate and ethyl acetate, respectively. ^{13}C-hyperpolarized methanolic and aqueous solutions of allyl pyruvate and ethyl acetate were employed for in vitro MRI visualization, demonstrating the prospects for translation of the presented approach to biomedical in vivo studies.

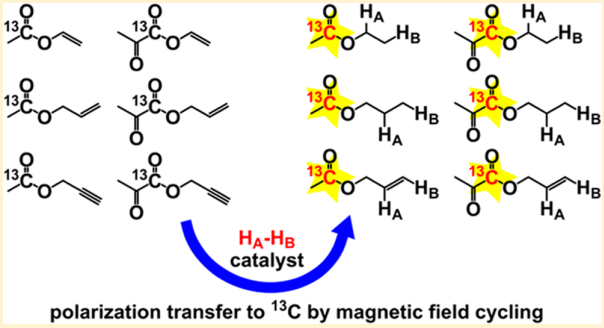

INTRODUCTION

Hyperpolarization of nuclear spins allows one to enhance the NMR signal by several orders of magnitude at magnetic fields of a few tesla.[1−4] The obtained hyperpolarized (HP) molecules can be used as contrast agents for metabolic studies and molecular imaging.[5,6] Currently, in this context, the most important HP compound is pyruvate, which is metabolized to lactate in vivo.[7] In tumor tissues, the rates of aerobic glycolysis and reduction of pyruvate to lactate are usually significantly higher compared to those of normal tissues (the so-called Warburg effect[8]). Thus, HP magnetic resonance spectroscopic imaging quantification of the lactate-to-pyruvate ratio can be used for cancer diagnosis using the intravenous injection of HP pyruvate, which significantly improves the sensitivity of this approach, allowing tumor diagnosis[6,9,10] as well as monitoring of tumor grading[11] and the response to cancer treatment.[12,13] The use of HP pyruvate has been already approved for the imaging of prostate cancer in clinical trials.[14,15] Another HP compound that attracts significant research (and future clinical) interest is acetate, which can be utilized for studying metabolism in the brain,[16,17] liver,[18] kidney,[19] and muscle.[20] It should be mentioned that for biomedical applications, hyperpolarization of ^{13}C nuclei in these compounds is strongly preferable due to significantly longer relaxation times and negligible in vivo background signal compared to those of protons.[21]

Currently, the dissolution dynamic nuclear polarization (d-DNP) technique is the most developed one for the production of HP molecules in solution for biomedical applications.[22−24] However, the high cost and complexity of d-DNP equipment limit its widespread use in research and future clinical use. A promising alternative is the use of the significantly more affordable parahydrogen-induced polarization (PHIP) technique.[25−29] PHIP is based on the pairwise addition of a

Received: March 4, 2019
Revised: April 17, 2019
Published: April 19, 2019

DOI: 10.1021/acs.jpcc.9b02041
J. Phys. Chem. C 2019, 123, 12827−12840

parahydrogen (p-H_2) molecule to an unsaturated substrate. Here, pairwise addition means that the molecule of a reaction product contains two H atoms that came from the same p-H_2 molecule. Pairwise addition of p-H_2 allows one to convert singlet spin order of parahydrogen into enhanced Zeeman magnetization of ^{1}H nuclei of the hydrogenation product.[30] The resultant hyperpolarization can be transferred to heteronuclei, including ^{13}C, either spontaneously[31,32] or by the use of magnetic field cycling (MFC)[33,34] or radiofrequency (RF) pulse sequences.[35−39] The possibility of the utilization of ^{13}C PHIP-hyperpolarized compounds as in vivo contrast agents for magnetic resonance imaging (MRI) was recently demonstrated in laboratory animals.[40−46] However, there are two major limitations that currently prevent PHIP from implementation in clinic. First of all, pairwise p-H_2 addition requires the use of a hydrogenation catalyst. Usually, PHIP experiments are performed with homogeneous catalysts, which represent transition-metal complexes dissolved in an organic solvent.[47] The toxicity of these catalysts demands their separation from the obtained HP compound before the injection into a patient. A possible solution of this problem is the use of heterogeneous catalysts,[48] which can be easily filtered out[49,50] or employed in continuous flow hydrogenation of unsaturated substrate vapors with subsequent dissolution of the HP reaction product,[51] though improving of polarization levels provided by these catalysts is highly desirable. Another approach is to perform hydrogenation of an unsaturated precursor with p-H_2 over a homogeneous catalyst in an organic solvent and then to chemically transform the resulting HP reaction product into a water-soluble form, which can be separated into an aqueous phase by extraction.[52] The second limitation of PHIP is the availability of an unsaturated precursor, which could be hydrogenated into the product of interest. This requirement makes it challenging to hyperpolarize such molecules as pyruvate or acetate by PHIP directly. The PHIP sidearm hydrogenation (PHIP-SAH) approach,[53−55] recently introduced by Reineri and co-workers, allows one to overcome this problem and to produce ^{13}C HP carboxylates by PHIP. The idea of PHIP-SAH is based on hydrogenation of a ^{13}C containing unsaturated ester (e.g., 1-^{13}C-propargyl pyruvate) with p-H_2 with subsequent polarization transfer from protons to the ^{13}C carboxyl nucleus, followed by hydrolysis of the hydrogenated ester to form ^{13}C HP carboxylate. The combination of PHIP-SAH with aqueous phase extraction after hydrolysis allows one to obtain a pure aqueous solution of ^{13}C HP pyruvate, which has been already demonstrated to be useful for metabolic studies.[56,57] When polarization transfer was performed with the use of magnetic field cycling, ^{13}C polarization up to ∼5% for 1-^{13}C-pyruvate in the aqueous phase was demonstrated.[55] Korchak et al. showed that up to ∼19% ^{13}C polarization can be obtained for 1-^{13}C-acetate-d_3 with the use of a fully deuterated vinyl acetate precursor as a substrate and the ESOTHERIC RF pulse sequence for polarization transfer.[58] Importantly, to obtain the maximum ^{13}C polarization in PHIP-SAH experiments, one needs to optimize all parameters, including the choice of the unsaturated moiety, hydrogenation reaction conditions, and the polarization transfer procedure. Though several different unsaturated esters were employed in PHIP-SAH studies before,[53,54,59] the effect of unsaturated moiety nature on the obtained polarization has not been reported. In this work, we present a systematic study of ^{1}H and ^{13}C PHIP-SAH hyperpolarization of acetate and pyruvate esters with ethyl, propyl, and allyl moieties. These esters were obtained by homogeneous hydrogenation of the corresponding unsaturated precursors (vinyl, allyl, and propargyl esters, respectively) with p-H_2 in organic and aqueous phases.

EXPERIMENTAL SECTION

Materials. Commercially available bis(norbornadiene)-rhodium(I) tetrafluoroborate ([Rh(NBD)$_2$]BF$_4$, NBD = norbornadiene, Strem 45-0230), 1,4-bis(diphenylphosphino)-butane (dppb, Sigma-Aldrich, 98%), (norbornadiene)[1,4-bis(diphenylphosphino)butane]rhodium(I) tetrafluoroborate ([Rh(NBD)(dppb)]BF$_4$, Sigma-Aldrich), and ultrapure hydrogen (>99.999%) were used as received. Unsaturated precursors (vinyl acetate, allyl acetate, propargyl acetate, vinyl pyruvate, allyl pyruvate, and propargyl pyruvate; see Chart 1) were synthesized according to procedures reported elsewhere.[60] In this study, we used propargyl and allyl esters with both natural abundance of ^{13}C nuclei (1.1%) and ∼98% ^{13}C enrichment in the carboxyl group. Vinyl acetate was used with ∼98% ^{13}C enrichment only because detailed homogeneous PHIP-SAH investigation of this substrate was reported previously.[61] In contrast, vinyl pyruvate was used only with ∼1.1% ^{13}C content because the ^{13}C-labeled precursor was not available to us (see the previous paper[60] for details).

Chart 1. Structures of Unsaturated Precursors Used for PHIP-SAH Experiments in This Study[a]

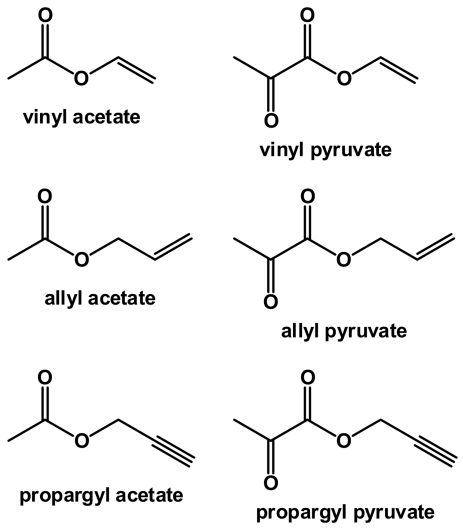

[a]Structures of all compounds employed in this study (including unsaturated precursors, reaction products, ligands, products of ligand hydrogenation, etc.) are presented in Chart S1.

PHIP Experiments. In most of the experiments, H_2 gas was enriched with parahydrogen using a custom-built p-H_2 generator based on a cryocooler module (SunPower, P/N 100490, CryoTel GT; a more detailed description of the generator was published elsewhere[60]). For the work presented here, the generator was operated at 43−66 K, resulting in approximately 85−60% p-H_2 enrichment. The ^{1}H NMR data for hyperpolarization of ethyl acetate was obtained with 88.5% parahydrogen produced using Bruker Parahydrogen Generator BPHG 90. The samples for homogeneous PHIP experiments were prepared as follows. For hydrogenation in CD_3OD, [Rh(NBD)$_2$]BF$_4$, dppb, and unsaturated precursor (in a 1:1:16

DOI: 10.1021/acs.jpcc.9b02041
J. Phys. Chem. C 2019, 123, 12827−12840

molar ratio) were dissolved in a required amount of CD_3OD and mixed using a vortex mixer to obtain a solution with 5 mM concentration of the catalyst and the ligand and 80 mM concentration of the substrate. The obtained solutions were placed in standard 5 mm Wilmad NMR tubes tightly connected with 1/4 in. outer-diameter poly(tetrafluoroethylene) (PTFE) tubes (the sample volume was 0.7 mL). The exception was the case of ^{13}C MRI experiments where medium-wall 5 mm NMR tubes were used (Wilmad glass P/N 503-PS-9; the sample volume was 0.5 mL). For hydrogenation in D_2O, a previously described procedure was employed for the preparation of an aqueous catalyst solution (~5.3 or 10 mM concentration) in D_2O.[62] In brief, the solution of disodium salt of 1,4-bis[(phenyl-3-propanesulfonate)phosphine]butane in D_2O was degassed with a rotary evaporator. Then, the solution of $[Rh(NBD)_2]$-BF_4 in acetone was added dropwise with subsequent degassing. Next, the required amount of unsaturated precursor was added, resulting in ~80 mM concentration. The obtained solutions were placed in medium-wall 5 mm NMR tubes (Wilmad glass P/N 503-PS-9; the sample volume was 0.5 mL), tightly connected with 1/4 in. outer-diameter PTFE tubes. All glassware was flushed with argon right before the addition of any solution inside.

The overall scheme of the experimental setup is presented in Figure 1. In the case of PHIP experiments with methanolic

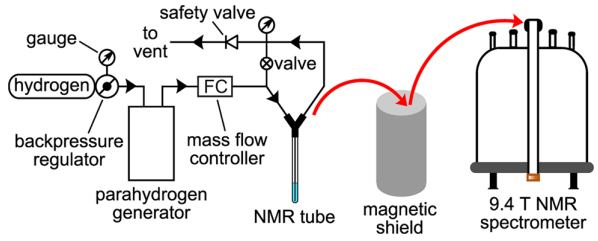

Figure 1. Diagram of the experimental setup for ^{13}C hyperpolarization and NMR spectroscopic detection of acetate and pyruvate esters. Adopted with permission from refs 60, 64. Copyright 2018 American Chemical Society.

solutions, the samples were pressurized up to 40 psig and preheated up to 40 °C using an NMR spectrometer temperature control unit (except the ^1H NMR data for hyperpolarization of ethyl acetate that was obtained at 35 psig pressure). The hydrogen gas flow rate (40 sccm) was regulated with a mass flow controller (SmartTrak 50, Sierra Instruments, Monterey, CA). After termination of p-H_2 bubbling, the samples were placed either directly inside the probe of the NMR spectrometer (in the case of ALTADENA[63] experiments) or inside the MuMETAL magnetic shield described in detail elsewhere[61] (in the case of MFC experiments). The magnetic field inside the shield was adjusted using an additional solenoid placed inside the previously degaussed three-layered MuMETAL shield (Magnetic Shield Corp., Bensenville, IL, P/N ZG-206). This previously calibrated solenoid was powered by a direct current (DC) power supply (GW-Instek, GPR-30600), and the DC current was attenuated by a resistor bank (Global Specialties, RDB-10) to achieve the desired magnetic field inside the MuMETAL shield. The MuMETAL shield provides an isolation of approximately 1200-fold according to the manufacturer's specification; therefore, the use of the shield in the Earth's magnetic field results in the minimum residual magnetic field of approximately 40 nT. After placing inside the magnetic shield, the samples were slowly (~1 s) pulled out of the shield and quickly placed inside the probe of the NMR spectrometer. The total sample transfer time was ~8 s after the termination of H_2 gas bubbling. Experiments with aqueous solutions were carried out using the same experimental procedure except that higher pressure (70 or 80 psig), temperature (55–95 °C), and hydrogen gas flow rate (140 sccm) were used. Heating to temperatures higher than 60 °C was performed using a beaker with hot water. Moreover, in the case of aqueous solutions, PASADENA[25] experiments were performed in addition to ALTADENA and MFC experiments. In this case, the samples were residing inside the NMR spectrometer probe during all operations. In MFC experiments with MRI detection, also higher pressure (70 psig), temperature (80–95 °C), and hydrogen gas flow rate (140 sccm) were used. After pulling the samples out of the shield, they were depressurized, the NMR tube was disconnected from the setup, and the solution was injected into an imaging phantom (~2.8 mL hollow spherical plastic ball) located inside the RF coil of an MRI scanner using a syringe. The sample transfer time to an MRI scanner was ~20 s.

NMR spectra were acquired on a 9.4 T Bruker NMR spectrometer (except the ^1H NMR data for hyperpolarization of ethyl acetate that was obtained on a 7.05 T Bruker AV 300 NMR spectrometer) using a 90° RF pulse, except PASADENA[25] experiments, which were performed using a 45° RF pulse. The ^1H ALTADENA and ^{13}C PHIP spectra were acquired as pseudo-two-dimensional (2D) sets consisting of 64 one-dimensional NMR spectra (acquisition time 1 s) to avoid delays between placing the sample into the probe and starting the acquisition. The acquisition always started before placing the sample inside the NMR probe. MR images were obtained on a 15.2 T small-animal Bruker MRI scanner using a 15 mm outer-diameter round surface RF coil and true fast imaging steady-state precession RF pulse sequence. The excitation pulse angle was optimized on a thermally polarized phantom containing 2.8 mL of 3 M solution of sodium 1-^{13}C-acetate in D_2O. For three-dimensional (3D) imaging experiments, the isotropic field of view (FOV) was 48 mm, and the imaging matrix was 64 × 64 × 8, resulting in 0.75 × 0.75 × 6 mm^3 spatial resolution. The repetition time (TR) was ~5 ms, and the echo time (TE) was ~2.5 ms. The total acquisition time was ~2.5 s. For 2D MRI experiments, FOV of 48 × 48 mm^2 was used with the slab thickness of 48 mm, resulting in effectively no slice selection with respect to the phantom depth. The TR and TE parameters were the same.

Calculation of NMR Signal Enhancement and Nuclear Spin Polarization. ^1H NMR signal enhancement factors ($\varepsilon_{^1H}$) were calculated using NMR signals of thermally polarized reaction product molecules as a reference, according to the following equation

$$\varepsilon_{^1H} = \frac{I_{^1H\text{-PHIP}}}{I_{^1H\text{-thermal}}}$$

where $I_{^1H\text{-PHIP}}$ is the intensity of the PHIP signal of a particular group of protons and $I_{^1H\text{-thermal}}$ is the averaged signal per proton in a thermally polarized molecule. The $I_{^1H\text{-thermal}}$ values were calculated as follows

DOI: 10.1021/acs.jpcc.9b02041
J. Phys. Chem. C 2019, 123, 12827–12840

$$I_{^1\text{H-thermal}} = \frac{\sum_{i=1}^{M} (I_i/N_i)}{M}$$

where M is the number of different groups of protons in a molecule, I_i is the intensity of the NMR signal for the group of protons with index i, and N_i is the number of protons in this group. The overlapping NMR signals (e.g., signals of CH_3 groups of carboxyl moieties) were omitted from these calculations. It should be noted that, in principle, the hydrogenation reaction may continue during the delay between acquisition of PHIP and thermal NMR spectra, leading to underestimation of NMR signal enhancements. It was found that in our conditions this effect does not have a significant impact on the obtained ε values. Figure S1 in the Supporting Information presents two thermal ^{1}H NMR spectra acquired after bubbling of p-H_2 for 4 s through the solution of propargyl pyruvate and [Rh(NBD)(dppb)]BF_4 catalyst in CD_3OD with a 30 min delay between them. These two spectra were found to be almost identical despite the facts that (i) conversion of propargyl pyruvate was only ∼16%, that is, there is a significant amount of reactant left; (ii) there is a significant amount of dissolved hydrogen manifested in the NMR signal of ortho-H_2 at 4.52 ppm; and (iii) propargyl pyruvate is the most reactive substrate among those under study; see the Results and Discussion section. Therefore, it is concluded that hydrogenation reaction proceeds to a significant extent only under conditions of hydrogen bubbling when the solution is intensely agitated.

In experiments with substrates containing ^{13}C nuclei at natural abundance, ^{13}C NMR signal enhancement factors ($\varepsilon_{^{13}\text{C}}$) were calculated using the NMR signal of 740 mM solution of 1-^{13}C-vinyl acetate (with 98% ^{13}C enrichment) in CD_3OD as an external reference, according to the following equation

$$\varepsilon_{^{13}\text{C}} = \frac{I_{^{13}\text{C-PHIP}}}{I_{^{13}\text{C-ref}}} \times \frac{C_{\text{ref}}}{C_{\text{reactant}} \times \frac{X}{100\,\%}} \times \frac{\varphi_{\text{ref}}}{\varphi_{\text{reactant}}}$$

where $I_{^{13}\text{C-PHIP}}$ is the intensity of the ^{13}C PHIP NMR signal, $I_{^{13}\text{C-ref}}$ is the intensity of the ^{13}C NMR signal of the reference sample, C_{ref} = 740 mM is the concentration of vinyl acetate in the reference sample, C_{reactant} = 80 mM is the initial concentration of the reactant before hydrogenation, X (%) is the chemical conversion of the reactant estimated using ^{1}H NMR spectra acquired after relaxation of polarization, φ_{ref} = 0.98 is ^{13}C enrichment of vinyl acetate in the reference sample, and $\varphi_{\text{reactant}}$ = 0.011 is the ^{13}C enrichment of the substrate. The use of an external reference was necessary because it was not possible to acquire thermal ^{13}C NMR signals for the hydrogenated samples in reasonable amount of time.

In experiments with ^{13}C-enriched substrates, ^{13}C NMR signal enhancement factors ($\varepsilon_{^{13}\text{C}}$) were calculated using ^{13}C NMR signals of thermally polarized reaction product molecules as a reference

$$\varepsilon_{^{13}\text{C}} = \frac{I_{^{13}\text{C-PHIP}}}{I_{^{13}\text{C-thermal}}} \times \frac{\text{RG}_{\text{thermal}}}{\text{RG}_{\text{PHIP}}} \times \frac{\text{NS}_{\text{thermal}}}{\text{NS}_{\text{PHIP}}}$$

where $I_{^{13}\text{C-PHIP}}$ is the intensity of the ^{13}C PHIP NMR signal, $I_{^{13}\text{C-thermal}}$ is the intensity of the ^{13}C NMR signal of the thermally polarized sample, $\text{RG}_{\text{thermal}}$ = 203 or 1 is the receiver gain used for acquisition of the thermal signal, RG_{PHIP} = 1 is the receiver gain used for acquisition of the PHIP signal, and $\text{NS}_{\text{thermal}}$ = 1, 2, 4, or 8 and NS_{PHIP} = 1 are the numbers of signal accumulations used for the acquisition of thermal and PHIP NMR spectra, respectively. The use of different receiver gain values was necessary because it usually was not possible to obtain thermal ^{13}C NMR signals for the hydrogenated samples with RG = 1 in reasonable amount of time. On the other hand, acquisition of PHIP spectra with RG = 203 led to signal overflow. According to vendor specifications, there is a linear dependence between the observed NMR signal and RG. The deviation of the RG function from linearity is expected to be less than 10%,[65] which we consider satisfactory for our purposes. In most of the experiments, thermal ^{13}C NMR spectra were acquired with several signal accumulations to obtain the signal that can be integrated with sufficient accuracy.

Nuclear spin polarizations $P_{^1\text{H}}$ and $P_{^{13}\text{C}}$ were calculated using the formula

$$P = \varepsilon \times P_0$$

where P_0 is the equilibrium nuclear spin polarization of ^{1}H or ^{13}C at the 9.4 T magnetic field (at 313 K, $P_0 = 3.1 \times 10^{-3}$% for ^{1}H and $P_0 = 7.7 \times 10^{-4}$% for ^{13}C). Because experiments were performed with broadly varied p-H_2 fractions (60−85%, with the exception of the ^{1}H hyperpolarization of ethyl acetate in CD_3OD, where 88.5% p-H_2 was employed), the observed polarizations were also recalculated to the highest utilized p-H_2 fraction (85%) for the sake of comparison using the following equation[29]

$$P_{85\%} = P \times \frac{4 \times 0.85 - 1}{4\chi_p - 1}$$

where $P_{85\%}$ is the polarization recalculated to the 85% p-H_2 fraction and χ_p is the p-H_2 fraction employed in a particular experiment. Polarization transfer efficiency η was calculated as a ratio of the maximum obtained $P_{^{13}\text{C}}$ and $P_{^1\text{H}}$ values for each HP compound

$$\eta = \frac{P_{^{13}\text{C}}}{P_{^1\text{H}}}$$

Since the samples were manually transferred from the low to the high magnetic field and the duration of p-H_2 bubbling was also manually controlled, the reproducibility test was carried out. For this, hyperpolarization of ethyl acetate was followed using ^{1}H NMR spectroscopy. Ten repetitions of p-H_2 addition to vinyl acetate were performed, which yielded relative standard errors of 6% or less for the vinyl acetate conversion, ^{1}H ALTADENA signal intensities, signal enhancements, and ^{1}H polarization (Table S1). Therefore, we expect the numerical data presented in this work to have standard errors on the order of ∼6% due to shot-to-shot reproducibility in most cases.

RESULTS AND DISCUSSION

General Considerations. The PHIP experiments were generally performed according to the following scenario. First, ^{1}H ALTADENA experiments with various durations of p-H_2 bubbling were carried out. Then, the duration of p-H_2 bubbling, which was optimal in terms of the resultant ^{1}H ALTADENA signal, was used for MFC experiments with magnetic field variation. Generally, these experiments were first performed with unsaturated precursors with natural abundance of ^{13}C nuclei for the optimization of experimental parameters, and then MFC experiments were repeated with isotopically

DOI: 10.1021/acs.jpcc.9b02041
J. Phys. Chem. C 2019, 123, 12827−12840

labeled precursors. This screening of substrates was performed in CD_3OD solutions at 40 psig hydrogen pressure. Then, the two precursors that provided the highest ^1H and ^{13}C polarizations were used in aqueous phase hydrogenation and for MRI demonstration in vitro.

PHIP of Ethyl 1-^{13}C-Acetate. PHIP of ethyl 1-^{13}C-acetate produced by homogeneous hydrogenation of vinyl 1-^{13}C-acetate with p-H_2 in CD_3OD was reported previously.[61] In that study, $P_{^1H}$ = 3.3% and $P_{^{13}C}$ = 1.8% were demonstrated at 50% p-H_2 enrichment and 90 psig pressure. At 85% p-H_2 enrichment, these polarizations would be 2.4 times higher,[29] resulting in $P_{^1H}$ = 7.9% and $P_{^{13}C}$ = 4.3%. Similar polarization values were obtained in this work in a hyperpolarization protocol reproducibility test (average $P_{^1H}$ = 7.5%, maximum $P_{^1H}$ = 8.1%, recalculated to 85% p-H_2 enrichment; see Figure 2c,d and Table S1). Because vinyl acetate hydrogenation was studied in detail before,[61] here we used this substrate to test the alternative experimental protocol for the sample preparation. Previous experiments employed the commercially available [Rh(NBD)(dppb)]BF_4 catalyst. In the alternative experimental protocol, the [Rh(NBD)(dppb)]$^+$ species were formed during the sample preparation procedure from commercially available [Rh(NBD)$_2$]BF_4 and dppb in a 1:1 ratio, and the resultant solution was used for PHIP experiments without any purification. Therefore, in the alternative experimental protocol, the solution contains 2 equiv of norbornadiene instead of 1 equiv in the solution prepared from the commercially available [Rh(NBD)(dppb)]-BF_4 complex. On the other hand, the reactants required for the alternative experimental protocol are several times cheaper. The obtained results are presented in Figure 2. It was found that both variants of the experimental protocols have similar efficiency (Figure 2g). Therefore, in further experiments reported here, the catalyst was prepared from [Rh(NBD)$_2$]BF_4 and dppb. The maximum obtained $P_{^{13}C}$ was 4.4% (at 85% p-H_2 fraction), which is in a good agreement with the previously reported[61] value despite the use of lower hydrogen pressure (40 psig instead of 90 psig; the polarization values are recalculated to 85% p-H_2 enrichment).

PHIP of Propyl 1-^{13}C-Acetate. HP propyl acetate was produced by homogeneous hydrogenation of allyl acetate in methanol over the [Rh(NBD)(dppb)]BF_4 catalyst prepared from [Rh(NBD)$_2$]BF_4 and dppb. According to ^1H NMR, the catalyst activity was quite low since 50% conversion of allyl acetate was reached only after ~50 s of hydrogen bubbling at 40 psig pressure (Figure 3g). The estimation of ^1H polarization values for propyl acetate was complicated because ^1H NMR signals 5c and 5d of propyl acetate overlapped with signals 19c and 19d of norbornene, respectively (Figure 3c). Since it was not possible to reliably estimate the relative contribution of propyl acetate and norbornene protons to the observed ALTADENA signals, ^1H polarization of propyl acetate was calculated on the basis of NMR signal 5b. The maximum obtained ALTADENA $P_{^1H}$ of the corresponding protons of propyl acetate was 3.0% (at 85% p-H_2 fraction) (Figure 3i). Next, MFC experiments with magnetic field variation were performed at 30 s duration of p-H_2 bubbling (at which the maximum ^1H ALTADENA signal was observed). The maximum obtained $P_{^{13}C}$ was 0.35% (at 85% p-H_2 fraction) (Figure 3e,f,j).

PHIP of Allyl 1-^{13}C-Acetate. HP allyl acetate was produced by homogeneous hydrogenation of propargyl acetate in methanol over the [Rh(NBD)(dppb)]BF_4 catalyst prepared from [Rh(NBD)$_2$]BF_4 and dppb. The catalyst was significantly more active in hydrogenation of this compound than in hydrogenation of allyl acetate at the same conditions: 50% conversion of propargyl acetate was achieved after ~5.5 s of hydrogen bubbling at 40 psig pressure (Figure 4g). Due to overlapping of ^1H NMR signal 4c of allyl acetate with signal 19a of norbornene (Figure 4c), ^1H polarization of allyl acetate was calculated on the basis of NMR signal 4e. The maximum obtained ALTADENA $P_{^1H}$ of the corresponding protons of

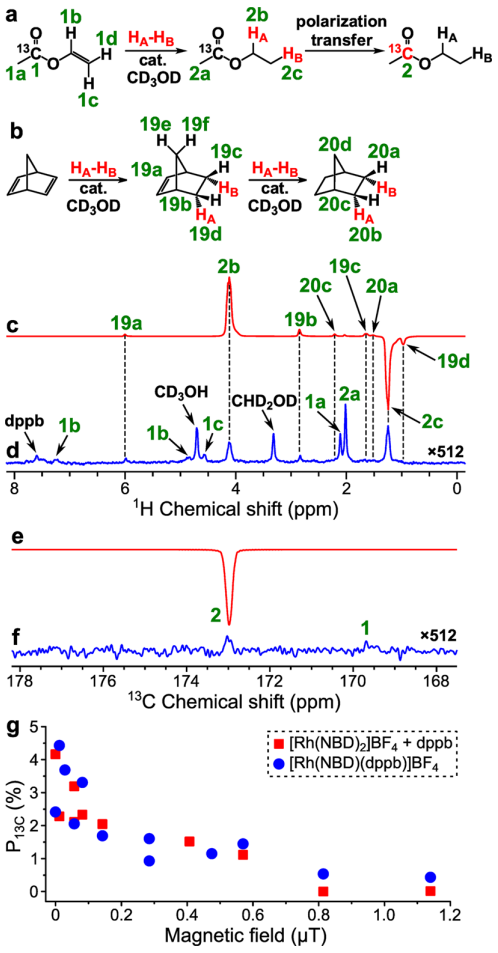

Figure 2. (a) Reaction scheme of pairwise addition of p-H_2 to vinyl 1-^{13}C-acetate in CD_3OD followed by polarization transfer to ^{13}C nuclei (H_A and H_B are two atoms from the same p-H_2 molecule, cat. = [Rh(NBD)(dppb)]BF_4). (b) Reaction scheme of the competing process of norbornadiene hydrogenation with p-H_2. (c) ^1H NMR spectrum acquired after ^1H ALTADENA hyperpolarization of ethyl acetate with 15 s p-H_2 bubbling duration. (d) Corresponding thermal ^1H NMR spectrum acquired after relaxation of hyperpolarization (multiplied by a factor of 512). $\varepsilon_{^1H}$ = 3750, $P_{^1H}$ = 8.6% (8.1% at 85% p-H_2 fraction). Note that spectra (c) and (d) were acquired on a 7.05 T NMR spectrometer. (e) ^{13}C NMR spectrum acquired after ^{13}C hyperpolarization of ethyl 1-^{13}C-acetate using MFC at near 0 μT magnetic field. (f) Corresponding thermal ^{13}C NMR spectrum acquired after relaxation of hyperpolarization (multiplied by a factor of 512). $\varepsilon_{^{13}C}$ = 3560, $P_{^{13}C}$ = 2.75% (4.2% at 85% p-H_2 fraction). (g) Dependence of $P_{^{13}C}$ (at 85% p-H_2 fraction) of ethyl 1-^{13}C-acetate on magnetic field used in MFC experiments (red squares, data points obtained with the [Rh(NBD)(dppb)]BF_4 catalyst prepared from [Rh(NBD)$_2$]BF_4 and dppb; blue circles, data points obtained with the commercial [Rh(NBD)(dppb)]BF_4 catalyst).

DOI: 10.1021/acs.jpcc.9b02041
J. Phys. Chem. C 2019, 123, 12827−12840

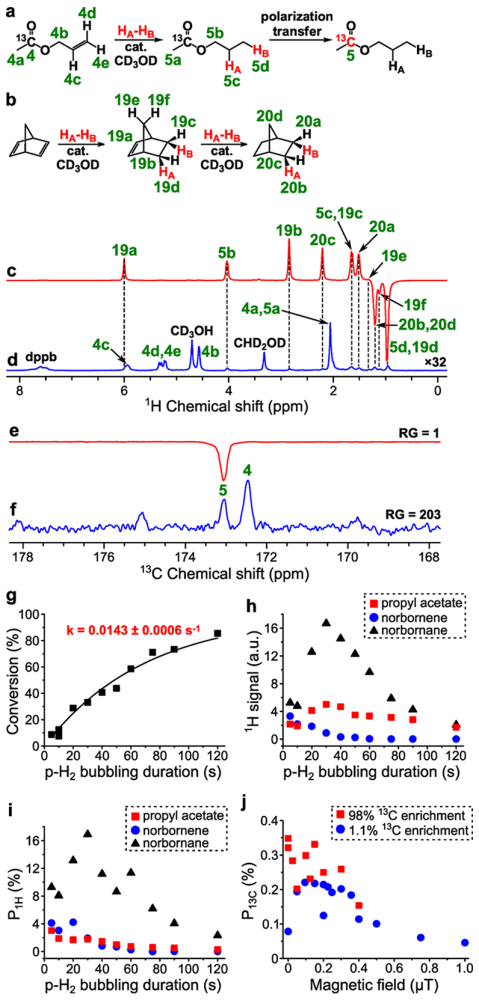

Figure 3. (a) Reaction scheme of pairwise addition of p-H_2 to allyl 1-^{13}C-acetate in CD_3OD followed by polarization transfer to ^{13}C nuclei (H_A and H_B are two atoms from the same p-H_2 molecule, cat. = [Rh(NBD)(dppb)]BF_4). (b) Reaction scheme of the competing process of norbornadiene hydrogenation with p-H_2. (c) ^{1}H NMR spectrum acquired after ^{1}H ALTADENA hyperpolarization of propyl 1-^{13}C-acetate with 5 s p-H_2 bubbling duration. (d) Corresponding thermal ^{1}H NMR spectrum acquired after relaxation of hyperpolarization (multiplied by a factor of 32). ε^{1}_{H} = 630, P^{1}_{H} = 1.9% (3.0% at 85% p-H_2 fraction). (e) ^{13}C NMR spectrum acquired after ^{13}C hyperpolarization of propyl 1-^{13}C-acetate using MFC at near 0 μT magnetic field with RG = 1. (f) Corresponding thermal ^{13}C NMR spectrum acquired after relaxation of hyperpolarization with RG = 203. ε^{13}_{C} = 350, P^{13}_{C} = 0.27% (0.35% at 85% p-H_2 fraction). (g) Dependence of conversion of allyl acetate to propyl acetate on p-H_2 bubbling duration (estimated pseudo-first-order rate constant k = 0.0143 ± 0.0006 s^{-1}). (h) Dependence of ^{1}H ALTADENA signals (absolute value) of HP propyl acetate (signal 5b, red squares), norbornene (signal 19b, blue circles), and norbornane (signal 20b + 20d, black triangles) on p-H_2 bubbling duration. (i) Dependence of P^{1}_{H} (at 85% p-H_2 fraction) of propyl acetate (signal 5b, red squares), norbornene (signal 19b, blue circles), and norbornane (signal 20b + 20d, black triangles) on p-H_2 bubbling duration. (j) Dependence of P^{13}_{C} (at 85% p-H_2 fraction) of propyl 1-^{13}C-acetate on magnetic field used in MFC experiments (red squares, data points obtained with the 98% ^{13}C-enriched precursor; blue circles, data points obtained with the 1.1% ^{13}C-enriched precursor).

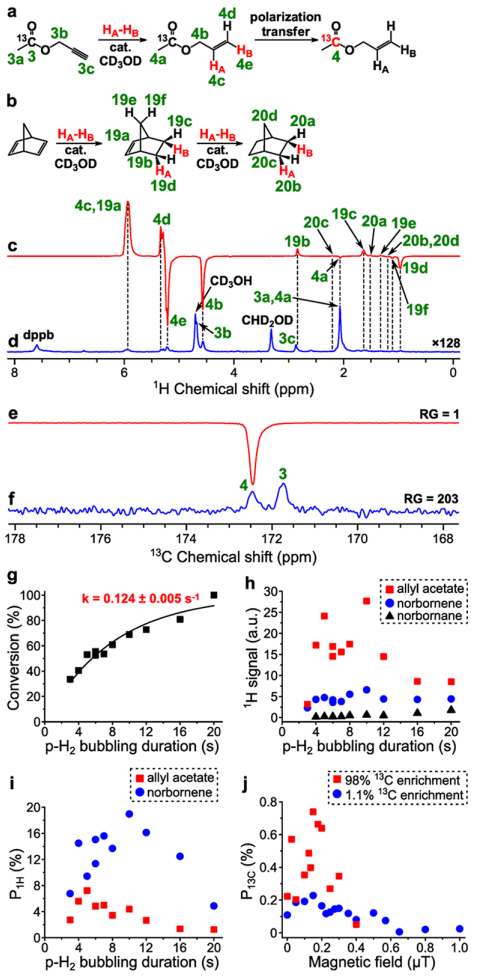

Figure 4. (a) Reaction scheme of pairwise addition of p-H_2 to propargyl 1-^{13}C-acetate in CD_3OD followed by polarization transfer to ^{13}C nuclei (H_A and H_B are two atoms from the same p-H_2 molecule, cat. = [Rh(NBD)(dppb)]BF_4). (b) Reaction scheme of the competing process of norbornadiene hydrogenation with p-H_2. (c) ^{1}H NMR spectrum acquired after ^{1}H ALTADENA hyperpolarization of allyl 1-^{13}C-acetate with 5 s p-H_2 bubbling duration. (d) Corresponding thermal ^{1}H NMR spectrum acquired after relaxation of hyperpolarization (multiplied by a factor of 128). ε^{1}_{H} = 2090, P^{1}_{H} = 6.4% (7.2% at 85% p-H_2 fraction) (calculated using signal 4e). (e) ^{13}C NMR spectrum acquired after ^{13}C hyperpolarization of allyl 1-^{13}C-acetate using MFC at 0.15 μT magnetic field with RG = 1. (f) Corresponding thermal ^{13}C NMR spectrum acquired after relaxation of hyperpolarization with RG = 203. ε^{13}_{C} = 580, P^{13}_{C} = 0.45% (0.74% at 85% p-H_2 fraction). (g) Dependence of conversion of propargyl acetate to allyl acetate on p-H_2 bubbling duration (estimated pseudo-first-order rate constant k = 0.124 ± 0.005 s^{-1}). (h) Dependence of the ^{1}H ALTADENA signals (absolute value) of HP allyl acetate (signal 4e, red squares), norbornene (signal 19d, blue circles), and norbornane (signal 20b + 20d, black triangles) on p-H_2 bubbling duration. (i) Dependence of P^{1}_{H} (at 85% p-H_2 fraction) of allyl acetate (signal 4e, red squares) and norbornene (signal 19d, blue circles) on p-H_2 bubbling duration. P^{1}_{H} for norbornane is not presented because it cannot be estimated reliably due to low conversion of norbornadiene to norbornane. (j) Dependence of P^{13}_{C} (at 85% p-H_2 fraction) of allyl 1-^{13}C-acetate on magnetic field used in MFC experiments (red squares, data points obtained with the 98% ^{13}C-enriched precursor; blue circles, data points obtained with the 1.1% ^{13}C-enriched precursor).

DOI: 10.1021/acs.jpcc.9b02041
J. Phys. Chem. C 2019, 123, 12827−12840

allyl acetate was 7.2% (at 85% p-H_2 fraction) (Figure 4i). Next, MFC experiments with magnetic field variation were performed at 5 s duration of p-H_2 bubbling (at which the maximum ^{1}H ALTADENA signal was observed). The maximum obtained $P_{^{13}C}$ was 0.74% (at 85% p-H_2 fraction) (Figure 4e,f,j).

PHIP of Ethyl 1-^{13}C-Pyruvate. HP ethyl pyruvate was produced by homogeneous hydrogenation of vinyl pyruvate in methanol over the [Rh(NBD)(dppb)]BF_4 catalyst prepared from [Rh(NBD)$_2$]BF_4 and dppb. Importantly, both vinyl and ethyl pyruvate esters are present in two forms in methanolic solution (Figure 5a). The hemiketal form is prevalent, whereas the contribution of the ketone form is also quite substantial. However, because these two forms have similar ^{1}H NMR chemical shifts for the protons of alcoholic moiety, calculations of conversion and $P_{^1H}$ can be performed in the same way as for acetates using the total amounts of both forms of pyruvate esters. The catalyst activity was moderate: 50% conversion of vinyl pyruvate was achieved after ~20 s of hydrogen bubbling at 40 psig pressure (Figure 5g). The maximum obtained ALTADENA $P_{^1H}$ of ethyl pyruvate was 5.2% (at 85% p-H_2 fraction), estimated on the basis of signal 8b + 9b (Figure 5i). Since we do not have ^{13}C-labeled vinyl pyruvate, MFC experiments were performed only with the substrate with natural abundance of ^{13}C nuclei. For calculations of $P_{^{13}C}$ for ethyl pyruvate, the sum of intensities of ^{13}C PHIP NMR signals of ketone and hemiketal forms was used as the PHIP signal intensity $I_{^{13}C\text{-PHIP}}$ because it was not possible to estimate the ratio of these two forms of ethyl pyruvate using ^{1}H NMR. The maximum obtained $P_{^{13}C}$ was 0.88% (at 85% p-H_2 fraction) (Figure 5e,f,j). It should be noted that HP ethyl pyruvate is the only HP ester obtained in this study that was previously employed for metabolic imaging directly without preliminary hydrolysis.[66] The use of HP ethyl pyruvate is especially advantageous for brain imaging due to its faster transport from blood to brain compared to HP pyruvate.[66] The fact that ethyl pyruvate is used as a food additive and also has been studied as an anti-inflammatory compound makes it a promising HP molecule for the future use in clinics despite the fact that it did not demonstrate high levels of polarization in our studies.

PHIP of Propyl 1-^{13}C-Pyruvate. HP propyl pyruvate was produced by homogeneous hydrogenation of allyl pyruvate in methanol over the [Rh(NBD)(dppb)]BF_4 catalyst prepared from [Rh(NBD)$_2$]BF_4 and dppb. Similar to vinyl and ethyl pyruvates, allyl and propyl pyruvates were present in hemiketal and ketone forms in methanolic solution with the prevalence of the hemiketal form (Figure 6a). These two forms also had similar ^{1}H NMR chemical shifts for the protons of alcoholic moiety except protons 13b and 14b. Therefore, calculations of conversion and $P_{^1H}$ were carried out using the total amounts of these two forms of pyruvates. The catalyst activity was very low: after 2 min of hydrogen bubbling at 40 psig pressure, the conversion of allyl pyruvate was only ~30% (Figure 6g). Due to overlapping of ^{1}H NMR signals 16c + 17c and 16d + 17d of propyl pyruvate with signals 19c and 19d of norbornene, respectively (Figure 6c), ^{1}H polarization of propyl pyruvate was calculated on the basis of NMR signal 16b + 17b. The maximum obtained ALTADENA $P_{^1H}$ of the corresponding protons of propyl pyruvate was 2.0% (at 85% p-H_2 fraction) (Figure 6i). Next, MFC experiments with magnetic field variation were performed at 20 s duration of p-H_2 bubbling (at which the maximum ^{1}H ALTADENA signal was observed). For calculations of $P_{^{13}C}$ for propyl pyruvate with ^{13}C nuclei at

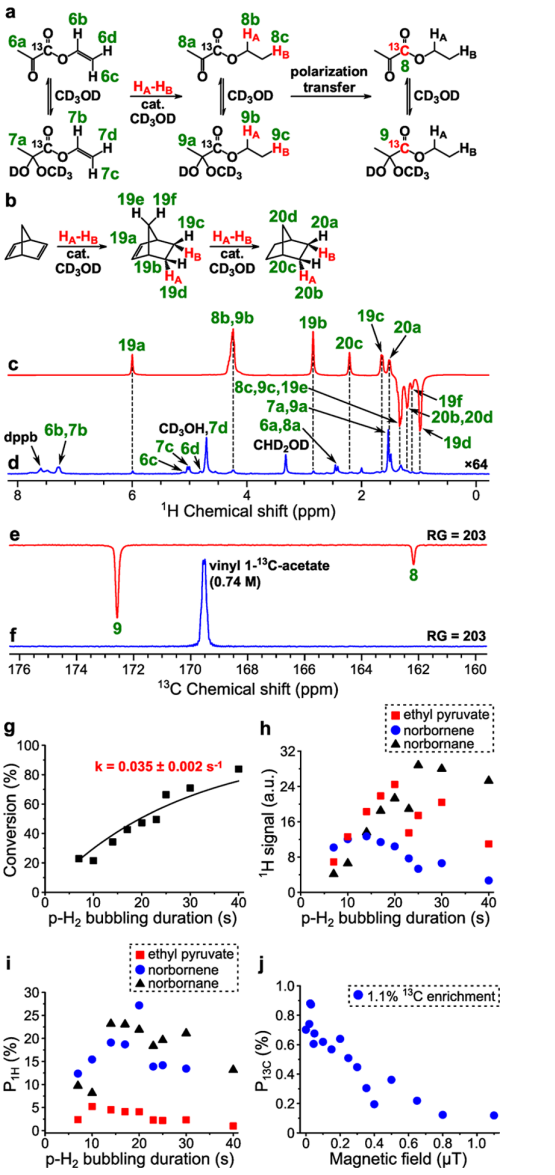

Figure 5. (a) Reaction scheme of pairwise addition of p-H_2 to vinyl 1-^{13}C-pyruvate in CD_3OD followed by polarization transfer to ^{13}C nuclei (H_A and H_B are two atoms from the same p-H_2 molecule, cat. = [Rh(NBD)(dppb)]BF_4). (b) Reaction scheme of the competing process of norbornadiene hydrogenation with p-H_2. (c) ^{1}H NMR spectrum acquired after ^{1}H ALTADENA hyperpolarization of ethyl 1-^{13}C-pyruvate with 10 s p-H_2 bubbling duration. (d) Corresponding thermal ^{1}H NMR spectrum acquired after relaxation of hyperpolarization (multiplied by a factor of 64). $\varepsilon_{^1H}$ = 1650, $P_{^1H}$ = 5.1% (5.2% at 85% p-H_2 fraction) (calculated using signal 8b + 9b). (e) ^{13}C NMR spectrum acquired after ^{13}C hyperpolarization of ethyl pyruvate (1.1% ^{13}C enrichment) using MFC at 0.025 μT magnetic field with RG = 203 (p-H_2 bubbling duration = 20 s). (f) ^{13}C NMR spectrum of 0.74 M solution of vinyl 1-^{13}C-acetate used as an external reference acquired with RG = 203. $\varepsilon_{^{13}C}$ = 900, $P_{^{13}C}$ = 0.70% (0.88% at 85% p-H_2 fraction). (g) Dependence of conversion of vinyl pyruvate to ethyl pyruvate on p-H_2 bubbling duration (estimated pseudo-first-order rate constant $k = 0.035 \pm 0.002$ s^{-1}). (h) Dependence of ^{1}H ALTADENA signals (absolute value) of HP ethyl pyruvate (signal 8b + 9b, red squares), norbornene (signal 19d, blue circles), and norbornane (signal 20b + 20d, black triangles) on p-H_2 bubbling duration. (i) Dependence of $P_{^1H}$ (at 85% p-H_2 fraction) of ethyl pyruvate (signal

DOI: 10.1021/acs.jpcc.9b02041
J. Phys. Chem. C 2019, 123, 12827−12840

Figure 5. continued

8b + 9b, red squares), norbornene (signal 19d, blue circles), and norbornane (signal 20b + 20d, black triangles) on p-H_2 bubbling duration. (j) Dependence of $P_{^{13}C}$ (at 85% p-H_2 fraction) of ethyl pyruvate on magnetic field used in MFC experiments (data obtained with the 1.1% ^{13}C-enriched precursor).

natural abundance, the sum of intensities of ^{13}C PHIP NMR signals of ketone and hemiketal forms was used as the PHIP signal intensity $I_{^{13}C\text{-PHIP}}$ because it was not possible to estimate the ratio of these two forms of propyl pyruvate using ^{1}H NMR. For calculations of $P_{^{13}C}$ for 98% ^{13}C-enriched propyl pyruvate, we used the ^{13}C PHIP NMR signals of the prevalent hemiketal form because it was not possible to detect the thermally polarized ketone form using ^{13}C NMR in reasonable amount of time (and sometimes it was also not possible to detect ^{13}C PHIP NMR signals of the ketone form). The maximum obtained $P_{^{13}C}$ was 0.49% (at 85% p-H_2 fraction) (Figure 6e,f,j).

PHIP of Allyl 1-^{13}C-Pyruvate. HP allyl pyruvate was produced by homogeneous hydrogenation of propargyl pyruvate in methanol over the [Rh(NBD)(dppb)]BF_4 catalyst prepared from [Rh(NBD)$_2$]BF_4 and dppb. Similar to other pyruvate esters, propargyl and allyl pyruvates were present in hemiketal and ketone forms in methanolic solution with the prevalence of the hemiketal form (Figure 7a). These two forms also had similar ^{1}H NMR chemical shifts for the protons of alcoholic moiety except protons 13b and 14b. Therefore, calculations of conversion were carried out using the total amounts of these two forms of pyruvates. The catalyst demonstrated high activity: 50% conversion of propargyl pyruvate was achieved after ~7 s of p-H_2 bubbling at 40 psig pressure (Figure 7g). Due to overlapping of ^{1}H NMR signal 13c + 14c of allyl pyruvate with signal 19a of norbornene (Figure 7c), ^{1}H polarization of allyl pyruvate was calculated either on the basis of the NMR signal 13e + 14e or on the basis of sum of NMR signals 13b and 14b, depending on what signals yielded the highest $\varepsilon_{^1H}$. The sum of signals 13b and 14b was used due to the fact that it was not possible to reliably estimate the ratio of hemiketal and ketone forms of allyl pyruvate using thermal spectra (signal 14b overlaps with the signal of the solvent and signal 13b is too weak). The maximum obtained ALTADENA $P_{^1H}$ of the corresponding protons of allyl pyruvate was 21% (at 85% p-H_2 fraction) (Figure 7i). Next, MFC experiments with magnetic field variation were performed at 10 s duration of p-H_2 bubbling. For calculations of $P_{^{13}C}$ for allyl pyruvate with ^{13}C nuclei at natural abundance, the sum of intensities of ^{13}C PHIP NMR signals of ketone and hemiketal forms was used as the PHIP signal intensity $I_{^{13}C\text{-PHIP}}$ because it was not possible to estimate the ratio of these two forms of allyl pyruvate using ^{1}H NMR. For calculations of $P_{^{13}C}$ for 98% ^{13}C-enriched allyl pyruvate, we used the ^{13}C PHIP NMR signals of the prevalent hemiketal form; the estimated $\varepsilon_{^{13}C}$ values for the ketone form were on average 1.5 times lower. The maximum obtained $P_{^{13}C}$ was 5.4% (at 85% p-H_2 fraction) (Figure 7e,f,j).

PHIP of Ethyl 1-^{13}C-Acetate and Allyl 1-^{13}C-Pyruvate in Aqueous Phase. In CD_3OD solutions, the highest polarizations were observed for ethyl 1-^{13}C-acetate and allyl 1-^{13}C-pyruvate (e.g., for these compounds $P_{^{13}C}$ = 4.4 and 5.4%, respectively, were obtained, whereas for other esters $P_{^{13}C}$ values were less than 1%). Therefore, these compounds were chosen as targets for hyperpolarization experiments in the aqueous

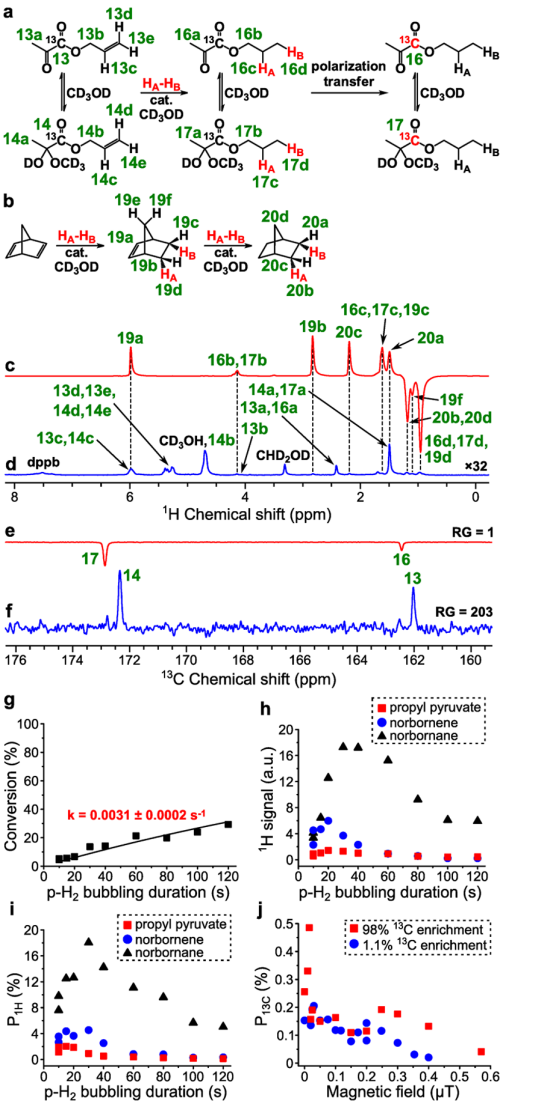

Figure 6. (a) Reaction scheme of pairwise addition of p-H_2 to allyl 1-^{13}C-pyruvate in CD_3OD followed by polarization transfer to ^{13}C nuclei (H_A and H_B are two atoms from the same p-H_2 molecule, cat. = [Rh(NBD)(dppb)]BF_4). (b) Reaction scheme of the competing process of norbornadiene hydrogenation with p-H_2. (c) ^{1}H NMR spectrum acquired after ^{1}H ALTADENA hyperpolarization of propyl 1-^{13}C-pyruvate with 15 s p-H_2 bubbling duration. (d) Corresponding thermal ^{1}H NMR spectrum acquired after relaxation of hyperpolarization (multiplied by a factor of 32). $\varepsilon_{^1H}$ = 480, $P_{^1H}$ = 1.5% (2.0% at 85% p-H_2 fraction) (calculated using signal 16b + 17b). (e) ^{13}C NMR spectrum acquired after ^{13}C hyperpolarization of propyl 1-^{13}C-pyruvate using MFC at 0.015 μT magnetic field with RG = 1. (f) Corresponding thermal ^{13}C NMR spectrum acquired after relaxation of hyperpolarization with RG = 203. $\varepsilon_{^{13}C}$ = 610, $P_{^{13}C}$ = 0.47% (0.49% at 85% p-H_2 fraction). (g) Dependence of conversion of allyl pyruvate to propyl pyruvate on p-H_2 bubbling duration (estimated pseudo-first-order rate constant k = 0.0031 ± 0.0002 s^{-1}). (h) Dependence of ^{1}H ALTADENA signals (absolute value) of HP propyl pyruvate (signal 16b + 17b, red squares), norbornene (signal 19b, blue circles), and norbornane (signal 20b + 20d, black triangles) on p-H_2 bubbling duration. (i) Dependence of $P_{^1H}$ (at 85% p-H_2 fraction) of allyl acetate (signal 16b + 17b, red squares), norbornene (signal 19b, blue circles), and norbornane (signal 20b + 20d, black triangles) on p-H_2 bubbling duration. (j) Dependence of $P_{^{13}C}$ (at 85%

DOI: 10.1021/acs.jpcc.9b02041
J. Phys. Chem. C 2019, 123, 12827−12840

Figure 6. continued

p-H_2 fraction) of propyl 1-^{13}C-pyruvate on magnetic field used in MFC experiments (red squares, data points obtained with the 98% ^{13}C-enriched precursor; blue circles, data points obtained with the 1.1% ^{13}C-enriched precursor).

phase. These experiments employed the water-soluble [Rh(NBD)(Ph((CH$_2$)$_3$SO$_3^-$)P−(CH$_2$)$_4$−PPh((CH$_2$)$_3$SO$_3^-$))]BF$_4$ complex as a homogeneous hydrogenation catalyst. Due to generally lower efficiency of hydrogenation in the aqueous phase,[60] we used harsher experimental conditions (70−80 psig H_2 pressure, 60−85 °C temperature, and 140 sccm gas flow rate). Hydrogenation of vinyl acetate at 70 psig and 60 °C was highly efficient since 100% conversion of the reactant was achieved just after 7 s of p-H_2 bubbling (Table S2). The maximum obtained ALTADENA $P_{^1H}$ of ethyl 1-^{13}C-acetate was 5.7%, whereas $P_{^{13}C}$ was 2.1% (both at 85% p-H_2 fraction) (Figure 8). Hydrogenation of propargyl pyruvate was quite slow since after 20 s of p-H_2 bubbling at 70 psig and 80 °C, the conversion was only ∼7% (Table S3). ALTADENA $P_{^1H}$ was lower than in the case of vinyl acetate hydrogenation in the aqueous phase (the maximum $P_{^1H}$ = 3.6% at 85% p-H_2 fraction; see Table S3). However, at 80 psig, 85 °C, and ∼10 mM catalyst concentration (instead of ∼5.3 mM concentration used in other experiments in the aqueous phase), $P_{^1H}$ = 6.0% was obtained (at 85% p-H_2 fraction) (Figure 9). Moreover, PASADENA experiments were performed, yielding $P_{^1H}$ = 1.7% (at 85% p-H_2 fraction) for HP allyl 1-^{13}C-pyruvate (Figure S2). In MFC experiments with HP allyl 1-^{13}C-pyruvate, the maximum $P_{^{13}C}$ was only 0.82% (at 85% p-H_2 fraction), which is ∼2.5 times lower than that obtained for ethyl 1-^{13}C-acetate (Figure 9). The magnetic field profile of $P_{^{13}C}$ for allyl 1-^{13}C-pyruvate is presented in Figure S3. Thus, we demonstrate the feasibility of obtaining HP ethyl acetate and allyl pyruvate in aqueous solution using a water-soluble hydrogenation catalyst.

Efficiency of Homogeneous PHIP of Acetate and Pyruvate Esters. The summary of PHIP results for the six esters under study is presented in Table 1. Propyl acetate and propyl pyruvate were found to be the two least efficiently hyperpolarized compounds. From acetate esters, ethyl acetate was found to be the most efficiently hyperpolarized one, with up to 4.4% ^{13}C polarization in methanol. In contrast, allyl pyruvate hyperpolarization was more efficient than that of ethyl pyruvate, with up to 21% ^{1}H and up to 5.4% ^{13}C polarization in methanol. The attainable ^{1}H and ^{13}C polarizations clearly qualitatively correlate well with the hydrogenation rate constants (Table 1). The highest polarizations were obtained in cases when unsaturated precursors are hydrogenated faster. This result can be explained by the fact that the observed PHIP signal is proportional to both concentration and nuclear spin polarization of the hydrogenation product. While concentration increases with reaction time, polarization decreases simultaneously because of the nuclear spin relaxation. This means that the dependence of PHIP signal intensity on reaction time should have a maximum. The slower the hydrogenation reaction, the longer is the reaction time at which the PHIP signal intensity reaches this maximum[67] and the lower are the polarization and PHIP signal intensity at this maximum due to disproportionately greater relaxation effects of ^{1}H HP state depolarization. Future catalyst development is certainly warranted for the compounds

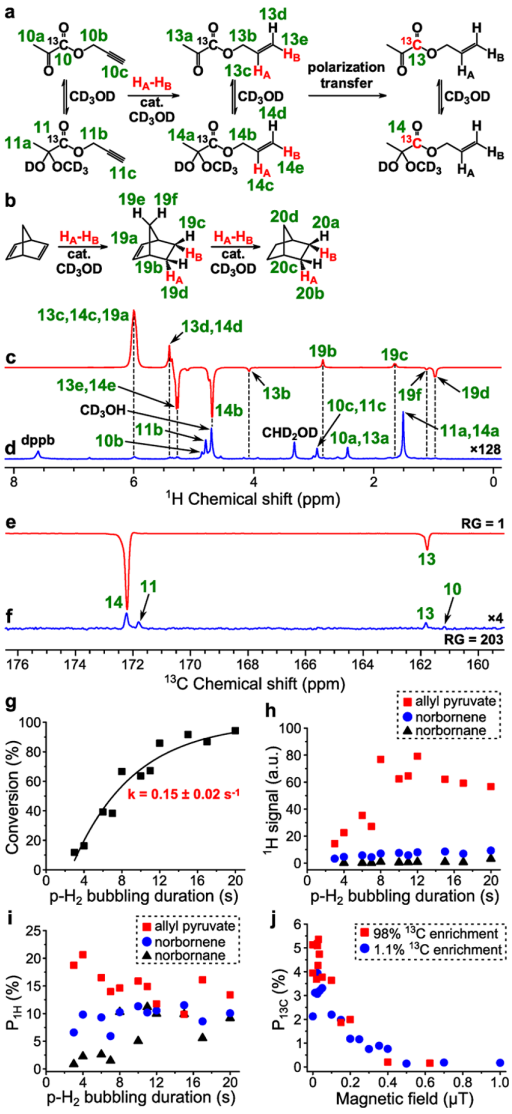

Figure 7. (a) Reaction scheme of pairwise addition of p-H_2 to propargyl 1-^{13}C-pyruvate in CD_3OD followed by polarization transfer to ^{13}C nuclei (H_A and H_B are two atoms from the same p-H_2 molecule, cat. = [Rh(NBD)(dppb)]BF$_4$). (b) Reaction scheme of the competing process of norbornadiene hydrogenation with p-H_2. (c) ^{1}H NMR spectrum acquired after ^{1}H ALTADENA hyperpolarization of allyl 1-^{13}C-pyruvate with 4 s p-H_2 bubbling duration. (d) Corresponding thermal ^{1}H NMR spectrum acquired after relaxation of hyperpolarization (multiplied by a factor of 128). $\varepsilon_{^1H}$ = 4320, $P_{^1H}$ = 13% (21% at 85% p-H_2 fraction) (calculated using sum of signals 13b and 14b). (e) ^{13}C NMR spectrum acquired after ^{13}C hyperpolarization of allyl 1-^{13}C-pyruvate using MFC at 0.030 μT magnetic field with RG = 1. (f) Corresponding thermal ^{13}C NMR spectrum acquired after relaxation of hyperpolarization with RG = 203 (multiplied by a factor of 4). $\varepsilon_{^{13}C}$ = 4340, $P_{^{13}C}$ = 3.3% (5.4% at 85% p-H_2 fraction). (g) Dependence of conversion of propargyl pyruvate to allyl pyruvate on p-H_2 bubbling duration (estimated pseudo-first-order rate constant k = 0.15 ± 0.02 s^{-1}). (h) Dependence of ^{1}H ALTADENA signals (absolute value) of HP allyl pyruvate (signal 14b, red squares), norbornene (signal 19d, blue circles), and norbornane (signal 20b + 20d, black triangles) on p-H_2 bubbling duration. (i) Dependence of $P_{^1H}$ (at 85% p-H_2 fraction) of allyl pyruvate (signal 13e + 14e or the sum of NMR signals 13b and 14b, red squares), norbornene (signal 19d, blue circles), and norbornane

DOI: 10.1021/acs.jpcc.9b02041
J. Phys. Chem. C 2019, 123, 12827−12840

Figure 7. continued

(signal 20b + 20d or signal 20a, black triangles) on p-H_2 bubbling duration. (j) Dependence of P^{13}_C (at 85% p-H_2 fraction) of allyl 1-^{13}C-pyruvate on magnetic field used in MFC experiments (red squares, data points obtained with the 98% ^{13}C-enriched precursor; blue circles, data points obtained with the 1.1% ^{13}C-enriched precursor).

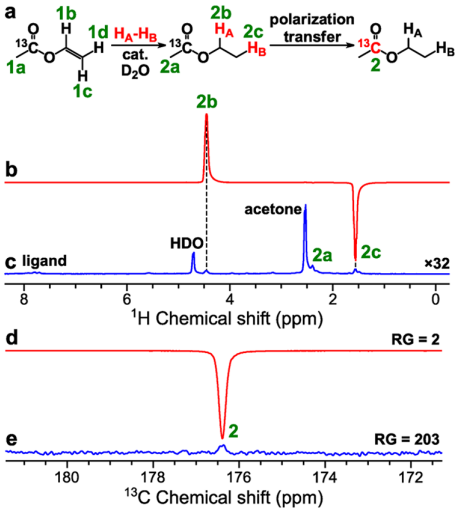

Figure 8. (a) Reaction scheme of pairwise addition of p-H_2 to vinyl 1-^{13}C-acetate in D_2O over a water-soluble Rh catalyst followed by polarization transfer to ^{13}C nuclei (H_A and H_B are two atoms from the same p-H_2 molecule). (b) ^{1}H NMR spectrum acquired after ^{1}H ALTADENA hyperpolarization of ethyl 1-^{13}C-acetate with 7 s p-H_2 bubbling duration at 70 psig and 60 °C. (c) Corresponding thermal ^{1}H NMR spectrum acquired after relaxation of hyperpolarization (multiplied by a factor of 32). Acetone was used during the sample preparation step.[62] ε^1_H = 1680, P^1_H = 5.2% (5.3% at 85% p-H_2 fraction) (calculated using signal 2b). (d) ^{13}C NMR spectrum acquired after ^{13}C hyperpolarization of ethyl 1-^{13}C-acetate using MFC at near 0 μT magnetic field with RG = 2 (p-H_2 bubbling duration = 7 s at 70 psig and 60 °C). (e) Corresponding thermal ^{13}C NMR spectrum acquired after relaxation of hyperpolarization with RG = 203. ε^{13}_C = 1550, P^{13}_C = 1.2% (2.1% at 85% p-H_2 fraction).

that react too slowly. The alternative approach is the employment of reaction conditions with elevated temperature and p-H_2 pressure, which can be achieved by the use of more efficient PHIP polarizer setups.[68,69] It should be noted that ^{1}H relaxation is significantly faster than ^{13}C relaxation—T_1 at 9.4 T is on the order of several seconds for ^{1}H and on the order of several tens of seconds for ^{13}C nuclei (e.g., for protons of the allylic CH_2 group of allyl 1-^{13}C-pyruvate (signal 13b in Figure 7) T_1 = 7.8 ± 0.4 s, whereas for ^{13}C nuclei of the same compound T_1 = 35 ± 1 s in the case of the ketone form and T_1 = 38 ± 4 s in the case of the hemiketal form). Since the time required for transfer of the sample to the NMR spectrometer after field cycling was relatively short (~2 s), ^{13}C relaxation has a minor effect on the observed P^{13}_C. On the other hand, the effect of ^{1}H relaxation is dramatic since the reaction time was on the order of relaxation time or several times larger depending on the substrate.[64] Therefore, minimization of reaction time is certainly warranted for achieving higher ^{13}C polarizations. Another factor that is important to optimize is the polarization transfer efficiency. In our experiments, polarization transfer efficiency did not exceed 54%, which is

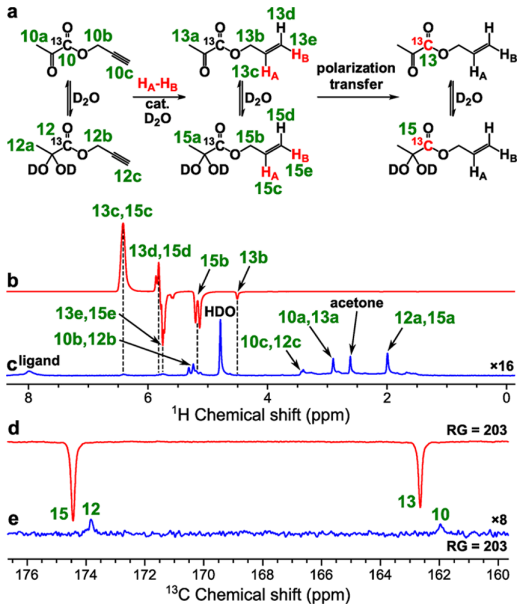

Figure 9. (a) Reaction scheme of pairwise addition of p-H_2 to propargyl 1-^{13}C-pyruvate in D_2O over a water-soluble Rh catalyst followed by polarization transfer to ^{13}C nuclei (H_A and H_B are two atoms from the same p-H_2 molecule). (b) ^{1}H NMR spectrum acquired after ^{1}H ALTADENA hyperpolarization of allyl 1-^{13}C-pyruvate with ~10 mM catalyst concentration and 30 s p-H_2 bubbling duration at 80 psig and 85 °C. (c) Corresponding thermal ^{1}H NMR spectrum acquired after relaxation of hyperpolarization (multiplied by a factor of 16). Acetone was used during the sample preparation step.[62] ε^1_H = 1090, P^1_H = 3.2% (6.0% at 85% p-H_2 fraction) (calculated using signal 13c + 15c). (d) ^{13}C NMR spectrum acquired after ^{13}C hyperpolarization of allyl 1-^{13}C-pyruvate using MFC at 0.025 μT magnetic field with ~5.3 mM catalyst concentration and 20 s p-H_2 bubbling duration at 70 psig and 80 °C. (e) Corresponding thermal ^{13}C NMR spectrum acquired after relaxation of hyperpolarization. ε^{13}_C = 760, P^{13}_C = 0.55% (0.82% at 85% p-H_2 fraction).

~1.3 times lower than that achieved by Cavallari et al. for allyl pyruvate using the MFC approach.[55] Therefore, design of better MFC hardware is also warranted for achieving higher ^{13}C polarizations.[33]

^{13}C MRI in Vitro. Feasibility of the utilization of the obtained HP acetates and pyruvates for ^{13}C MRI was demonstrated on the examples of ethyl 1-^{13}C-acetate and allyl 1-^{13}C-pyruvate, which showed the highest levels of polarization. Two-dimensional projections of 3D ^{13}C MR images of the 80 mM methanolic solutions of these compounds in a hollow spherical phantom are presented in Figure 10. The maximum signal-to-noise ratio (SNR) values in these images were more than 2 times higher than that obtained in MRI of 3 M solution of thermally polarized sodium 1-^{13}C-acetate in the same phantom despite the ~40-fold difference in concentrations. We have also performed 2D ^{13}C MRI of aqueous solutions of HP ethyl 1-^{13}C-acetate and allyl 1-^{13}C-pyruvate produced by homogeneous hydrogenation of the corresponding unsaturated precursors with p-H_2 over the water-soluble rhodium catalyst (Figure 11). As expected from data presented in Table 1, SNR for allyl 1-^{13}C-pyruvate in aqueous solution was significantly lower than that obtained for the same compound in methanol. On the other hand, SNR values for ethyl 1-^{13}C-acetate were similar for both solvents.

DOI: 10.1021/acs.jpcc.9b02041
J. Phys. Chem. C 2019, 123, 12827−12840

Table 1. Summary of the Results Obtained in Homogeneous PHIP of Acetate and Pyruvate Esters[a]

HP ester	solvent	k, s^{-1}	maximal ^{1}H PHIP signal, au	maximal ^{13}C PHIP signal, au[b]	maximal $P_{^1H}$, %	maximal $P_{^{13}C}$, %	η, %
ethyl acetate	CD_3OD	not estimated	not estimated	34	8.1	4.4	54
propyl acetate	CD_3OD	0.0143 ± 0.0006	3.5	4.4	3.0	0.35	12
allyl acetate	CD_3OD	0.124 ± 0.005	19	6.4	7.2	0.74	10
ethyl pyruvate	CD_3OD	0.035 ± 0.002	17	27	5.2	0.88	17
propyl pyruvate	CD_3OD	0.0031 ± 0.0002	1.0	1.0	2.0	0.49	24
allyl pyruvate	CD_3OD	0.15 ± 0.02	64	96	21	5.4	26
ethyl acetate	D_2O	not estimated	9.6	8.4	5.7	2.1	36
allyl pyruvate	D_2O	not estimated	3.6	1.8	3.6	0.82	23

[a]Pseudo-first-order rate constants, maximal ^{1}H and ^{13}C PHIP signal intensities and polarizations (at 85% p-H_2 fraction), and polarization transfer efficiency (η). [b]These values were calculated taking into account the differences in ^{13}C enrichment and NMR acquisition parameters used in different experiments.

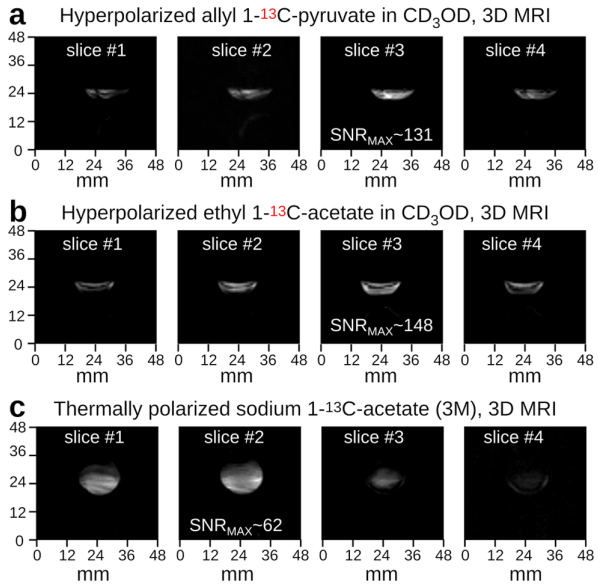

Figure 10. Two-dimensional projections of 3D ^{13}C MR images of (a) HP allyl 1-^{13}C-pyruvate solution in CD_3OD produced via pairwise addition of p-H_2 to propargyl 1-^{13}C-pyruvate (80 mM), (b) HP ethyl 1-^{13}C-acetate in CD_3OD produced via pairwise addition of p-H_2 to vinyl 1-^{13}C-acetate (80 mM), and (c) 3 M aqueous solution of thermally polarized sodium 1-^{13}C-acetate (signal reference phantom). The phantoms represented hollow spherical balls (~2.8 mL volume) with solutions located in the bottom. The double image in display (a) is due to two HP species present with two distinctly different chemical shifts (see Figure 7 for more details).

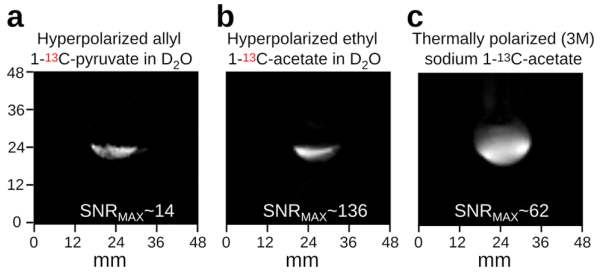

Figure 11. Two-dimensional ^{13}C MR images of (a) HP allyl 1-^{13}C-pyruvate produced via pairwise addition of p-H_2 to propargyl 1-^{13}C-pyruvate in D_2O, (b) HP ethyl 1-^{13}C-acetate produced via pairwise addition of p-H_2 to vinyl 1-^{13}C-acetate in D_2O, and (c) 3 M solution of thermally polarized sodium 1-^{13}C-acetate (signal reference phantom). The double image in display (a) is due to two HP species present with two distinctly different chemical shifts (see Figure 9 for more details).

These results clearly show the prospects for utilization of ^{13}C HP ethyl 1-^{13}C-acetate and allyl 1-^{13}C-pyruvate as molecular contrast agents for in vivo use and ultimately clinical MRI use. Moreover, the obtained ^{13}C HP esters can be cleaved using alkaline hydrolysis, resulting in formation of ^{13}C HP carboxylates.[53] Though we did not perform such experiments in this work, we do not anticipate significant challenges with removal of the sidearm in any of the molecules studied here based on the work of others and our own experience. For example, Reineri et al. successfully obtained hyperpolarized acetate and pyruvate by removing sidearms in ethyl acetate and allyl pyruvate, respectively.[53] Later, the same team obtained HP lactate by hydrolysis of HP allyl lactate ester.[54] Moreover, Korchak et al. used the same approach to cleave cinnamyl acetate and cinnamyl pyruvate.[59] Given these multiple examples, the ester structure does not significantly influence the possibility of successful ester hydrolysis on the desired time scale for preserving the ^{13}C HP state. Furthermore, our own experience with hydrolysis of ethyl acetate is that this reaction proceeds rapidly and quantitatively.[51] Therefore, we expect that removal of sidearms in ethyl pyruvate, propyl acetate, propyl pyruvate, and allyl acetate should also be feasible and efficient.

CONCLUSIONS

Acetate and pyruvate esters with ethyl, propyl, and allyl alcoholic moieties were successfully hyperpolarized using homogeneous hydrogenation of the corresponding unsaturated precursors in CD_3OD with parahydrogen. Polarization transfer from ^{1}H to ^{13}C nuclei was performed using magnetic field cycling. It was found that the polarization of the obtained HP state strongly depends on the rate of hydrogenation. The highest polarizations (21% for ^{1}H and 5.4% for ^{13}C nuclei) were obtained for allyl pyruvate produced by hydrogenation of propargyl pyruvate, the most readily hydrogenated compound among those under study. Allyl pyruvate and ethyl acetate were also hyperpolarized using hydrogenation with parahydrogen in the aqueous phase over the water-soluble homogeneous rhodium catalyst, yielding 0.82 and 2.1% ^{13}C polarization, respectively. Feasibility of utilization of the obtained ^{13}C-hyperpolarized compounds for MRI was demonstrated on the examples of allyl 1-^{13}C-pyruvate and ethyl 1-^{13}C-acetate; 3D ^{13}C MR images with SNR ~131 and ~148, respectively, were obtained for methanolic solutions of these compounds. Two-dimensional ^{13}C MRI visualization of aqueous solutions of allyl

DOI: 10.1021/acs.jpcc.9b02041
J. Phys. Chem. C 2019, 123, 12827−12840

1-^{13}C-pyruvate and ethyl 1-^{13}C-acetate was also carried out. This systematic study will guide the future development of the PHIP-SAH hyperpolarization in terms of the optimization of catalysts, hyperpolarization hardware, and experimental protocols.

■ ASSOCIATED CONTENT

Supporting Information

The Supporting Information is available free of charge on the ACS Publications website at DOI: 10.1021/acs.jpcc.9b02041.

Structures of all compounds employed in this study; ^{1}H NMR results for hyperpolarization of ethyl acetate in CD_3OD and in D_2O; ^{1}H NMR results for hyperpolarization of allyl pyruvate in D_2O; dependence of P_{13C} of allyl 1-^{13}C-pyruvate on magnetic field used in MFC experiments (PDF)

■ AUTHOR INFORMATION

Corresponding Authors

*E-mail: salnikov@tomo.nsc.ru (O.G.S.).
*E-mail: chekmenev@wayne.edu (E.Y.C.).

ORCID

Oleg G. Salnikov: 0000-0003-2266-7335
Kirill V. Kovtunov: 0000-0001-7577-9619
Igor V. Koptyug: 0000-0003-3480-7649
Eduard Y. Chekmenev: 0000-0002-8745-8801

Author Contributions

The manuscript was written through contributions of all authors. All authors have given approval to the final version of the manuscript.

Notes

The authors declare no competing financial interest.

■ ACKNOWLEDGMENTS

K.V.K., O.G.S., and N.V.C. thank RSF (17-73-20030) for the support of synthesis of labeled compounds. I.V.K. thanks the Russian Ministry of Science and Higher Education for financial support. The U.S. team thanks the following support for funding: by NSF under grants CHE-1416268 and CHE-1836308, by the National Cancer Institute under 1R21CA220137, by DOD CDMRP under BRP W81XWH-12-1-0159/BC112431 and W81XWH-15-1-0271, and by RFBR under grant 17-54-33037 OHKO_a.

■ REFERENCES

(1) Nikolaou, P.; Goodson, B. M.; Chekmenev, E. Y. NMR Hyperpolarization Techniques for Biomedicine. *Chem. - Eur. J.* **2015**, *21*, 3156−3166.

(2) Kovtunov, K. V.; Pokochueva, E. V.; Salnikov, O. G.; Cousin, S. F.; Kurzbach, D.; Vuichoud, B.; Jannin, S.; Chekmenev, E. Y.; Goodson, B. M.; Barskiy, D. A.; et al. Hyperpolarized NMR Spectroscopy: d-DNP, PHIP, and SABRE Techniques. *Chem. - Asian J.* **2018**, *13*, 1857−1871.

(3) Dumez, J.-N. Perspectives on Hyperpolarised Solution-State Magnetic Resonance in Chemistry. *Magn. Reson. Chem.* **2017**, *55*, 38−46.

(4) Barskiy, D. A.; Coffey, A. M.; Nikolaou, P.; Mikhaylov, D. M.; Goodson, B. M.; Branca, R. T.; Lu, G. J.; Shapiro, M. G.; Telkki, V.-V.; Zhivonitko, V. V.; et al. NMR Hyperpolarization Techniques of Gases. *Chem. - Eur. J.* **2017**, *23*, 725−751.

(5) Skinner, J. G.; Menichetti, L.; Flori, A.; Dost, A.; Schmidt, A. B.; Plaumann, M.; Gallagher, F. A.; Hövener, J.-B. Metabolic and Molecular Imaging with Hyperpolarised Tracers. *Mol. Imaging Biol.* **2018**, *20*, 902−918.

(6) Golman, K.; in 't Zandt, R.; Thaning, M. Real-Time Metabolic Imaging. *Proc. Natl. Acad. Sci. U.S.A.* **2006**, *103*, 11270−11275.

(7) Harrison, C.; Yang, C.; Jindal, A.; DeBerardinis, R. J.; Hooshyar, M. A.; Merritt, M.; Sherry, A. D.; Malloy, C. R. Comparison of Kinetic Models for Analysis of Pyruvate-to-Lactate Exchange by Hyperpolarized ^{13}C NMR. *NMR Biomed.* **2012**, *25*, 1286−1294.

(8) Liberti, M. V.; Locasale, J. W. The Warburg Effect: How Does It Benefit Cancer Cells? *Trends Biochem. Sci.* **2016**, *41*, 211−218.

(9) Golman, K.; in't Zandt, R.; Lerche, M.; Pehrson, R.; Ardenkjaer-Larsen, J. H. Metabolic Imaging by Hyperpolarized ^{13}C Magnetic Resonance Imaging for In Vivo Tumor Diagnosis. *Cancer Res.* **2006**, *66*, 10855−10860.

(10) Brindle, K. M.; Bohndiek, S. E.; Gallagher, F. A.; Kettunen, M. I. Tumor Imaging Using Hyperpolarized ^{13}C Magnetic Resonance Spectroscopy. *Magn. Reson. Med.* **2011**, *66*, 505−519.

(11) Albers, M. J.; Bok, R.; Chen, A. P.; Cunningham, C. H.; Zierhut, M. L.; Zhang, V. Y.; Kohler, S. J.; Tropp, J.; Hurd, R. E.; Yen, Y.-F.; et al. Hyperpolarized ^{13}C Lactate, Pyruvate, and Alanine: Noninvasive Biomarkers for Prostate Cancer Detection and Grading. *Cancer Res.* **2008**, *68*, 8607−8615.

(12) Day, S. E.; Kettunen, M. I.; Gallagher, F. A.; Hu, D.-E.; Lerche, M.; Wolber, J.; Golman, K.; Ardenkjaer-Larsen, J. H.; Brindle, K. M. Detecting Tumor Response to Treatment Using Hyperpolarized ^{13}C Magnetic Resonance Imaging and Spectroscopy. *Nat. Med.* **2007**, *13*, 1382−1387.

(13) Park, I.; Bok, R.; Ozawa, T.; Phillips, J. J.; James, C. D.; Vigneron, D. B.; Ronen, S. M.; Nelson, S. J. Detection of Early Response to Temozolomide Treatment in Brain Tumors Using Hyperpolarized ^{13}C MR Metabolic Imaging. *J. Magn. Reson. Imaging* **2011**, *33*, 1284−1290.

(14) Nelson, S. J.; Kurhanewicz, J.; Vigneron, D. B.; Larson, P. E. Z.; Harzstark, A. L.; Ferrone, M.; van Criekinge, M.; Chang, J. W.; Bok, R.; Park, I.; et al. Metabolic Imaging of Patients with Prostate Cancer Using Hyperpolarized [1-^{13}C]Pyruvate. *Sci. Transl. Med.* **2013**, *5*, No. 198ra108.

(15) Kurhanewicz, J.; Vigneron, D. B.; Ardenkjaer-Larsen, J. H.; Bankson, J. A.; Brindle, K.; Cunningham, C. H.; Gallagher, F. A.; Keshari, K. R.; Kjaer, A.; Laustsen, C.; et al. Hyperpolarized ^{13}C MRI: Path to Clinical Translation in Oncology. *Neoplasia* **2019**, *21*, 1−16.

(16) Lai, M.; Gruetter, R.; Lanz, B. Progress towards in Vivo Brain ^{13}C-MRS in Mice: Metabolic Flux Analysis in Small Tissue Volumes. *Anal. Biochem.* **2017**, *529*, 229−244.

(17) Morris, P.; Bachelard, H. Reflections on the Application of ^{13}C-MRS to Research on Brain Metabolism. *NMR Biomed.* **2003**, *16*, 303−312.

(18) Jensen, P. R.; Peitersen, T.; Karlsson, M.; in 't Zandt, R.; Gisselsson, A.; Hansson, G.; Meier, S.; Lerche, M. H. Tissue-Specific Short Chain Fatty Acid Metabolism and Slow Metabolic Recovery after Ischemia from Hyperpolarized NMR in Vivo. *J. Biol. Chem.* **2009**, *284*, 36077−36082.

(19) Mikkelsen, E. F. R.; Mariager, C. Ø.; Nørlinger, T.; Qi, H.; Schulte, R. F.; Jakobsen, S.; Frøkiær, J.; Pedersen, M.; Stødkilde-Jørgensen, H.; Laustsen, C. Hyperpolarized [1-^{13}C]-Acetate Renal Metabolic Clearance Rate Mapping. *Sci. Rep.* **2017**, *7*, No. 16002.

(20) Bastiaansen, J. A. M.; Cheng, T.; Mishkovsky, M.; Duarte, J. M. N.; Comment, A.; Gruetter, R. In Vivo Enzymatic Activity of AcetylCoA Synthetase in Skeletal Muscle Revealed by ^{13}C Turnover from Hyperpolarized [1-^{13}C]Acetate to [1-^{13}C]Acetylcarnitine. *Biochim. Biophys. Acta* **2013**, *1830*, 4171−4178.

(21) Kurhanewicz, J.; Vigneron, D. B.; Brindle, K.; Chekmenev, E. Y.; Comment, A.; Cunningham, C. H.; DeBerardinis, R. J.; Green, G. G.; Leach, M. O.; Rajan, S. S.; et al. Analysis of Cancer Metabolism by Imaging Hyperpolarized Nuclei: Prospects for Translation to Clinical Research. *Neoplasia* **2011**, *13*, 81−97.

(22) Ardenkjær-Larsen, J. H.; Fridlund, B.; Gram, A.; Hansson, G.; Hansson, L.; Lerche, M. H.; Servin, R.; Thaning, M.; Golman, K.

Increase in Signal-to-Noise Ratio of >10,000 Times in Liquid-State NMR. *Proc. Natl. Acad. Sci. U.S.A.* **2003**, *100*, 10158−10163.
(23) Ardenkjaer-Larsen, J. H. On the Present and Future of Dissolution-DNP. *J. Magn. Reson.* **2016**, *264*, 3−12.
(24) Niedbalski, P.; Kiswandhi, A.; Parish, C.; Wang, Q.; Khashami, F.; Lumata, L. NMR Spectroscopy Unchained: Attaining the Highest Signal Enhancements in Dissolution Dynamic Nuclear Polarization. *J. Phys. Chem. Lett.* **2018**, *9*, 5481−5489.
(25) Bowers, C. R.; Weitekamp, D. P. Parahydrogen and Synthesis Allow Dramatically Enhanced Nuclear Alignment. *J. Am. Chem. Soc.* **1987**, *109*, 5541−5542.
(26) Eisenschmid, T. C.; Kirss, R. U.; Deutsch, P. P.; Hommeltoft, S. I.; Eisenberg, R.; Bargon, J.; Lawler, R. G.; Balch, A. L. Para Hydrogen Induced Polarization in Hydrogenation Reactions. *J. Am. Chem. Soc.* **1987**, *109*, 8089−8091.
(27) Hövener, J.-B.; Pravdivtsev, A. N.; Kidd, B.; Bowers, C. R.; Glöggler, S.; Kovtunov, K. V.; Plaumann, M.; Katz-Brull, R.; Buckenmaier, K.; Jerschow, A.; et al. Parahydrogen-Based Hyperpolarization for Biomedicine. *Angew. Chem., Int. Ed.* **2018**, *57*, 11140−11162.
(28) Green, R. A.; Adams, R. W.; Duckett, S. B.; Mewis, R. E.; Williamson, D. C.; Green, G. G. R. The Theory and Practice of Hyperpolarization in Magnetic Resonance Using Parahydrogen. *Prog. Nucl. Magn. Reson. Spectrosc.* **2012**, *67*, 1−48.
(29) Bowers, C. R. Sensitivity Enhancement Utilizing Parahydrogen. *eMagRes* **2007**, DOI: 10.1002/9780470034590.emrstm0489.
(30) Bowers, C. R.; Weitekamp, D. P. Transformation of Symmetrization Order to Nuclear-Spin Magnetization by Chemical Reaction and Nuclear Magnetic Resonance. *Phys. Rev. Lett.* **1986**, *57*, 2645−2648.
(31) Barkemeyer, J.; Haake, M.; Bargon, J. Hetero-NMR Enhancement via Parahydrogen Labeling. *J. Am. Chem. Soc.* **1995**, *117*, 2927−2928.
(32) Kuhn, L. T.; Bommerich, U.; Bargon, J. Transfer of Parahydrogen-Induced Hyperpolarization to ^{19}F. *J. Phys. Chem. A* **2006**, *110*, 3521−3526.
(33) Jóhannesson, H.; Axelsson, O.; Karlsson, M. Transfer of Para-Hydrogen Spin Order into Polarization by Diabatic Field Cycling. *C. R. Phys.* **2004**, *5*, 315−324.
(34) Cavallari, E.; Carrera, C.; Boi, T.; Aime, S.; Reineri, F. Effects of Magnetic Field Cycle on the Polarization Transfer from Parahydrogen to Heteronuclei through Long-Range J-Couplings. *J. Phys. Chem. B* **2015**, *119*, 10035−10041.
(35) Bär, S.; Lange, T.; Leibfritz, D.; Hennig, J.; von Elverfeldt, D.; Hövener, J.-B. On the Spin Order Transfer from Parahydrogen to Another Nucleus. *J. Magn. Reson.* **2012**, *225*, 25−35.
(36) Haake, M.; Natterer, J.; Bargon, J. Efficient NMR Pulse Sequences to Transfer the Parahydrogen-Induced Polarization to Hetero Nuclei. *J. Am. Chem. Soc.* **1996**, *118*, 8688−8691.
(37) Stevanato, G. Alternating Delays Achieve Polarization Transfer (ADAPT) to Heteronuclei in PHIP Experiments. *J. Magn. Reson.* **2017**, *274*, 148−162.
(38) Stevanato, G.; Eills, J.; Bengs, C.; Pileio, G. A Pulse Sequence for Singlet to Heteronuclear Magnetization Transfer: S2hM. *J. Magn. Reson.* **2017**, *277*, 169−178.
(39) Pravdivtsev, A. N.; Yurkovskaya, A. V.; Lukzen, N. N.; Ivanov, K. L.; Vieth, H.-M. Highly Efficient Polarization of Spin-1/2 Insensitive NMR Nuclei by Adiabatic Passage through Level Anticrossings. *J. Phys. Chem. Lett.* **2014**, *5*, 3421−3426.
(40) Golman, K.; Axelsson, O.; Jóhannesson, H.; Månsson, S.; Olofsson, C.; Petersson, J. S. Parahydrogen-Induced Polarization in Imaging: Subsecond ^{13}C Angiography. *Magn. Reson. Med.* **2001**, *46*, 1−5.
(41) Bhattacharya, P.; Harris, K.; Lin, A. P.; Mansson, M.; Norton, V. A.; Perman, W. H.; Weitekamp, D. P.; Ross, B. D. Ultra-Fast Three Dimensional Imaging of Hyperpolarized ^{13}C in Vivo. *MAGMA* **2005**, *18*, 245−256.
(42) Olsson, L. E.; Chai, C.-M.; Axelsson, O.; Karlsson, M.; Golman, K.; Petersson, J. S. MR Coronary Angiography in Pigs With Intraarterial Injections of a Hyperpolarized ^{13}C Substance. *Magn. Reson. Med.* **2006**, *55*, 731−737.
(43) Bhattacharya, P.; Chekmenev, E. Y.; Perman, W. H.; Harris, K. C.; Lin, A. P.; Norton, V. A.; Tan, C. T.; Ross, B. D.; Weitekamp, D. P. Towards Hyperpolarized ^{13}C-Succinate Imaging of Brain Cancer. *J. Magn. Reson.* **2007**, *186*, 150−155.
(44) Bhattacharya, P.; Chekmenev, E. Y.; Reynolds, W. F.; Wagner, S.; Zacharias, N.; Chan, H. R.; Bünger, R.; Ross, B. D. Parahydrogen-Induced Polarization (PHIP) Hyperpolarized MR Receptor Imaging in Vivo: A Pilot Study of ^{13}C Imaging of Atheroma in Mice. *NMR Biomed.* **2011**, *24*, 1023−1028.
(45) Zacharias, N. M.; Chan, H. R.; Sailasuta, N.; Ross, B. D.; Bhattacharya, P. Real-Time Molecular Imaging of Tricarboxylic Acid Cycle Metabolism in Vivo by Hyperpolarized 1-^{13}C Diethyl Succinate. *J. Am. Chem. Soc.* **2012**, *134*, 934−943.
(46) Schmidt, A. B.; Berner, S.; Braig, M.; Zimmermann, M.; Hennig, J.; von Elverfeldt, D.; Hövener, J.-B. In Vivo ^{13}C-MRI Using SAMBADENA. *PLoS One* **2018**, *13*, No. e0200141.
(47) Buljubasich, L.; Franzoni, M. B.; Münnemann, K. Parahydrogen Induced Polarization by Homogeneous Catalysis: Theory and Applications. *Top. Curr. Chem.* **2013**, *338*, 33−74.
(48) Kovtunov, K. V.; Zhivonitko, V. V.; Skovpin, I. V.; Barskiy, D. A.; Koptyug, I. V. Parahydrogen-Induced Polarization in Heterogeneous Catalytic Processes. *Top. Curr. Chem.* **2013**, *338*, 123−180.
(49) Kovtunov, K. V.; Barskiy, D. A.; Shchepin, R. V.; Salnikov, O. G.; Prosvirin, I. P.; Bukhtiyarov, A. V.; Kovtunova, L. M.; Bukhtiyarov, V. I.; Koptyug, I. V.; Chekmenev, E. Y. Production of Pure Aqueous ^{13}C-Hyperpolarized Acetate Via Heterogeneous Parahydrogen-Induced Polarization. *Chem. - Eur. J.* **2016**, *22*, 16446−16449.
(50) Kovtunov, K. V.; Barskiy, D. A.; Salnikov, O. G.; Shchepin, R. V.; Coffey, A. M.; Kovtunova, L. M.; Bukhtiyarov, V. I.; Koptyug, I. V.; Chekmenev, E. Y. Toward Production of Pure ^{13}C Hyperpolarized Metabolites Using Heterogeneous Parahydrogen-Induced Polarization of Ethyl [1-^{13}C]Acetate. *RSC Adv.* **2016**, *6*, 69728−69732.
(51) Salnikov, O. G.; Kovtunov, K. V.; Koptyug, I. V. Production of Catalyst-Free Hyperpolarised Ethanol Aqueous Solution via Heterogeneous Hydrogenation with Parahydrogen. *Sci. Rep.* **2015**, *5*, No. 13930.
(52) Reineri, F.; Viale, A.; Ellena, S.; Boi, T.; Daniele, V.; Gobetto, R.; Aime, S. Use of Labile Precursors for the Generation of Hyperpolarized Molecules from Hydrogenation with Parahydrogen and Aqueous-Phase Extraction. *Angew. Chem., Int. Ed.* **2011**, *50*, 7350−7353.
(53) Reineri, F.; Boi, T.; Aime, S. ParaHydrogen Induced Polarization of ^{13}C Carboxylate Resonance in Acetate and Pyruvate. *Nat. Commun.* **2015**, *6*, No. 5858.
(54) Cavallari, E.; Carrera, C.; Aime, S.; Reineri, F. ^{13}C MR Hyperpolarization of Lactate by Using ParaHydrogen and Metabolic Transformation in Vitro. *Chem. - Eur. J.* **2017**, *23*, 1200−1204.
(55) Cavallari, E.; Carrera, C.; Aime, S.; Reineri, F. Studies to Enhance the Hyperpolarization Level in PHIP-SAH-Produced C13-Pyruvate. *J. Magn. Reson.* **2018**, *289*, 12−17.
(56) Cavallari, E.; Carrera, C.; Sorge, M.; Bonne, G.; Muchir, A.; Aime, S.; Reineri, F. The ^{13}C Hyperpolarized Pyruvate Generated by ParaHydrogen Detects the Response of the Heart to Altered Metabolism in Real Time. *Sci. Rep.* **2018**, *8*, No. 8366.
(57) Cavallari, E.; Carrera, C.; Aime, S.; Reineri, F. Metabolic Studies of Tumor Cells Using [1-^{13}C] Pyruvate Hyperpolarized by Means of PHIP-Side Arm Hydrogenation. *ChemPhysChem* **2019**, *20*, 318−325.
(58) Korchak, S.; Mamone, S.; Glöggler, S. Over 50% ^{1}H and ^{13}C Polarization for Generating Hyperpolarized Metabolites—A Para-Hydrogen Approach. *ChemistryOpen* **2018**, *7*, 672−676.
(59) Korchak, S.; Yang, S.; Mamone, S.; Glöggler, S. Pulsed Magnetic Resonance to Signal-Enhance Metabolites within Seconds by Utilizing Para-Hydrogen. *ChemistryOpen* **2018**, *7*, 344−348.
(60) Chukanov, N. V.; Salnikov, O. G.; Shchepin, R. V.; Kovtunov, K. V.; Koptyug, I. V.; Chekmenev, E. Y. Synthesis of Unsaturated Precursors for Parahydrogen-Induced Polarization and Molecular

DOI: 10.1021/acs.jpcc.9b02041
J. Phys. Chem. C 2019, 123, 12827−12840

Imaging of 1-^{13}C-Acetates and 1-^{13}C-Pyruvates via Side Arm Hydrogenation. *ACS Omega* **2018**, *3*, 6673−6682.
(61) Shchepin, R. V.; Barskiy, D. A.; Coffey, A. M.; Manzanera Esteve, I. V.; Chekmenev, E. Y. Efficient Synthesis of Molecular Precursors for Para-Hydrogen-Induced Polarization of Ethyl Acetate-1-^{13}C and Beyond. *Angew. Chem., Int. Ed.* **2016**, *55*, 6071−6074.
(62) Cai, C.; Coffey, A. M.; Shchepin, R. V.; Chekmenev, E. Y.; Waddell, K. W. Efficient Transformation of Parahydrogen Spin Order into Heteronuclear Magnetization. *J. Phys. Chem. B* **2013**, *117*, 1219−1224.
(63) Pravica, M. G.; Weitekamp, D. P. Net NMR Alignment by Adiabatic Transport of Parahydrogen Addition Products to High Magnetic Field. *Chem. Phys. Lett.* **1988**, *145*, 255−258.
(64) Salnikov, O. G.; Shchepin, R. V.; Chukanov, N. V.; Jaigirdar, L.; Pham, W.; Kovtunov, K. V.; Koptyug, I. V.; Chekmenev, E. Y. Effects of Deuteration of ^{13}C-Enriched Phospholactate on Efficiency of Parahydrogen-Induced Polarization by Magnetic Field Cycling. *J. Phys. Chem. C* **2018**, *122*, 24740−24749.
(65) Mo, H.; Harwood, J. S.; Raftery, D. Receiver Gain Function: The Actual NMR Receiver Gain. *Magn. Reson. Chem.* **2010**, *48*, 235−238.
(66) Hurd, R. E.; Yen, Y.-F.; Mayer, D.; Chen, A.; Wilson, D.; Kohler, S.; Bok, R.; Vigneron, D.; Kurhanewicz, J.; Tropp, J.; et al. Metabolic Imaging in the Anesthetized Rat Brain Using Hyperpolarized [1-^{13}C] Pyruvate and [1-^{13}C] Ethyl Pyruvate. *Magn. Reson. Med.* **2010**, *63*, 1137−1143.
(67) Barskiy, D. A.; Salnikov, O. G.; Kovtunov, K. V.; Koptyug, I. V. NMR Signal Enhancement for Hyperpolarized Fluids Continuously Generated in Hydrogenation Reactions with Parahydrogen. *J. Phys. Chem. A* **2015**, *119*, 996−1006.
(68) Coffey, A. M.; Shchepin, R. V.; Truong, M. L.; Wilkens, K.; Pham, W.; Chekmenev, E. Y. Open-Source Automated Parahydrogen Hyperpolarizer for Molecular Imaging Using ^{13}C Metabolic Contrast Agents. *Anal. Chem.* **2016**, *88*, 8279−8288.
(69) Waddell, K. W.; Coffey, A. M.; Chekmenev, E. Y. In Situ Detection of PHIP at 48 mT: Demonstration Using a Centrally Controlled Polarizer. *J. Am. Chem. Soc.* **2011**, *133*, 97−101.

DOI: 10.1021/acs.jpcc.9b02041
J. Phys. Chem. C 2019, 123, 12827−12840

CHEMISTRY
A European Journal

www.chemeurj.org

Reprint

A Journal of
ChemPubSoc Europe
ACES
Asian Chemical Editorial Society
WILEY-VCH

ChemPubSoc Europe

DOI: 10.1002/chem.201901192

CHEMISTRY A European Journal Full Paper

Hyperpolarization

Hyperpolarizing Concentrated Metronidazole $^{15}NO_2$ Group over Six Chemical Bonds with More than 15% Polarization and a 20 Minute Lifetime

Roman V. Shchepin,[a] Jonathan R. Birchall,[b] Nikita V. Chukanov,[c, d] Kirill V. Kovtunov,[c, d] Igor V. Koptyug,[c, d] Thomas Theis,[e] Warren S. Warren,[f] Juri G. Gelovani,[b] Boyd M. Goodson,[g] Sepideh Shokouhi,[a] Matthew S. Rosen,[h] Yi-Fen Yen,[h] Wellington Pham,[a] and Eduard Y. Chekmenev*[b, i]

Abstract: The NMR hyperpolarization of uniformly ^{15}N-labeled [$^{15}N_3$]metronidazole is demonstrated by using SABRE-SHEATH. In this antibiotic, the $^{15}NO_2$ group is hyperpolarized through spin relays created by ^{15}N spins in [$^{15}N_3$]metronidazole, and the polarization is transferred from parahydrogen-derived hydrides over six chemical bonds. In less than a minute of parahydrogen bubbling at approximately 0.4 μT, a high level of nuclear spin polarization (P_{15N}) of around 16% is achieved on all three ^{15}N sites. This product of ^{15}N polarization and concentration of ^{15}N spins is around six-fold better than any previous value determined for ^{15}N SABRE-derived hyperpolarization. At 1.4 T, the hyperpolarized state persists for tens of minutes (relaxation time, $T_1 \approx 10$ min). A novel synthesis of uniformly ^{15}N-enriched metronidazole is reported with a yield of 15%. This approach can potentially be used for synthesis of a wide variety of in vivo metabolic probes with potential uses ranging from hypoxia sensing to theranostic imaging.

[a] *Prof. Dr. R. V. Shchepin, Prof. Dr. S. Shokouhi, Prof. Dr. W. Pham*
Department of Radiology, Vanderbilt University Institute of Imaging Science (VUIIS), Vanderbilt University Medical Center (VUMC)
Nashville, Tennessee 37232-2310 (USA)

[b] *Dr. J. R. Birchall, Prof. Dr. J. G. Gelovani, Prof. Dr. E. Y. Chekmenev*
Department of Chemistry, Integrative Biosciences (Ibio)
Karmanos Cancer Institute (KCI), Wayne State University
Detroit, Michigan 48202 (USA)
E-mail: chekmenev@wayne.edu

[c] *Dr. N. V. Chukanov, Dr. K. V. Kovtunov, Prof. Dr. I. V. Koptyug*
International Tomography Center, SB RAS
3A Institutskaya St., Novosibirsk 630090 (Russia)

[d] *Dr. N. V. Chukanov, Dr. K. V. Kovtunov, Prof. Dr. I. V. Koptyug*
Novosibirsk State University
2 Pirogova St., Novosibirsk 630090 (Russia)

[e] *Prof. Dr. T. Theis*
Department of Chemistry, North Carolina State University
Raleigh, North Carolina, 27695-8204 (USA)

[f] *Prof. Dr. W. S. Warren*
Department of Chemistry, Duke University
Durham, North Carolina 27708 (USA)

[g] *Prof. Dr. B. M. Goodson*
Department of Chemistry and Biochemistry and Materials Technology Center, Southern Illinois University
Carbondale, Illinois 62901 (USA)

[h] *Prof. Dr. M. S. Rosen, Prof. Dr. Y.-F. Yen*
Massachusetts General Hospital
Athinoula A. Martinos Center for Biomedical Imaging
Boston, Massachusetts 02129 (USA)

[i] *Prof. Dr. E. Y. Chekmenev*
Russian Academy of Sciences
Leninskiy Prospekt 14, Moscow, 119991 (Russia)

Supporting information and the ORCID identification number(s) for the author(s) of this article can be found under: https://doi.org/10.1002/chem.201901192.

Introduction

NMR hyperpolarization techniques transiently increase nuclear spin polarization (P) by several orders of magnitude.[1–3] This significant increase in P enables metabolic magnetic resonance spectroscopy (MRS) and MRS imaging (MRSI) after a bolus injection of a hyperpolarized (HP) compound to detect abnormal metabolism in cancer and other diseases.[4–10] The ^{13}C isotope has been widely employed in a number of biomolecules, most notably in [1-^{13}C]pyruvate,[6,8] which is typically hyperpolarized by dissolution dynamic nuclear polarization (d-DNP).[11,12] However, this approach has a number of shortcomings. First, the lifetime of the HP state (governed by the spin–lattice constant of exponential decay) is relatively short [e.g., compared with those of ^{18}F and ^{11}C positron emission tomography (PET) tracers], with the relaxation time (T_1) on the order of 1 min.[13] As a result, only a limited number of metabolic pathways are amenable to MRSI, because sufficient levels of nuclear spin polarization must persist until detection.[11,14] Secondly, d-DNP generally requires several tens of minutes (or longer) of hyperpolarization buildup time as well as sophisticated, costly equipment.[15,16]

The hyperpolarization of ^{15}N sites in biomolecules is a viable alternative approach,[17–19] because ^{15}N sites can generally retain nuclear spin polarization for significantly longer periods of time, with T_1 values of more than 10 minutes having been observed in quaternary nitrogen sites in several model compounds.[20,21] However, HP ^{15}N-labeled choline (along with its derivatives) is the only quaternary amine with biomedical rele-

vance in the context of HP MRS.[22] Unfortunately, the small difference in chemical shift observed for [^{15}N]choline and its metabolites (ca. 0.2 ppm) would make them difficult to distinguish in vivo.[5,22] On the other hand, nitro groups occur in a wide range of drugs approved by the US Food and Drug Administration (FDA), including antibiotics, cancer radio-sensitizing agents,[23] hypoxia sensors,[24] and chemotherapeutics,[25] and can therefore potentially serve as convenient biocompatible moieties to retain the HP state for tens of minutes.

Signal amplification by reversible exchange (SABRE) is a hyperpolarization technique that employs parahydrogen as the source of hyperpolarization.[26–33] In this work we employed the SABRE in the shield enables alignment transfer to heteronuclei (SABRE-SHEATH)[34,35] variant of SABRE, which relies on simultaneous chemical exchange between parahydrogen (pH_2) and the to-be-hyperpolarized biomolecules (without altering their structures) within the ligand sphere of a catalyst in microtesla (μT) magnetic fields (Figure 1 a). SABRE-SHEATH has been shown to produce ^{15}N HP states with P values of up to 30% in under 1 minute (although these high polarization levels have previously been obtained at a relatively low concentration of ^{15}N spins).[36–38] Unlike d-DNP,[12] SABRE-SHEATH requires relatively simple and inexpensive hardware.[34,35]

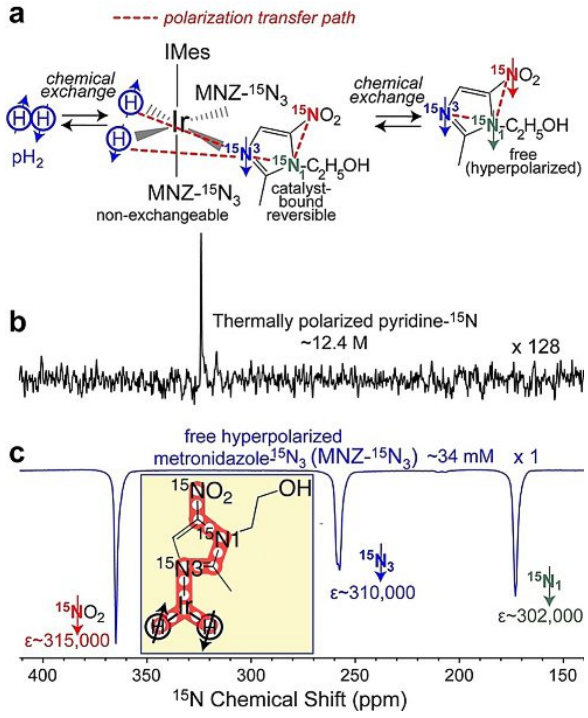

Figure 1. a) Schematic of the simultaneous chemical exchange of pH_2 and [$^{15}N_3$]metronidazole (MNZ-$^{15}N_3$) on the Ir-IMes polarization transfer catalyst.[39] Note the dashed red lines indicate the likely path of spin-relayed polarization transfer from pH_2-derived hydrides to the $^{15}NO_2$ group via the ^{15}N3 and ^{15}N1 sites. b) Single-scan ^{15}N NMR signal reference spectrum of thermally polarized neat (no solvent) [^{15}N]pyridine (12.4 M). c) Single-scan ^{15}N NMR spectrum of HP [$^{15}N_3$]metronidazole in [D_4]MeOH. All NMR spectra were recorded at 1.4 T. The inset displays (in red) the path of chemical bonds over which the network of $I = 1/2$ spin relays is established. The following experimental conditions were employed for SABRE-SHEATH hyperpolarization: Room temperature, 6.7 atm overpressure of the medium-walled NMR tube, and a flow rate of 70 sccm (standard cubic centimeters per minute) of pH_2 controlled by a mass-flow controller (MFC).

Results and Discussion

Although to date ^{15}N hyperpolarization of several biomolecules has been demonstrated by SABRE-SHEATH, which opens up a range of potential contrast agents,[38] nearly all previous reports have focused on the hyperpolarization of ^{15}N sites that directly interact with the iridium catalytic center of the Ir-IMes (IMes = 1,3-dimesitylimidazol-2-ylidene) polarization transfer catalyst, which is the catalyst typically used in most SABRE experiments.[39] The direct polarization transfer from pH_2-derived hydrides to these ^{15}N sites is efficient (i.e., fast and yielding high values of P_{15N}), because the two-bond ^{1}H–^{15}N spin–spin couplings are relatively strong (e.g., 10–20 Hz) and sufficiently different from each other as to render the exchangeable catalyst binding sites magnetically inequivalent from one another.[34,35]

Spin-relayed polarization transfer

Although in general direct SABRE-SHEATH of remote spin $I = {}^1/_2$ sites over three or more chemical bonds is inefficient,[40] we have recently demonstrated the concept of spin-relayed polarization transfer from SABRE-SHEATH-hyperpolarized ^{15}N sites to other ^{13}C and ^{15}N sites within the same molecule.[41–43] In this approach, a network of J-coupled spin $I = {}^1/_2$ nuclei can transmit polarization several chemical bonds away from the pH_2-derived hydrides.[41,42]

In this paper we show that uniformly ^{15}N-labeled [$^{15}N_3$]metronidazole (MNZ-$^{15}N_3$) can be efficiently hyperpolarized by the SABRE-SHEATH approach to $P_{15N} > 16\%$ for each of the three ^{15}N sites by using 87% pH_2. Figure 1 c shows the spectrum of HP MNZ-$^{15}N_3$, in which all three ^{15}N peaks are dramatically enhanced, with ^{15}N polarization increased by over 300 000-fold compared with thermal ^{15}N polarization (for an NMR spectrum of a thermally polarized signal reference compound at 1.4 T, see Figure 1 b). The signal enhancements are field-dependent, because thermal polarization varies linearly with the applied magnetic field. We note that four-, five- and six-bond spin–spin couplings between pH_2-derived hydrides and ^{15}N1 and $^{15}NO_2$ sites, respectively, are negligible, and therefore direct polarization transfer is highly inefficient, as described previously.[37] Analysis of the ^{15}N–^{15}N spin–spin couplings in MNZ-$^{15}N_3$ (see Figure S2 in the Supporting Information) revealed $J_{15N\text{-}15N}$ values of around 1.65 Hz between the ^{15}N3 and ^{15}N1 sites and around 1.45 Hz between the ^{15}N1 and $^{15}NO_2$ sites. No spin–spin coupling between the $^{15}NO_2$ and ^{15}N3 sites was detected. Therefore, we conclude that the ^{15}N3 site is likely hyperpolarized first by SABRE-SHEATH from pH_2-derived hydrides, the ^{15}N1 site is hyperpolarized next by spin-relayed polarization transfer from the HP ^{15}N3 site, and the $^{15}NO_2$ site is hyperpolarized last by spin-relayed transfer from the ^{15}N1 site. We note that the $^{15}NO_2$ site is not significantly spin–spin cou-

pled to any other nucleus besides ^{15}N1, further supporting our conclusion.

^{15}N polarization dynamics

Studies of the polarization field dependence, dynamics, and decay for [$^{15}N_3$]metronidazole are summarized in Figure 2. In part because the $^{15}NO_2$ site is effectively isolated from protons in the [$^{15}N_3$]metronidazole molecule, we found that it has a significantly longer T_1 (9.7 ± 1.0 min) than the ^{15}N3 (3.1 ± 0.4 min) and ^{15}N1 (3.8 ± 0.3 min) sites, respectively (Figure 2 f). The relayed (versus direct) nature of the polarization transfer mechanism is also supported by the magnetic field dependence (Figure 2 a) of P_{15N} for the three ^{15}N sites, which reveals that the maxima of P_{15N} for the $^{15}NO_2$ and ^{15}N1 sites coincide with that for the ^{15}N3 site, which is consistent with the notion that the

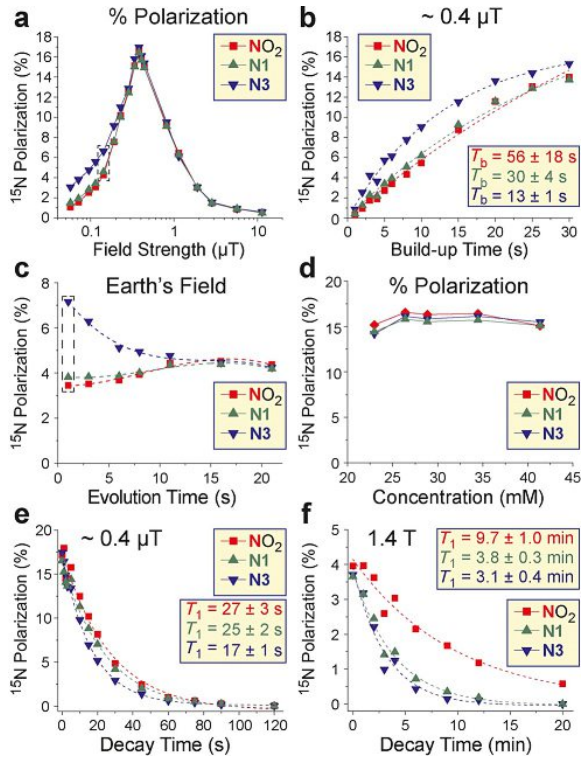

Figure 2. Studies of SABRE-SHEATH hyperpolarization of [$^{15}N_3$]metronidazole (MNZ-$^{15}N_3$) by using NMR spectroscopy at 1.4 T. a) Dependence of P_{15N} on the magnetic field for the three ^{15}N sites. b) Dynamics of P_{15N} at the three ^{15}N sites at approx. 0.4 μT with single-exponential fitting. Note that the buildup of P_{15N} at the $^{15}NO_2$ and ^{15}N1 sites is not well described by mono-exponential growth due to the complex dynamics of the buildup process at multiple sites (the mono-exponential buildup curves and time constants are provided for comparative purposes (with respect to the ^{15}N3 site) only). c) Evolution of P_{15N} at the three ^{15}N sites in the Earth's magnetic field (ca. 30 μT) using the initial conditions of $P_{15N3} > P_{15N1} > P_{15NO2}$ (the initial points within the dashed box correspond to those in (a), denoting the magnetic field of HP state preparation). d) Concentration dependence of P_{15N} at the three ^{15}N sites. e) Decay of P_{15N} at the three ^{15}N sites at approx. 0.4 μT. The sample was transferred to a 1.4 T NMR spectrometer for detection. f) Decay of P_{15N} at the three ^{15}N sites at 1.4 T. The color coding indicates the three ^{15}N sites: ^{15}N1: green; ^{15}N3: blue; $^{15}NO_2$: red.

^{15}N3 site acts as the local source of polarization. Moreover, the kinetics of ^{15}N polarization buildup at the optimal magnetic field (ca. 0.4 μT) clearly indicates that, during the buildup process, $P_{15N3} > P_{15N1} > P_{15NO2}$ (Figure 2 b). It is worth noting that the three P_{15N} values tend towards similar values when the buildup is nearly complete (Figure 2 a). On the other hand, during the ^{15}N polarization decay process in a field of around 0.4 μT, this order of P_{15N} values is reversed, that is, $P_{15N3} < P_{15N1} < P_{15NO2}$ (Figure 2 e). It is also worth noting that when the magnetic field is below the optimal value (left-hand slope in Figure 2 a), the ^{15}N3 site is hyperpolarized better than the ^{15}N1 and $^{15}NO_2$ sites. The lower levels of polarization observed below 0.4 μT and the fact that the polarization of ^{15}N1 is lower than that of ^{15}N3 are likely explained by the "strong coupling" of protons and heteronuclei in magnetic fields in the range 100 nT–1 μT observed by Kiryutin et al.,[44] which may lead to more efficient depolarization of the ^{15}N1 site, which is coupled more efficiently to the proton spin network (see the Supporting Information for details) compared with the ^{15}N3 site. Because ^{15}N polarization of the $^{15}NO_2$ site is dependent on that of ^{15}N1 (because the strongest spin–spin coupling of the $^{15}NO_2$ site is with the ^{15}N1 site), the lower ^{15}N polarization of the $^{15}NO_2$ site (compared with that of the ^{15}N3 site) is also expected. We have employed the nonequal HP spin-state condition, that is, $P_{15N3} > P_{15N1} > P_{15NO2}$, to study the dynamics of polarization evolution in the Earth's magnetic field (ca. 30 μT), in which pH_2 can no longer efficiently hyperpolarize any heteronuclei and therefore the polarization can only decay.[34,35,45] Figure 2 c shows that P_{15N3} is redistributed relatively quickly, on the timescale of seconds, to the^{15}N1 and $^{15}NO_2$ sites (it is worth noting that P_{15N1} and P_{15NO2} grow for the first approx. 15 s, whereas P_{15N3} decreases). Although this redistribution of polarization occurs in the Earth's magnetic field, which is approximately 30 μT (as measured in our laboratory) and significantly exceeds 0.4 μT, this observation provides additional support for the spin-relayed mechanism of SABRE-SHEATH polarization transfer in [$^{15}N_3$]metronidazole in microtesla magnetic fields.

^{15}N polarization levels

It should be noted that over the MNZ concentration range studied (23–41 mM), P_{15N} was 15.6 ± 0.7 % on all three ^{15}N sites, as detected by 1.4 T NMR spectroscopy (Figure 2 d; notably, the ratio of MNZ and the catalyst was maintained constant at 20:1). This polarization level is lower (by around two-fold) than the best P_{15N} values (ca. 34 %) obtained for metronidazole with a natural abundance of ^{15}N (< 0.3 %) under similar conditions (Figure 3 a).[36] This observation can likely be explained by two effects: First, the labeled compound produces an active complex with two ^{15}N sites in the equatorial plane and the polarization is transferred in the AA′BB′ four-spin system, whereas in the case of metronidazole with a natural abundance of ^{15}N, polarization transfer from the pH_2-derived hydrides to ^{15}N occurs in an AA′B three-spin system. It has been shown previously that polarization transfer in such three-spin systems may be more efficient than that in four-spin systems.[34,35,45,46] The second contributing factor is access to fresh pH_2, which can be

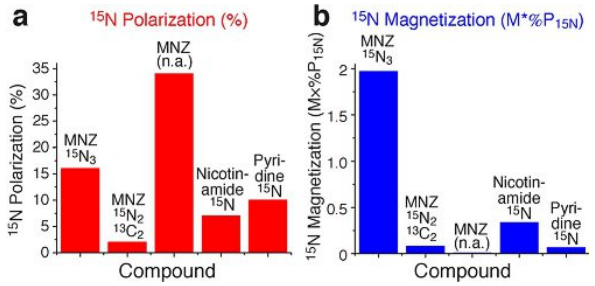

Figure 3. a) ^{15}N polarization and b) ^{15}N magnetization, defined as the product of the molar concentration of ^{15}N spins in the HP substrate and ^{15}N polarization, in [$^{15}N_3$]metronidazole (MNZ-$^{15}N_3$) studied here, [$^{15}N_2$,$^{13}C_2$]metronidazole (MNZ-$^{15}N_2$,$^{13}C_2$),[41] natural abundant metronidazole [MNZ (n.a.)],[36] mono-^{15}N-labeled [$^{15}N_1$]nicotinamide,[36] and [^{15}N]pyridine.[34] Note the multiple spin labels in some compounds.

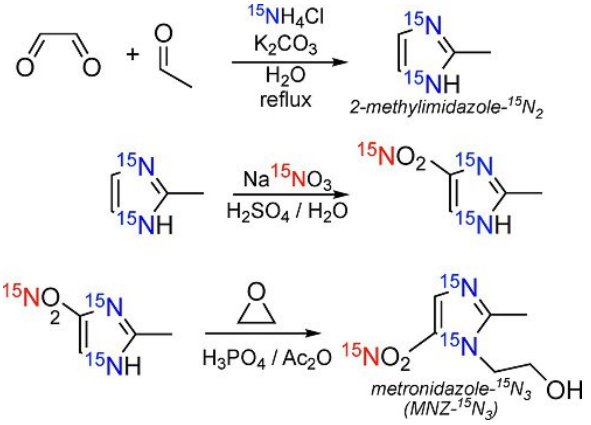

Scheme 1. Three-step ^{15}N-enrichment of [$^{15}N_3$]metronidazole (MNZ-$^{15}N_3$). Note the color coding of the ^{15}N sources, $^{15}NH_4Cl$ and $Na^{15}NO_3$, the color coding (blue and red, respectively) in the products indicating the source of the ^{15}N label.

more limited under conditions of high ^{15}N density (i.e., local pH_2 can be depleted more quickly if there are more ^{15}N sites present);[45] the labeled sample studied here contains more than 600-fold more ^{15}N sites than the natural abundance compound studied previously.[36]

^{15}N polarization payload and ^{15}N magnetization

Comparison of the polarization payload (defined as the product of the concentration of ^{15}N spins, ^{15}N polarization, and the volume of the HP contrast agent) is more relevant in the context of biomedical applications, because in vivo experiments greatly benefit from a higher HP payload to enhance the signal-to-noise ratio and improve spatial and temporal resolution.[47] Because SABRE is a highly scalable hyperpolarization technique (i.e., varying the volume of HP liquids is relatively straightforward), it is important to highlight the ^{15}N magnetization achieved, that is, the product of ^{15}N spin concentration and ^{15}N polarization. The ^{15}N polarization levels of several biomolecules hyperpolarized by SABRE are compared in Figure 3a, and the ^{15}N magnetization determined for the same five compounds hyperpolarized by SABRE are presented in Figure 3b. The ^{15}N magnetization for [$^{15}N_3$]metronidazole is improved by around 25-fold or more compared with the previously studied molecules [i.e., compared with MZN(n.a.) and MNZ-$^{15}N_2$,$^{13}C_2$].[36] Moreover, the ^{15}N magnetization calculated here for [$^{15}N_3$]metronidazole is approximately six-fold greater than that of mono-^{15}N-labeled [^{15}N]nicotinamide.[34]

Synthesis of ^{15}N-enriched metronidazole

Importantly, the above NMR results were enabled by ^{15}N enrichment of all three nitrogen sites of the substrate, achieved by a novel but straightforward spin-labeling synthetic procedure (Scheme 1). First, 2-methyl[$^{15}N_2$]imidazole was prepared by using a modification of the procedure previously developed for the synthesis of [$^{15}N_2$]imidazole,[48] in which inexpensive $^{15}NH_4Cl$ was employed as the ^{15}N source. In the second step, the $^{15}NO_2$ group was added by a nitration reaction using $Na^{15}NO_3$ as the second inexpensive ^{15}N source. Ethylene oxide was employed in the last step to introduce the hydroxyethyl moiety. The overall yield over three steps (Scheme 1) was around 15% (see Section 9 of the Supporting Information). This synthetic approach for introducing ^{15}N spin into the nitroimidazole moiety can be potentially applied to a wide range of nitroimidazole-based drugs, for example, azomycin, benznidazole, secnidazole, ornidazole, nimorazole, TH-4000, and evofosfamide, used as hypoxia sensors, radio-sensitizing therapeutics, and theranostic imaging agents.[25]

Biomedical outlook

Metronidazole is an FDA-approved antibiotic that can be safely administered orally and intravenously in large (multigram) doses.[49] Moreover, we have recently reported the preparation of pure (i.e., catalyst-free) HP metronidazole solutions[36] as well as heterogeneous ^{15}N SABRE-SHEATH[50] and ^{15}N SABRE-SHEATH HP metronidazole in aqueous media,[51] thereby potentially enabling the preparation of biologically compatible HP MNZ-$^{15}N_3$ injectable formulation(s). We envision this contrast agent to have potential in hypoxia sensing (the focus of our future studies) in a manner similar to that of [^{18}F]fluoromisonidazole (FMISO) and other nitro-containing radiotracers employed in positron emission tomography (PET).[52,53] The nitroimidazole moiety is chemically reduced in the hypoxic environment by upregulated nitroreductases (i.e., in tumors or ischemic tissues),[24,54] which will likely result in large (tens of ppm) changes in the ^{15}N chemical shifts of the three ^{15}N sites. Although future studies are required to investigate the utility of HP MNZ-$^{15}N_3$ for hypoxia sensing and other applications, the results presented here ($P_{15N} \approx 16\%$ at $\geq 98\%$ ^{15}N enrichment, $T_1 \approx 10$ min, fast polarization, and straightforward isotopic enrichment) bode well for such envisioned cellular and in vivo experiments. Moreover, an in vivo study of ^{15}N relaxation with HP choline revealed an approximate 1.35-fold decrease in T_1 (from 172 ± 16 to 126 ± 15 s) compared with that in vitro at 9.4 T.[22] The effective reduction of the ^{15}N T_1

value for HP choline in vivo was attributed to choline uptake and metabolism versus depolarization,[22] which indicates that the ^{15}N T_1 value is reduced marginally in vivo compared with in vitro, largely because of the very low gyromagnetic ratio of ^{15}N spin (a tenth of that of proton spins). Therefore, we anticipate a relatively small (30% or less) reduction in the T_1 values presented here for [$^{15}N_3$]metronidazole in future in vivo studies.

Although the level of ^{15}N polarization obtained here is lower than the ^{13}C polarization obtained by using d-DNP hyperpolarizers (^{13}C polarization, ca. 40%[47]), the amount of actual polarization at the time of MR image acquisition will likely exceed that of ^{13}C, because the $^{15}NO_2$ group of [$^{15}N_3$]metronidazole has a significantly longer T_1 (by approximately an order of magnitude) and therefore will enjoy disproportionately lower depolarization during injection, circulation, and imaging. For example, the current time for injection of HP contrast agents in humans is around 55 s,[47] which causes an approximate three-fold decay of the ^{13}C polarization level, whereas the $^{15}NO_2$ polarization of HP [$^{15}N_3$]metronidazole will decay only by roughly 1.1-fold in that time, that is, it will experience a negligible loss.

However, the low gyromagnetic ratio of ^{15}N spins, which in part endows the long T_1 values demonstrated here, is a double-edged sword, because the NMR detection of low-γ nuclei is generally significantly less sensitive even at the same nominal polarization level.[55,56] The detected signal is directly proportional to the nuclear magnetic moment (which varies linearly with gyromagnetic ratio), and the NMR signal is also directly proportional to the resonance frequency (which also varies linearly with gyromagnetic ratio). Therefore, it follows that proton detection is around 100 times more sensitive than ^{15}N detection, $(\gamma_{1H}/\gamma_{15N})^2 \approx 100$, and ^{13}C detection is approximately six times more sensitive than ^{15}N detection, $(\gamma_{13C}/\gamma_{15N})^2 \approx 6$. Moreover, in the case of MRI and MRSI applications, spatial imaging encoding of low-γ nuclei carries two additional disadvantages. First, the gradient strength required to achieve the same spatial resolution is directly proportional to the gyromagnetic ratio (and therefore ^{15}N imaging requires ca. 2.5-fold greater gradient strength than ^{13}C imaging and ca. 10-fold greater gradient strength than ^{1}H imaging). Secondly, the gradient ramp rate is also directly proportional to the gyromagnetic ratio, thereby making gradient rise/fall durations of ^{15}N imaging around 2.5-fold slower than those of ^{13}C imaging and around 10-fold slower than those of ^{1}H imaging at a fixed gradient strength (i.e, the condition of maximum gradient power).

To summarize, ^{15}N MRI and MRSI face significant fundamental challenges. However, we envision proton detection of ^{15}N HP contrast agents in general and HP [$^{15}N_3$]nitroimidazole in particular, similarly to the concept of indirect proton detection recently introduced for ^{13}C HP contrast agents,[17,57–59] which means that the detection sensitivity of ^{15}N HP agents will be similar to that of ^{13}C HP agents when indirect (^{1}H) proton detection is employed. [$^{15}N_3$]Metronidazole has protons in its molecular structure that are weakly (2–9 Hz) coupled to the ^{15}N sites through spin–spin interactions. As a result, it is possible to use these spin–spin couplings for hyperpolarization transfer from ^{15}N to ^{1}H[17,60,61] by using conventional polarization transfer techniques such as insensitive nuclei enhanced by polarization transfer (INEPT).[62] This hyperpolarization transfer approach leads to a large increase in sensitivity of approximately 100-fold, as described above and elsewhere,[55,57,63] and the speed of imaging readout in the case of MRI and MRSI applications is also enhanced, as described above.

In this work [$^{15}N_3$]metronidazole was hyperpolarized in alcoholic solution. Although SABRE hyperpolarization in aqueous media has been demonstrated,[51,64–67] so far, the SABRE polarization levels in aqueous solutions are more than 10-fold lower than those in alcoholic solutions,[68] for example, in methanol here, largely due to significantly lower H_2 solubility in water.[69,70] Two potential work-arounds that can be envisioned in the context of biomedical applications are 1) the use of high-pressure hyperpolarizers[71] to increase the concentration of pH_2 in aqueous solutions or 2) the dilution of alcoholic solutions (e.g., based on ethanol) with a biocompatible buffer followed by in vivo injection, because the ^{15}N T_1 value is nearly 10 minutes in vitro and therefore the slow injection of larger volumes over several minutes may be feasible in the context of future in-human applications.

Conclusion

We have demonstrated in this report the ^{15}N SABRE-SHEATH hyperpolarization of [$^{15}N_3$]metronidazole. Efficient hyperpolarization ($P_{15N} \approx 16\%$) of the $^{15}NO_2$ group is accomplished by spin relays created by the network of ^{15}N spins in the molecular structure of [$^{15}N_3$]metronidazole. In this process, the parahydrogen-derived hyperpolarization of iridium hydrides is transferred over up to six chemical bonds. The high level of nuclear spin polarization P_{15N} of around 16% is achieved in about 1 minute on all three ^{15}N sites of [$^{15}N_3$]metronidazole at concentrations up to approximately 41 mM. The HP state of the $^{15}NO_2$ group has a long lifetime in vitro with an exponential decay constant T_1 of 9.7 ± 1.0 minutes at the clinically relevant magnetic field of 1.4 T. Such a long lifetime of the HP state is possible as a result of the low gyromagnetic ratio of the ^{15}N nucleus, and in part because the ^{15}N spin of the $^{15}NO_2$ group in metronidazole has no detectable spin–spin couplings with any of the protons in the molecule. We have also reported herein on the novel robust synthesis of [$^{15}N_2$]metronidazole (see the Experimental Section) and [$^{15}N_3$]metronidazole compounds in a yield of 15% over three steps. This synthetic approach employs inexpensive sources of ^{15}N label ($^{15}NH_4Cl$ and $Na^{15}NO_3$) and can be potentially tailored for the ^{15}N enrichment of other nitroimidazole derivatives, for example, FDA-approved nimorazole.

Experimental Section

General: The details of the experimental setup (Scheme 2) employed for the studies reported herein have been described previously.[42,68] All synthetic and spectral characterization details relating to the preparation of [$^{15}N_2$]metronidazole and [$^{15}N_3$]metronidazole are provided in the Supporting Information.

SABRE-SHEATH hyperpolarization: The solutions for SABRE hyperpolarization were prepared with a 1:20 catalyst/substrate ratio. A

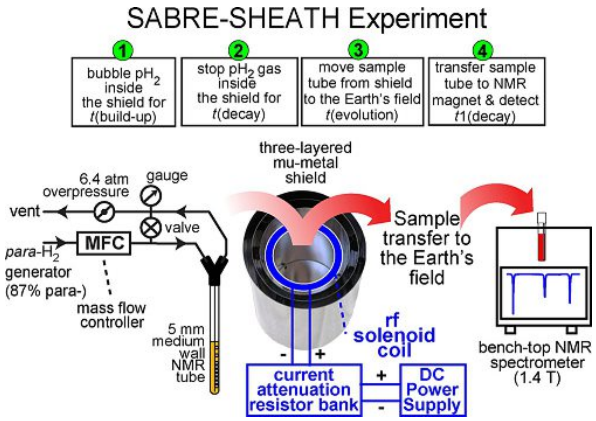

Scheme 2. Schematic of the experimental setup employed for the SABRE-SHEATH experiments.

known mass of [$^{15}N_3$]metronidazole was placed in a plastic Eppendorf tube and a 1 mM solution of the Ir-IMes catalyst in [D_4]MeOH (0.6 mL) was added to yield a 20 mM concentration of [$^{15}N_3$]metronidazole. The mixture was flushed with ultrapure argon gas immediately after preparation. Each solution prepared in this manner was used for SABRE activation and SABRE-SHEATH hyperpolarization experiments typically within 2 h of its initial formulation.

The Ir-IMes catalyst precursor[39] was synthesized according to our previously published protocol.[72] The catalyst was activated by pH_2 bubbling for approximately 1 h to achieve maximum performance.

Each sample was placed in a medium-walled 5 mm NMR tube (0.6 mL aliquot) and connected to the SABRE hyperpolarization setup, which has been described in detail previously.[34,35,42] NMR spectra were recorded by using a 1.4 T benchtop NMR spectrometer (NMR Pro 60, Nanalysis, Canada) with a flow rate of 50 sccm (standard cubic centimeters per minute, the flow rate was controlled by a mass flow controller) and a 6.4 atm overpressure of pH_2 gas in the NMR tube at room temperature (ca. 20–22 °C; Scheme 2). The thermally polarized reference spectrum of neat [^{15}N]pyridine was recorded by ^{15}N NMR spectroscopy with proton decoupling, whereas all ^{15}N NMR spectra of HP [$^{15}N_3$]metronidazole were recorded under conditions without proton decoupling.

The duration of pH_2 bubbling in the shield was about 1 min (unless otherwise noted), and the durations of t(decay) (< 1 s), t(evolution) (ca. 1–2 s), and sample depolarization in the 1.4 T NMR spectrometer, $t1$(decay) (ca. 1–2 s) were kept to a minimum to reduce ^{15}N polarization losses (Figure 1 c). Varying the durations of pH_2 bubbling [t(buildup)], the polarization decay in the shield after cessation of pH_2 bubbling [t(decay)], the evolution of polarization in the Earth's magnetic field [t(evolution)], and sample depolarization in the 1.4 T NMR spectrometer [$t1$(decay)] shown in Scheme 2 allowed for systematic mapping of the SABRE-SHEATH process and the spin dynamics of ^{15}N polarization shown in Figure 2 b,e,c,f, respectively. Systematic mapping of the static magnetic field inside the shield (using a variable resistor bank and dc power supply (GW INSTEK, GPRS series), Scheme 2) is shown in Figure 2 a.

Some samples were heated to approximately 55 °C to evaporate [D_4]MeOH to increase the concentration of [$^{15}N_3$]metronidazole for the experiments summarized in Figure 2 d.

Preparation of parahydrogen: Parahydrogen (pH_2) enrichment was performed by using a home-made parahydrogen generator equipped with a SunPower cryocooler. The pH_2 fraction was determined by ^1H NMR spectroscopy as discussed previously.[10] Briefly, the signal of orthohydrogen in "normal" hydrogen gas (consisting of 75% *ortho* and 25% *para* states) was employed as a signal reference. The orthohydrogen fraction/percentage signal from the pH_2-enriched mixture was determined next (by using a signal reference obtained from "normal" hydrogen gas)and the fraction/percentage of pH_2 was determined as the difference between 100% and the percentage of detected orthohydrogen. The NMR spectra of normal (25% pH_2) and pH_2-enriched mixtures are shown in Figure S1 in the Supporting Information. The NMR spectra of several samples were recorded (for reproducibility) and a variability of less than 2% was achieved.

Acknowledgements

This work was supported by the NSF under grants CHE-1836308 (E.Y.C.) and CHE-1416432 (B.M.G.), NIH R21CA220137 (E.Y.C., B.M.G.), DOD CDMRP BRP W81XWH-12-1-0159/BC112431 (E.Y.C., B.M.G., W.P.), DOD PRMRP awards W81XWH-15-1-0271 (E.Y.C.) and W81XWH-15-1-0272 (B.M.G.), and R01CA16700 (W.P.). N.V.C. and K.V.K. thank the Russian Science Foundation (Grant #17-73-20030) for their support in the synthesis of ^{15}N-labeled compounds. I.V.K. thanks the Russian Ministry of Science and Higher Education (Project AAAA-A16-116121510087-5).

Conflict of interest

The authors declare no conflict of interest.

Keywords: hyperpolarization · isotopic labeling · nitrogen heterocycles · NMR spectroscopy · SABRE · spin relays

[1] P. Nikolaou, B. M. Goodson, E. Y. Chekmenev, *Chem. Eur. J.* **2015**, *21*, 3156 – 3166.
[2] P. J. Rayner, M. J. Burns, A. M. Olaru, P. Norcott, M. Fekete, G. G. R. Green, L. A. R. Highton, R. E. Mewis, S. B. Duckett, *Proc. Natl. Acad. Sci. USA* **2017**, *114*, E3188 – E3194.
[3] B. M. Goodson, N. Whiting, A. M. Coffey, P. Nikolaou, F. Shi, B. M. Gust, M. E. Gemeinhardt, R. V. Shchepin, J. G. Skinner, J. R. Birchall, M. J. Barlow, E. Y. Chekmenev, *Emagres* **2015**, *4*, 797 – 810.
[4] M. J. Albers, R. Bok, A. P. Chen, C. H. Cunningham, M. L. Zierhut, V. Y. Zhang, S. J. Kohler, J. Tropp, R. E. Hurd, Y.-F. Yen, S. J. Nelson, D. B. Vigneron, J. Kurhanewicz, *Cancer Res.* **2008**, *68*, 8607 – 8615.
[5] J. Kurhanewicz, D. B. Vigneron, K. Brindle, E. Y. Chekmenev, A. Comment, C. H. Cunningham, R. J. DeBerardinis, G. G. Green, M. O. Leach, S. S. Rajan, R. R. Rizi, B. D. Ross, W. S. Warren, C. R. Malloy, *Neoplasia* **2011**, *13*, 81 – 97.
[6] S. J. Nelson, J. Kurhanewicz, D. B. Vigneron, P. E. Z. Larson, A. L. Harzstark, M. Ferrone, M. van Criekinge, J. W. Chang, R. Bok, I. Park, G. Reed, L. Carvajal, E. J. Small, P. Munster, V. K. Weinberg, J. H. Ardenkjaer-Larsen, A. P. Chen, R. E. Hurd, L. I. Odegardstuen, F. J. Robb, J. Tropp, J. A. Murray, *Sci. Transl. Med.* **2013**, *5*, 198ra108.
[7] K. Golman, R. in't Zandt, M. Thaning, *Proc. Natl. Acad. Sci. USA* **2006**, *103*, 11270 – 11275.
[8] S. E. Day, M. I. Kettunen, F. A. Gallagher, D. E. Hu, M. Lerche, J. Wolber, K. Golman, J. H. Ardenkjaer-Larsen, K. M. Brindle, *Nat. Med.* **2007**, *13*, 1382 – 1387.
[9] M. Merritt, C. Harrison, C. Storey, F. Jeffrey, A. Sherry, C. Malloy, *Proc. Natl. Acad. Sci. USA* **2007**, *104*, 19773 – 19777.

[10] J.-B. Hövener, A. N. Pravdivtsev, B. Kidd, C. R. Bowers, S. Glöggler, K. V. Kovtunov, M. Plaumann, R. Katz-Brull, K. Buckenmaier, A. Jerschow, F. Reineri, T. Theis, R. V. Shchepin, S. Wagner, P. Bhattacharya, N. M. Zacharias, E. Y. Chekmenev, *Angew. Chem. Int. Ed.* **2018**, *57*, 11140 – 11162; *Angew. Chem.* **2018**, *130*, 11310 – 11333.
[11] K. M. Brindle, *J. Am. Chem. Soc.* **2015**, *137*, 6418 – 6427.
[12] J. H. Ardenkjaer-Larsen, B. Fridlund, A. Gram, G. Hansson, L. Hansson, M. H. Lerche, R. Servin, M. Thaning, K. Golman, *Proc. Natl. Acad. Sci. USA* **2003**, *100*, 10158 – 10163.
[13] K. R. Keshari, D. M. Wilson, *Chem. Soc. Rev.* **2014**, *43*, 1627 – 1659.
[14] A. Comment, M. E. Merritt, *Biochemistry* **2014**, *53*, 7333 – 7357.
[15] J. H. Ardenkjaer-Larsen, *J. Magn. Reson.* **2016**, *264*, 3 – 12.
[16] J.-H. Ardenkjaer-Larsen, G. S. Boebinger, A. Comment, S. Duckett, A. S. Edison, F. Engelke, C. Griesinger, R. G. Griffin, C. Hilty, H. Maeda, G. Parigi, T. Prisner, E. Ravera, J. van Bentum, S. Vega, A. Webb, C. Luchinat, H. Schwalbe, L. Frydman, *Angew. Chem. Int. Ed.* **2015**, *54*, 9162 – 9185; *Angew. Chem.* **2015**, *127*, 9292 – 9317.
[17] R. Sarkar, A. Comment, P. R. Vasos, S. Jannin, R. Gruetter, G. Bodenhausen, H. Hall, D. Kirik, V. P. Denisov, *J. Am. Chem. Soc.* **2009**, *131*, 16014 – 16015.
[18] W. Jiang, L. Lumata, W. Chen, S. Zhang, Z. Kovacs, A. D. Sherry, C. Khemtong, *Sci. Rep.* **2015**, *5*, 9104.
[19] A. N. Pravdivtsev, A. V. Yurkovskaya, P. A. Petrov, H.-M. Vieth, K. L. Ivanov, *Appl. Magn. Reson.* **2016**, *47*, 711 – 725.
[20] H. Nonaka, R. Hata, T. Doura, T. Nishihara, K. Kumagai, M. Akakabe, M. Tsuda, K. Ichikawa, S. Sando, *Nat. Commun.* **2013**, *4*, 2411.
[21] J. McCormick, S. Korchak, S. Mamone, Y. N. Ertas, Z. Liu, L. Verlinsky, S. Wagner, S. Glöggler, L.-S. Bouchard, *Angew. Chem. Int. Ed.* **2018**, *57*, 10692 – 10696; *Angew. Chem.* **2018**, *130*, 10852 – 10856.
[22] C. Cudalbu, A. Comment, F. Kurdzesau, R. B. van Heeswijk, K. Uffmann, S. Jannin, V. Denisov, D. Kirik, R. Gruetter, *Phys. Chem. Chem. Phys.* **2010**, *12*, 5818 – 5823.
[23] M. Bonnet, C. R. Hong, W. W. Wong, L. P. Liew, A. Shome, J. Wang, Y. Gu, R. J. Stevenson, W. Qi, R. F. Anderson, F. B. Pruijn, W. R. Wilson, S. M. F. Jamieson, K. O. Hicks, M. P. Hay, *J. Med. Chem.* **2018**, *61*, 1241 – 1254.
[24] S. Kizaka-Kondoh, H. Konse-Nagasawa, *Cancer Sci.* **2009**, *100*, 1366 – 1373.
[25] K. Nepali, H.-Y. Lee, J.-P. Liou, *J. Med. Chem.* **2019**, *62*, 2851 – 2893.
[26] R. W. Adams, J. A. Aguilar, K. D. Atkinson, M. J. Cowley, P. I. P. Elliott, S. B. Duckett, G. G. R. Green, I. G. Khazal, J. Lopez-Serrano, D. C. Williamson, *Science* **2009**, *323*, 1708 – 1711.
[27] R. W. Adams, S. B. Duckett, R. A. Green, D. C. Williamson, G. G. R. Green, *J. Chem. Phys.* **2009**, *131*, 194505.
[28] K. D. Atkinson, M. J. Cowley, S. B. Duckett, P. I. P. Elliott, G. G. R. Green, J. López-Serrano, I. G. Khazal, A. C. Whitwood, *Inorg. Chem.* **2009**, *48*, 663 – 670.
[29] K. D. Atkinson, M. J. Cowley, P. I. P. Elliott, S. B. Duckett, G. G. R. Green, J. Lopez-Serrano, A. C. Whitwood, *J. Am. Chem. Soc.* **2009**, *131*, 13362 – 13368.
[30] P. J. Rayner, S. B. Duckett, *Angew. Chem. Int. Ed.* **2018**, *57*, 6742 – 6753; *Angew. Chem.* **2018**, *130*, 6854 – 6866.
[31] S. Knecht, A. N. Pravdivtsev, J.-B. Hovener, A. V. Yurkovskaya, K. L. Ivanov, *RSC Adv.* **2016**, *6*, 24470 – 24477.
[32] A. N. Pravdivtsev, A. V. Yurkovskaya, H. Zimmermann, H.-M. Vieth, K. L. Ivanov, *RSC Adv.* **2015**, *5*, 63615 – 63623.
[33] B. J. A. van Weerdenburg, S. Gloggler, N. Eshuis, A. H. J. Engwerda, J. M. M. Smits, R. de Gelder, S. Appelt, S. S. Wymenga, M. Tessari, M. C. Feiters, B. Blumich, F. P. J. T. Rutjes, *Chem. Commun.* **2013**, *49*, 7388 – 7390.
[34] T. Theis, M. L. Truong, A. M. Coffey, R. V. Shchepin, K. W. Waddell, F. Shi, B. M. Goodson, W. S. Warren, E. Y. Chekmenev, *J. Am. Chem. Soc.* **2015**, *137*, 1404 – 1407.
[35] M. L. Truong, T. Theis, A. M. Coffey, R. V. Shchepin, K. W. Waddell, F. Shi, B. M. Goodson, W. S. Warren, E. Y. Chekmenev, *J. Phys. Chem. C* **2015**, *119*, 8786 – 8797.
[36] B. E. Kidd, J. L. Gesiorski, M. E. Gemeinhardt, R. V. Shchepin, K. V. Kovtunov, I. V. Koptyug, E. Y. Chekmenev, B. M. Goodson, *J. Phys. Chem. C* **2018**, *122*, 16848 – 16852.
[37] D. A. Barskiy, R. V. Shchepin, A. M. Coffey, T. Theis, W. S. Warren, B. M. Goodson, E. Y. Chekmenev, *J. Am. Chem. Soc.* **2016**, *138*, 8080 – 8083.
[38] J. F. P. Colell, A. W. J. Logan, Z. Zhou, R. V. Shchepin, D. A. Barskiy, G. X. Ortiz, Q. Wang, S. J. Malcolmson, E. Y. Chekmenev, W. S. Warren, T. Theis, *J. Phys. Chem. C* **2017**, *121*, 6626 – 6634.
[39] M. J. Cowley, R. W. Adams, K. D. Atkinson, M. C. R. Cockett, S. B. Duckett, G. G. R. Green, J. A. B. Lohman, R. Kerssebaum, D. Kilgour, R. E. Mewis, *J. Am. Chem. Soc.* **2011**, *133*, 6134 – 6137.
[40] D. A. Barskiy, R. V. Shchepin, C. P. N. Tanner, J. F. P. Colell, B. M. Goodson, T. Theis, W. S. Warren, E. Y. Chekmenev, *ChemPhysChem* **2017**, *18*, 1493 – 1498.
[41] R. V. Shchepin, L. Jaigirdar, T. Theis, W. S. Warren, B. M. Goodson, E. Y. Chekmenev, *J. Phys. Chem. C* **2017**, *121*, 28425 – 28434.
[42] R. V. Shchepin, L. Jaigirdar, E. Y. Chekmenev, *J. Phys. Chem. C* **2018**, *122*, 4984 – 4996.
[43] B. Kidd, J. Mashni, M. Limbach, F. Shi, E. Y. Chekmenev, Y. Hou, B. M. Goodson, *Chem. Eur. J.* **2018**, *24*, 10641 – 10645.
[44] A. S. Kiryutin, A. V. Yurkovskaya, H. Zimmermann, H.-M. Vieth, K. L. Ivanov, *Magn. Reson. Chem.* **2018**, *56*, 651 – 662.
[45] R. V. Shchepin, M. L. Truong, T. Theis, A. M. Coffey, F. Shi, K. W. Waddell, W. S. Warren, B. M. Goodson, E. Y. Chekmenev, *J. Phys. Chem. Lett.* **2015**, *6*, 1961 – 1967.
[46] M. H. Levitt, *J. Magn. Reson.* **2016**, *262*, 91 – 99.
[47] J. Kurhanewicz, D. B. Vigneron, J. H. Ardenkjaer-Larsen, J. A. Bankson, K. Brindle, C. H. Cunningham, F. A. Gallagher, K. R. Keshari, A. Kjaer, C. Laustsen, D. A. Mankoff, M. E. Merritt, S. J. Nelson, J. M. Pauly, P. Lee, S. Ronen, D. J. Tyler, S. S. Rajan, D. M. Spielman, L. Wald, X. Zhang, C. R. Malloy, R. Rizi, *Neoplasia* **2019**, *21*, 1 – 16.
[48] R. V. Shchepin, D. A. Barskiy, A. M. Coffey, M. A. Feldman, L. M. Kovtunova, V. I. Bukhtiyarov, K. V. Kovtunov, B. M. Goodson, I. V. Koptyug, E. Y. Chekmenev, *ChemistrySelect* **2017**, *2*, 4478 – 4483.
[49] S. H. Erickson, G. L. Oppenheim, G. H. Smith, *Obstet. Gynecol.* **1981**, *57*, 48 – 50.
[50] K. V. Kovtunov, L. M. Kovtunova, M. E. Gemeinhardt, A. V. Bukhtiyarov, J. Gesiorski, V. I. Bukhtiyarov, E. Y. Chekmenev, I. V. Koptyug, B. M. Goodson, *Angew. Chem. Int. Ed.* **2017**, *56*, 10433 – 10437; *Angew. Chem.* **2017**, *129*, 10569 – 10573.
[51] J. F. P. Colell, M. Emondts, A. W. J. Logan, K. Shen, J. Bae, R. V. Shchepin, G. X. Ortiz, P. Spannring, Q. Wang, S. J. Malcolmson, E. Y. Chekmenev, M. C. Feiters, F. P. J. T. Rutjes, B. Bluemich, T. Theis, W. S. Warren, *J. Am. Chem. Soc.* **2017**, *139*, 7761 – 7767.
[52] K. Hendrickson, M. Phillips, W. Smith, L. Peterson, K. Krohn, J. Rajendran, *Radiother. Oncol.* **2011**, *101*, 369 – 375.
[53] Y. Masaki, Y. Shimizu, T. Yoshioka, Y. Tanaka, K.-i. Nishijima, S. Zhao, K. Higashino, S. Sakamoto, Y. Numata, Y. Yamaguchi, N. Tamaki, Y. Kuge, *Sci. Rep.* **2015**, *5*, 16802.
[54] J. L. Bolton, R. A. McClelland, *J. Am. Chem. Soc.* **1989**, *111*, 8172 – 8181.
[55] D. I. Hoult, R. E. Richards, *J. Magn. Reson. (1969)* **1976**, *24*, 71 – 85.
[56] A. M. Coffey, K. V. Kovtunov, D. Barskiy, I. V. Koptyug, R. V. Shchepin, K. W. Waddell, P. He, K. A. Groome, Q. A. Best, F. Shi, B. M. Goodson, E. Y. Chekmenev, *Anal. Chem.* **2014**, *86*, 9042 – 9049.
[57] J. Wang, F. Kreis, A. J. Wright, R. L. Hesketh, M. H. Levitt, K. M. Brindle, *Magn. Reson. Med.* **2018**, *79*, 741 – 747.
[58] M. L. Truong, A. M. Coffey, R. V. Shchepin, K. W. Waddell, E. Y. Chekmenev, *Contrast Media Mol. Imaging* **2014**, *9*, 333 – 341.
[59] M. Mishkovsky, T. Cheng, A. Comment, R. Gruetter, *Magn. Reson. Med.* **2012**, *68*, 349 – 352.
[60] J. A. Pfeilsticker, J. E. Ollerenshaw, V. A. Norton, D. P. Weitekamp, *J. Magn. Reson.* **2010**, *205*, 125 – 129.
[61] V. A. Norton, D. P. Weitekamp, *J. Chem. Phys.* **2011**, *135*, 141107.
[62] G. A. Morris, R. Freeman, *J. Am. Chem. Soc.* **1979**, *101*, 760 – 762.
[63] D. I. Hoult, P. C. Lauterbur, *J. Magn. Reson.(1969)* **1979**, *34*, 425 – 433.
[64] H. Zeng, J. Xu, M. T. McMahon, J. A. B. Lohman, P. C. M. van Zijl, *J. Magn. Reson.* **2014**, *246*, 119 – 121.
[65] J.-B. Hövener, N. Schwaderlapp, R. Borowiak, T. Lickert, S. B. Duckett, R. E. Mewis, R. W. Adams, M. J. Burns, L. A. R. Highton, G. G. R. Green, A. Olaru, J. Hennig, D. von Elverfeldt, *Anal. Chem.* **2014**, *86*, 1767 – 1774.
[66] R. V. Shchepin, D. A. Barskiy, A. M. Coffey, T. Theis, F. Shi, W. S. Warren, B. M. Goodson, E. Y. Chekmenev, *ACS Sens.* **2016**, *1*, 640 – 644.
[67] P. Spannring, I. Reile, M. Emondts, P. P. M. Schleker, N. K. J. Hermkens, N. G. J. van der Zwaluw, B. J. A. van Weerdenburg, P. Tinnemans, M. Tessari, B. Blümich, F. P. J. T. Rutjes, M. C. Feiters, *Chem. Eur. J.* **2016**, *22*, 9277 – 9282.

[68] M. L. Truong, F. Shi, P. He, B. Yuan, K. N. Plunkett, A. M. Coffey, R. V. Shchepin, D. A. Barskiy, K. V. Kovtunov, I. V. Koptyug, K. W. Waddell, B. M. Goodson, E. Y. Chekmenev, *J. Phys. Chem. B* **2014**, *118*, 13882 – 13889.
[69] M. Herskowitz, J. Wisniak, L. Skladman, *J. Chem. Eng. Data* **1983**, *28*, 164 – 166.
[70] Purwanto, R. M. Deshpande, R. V. Chaudhari, H. Delmas, *J. Chem. Eng. Data* **1996**, *41*, 1414 – 1417.
[71] A. M. Coffey, R. V. Shchepin, B. Feng, R. D. Colon, K. Wilkens, K. W. Waddell, E. Y. Chekmenev, *J. Magn. Reson.* **2017**, *284*, 115 – 124.
[72] D. A. Barskiy, K. V. Kovtunov, I. V. Koptyug, P. He, K. A. Groome, Q. A. Best, F. Shi, B. M. Goodson, R. V. Shchepin, A. M. Coffey, K. W. Waddell, E. Y. Chekmenev, *J. Am. Chem. Soc.* **2014**, *136*, 3322 – 3325.

Manuscript received: March 13, 2019
Revised manuscript received: April 4, 2019
Accepted manuscript online: April 9, 2019
Version of record online: May 30, 2019

analytical chemistry

Article

Cite This: Anal. Chem. 2019, 91, 4741−4746

pubs.acs.org/ac

Clinical-Scale Batch-Mode Production of Hyperpolarized Propane Gas for MRI

Oleg G. Salnikov,[†,‡] Panayiotis Nikolaou,[§] Nuwandi M. Ariyasingha,[∥] Kirill V. Kovtunov,[†,‡] Igor V. Koptyug,[†,‡] and Eduard Y. Chekmenev*[,∥,⊥]

[†]International Tomography Center, SB RAS, 3A Institutskaya St., Novosibirsk 630090, Russia

[‡]Novosibirsk State University, 2 Pirogova St., Novosibirsk 630090, Russia

[§]Department of Radiology, Vanderbilt University Institute of Imaging Science (VUIIS), Nashville, Tennessee 37232-2310, United States

[∥]Department of Chemistry, Integrative Biosciences (Ibio), Wayne State University, Karmanos Cancer Institute (KCI), Detroit, Michigan 48202, United States

[⊥]Russian Academy of Sciences, Leninskiy Prospekt 14, Moscow 119991, Russia

Supporting Information

ABSTRACT: NMR spectroscopy and imaging (MRI) are two of the most important methods to study structure, function, and dynamics from atom to organism scale. NMR approaches often suffer from an insufficient sensitivity, which, however, can be transiently boosted using hyperpolarization techniques. One of these techniques is parahydrogen-induced polarization, which has been used to produce catalyst-free hyperpolarized propane gas with proton polarization that is 3 orders of magnitude greater than equilibrium thermal polarization at a 1.5 T field of a clinical MRI scanner. Here we show that more than 0.3 L of hyperpolarized propane gas can be produced in 2 s. This production rate is more than an order of magnitude greater than that demonstrated previously, and the reported production rate is comparable to that employed for in-human MRI using HP noble gas (e.g., ^{129}Xe) produced via a spin exchange optical pumping (SEOP) hyperpolarization technique. We show that high polarization values can be retained despite the significant increase in the production rate of hyperpolarized propane. The enhanced signals of produced hyperpolarized propane gas were revealed by stopped-flow MRI visualization at 4.7 T. Achieving this high production rate enables the future use of this compound (already approved for unlimited use in foods by the corresponding regulating agencies, e.g., FDA in the USA, and more broadly as an E944 food additive) as a new inhalable contrast agent for diagnostic detection via MRI.

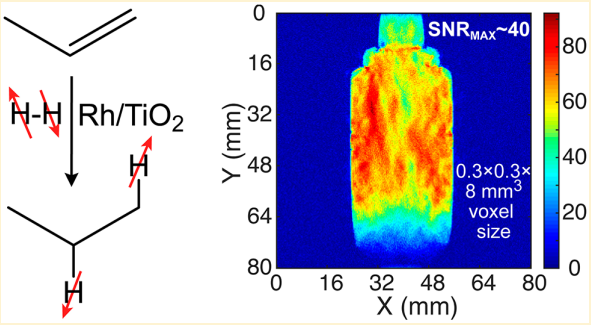

NMR spectroscopy and imaging (MRI) are versatile tools widely employed to study structure, function, and dynamics. NMR signal intensity is directly proportional to nuclear spin polarization P, which characterizes the degree of nuclear spin alignment with applied static magnetic field. In practice, P is on the order of 10^{-5} to 10^{-6} under thermal equilibrium conditions of 298 K and a magnetic field of several Tesla. For example, P is 1.0×10^{-5} for ^{1}H and 2.6×10^{-6} for ^{13}C nuclei at room temperature and 3 T, the magnetic field of a modern MRI scanner. Hyperpolarization techniques can transiently increase P up to unity, which leads to the temporary increase of magnetic resonance (MR) sensitivity by 4−5 orders of magnitude.[1,2] The additional and largely unrealized benefit of hyperpolarization is the fundamental possibility to obtain a higher signal-to-noise ratio at low (0.01−0.5 T) magnetic fields.[3] The main drivers behind the development of hyperpolarization techniques are their biomedical applications.[1,4−6] The inhalation or injection of hyperpolarized (HP) contrast agents enabled functional and metabolic imaging of lung disease, cancer, and others.[7−12]

Biomedical applications demand a sufficiently long lifetime of HP compounds.[5,11,13] The decay of the HP state is typically governed by the process of spin−lattice relaxation characterized by the T_1 constant. Since in a condensed phase, low-gamma nuclei, such as ^{13}C and ^{129}Xe, typically have greater T_1 than those of protons, the development of HP contrast agents have primarily employed these low-gamma nuclei.[5,14,15] This approach has a significant translational challenge because conventional clinical MRI scanners can only image protons, and therefore, ^{13}C/^{129}Xe-based contrast agents require highly specialized hardware and software, which are available to selected research sites around the globe. The unique properties

Received: January 15, 2019
Accepted: March 11, 2019
Published: March 11, 2019

DOI: 10.1021/acs.analchem.9b00259
Anal. Chem. 2019, 91, 4741−4746

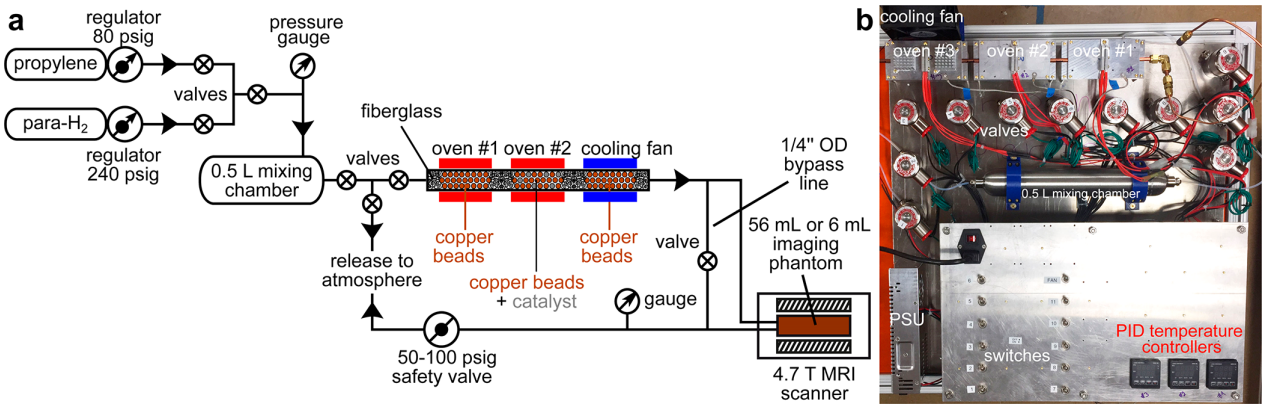

Figure 1. (a) Schematic of the experimental setup for batch-mode production and MRI detection of hyperpolarized propane gas. (b) Photograph of the constructed batch-mode propane hyperpolarizer.

of the long-lived spin states (LLSS), sometimes also termed as long-lived states (LLS), recently explored by Levitt and others, allow for preparing HP states with the exponential decay constant T_S, which can significantly exceed the T_1 constant.[16−19] As a result of this fundamental breakthrough, the interest in the use of HP protons sites has been rekindled[20−25] because the lifetime of the HP state can be sufficiently long, and such HP states can be readily imaged on conventional clinical MRI scanners.[26−29]

HP propane gas can be readily prepared through the process of parahydrogen-induced polarization (PHIP)[30−33] via para-hydrogen (p-H_2) addition to propylene over supported metal catalysts.[34−37] Previously, we have demonstrated the existence of LLSS in propane gas at a 0.05 T magnetic field with the T_S value approximately three times greater than the corresponding T_1 value. T_S exceeding 13 s has been demonstrated at a high pressure, although T_S is ∼3 s at atmospheric pressure.[38] Nevertheless, the extension of HP propane lifetime through LLSS increases the time window sufficiently for potential use as an inhalable contrast agent in a manner similar to that of HP noble gases, e.g., ^{129}Xe and ^{3}He.[10]

In this work, we show that the clinically relevant quantity (∼0.3 standard liters)[39−44] of HP propane gas can be produced in approximately 2 s, i.e., sufficiently fast to retain its hyperpolarized state. We demonstrate the utility of large-scale preparation of HP propane via MR imaging at 4.7 T. High-resolution slice-selective 2D MR imaging of stopped HP propane is reported here.

MATERIALS AND METHODS

We have developed a clinical-scale propane polarizer device (Figure 1) for hydrogenation of propylene with p-H_2 over a heterogeneous catalyst to produce HP propane gas. The core of the polarizer was comprised of 1/4 in. OD copper tubing, which was divided into three zones. The first zone was filled with Cu beads (10−40 mesh size, > 99.90% purity, Sigma-Aldrich #311405, approximately 12 g filled in a 10 cm-long section) and was employed for preheating the reagents using oven #1 (see Figure 1). The second zone was filled with ∼12 g of copper beads and a small quantity (60−280 mg) of 1 wt % Rh/TiO_2 catalyst. This type of Rh/TiO_2 catalyst was tested in previous studies.[36,38] The Cu particles provided a significantly more efficient dissipation of heat generated during the highly exothermic hydrogenation reaction, because the released heat was first absorbed by the Cu beads and then dissipated through the copper reactor tube by the plates and radiators. The second zone was heated with oven #2 and used for production of HP propane gas by the pairwise addition of p-H_2 to propylene over the heterogeneous Rh catalyst.[26] The third zone was filled with ∼12 g of copper particles and employed for cooling the HP gas exiting the polarizer using a cooling fan (see Figure 1). The third zone was also additionally equipped with oven #3, which could be used to adjust the temperature of the exiting gas. The zones of the reactor were separated by small quantities of glass wool. The reactor tube was sandwiched by ovens #1−3, which were comprised of aluminum plates with attached cartridge heaters and radiators. The temperature of all three zones was independently controlled by three PID controllers (Figure 1b,c). In most of our experiments, the observed temperature fluctuations measured by the thermocouples attached to aluminum plates did not exceed 5 °C from the set point values. The output of the polarizer was connected via 1/16 in. OD (1/32 in. ID) Teflon tubing for low-flow conditions (2000 standard cubic centimeters (sccm) or less) or 1/8 in. OD (1/16 in. ID) Teflon tubing for high-flow conditions to a 5 mm NMR tube via a Y-connector as described previously[45] or to an imaging phantom located inside the NMR spectrometer or the MRI scanner, respectively. The HP gas left the setup via the safety valve (Figure 1a).

RESULTS AND DISCUSSION

First, the constructed propane hyperpolarizer was operated in a continuous flow regime by mixing the reagents in real time using two mass flow controllers (MFCs, one for propylene and the other one for ∼81% p-H_2). The details of such a setup have been described previously[46] and are also presented in the Supporting Information (SI, see Figure S2). The continuous flow operation allows for recording ALTADENA[32] NMR spectra of HP propane gas in real time (Figure 2a), although T_1 relaxation losses are significant at very low flow conditions (e.g., 800 sccm or less, see Figure 2e). This mode of operation enabled a relatively low-flow regime (below 1440 sccm total flow rate) to confirm that sufficient levels of polarization enhancement were indeed achieved at a lower production rate, Figure 2a (P_H ∼ 0.58%) and Figure 2b (P_H ∼ 1.8%). More importantly, this mode of operation allows for monitoring the dynamics of the polarization production of HP propane. Figure

DOI: 10.1021/acs.analchem.9b00259
Anal. Chem. 2019, 91, 4741−4746

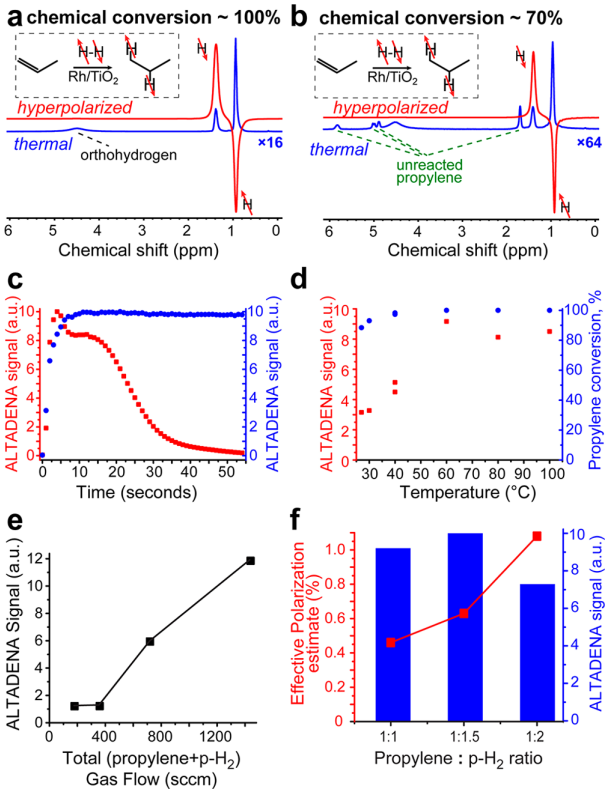

Figure 2. (a) ALTADENA ^{1}H NMR spectrum of continuously flowing HP propane gas and the corresponding thermal ^{1}H NMR spectrum acquired after interruption of gas flow (the thermal spectrum is multiplied by a factor of 16) under conditions of complete chemical conversion: catalyst mass = 280 mg; t = 130 °C; pressure = 90 psig; gas flow rates, 480 sccm for propylene and 960 sccm for p-H_2; signal enhancement ~180, and P_{1H} ~0.58%. (b) ALTADENA ^{1}H NMR spectrum of continuously flowing HP propane gas and the corresponding thermal ^{1}H NMR spectrum acquired after interruption of gas flow (the thermal spectrum is multiplied by a factor of 64) under conditions of partial (~70%) chemical conversion. Conditions: catalyst mass = 118 mg; t = 100 °C; pressure = 90 psig; and gas flow rates, 480 sccm for propylene and 960 sccm for p-H_2. The catalyst was extensively treated with cyclopropane before this test (see main text for details), with a signal enhancement of ~550, and P_{1H} = 1.8%. The insets in displays (a) and (b) show the reaction scheme of the pairwise addition of parahydrogen to propylene to form hyperpolarized propane. (c) Dependence of ALTADENA signal of the CH_2 group of HP propane obtained in batch mode (red squares) and in continuous flow mode (blue circles) on time on stream. Conditions for batch mode: propylene/p-H_2 ratio = 1:1.5, catalyst mass = 118 mg, and t = 100 °C. Conditions for continuous flow mode: catalyst mass = 118 mg; t = 120 °C; pressure = 90 psig; and gas flow rates, 480 sccm for propylene and 960 sccm for p-H_2. The plots are presented on different scales with the maximum ALTADENA signal in each set of experiments calibrated as 10 au (d) Dependence of ALTADENA signal of the CH_2 group of HP propane (red squares) and propylene conversion (blue circles) on reaction temperatures obtained in batch-mode propane hyperpolarization. Conditions: propylene/p-H_2 ratio = 1:1.5; catalyst mass = 118 mg; and average gas flow rate ~4000 sccm. (e) The dependence of the PHIP signal of HP propane on the gas flow in continuous-flow operation mode. Conditions: propylene/p-H_2 ratio = 1:2; catalyst mass = 118 mg; t = 100 °C; pressure = 90 psig; and chemical conversion was ~100% in all cases. (f) The dependence of HP propane effective polarization estimates on the propane:p-H_2 ratio using batch-mode production. Conditions: catalyst mass = 118 mg, and t = 100 °C. All data were acquired using a 9.4 T NMR spectrometer. Note, that the display (f) has dual axes of ALTADENA signal (in arbitrary units, a.u.), which has been employed to compute the effective polarization estimate via signal referencing to the thermally polarized signal.

2c (blue trace) shows that the reactor performs robustly delivering a constant level of polarization. Note, that the plateau is established in less than 10 s of gas flow.

The experiments at continuous flow conditions employing NMR detection at a 9.4 T NMR spectrometer (Figure 2a) revealed nearly complete chemical conversion of the reaction mixtures at temperatures as low as 40 °C (Figure 2d), with the maximum signal enhancement observed in the 60−100 °C range. Operation at this relatively low temperature regime is welcome in the context of biomedical applications.

In some cases, the reactor was treated with a cyclopropane gas stream,[46] which boosted polarization values (see Figures S3 and S4 for details), which we hypothesize is due to passivation of active catalytic sites, because cyclopropane is less amenable to hydrogenation than propane and, therefore, may potentially be retained by the active catalytic sites. The excessive treatment with cyclopropane leads to a decrease of propylene conversion to propane (from 100 to 70%), but the proton polarization levels are significantly increased to nearly 2% (Figure 2b).

Next, the polarizer was operated in a batch mode (see Figure S1 for experimental setup). In this case, the gases are mixed in the 0.5 L mixing chamber at 100 psig (7.8 atm) pressure, resulting in a total volume of 3.9 standard liters. Next, the valves connecting the mixing chamber and oven #1 are opened, enabling the gas flow through the reactor (during the gas flow, the pressure drops from 100 psig down to 50 psig, controlled by a safety valve located at the end of the lines). Note, that operation in a batch mode results in a significantly higher and varying gas flow rate (the average flow rate is ~4000 sccm). In principle, a high-flow regime (over 2000 sccm) would minimize the T_1 relaxation losses of HP propane during transportation from the polarizer to the NMR spectrometer. However, the detection efficiency of HP gas in this case is lower because the high velocity of HP gas in the NMR tube results in a situation when only a small fraction of HP propane gas can be detected after radio frequency (RF) pulse excitation as the RF-excited gas readily leaves the detection region of the NMR probe during signal acquisition. Nevertheless, it was still possible to detect HP propane gas, and Figure 2c (red trace) provides an example of the polarization dynamics monitoring using the batch mode of operation. In this operation mode, we noted an initial bump in the HP signal, which we attribute to a temporary NMR tube overpressurization. Next, the HP signal plateau is established, which is followed by the decay of the HP signal due to the decreasing flow rate, which results in polarization losses during gas transfer from the reactor to the NMR detector.

The obtained NMR signals of the HP propane exhibited an expected dependence on the propylene/p-H_2 ratio in the reactants mixture (Figure 2f). On one hand, the use of a higher fraction of p-H_2 results in dilution of the formed HP propane with the excess of p-H_2 gas, thus lowering the observed NMR signal of the HP propane. On the other hand, a larger fraction of p-H_2 also leads to a higher NMR signal enhancement, as was shown in the previous studies.[36] The maximum ALTADENA

DOI: 10.1021/acs.analchem.9b00259
Anal. Chem. 2019, 91, 4741−4746

signal of the HP propane was obtained at an 1:1.5 ratio of propylene and p-H_2 in the reactants mixture. Unfortunately, it is difficult to reliably estimate the polarization of the HP propane obtained in the batch mode (using this setup) due to complicated dynamics of the performance of the polarizer setup (Figure 2c, red squares), in particular, due to changing the gas flow and probable temporary overpressurization. We expect propane polarization to be on the order of ∼0.5−1% (and therefore, effective polarization level estimates are reported in Figure 2f), based on the results obtained in the continuous flow mode, which were carried out using the maximum PHIP signals in dynamic profiles, like the one presented in Figure 2c, and NMR signals of stopped propane gas as PHIP and thermal reference signals, respectively. These computations of % polarization yielded ∼0.5−1.1% effective polarization values (i.e., the values detected in the NMR spectrometer under continuous flow conditions) depending on the reaction conditions (gas mixture composition and reaction temperature, Figure 2f). We note, that these values may be ∼1.2−1.5 times overestimated due to overpressurization (i.e., transient pressure bump) during gas flow. However, on the other hand, the reported effective polarization values may also be underestimated due to lower efficiency of NMR detection of rapidly flowing gas (versus stopped gas yielding a thermally polarized reference signal). These two effects (under- and overestimation) likely partially cancel each other. Therefore, we expect that the actual polarization should be very close to (likely within 30%) the effective polarization estimate reported in Figure 2f.

Next, the experimental setup was modified, and 1/16 in. OD tubing connecting the reactor with the 5 mm NMR tube was replaced by 1/8 in. OD tubing with a four times greater cross-section to enable significantly higher flow rates of up to approximately 18 standard liters per minute (sLm) of the gas volume. The use of the bypass line (Figures 1, S1, and S2) serves two purposes in our setup. First, it allows to stop the gas flow through the NMR tube in the continuous flow mode as needed (e.g., to acquire thermal NMR spectra, Figure 2a,b). Second, the bypass valve allows to significantly reduce the gas flow through the NMR tube in the batch mode operation (which otherwise generates very high gas velocities exceeding 2 sLm incompatible with quantitative NMR detection). Figure 3a shows the NMR spectra of thermally polarized propane after production at a high flow rate (∼6.1 sLm), confirming the complete conversion of propylene to propane. No propylene NMR peaks were detected, and note the simulation (green trace, Figure 3a) assigned all experimental spectral features (blue trace, Figure 3a) to the reaction product propane. Figure 3b shows the NMR spectrum of the HP propane obtained under flow conditions using batch-mode production. The spectra shown in Figure 3 were acquired using an 1.4 T benchtop NMR spectrometer.

We demonstrate the utility of the batch-mode production approach of the HP propane gas for high-resolution MR imaging on the example of the HP propane production using the setup presented in Figure 1a at an average flow rate of ∼18 sLm using an 1:2 mixture of propylene with p-H_2, yielding a mixture of HP propane:residual p-H_2 of 1:1 (Figure 4). Approximately 0.6 sL of final mixture was produced in about 2 s, corresponding to the production of 0.3 sL of HP propane. Approximately 2/3 of the HP gas mixture was collected in an ∼56 mL plastic vessel pressurized to ∼7 atm of total pressure, corresponding to ∼0.2 sL of HP propane retained in this vessel. MR imaging was started before the HP gas flow was stopped. As a result, the first image shown in each series of coronal (Figure 4a) and axial (Figure 4b) projections has significant distortions due to fast flowing gas. Once the gas is stopped, high-resolution and high signal-to-noise ratio (SNR) images were acquired every 1.9 s (Figure 4a, SNR_{MAX} of 40) or every 0.85 s (Figure 4b, SNR_{MAX} > 60), respectively. The shape of the object is very well delineated in these images. Moreover, the 1.6 mm ID tubing filled with HP propane gas is also well delineated in the axial images (Figure 4b). No signal was detected after the decay of the HP state (image #11, Figure 4a). The corresponding image of a neat water phantom using thermal proton polarization revealed an image with a maximum SNR value (SNR_{MAX}) of ∼128 (Figure S5).

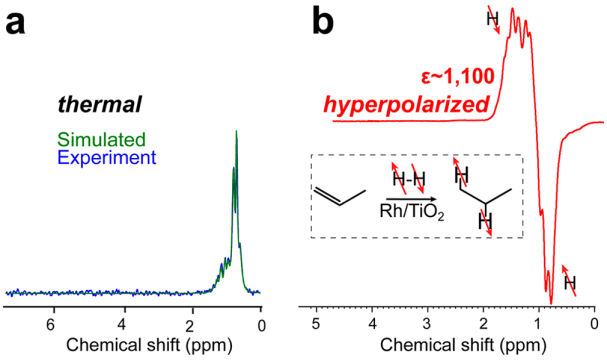

Figure 3. Proton NMR spectroscopy using an 1.4 T benchtop NMR spectrometer of (a) thermally polarized reaction gas mixtures after passing through a reactor filled with 118 mg of Rh/TiO_2 catalyst after cyclopropane treatment. Note, that all NMR peaks are attributed to propane product. (b) HP propane after passing through a reactor filled with 120 mg of unaltered Rh/TiO_2, with a signal enhancement of $\varepsilon \sim 1100$ corresponding to 0.5% polarization at 1.4 T. Other experimental conditions employed for spectra acquisition in displays (a) and (b) are t = 40 °C, 20% excess of p-H_2 over propylene, ∼6 sLm flow rate, and ∼4 atm total pressure.

CONCLUSION

We have demonstrated clinical-scale production of catalyst-free HP propane gas using a PHIP technique of up to 0.3 sL in 2 s. Complete (∼100%) chemical conversion of propylene substrate was achieved during its hydrogenation with para-hydrogen over the Rh/TiO_2 catalyst. The heterogeneous catalyst is robust and can be repeatedly used numerous times. We have not seen a significant catalyst deactivation after producing more than 100 sL of HP propane using propylene and p-H_2 as substrates. The produced HP propane dose is similar to that of HP ^{129}Xe produced by a spin exchange optical pumping (SEOP) technique,[47] which has been employed for in-human MRI.[10,48,49] For example, previous studies have employed 0.3−0.5 sL of HP ^{129}Xe.[39−44] Therefore, we expect that the presented approach can be potentially suitable for pulmonary imaging in large animals and humans. We note, that, although the nominal polarization values obtained here are on the order of 1−2% (versus more than 40% achieved by ^{129}Xe SEOP[50−55]), the HP propane molecule carries two HP nuclei versus one in HP noble gases. More importantly, protons have a higher gyromagnetic ratio and higher detection frequency resulting in a significantly more sensitive detection, that is at least several-fold greater than that of HP ^{129}Xe.[56] Therefore, in vivo MRI imaging of HP propane even at these

DOI: 10.1021/acs.analchem.9b00259
Anal. Chem. 2019, 91, 4741−4746

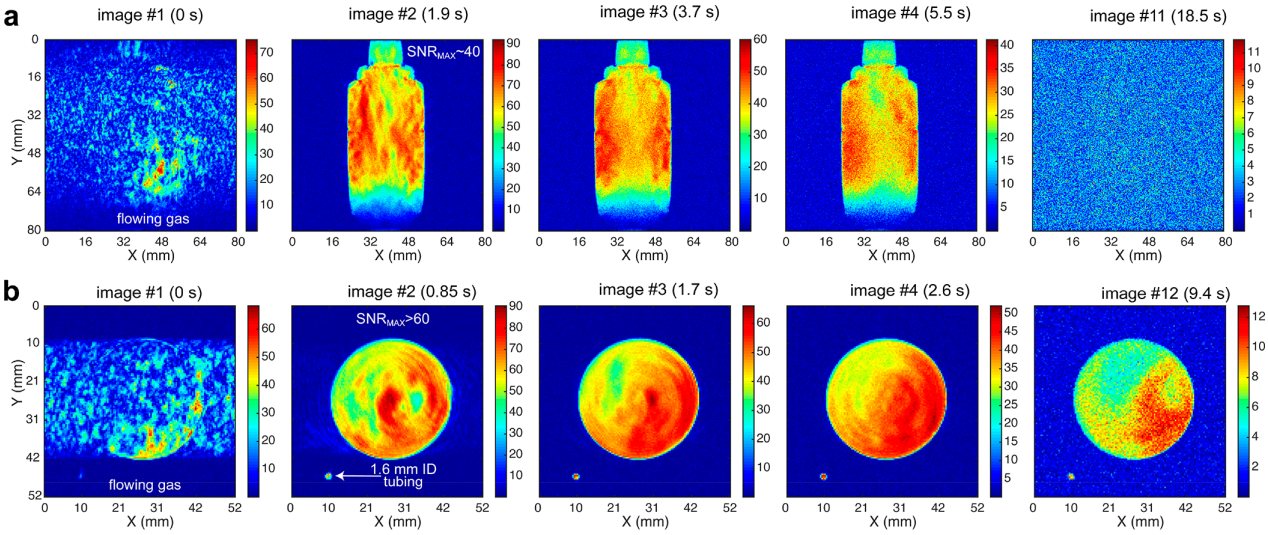

Figure 4. (a) 2D MRI of ~0.2 standard liters of HP propane gas in an ~56 mL collection container after production of an ~0.3-standard-liter (sL) batch of HP propane in ~2 s using an 1:2 mixture of propylene with p-H_2. These 2D slices were acquired on a 4.7 T MRI instrument with the following imaging parameters: 2D gradient echo (GRE) images were acquired every ~1.85 s/slice, with 256 × 256 matrix with a repetition time (TR) of ~7.2 ms, and slice thickness = 8 mm; field of view = 80 × 80 mm^2; pixel size (spatial resolution) of ~0.3 × 0.3 mm^2; and voxel size of ~78 μL. (b) Similar 2D acquisition (axial projection): ~0.85 s/slice; 128 × 128 matrix with TR ~6.6 ms; and slice thickness = 12 mm; field of view = 52 × 52 mm^2; pixel size (spatial resolution) ~0.4 × 0.4 mm^2; and voxel size ~200 μL. HP propane was produced using the following reaction conditions: batch-mode; propylene/p-H_2 ratio = 1:2; catalyst mass = 280 mg; and t = 100 °C.

polarization levels may be potentially feasible. Furthermore, we hope that the future development of novel catalysts in heterogeneous PHIP[57] may yield additional significant increase in attainable nuclear polarization in HP propane.

Since propane is already regulated by the FDA in the US with unlimited use in the food industry under good manufacturing practice (GMP), we envision a straightforward regulatory approval for HP propane use as an inhalable contrast agent. We note, however, that propane is a flammable gas, and this fact implies rather strict safety regulations for use with humans. High-resolution 2D MR images of stopped HP propane (~0.2 sL batch in an ~56 mL container) gas were obtained at 4.7 T, the field at which the LLSS no longer exist in HP propane,[26] and therefore, the relaxation is governed by T_1. We expect an approximately 3-fold greater lifetime of the HP propane state in a low (<0.4 T) magnetic field, where the LLSS is retained, and the relaxation process is governed by T_S,[38] and therefore, a longer time window will be available for gas administration and imaging. Moreover, other developments in the preparation of longer-lived HP propane states and storage, e.g., through the use of cyclopropane as a precursor[46] and longer lifetime in the dissolved phase,[58] may potentially additionally significantly increase the time window for manipulation with a batch of produced HP propane.

■ ASSOCIATED CONTENT

Ⓢ Supporting Information

The Supporting Information is available free of charge on the ACS Publications website at DOI: 10.1021/acs.analchem.9b00259.

Figures of experimental setup and additional NMR spectra (PDF)

■ AUTHOR INFORMATION

Corresponding Author

*E-mail: chekmenev@wayne.edu.

ORCID

Oleg G. Salnikov: 0000-0003-2266-7335
Kirill V. Kovtunov: 0000-0001-7577-9619
Igor V. Koptyug: 0000-0003-3480-7649
Eduard Y. Chekmenev: 0000-0002-8745-8801

Notes

The authors declare no competing financial interest.

■ ACKNOWLEDGMENTS

O.G.S. and K.V.K. thank the Russian Science Foundation (grant #17-73-20030) for the support of experiments with HP propane production. The ITC team thanks the Russian Ministry of Science and Higher Education (AAAA-A16-116121510087-5) for the use of NMR facilities. The US team thanks the following funding support, NSF under grants CHE-1416432 and CHE-1836308, NIH 1R21EB020323, DOD CDMRP W81XWH-15-1-0271, and RFBR 17-54-33037 OHKO_a.

■ REFERENCES

(1) Goodson, B. M.; Whiting, N.; Coffey, A. M.; Nikolaou, P.; Shi, F.; Gust, B. M.; Gemeinhardt, M. E.; Shchepin, R. V.; Skinner, J. G.; Birchall, J. R.; et al. *Emagres* **2015**, *4*, 797−810.

(2) Kovtunov, K. V.; Pokochueva, E. V.; Salnikov, O. G.; Cousin, S.; Kurzbach, D.; Vuichoud, B.; Jannin, S.; Chekmenev, E. Y.; Goodson, B. M.; Barskiy, D. A.; et al. *Chem. - Asian J.* **2018**, *13*, 1857−1871.

(3) Coffey, A. M.; Truong, M. L.; Chekmenev, E. Y. *J. Magn. Reson.* **2013**, *237*, 169−174.

(4) Hövener, J.-B.; Pravdivtsev, A. N.; Kidd, B.; Bowers, C. R.; Glöggler, S.; Kovtunov, K. V.; Plaumann, M.; Katz-Brull, R.; Buckenmaier, K.; Jerschow, A.; et al. *Angew. Chem., Int. Ed.* **2018**, *57*, 11140−11162.

DOI: 10.1021/acs.analchem.9b00259
Anal. Chem. 2019, 91, 4741−4746

(5) Kurhanewicz, J.; Vigneron, D. B.; Brindle, K.; Chekmenev, E. Y.; Comment, A.; Cunningham, C. H.; DeBerardinis, R. J.; Green, G. G.; Leach, M. O.; Rajan, S. S.; et al. *Neoplasia* **2011**, *13*, 81−97.
(6) Sriram, R.; Kurhanewicz, J.; Vigneron, D. B. Emrstm1 253. In *Emagres*; John Wiley & Sons, Ltd,, 2014; pp 311−324.
(7) Albert, M. S.; Cates, G. D.; Driehuys, B.; Happer, W.; Saam, B.; Springer, C. S.; Wishnia, A. *Nature* **1994**, *370*, 199−201.
(8) Barskiy, D. A.; Coffey, A. M.; Nikolaou, P.; Mikhaylov, D. M.; Goodson, B. M.; Branca, R. T.; Lu, G. J.; Shapiro, M. G.; Telkki, V.-V; Zhivonitko, V. V.; et al. *Chem. - Eur. J.* **2017**, *23*, 725−751.
(9) Goodson, B. M. *J. Magn. Reson.* **2002**, *155*, 157−216.
(10) Mugler, J. P.; Altes, T. A. *J. Magn. Reson. Imaging* **2013**, *37*, 313−331.
(11) Nelson, S. J.; Kurhanewicz, J.; Vigneron, D. B.; Larson, P. E. Z.; Harzstark, A. L.; Ferrone, M.; van Criekinge, M.; Chang, J. W.; Bok, R.; Park, I.; et al. *Sci. Transl. Med.* **2013**, *5*, 198ra108.
(12) Branca, R. T.; Cleveland, Z. I.; Fubara, B.; Kumar, C. S. S. R.; Maronpot, R. R.; Leuschner, C.; Warren, W. S.; Driehuys, B. *Proc. Natl. Acad. Sci. U. S. A.* **2010**, *107*, 3693−3697.
(13) Nikolaou, P.; Goodson, B. M.; Chekmenev, E. Y. *Chem. - Eur. J.* **2015**, *21*, 3156−3166.
(14) Brindle, K. M. *J. Am. Chem. Soc.* **2015**, *137*, 6418−6427.
(15) Schroder, L. *Phys. Medica* **2013**, *29*, 3−16.
(16) Carravetta, M.; Johannessen, O. G.; Levitt, M. H. *Phys. Rev. Lett.* **2004**, *92*, 153003.
(17) Carravetta, M.; Levitt, M. H. *J. Am. Chem. Soc.* **2004**, *126*, 6228−6229.
(18) Warren, W. S.; Jenista, E.; Branca, R. T.; Chen, X. *Science* **2009**, *323*, 1711−1714.
(19) Theis, T.; Ortiz, G. X.; Logan, A. W. J.; Claytor, K. E.; Feng, Y.; Huhn, W. P.; Blum, V.; Malcolmson, S. J.; Chekmenev, E. Y.; Wang, Q.; et al. *Sci. Adv.* **2016**, *2*, No. e1501438.
(20) Roy, S. S.; Rayner, P.; Norcott, P.; Green, G. G. R.; Duckett, S. B. *Phys. Chem. Chem. Phys.* **2016**, *18*, 24905−24911.
(21) Zhivonitko, V.; Kovtunov, K.; Chapovsky, P.; Koptyug, I. *Angew. Chem., Int. Ed.* **2013**, *52*, 13251−13255.
(22) Franzoni, M. B.; Buljubasich, L.; Spiess, H. W.; Munnemann, K. *J. Am. Chem. Soc.* **2012**, *134*, 10393−10396.
(23) Zhang, Y. N.; Soon, P. C.; Jerschow, A.; Canary, J. W. *Angew. Chem., Int. Ed.* **2014**, *53*, 3396−3399.
(24) Zhang, Y.; Basu, K.; Canary, J. W.; Jerschow, A. *Phys. Chem. Chem. Phys.* **2015**, *17*, 24370−24375.
(25) Zhang, Y. N.; Duan, X.; Soon, P. C.; Sychrovský, V.; Canary, J. W.; Jerschow, A. *ChemPhysChem* **2016**, *17*, 2967−2971.
(26) Kovtunov, K. V.; Barskiy, D. A.; Coffey, A. M.; Truong, M. L.; Salnikov, O. G.; Khudorozhkov, A. K.; Inozemtseva, E. A.; Prosvirin, I. P.; Bukhtiyarov, V. I.; Waddell, K. W.; et al. *Chem. - Eur. J.* **2014**, *20*, 11636−11639.
(27) Kovtunov, K. V.; Truong, M. L.; Barskiy, D. A.; Koptyug, I. V.; Coffey, A. M.; Waddell, K. W.; Chekmenev, E. Y. *Chem. - Eur. J.* **2014**, *20*, 14629−14632.
(28) Kovtunov, K. V.; Truong, M. L.; Barskiy, D. A.; Salnikov, O. G.; Bukhtiyarov, V. I.; Coffey, A. M.; Waddell, K. W.; Koptyug, I. V.; Chekmenev, E. Y. *J. Phys. Chem. C* **2014**, *118*, 28234−28243.
(29) Graafen, D.; Franzoni, M. B.; Schreiber, L. M.; Spiess, H. W.; Münnemann, K. *J. Magn. Reson.* **2016**, *262*, 68−72.
(30) Bowers, C. R.; Weitekamp, D. P. *Phys. Rev. Lett.* **1986**, *57*, 2645−2648.
(31) Bowers, C. R.; Weitekamp, D. P. *J. Am. Chem. Soc.* **1987**, *109*, 5541−5542.
(32) Pravica, M. G.; Weitekamp, D. P. *Chem. Phys. Lett.* **1988**, *145*, 255−258.
(33) Eisenschmid, T. C.; Kirss, R. U.; Deutsch, P. P.; Hommeltoft, S. I.; Eisenberg, R.; Bargon, J.; Lawler, R. G.; Balch, A. L. *J. Am. Chem. Soc.* **1987**, *109*, 8089−8091.
(34) Koptyug, I. V.; Kovtunov, K. V.; Burt, S. R.; Anwar, M. S.; Hilty, C.; Han, S. I.; Pines, A.; Sagdeev, R. Z. *J. Am. Chem. Soc.* **2007**, *129*, 5580−5586.
(35) Bouchard, L. S.; Burt, S. R.; Anwar, M. S.; Kovtunov, K. V.; Koptyug, I. V.; Pines, A. *Science* **2008**, *319*, 442−445.
(36) Barskiy, D. A.; Kovtunov, K. V.; Gerasimov, E. Y.; Phipps, M. A.; Salnikov, O. G.; Coffey, A. M.; Kovtunova, L. M.; Prosvirin, I. P.; Bukhtiyarov, V. I.; Koptyug, I. V.; et al. *J. Phys. Chem. C* **2017**, *121*, 10038−10046.
(37) Burueva, D. B.; Kovtunova, L. M.; Bukhtiyarov, V. I.; Kovtunov, K. V.; Koptyug, I. V. *Chem. - Eur. J.* **2019**, *25*, 1420−1431.
(38) Barskiy, D. A.; Salnikov, O. G.; Romanov, A. S.; Feldman, M. A.; Coffey, A. M.; Kovtunov, K. V.; Koptyug, I. V.; Chekmenev, E. Y. *J. Magn. Reson.* **2017**, *276*, 78−85.
(39) Wild, J. M.; Marshall, H.; Xu, X.; Norquay, G.; Parnell, S. R.; Clemence, M.; Griffiths, P. D.; Parra-Robles, J. *Radiology* **2013**, *267*, 251−255.
(40) Nikolaou, P.; Coffey, A. M.; Walkup, L. L.; Gust, B. M.; Whiting, N.; Newton, H.; Barcus, S.; Muradyan, I.; Dabaghyan, M.; Moroz, G. D.; et al. *Proc. Natl. Acad. Sci. U. S. A.* **2013**, *110*, 14150−14155.
(41) Nikolaou, P.; Coffey, A. M.; Walkup, L. L.; Gust, B. M.; Whiting, N. R.; Newton, H.; Muradyan, I.; Dabaghyan, M.; Ranta, K.; Moroz, G.; et al. *Magn. Reson. Imaging* **2014**, *32*, 541−550.
(42) Norquay, G.; Parnell, S. R.; Xu, X. J.; Parra-Robles, J.; Wild, J. M. *J. Appl. Phys.* **2013**, *113*, 044908.
(43) Walkup, L. L.; Woods, J. C. *NMR Biomed.* **2014**, *27*, 1429−1438.
(44) Walkup, L. L.; Thomen, R. P.; Akinyi, T. G.; Watters, E.; Ruppert, K.; Clancy, J. P.; Woods, J. C.; Cleveland, Z. I. *Pediatr. Radiol.* **2016**, *46*, 1651−1662.
(45) Truong, M. L.; Shi, F.; He, P.; Yuan, B.; Plunkett, K. N.; Coffey, A. M.; Shchepin, R. V.; Barskiy, D. A.; Kovtunov, K. V.; Koptyug, I. V.; et al. *J. Phys. Chem. B* **2014**, *118*, 13882−13889.
(46) Salnikov, O. G.; Kovtunov, K. V.; Nikolaou, P.; Kovtunova, L. M.; Bukhtiyarov, V. I.; Koptyug, I. V.; Chekmenev, E. Y. *ChemPhysChem* **2018**, *19*, 2621−2626.
(47) Walker, T. G.; Happer, W. *Rev. Mod. Phys.* **1997**, *69*, 629−642.
(48) Patz, S.; Hersman, F. W.; Muradian, I.; Hrovat, M. I.; Ruset, I. C.; Ketel, S.; Jacobson, F.; Topulos, G. P.; Hatabu, H.; Butler, J. P. *Eur. J. Radiol.* **2007**, *64*, 335−344.
(49) Kaushik, S. S.; Cleveland, Z. I.; Cofer, G. P.; Metz, G.; Beaver, D.; Nouls, J.; Kraft, M.; Auffermann, W.; Wolber, J.; McAdams, H. P.; et al. *Magn. Reson. Med.* **2011**, *65*, 1154−1165.
(50) Zook, A. L.; Adhyaru, B. B.; Bowers, C. R. *J. Magn. Reson.* **2002**, *159*, 175−182.
(51) Freeman, M. S.; Emami, K.; Driehuys, B. *Phys. Rev. A: At., Mol., Opt. Phys.* **2014**, *90*, 023406.
(52) Nikolaou, P.; Coffey, A. M.; Ranta, K.; Walkup, L. L.; Gust, B.; Barlow, M. J.; Rosen, M. S.; Goodson, B. M.; Chekmenev, E. Y. *J. Phys. Chem. B* **2014**, *118*, 4809−4816.
(53) Nikolaou, P.; Coffey, A. M.; Walkup, L. L.; Gust, B.; LaPierre, C.; Koehnemann, E.; Barlow, M. J.; Rosen, M. S.; Goodson, B. M.; Chekmenev, E. Y. *J. Am. Chem. Soc.* **2014**, *136*, 1636−1642.
(54) Ruset, I. C.; Ketel, S.; Hersman, F. W. *Phys. Rev. Lett.* **2006**, *96*, 053002.
(55) Norquay, G.; Collier, G. J.; Rao, M.; Stewart, N. J.; Wild, J. M. *Phys. Rev. Lett.* **2018**, *121*, 153201.
(56) Hoult, D. I.; Richards, R. E. *J. Magn. Reson.* **1976**, *24*, 71−85.
(57) Zhao, E. W.; Maligal-Ganesh, R.; Xiao, C.; Goh, T.-W.; Qi, Z.; Pei, Y.; Hagelin-Weaver, H. E.; Huang, W.; Bowers, C. R. *Angew. Chem., Int. Ed.* **2017**, *56*, 3925−3929.
(58) Burueva, D. B.; Romanov, A. S.; Salnikov, O. G.; Zhivonitko, V. V.; Chen, Y.-W.; Barskiy, D. A.; Chekmenev, E. Y.; Hwang, D. W.-H.; Kovtunov, K. V.; Koptyug, I. V. *J. Phys. Chem. C* **2017**, *121*, 4481−4487.

DOI: 10.1021/acs.analchem.9b00259
Anal. Chem. 2019, 91, 4741−4746

Received: 18 October 2017 | Revised: 30 November 2018 | Accepted: 2 December 2018

DOI: 10.1002/jlcr.3699

SPECIAL ISSUE ARTICLE

WILEY Journal of Labelled Compounds and Radiopharmaceuticals

A versatile synthetic route to the preparation of ^{15}N heterocycles

Nikita V. Chukanov[1,2] | Bryce E. Kidd[3] | Larisa M. Kovtunova[2,4] | Valerii I. Bukhtiyarov[4] | Roman V. Shchepin[5] | Eduard Y. Chekmenev[5,7,8] | Boyd M. Goodson[3,6] | Kirill V. Kovtunov[1,2] | Igor V. Koptyug[1,2]

[1] International Tomography Center SB RAS, Novosibirsk, Russia

[2] Department of Chemistry, Novosibirsk State University, Novosibirsk, Russia

[3] Department of Chemistry and Biochemistry, Southern Illinois University, Carbondale, Illinois, USA

[4] Surface Science Laboratory, Boreskov Institute of Catalysis SB RAS, Novosibirsk, Russia

[5] Department of Biomedical Engineering and Physics, Vanderbilt-Ingram Cancer Center (VICC), Vanderbilt Institute of Imaging Science (VUIIS), Department of Radiology, Vanderbilt University Medical Center, Nashville, Tennessee, USA

[6] Materials Technology Center, Southern Illinois University, Carbondale, Illinois, USA

[7] Russian Academy of Sciences, Moscow, Russia

[8] Ibio, Department of Chemistry, Wayne State University Karmanos Cancer Center, Detroit, Michigan, USA

Correspondence
Eduard Y. Chekmenev, Department of Biomedical Engineering and Physics, Vanderbilt-Ingram Cancer Center (VICC), Vanderbilt Institute of Imaging Science (VUIIS), Department of Radiology, Vanderbilt University Medical Center, Nashville, TN 37232, USA.
Email: chekmenev@wayne.edu

Kirill V. Kovtunov, International Tomography Center SB RAS, Novosibirsk, 630090, Russia.
Email: kovtunov@tomo.nsc.ru

Funding information
DOD, Grant/Award Numbers: W81XWH-12-1-0159/BC112431, W81XWH-15-1-0271 and W81XWH-15-1-0272; NIH, Grant/Award Numbers: NCI 1R21CA220137, NIBIB 1R21EB018014 and NIBIB 1R21EB020323; NSF, Grant/Award Numbers: CHE-1416268 and CHE-1416432; Russian Science Foundation, Grant/Award Number: 17-73-20030

A robust medium-scale (approximately 3 g) synthetic method for ^{15}N labeling of pyridine (^{15}N-Py) is reported based on the Zincke reaction. ^{15}N enrichment in excess of 81% was achieved with approximately 33% yield. ^{15}N-Py serves as a standard substrate in a wide range of studies employing a hyperpolarization technique for efficient polarization transfer from parahydrogen to heteronuclei; this technique, called SABRE (signal amplification by reversible exchange), employs a simultaneous chemical exchange of parahydrogen and a to-be-hyperpolarized substrate (e.g., pyridine) on metal centers. In studies aimed at the development of hyperpolarized contrast agents for in vivo molecular imaging, pyridine is often employed either as a model substrate (for hyperpolarization technique development, quality assurance, and phantom imaging studies) or as a co-substrate to facilitate more efficient hyperpolarization of a wide range of emerging contrast agents (e.g., nicotinamide). Here, the produced ^{15}N-Py was used for the feasibility study of spontaneous ^{15}N hyperpolarization at high magnetic (HF) fields (7 T and 9.4 T) of an NMR spectrometer and an MRI scanner. SABRE hyperpolarization enabled acquisition of 2D MRI imaging of catalyst-bound ^{15}N-pyridine with 75 × 75 mm^2 field of view (FOV), 32 × 32 matrix size, demonstrating the feasibility of ^{15}N HF-SABRE molecular imaging with 2.4 × 2.4 mm^2 spatial resolution.

KEYWORDS
^{15}N, contrast agent, hyperpolarization, MRI, parahydrogen, PHIP, pyridine

1 | INTRODUCTION

Isotopic labeling with stable isotopes of hydrogen, carbon, oxygen, and nitrogen is increasingly used in a growing number of applications.[1-4] ^{13}C and ^{15}N labels have also been recently employed for synthesis of a wide range of biomolecules with an eye towards magnetic resonance applications.[2] Indeed, for such applications, NMR hyperpolarization techniques are often employed to increase nuclear spin polarization (typically ca. 10^{-6}/Tesla at room temperature) all the way to near unity (or 100%) nuclear spin polarization.[5-8] The process of hyperpolarization (i.e., significant polarization enhancement above the thermal polarization level induced by the applied static magnetic field) results in corresponding gains (by several orders of magnitude) of NMR signals. These hyperpolarized (HP) biomolecules can be employed as contrast agents for in vivo studies, which opens up new opportunities for probing metabolism non-invasively by means of HP MRI.[9,10]

Despite the MRI signal boost provided by hyperpolarization, biomedical applications of HP contrast agents are often limited[2,11] when isotopic labeling is not employed due to low natural abundance of key biologically relevant spin-½ nuclei, e.g., ^{13}C (1.1%) and ^{15}N (0.37%). Therefore, ^{13}C and ^{15}N labeling is required to enhance the MRI signals in the context of biomedical applications, which are presently the main drivers behind the development of hyperpolarization techniques in general.[2,9,12]

Although proton spins have a higher detection sensitivity (compared with that of ^{13}C and ^{15}N nuclei) and are very abundant (near 100%) in the context of MRI applications, they are rarely employed for hyperpolarization of HP contrast agents owing to their relatively short spin-lattice relaxation time constant (T_1) values (typically in the range of a few seconds). As a result, proton-based HP contrast agents[13,14] undergo very rapid depolarization.[15-22] For example, a HP contrast agent loses ~95% of its initial polarization level (and effective potency) within $3 \times T_1$. ^{13}C and ^{15}N nuclear spins of biomolecules can have T_1 values of the order of tens of seconds[2,23-30] and several minutes[31,32] (in vivo), respectively. Therefore, HP ^{13}C and ^{15}N sites provide more efficient means of polarization storage in the context of preparation, administration, and MRI imaging of HP contrast agents.[9,33-40] Additionally, ^{13}C and ^{15}N HP contrast agents do not suffer from competition with any significant in vivo background signal, compared with the large water and lipid background signals in HP proton MRI.[11,41-43]

Historically, ^{13}C-based HP contrast agents have been introduced first, due to more readily available ^{13}C-enriched compounds and hyperpolarization processes using dissolution dynamic nuclear polarization (d-DNP)[44] in the context of ^{13}C hyperpolarization of carboxyl groups in a wide range of biomolecules.[2] Isolated ^{13}C carboxyl groups (i.e., without directly attached protons, which typically decrease T_1 of neighboring ^{13}C and ^{15}N sites) demonstrate relatively long in vivo T_1 values for HP contrast agents, often approaching 1 minute.[2]

Nevertheless, ^{15}N HP contrast agents have significantly longer T_1 values of more than 2 minutes[31] in vivo. A number of HP compounds exhibit in vitro ^{15}N T_1 values on the order of 3 to 10 minutes.[33,38,45] Moreover, the use of long-lived spin states[46] offer an intriguing possibility of extending the exponential decay constant to 20+ minutes for ^{15}N sites.[40] Furthermore, ^{15}N has a significantly greater (by at least several fold) chemical shift dispersion compared with that of ^{13}C, in part because many relevant N-containing species possess lone pairs on the nitrogen site; therefore, HP ^{15}N sites can serve as molecular probes for sensing characteristics of the local environment[37] such as pH.[43,47]

Technical improvements of the d-DNP technique have recently allowed for more efficient hyperpolarization of ^{15}N sites.[43] Additionally, a second method for the HP contrast agent production based on parahydrogen (a spin isomer of hydrogen) called signal amplification by reversible exchange (SABRE)[48,49] has been shown to be very efficient for hyperpolarization of ^{15}N sites in a number of molecular frameworks, including those found in several biomolecules.[47,50-55] A variant of SABRE, dubbed "SABRE-SHEATH" (SABRE in SHield Enables Alignment Transfer to Heteronuclei),[56,57] can produce ^{15}N polarization ($\%P_{15N}$) in excess of 20% in less than 1 minute.[52] Moreover, unlike the case with d-DNP, which requires expensive cryogenic and magnetic equipment, SABRE-SHEATH is technologically undemanding, and therefore, it is a relatively cheap hyperpolarization technique.[53] As a result of these recent developments in d-DNP and ^{15}N SABRE-SHEATH, the interest for use of HP ^{15}N-labeled biomolecules has been rekindled.[38,58-61]

Regardless of the technique employed (d-DNP or SABRE), the structure of a given synthesized ^{15}N-labeled compound is not altered during the hyperpolarization process. The reader is directed to other review papers on d-DNP hyperpolarization,[2,8,62] which is outside the scope of this work. In the SABRE approach, the to-be-hyperpolarized substrate and parahydrogen (pH_2) exchange reversibly with a metal complex (Figure 1).[67] The first observation of the SABRE effect was realized for pyridine, and in subsequent years, it was extended to many N-[40,48,52,53,67,68] and S-[69] containing heterocycles and other N-based functional groups.[40] Importantly, the SABRE approach allows the transfer of spin order not only to the protons of the corresponding substrates but also to the heteronuclei; to achieve that step,

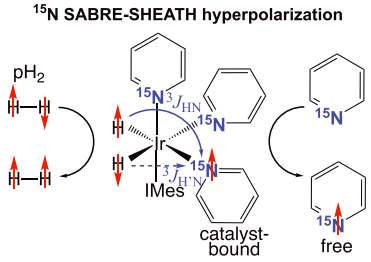

FIGURE 1 A schematic diagram of signal amplification by reversible exchange (SABRE)[48,49,63,64] for the case of efficient hyperpolarization of the ^{15}N site of ^{15}N-pyridine using the SABRE-SHEATH approach. Note the simultaneous chemical exchange of pH_2 and the to-be-hyperpolarized substrate (here, ^{15}N-pyridine) in the equatorial positions of this IrIMes hexacoordinate complex[65] and the spontaneous nature of polarization transfer via two-bond spin-spin couplings when the process is performed at the matching magnetic field of approximately 1 μT[56,57,66]

pulse sequences[70,71] or a magnetic shield[72] (SABRE-SHEATH)[56,57] can be successfully applied. Moreover, while SABRE-SHEATH (the most efficient technique in terms of both speed of polarization and maximum demonstrated $\%P_{15N}$[52]) has also been shown to successfully hyperpolarize ^{13}C[73,74] and ^{19}F[75] sites (and potentially other spin ½ nuclei[76]) in biomolecular frameworks, it has been recognized that the presence of a spin ½ ^{15}N at the site for catalyst binding[73] (i.e., the N atom directly participating in exchangeable binding to the metal center; Figure 1) enables significantly more efficient polarization of ^{13}C and other biologically relevant sites. To summarize, ^{15}N-labeling is critical for both ^{15}N-based HP contrast agents as well as other (^{13}C-, ^{19}F-based, etc.) HP contrast agents in the context of the SABRE-SHEATH hyperpolarization technique.

Recently, SABRE-SHEATH has been employed to hyperpolarize several ^{15}N-enriched molecules: ^{15}N-pyridine,[56] $^{15}N_2$-imidazole,[47,59] ^{15}N-nicotinamide,[56,58] etc. Most of these compounds in the ^{15}N-labeled form are not available commercially or available at a very high (>$500/0.1 g) cost not very well suitable for the development of biomedical applications on a human scale requiring approximately 1 g of HP contrast agent.[9] Robust synthetic approaches are certainly required to enable this field of molecular imaging with a broad range of ^{15}N-labeled biomolecules.

There are two major synthetic approaches/strategies for preparation of ^{15}N-labeled heterocycles. The first one is de novo, i.e., from Latin "from scratch," when the desired molecular framework is built using reagents (components) that are smaller than and different from the target product. We have recently demonstrated this approach in the context of ^{15}N SABRE-SHEATH for preparation of $^{15}N_2$-imidazole.[59] The second strategy employs the target contrast agent itself without ^{15}N enrichment as a starting material, where the ^{14}N-site (natural abundance of nitrogen isotopes) is effectively "replaced" by the ^{15}N isotope. While both approaches have their merits, the second approach is attractive because a number of complex biomolecules (including drugs) can be potentially enriched in just two steps. For example, we have recently demonstrated this approach using a Zincke salt[77] on ^{15}N-nicotinamide and obtained good yields along with approximately 98% ^{15}N enrichment.[58]

The work presented here focuses on the synthesis of ^{15}N-Py using the Zincke[77] reaction. ^{15}N-Py is an important molecular target in itself, because it is one of the most studied molecules by SABRE hyperpolarization methods in general, and therefore, it can be useful for mechanistic and phantom imaging studies.[71,73,78-82] Moreover, a variant of the SABRE-SHEATH approach has been demonstrated where Py is added to enhance polarization of other HP substrates (e.g., ^{15}N-nicotinamide[58] and ^{15}N-acetonitrile[73]), indicating that ^{15}N-Py-mediated SABRE catalyst activation could be useful for preparation of other HP contrast agents via SABRE-SHEATH. More importantly, ^{15}N-Py embodies a molecular framework around which many other useful ^{15}N HP contrast agents could be developed in the future in the form of the substituted ^{15}N-pyridines (which is an active and ongoing effort of our collaboration). While another synthetic approach for preparation of ^{15}N-pyridine has been reported,[83] it lacks versatility for preparation of substituted ^{15}N-pyridine–based biomolecules, e.g., nicotinamide, etc, which are of significant interest to the hyperpolarization MR community.[84] Therefore, the approach studied here would be of significant interest for future synthetic efforts in this field. We note that the starting material of the approach demonstrated here is the relatively inexpensive $^{15}NH_4Cl$ (less than $20/g, in 2017), and the product was produced with approximately 33% yield and greater than 81% ^{15}N enrichment, showing an efficient route for ^{15}N enrichment of pyridine-based (and potentially other) heterocycles. Finally, the demonstrated labeled ^{15}N-Py and potentially other ^{15}N-labeled compounds enabled by this approach can be hyperpolarized by both SABRE and d-DNP hyperpolarization techniques, and therefore, a broad community of those working in the field of HP molecular imaging would benefit from the work described here.

In particular, we have employed the prepared ^{15}N-Py material for the feasibility study of spontaneous ^{15}N hyperpolarization and ^{15}N molecular imaging at high magnetic field[85] of a 9.4 T MRI scanner and a 7.0 T NMR spectrometer.

2 | EXPERIMENTAL

2.1 | General

All solvents were purchased from common vendors and were used as received. All NMR spectra and images (^{1}H, ^{13}C, and ^{15}N) were recorded on Bruker 300 MHz and 400 MHz Avance III NMR spectrometers. 1-Chloro-2,4-dinitrobenzene was recrystallized from ethanol. *N*-(2,4-Dinitrophenyl)pyridinium chloride was prepared by raction of pyridine with 1-chloro-2,4-dinitrobenzene in acetone according to a procedure similar to that reported previously.[86]

2.2 | Synthesis of ^{15}N-pyridine

2.2.1 | First (small-scale) procedure

A total of 150 mL of anhydrous methanol at 0°C was placed in a round bottom flask. Next, sodium metal (0.43 g, 18.7 mmol) was added with continuous stirring. As soon as the sodium has completely reacted (no hydrogen gas observed), $^{15}NH_4Cl$ (1.00 g, 18.35 mmol) was added. Next, (1) a solution of *N*-(2,4-dinitrophenyl) pyridinium chloride (2.63 g, 9.34 mmol) in anhydrous methanol (20 mL) was added drop-by-drop to the mixture under stirring and the mixture was stirred for one week at room temperature, and (2) activated carbon (2.00 g) was added and stirred for 30 minutes and then was filtered. The supernatant solution was distilled, and a concentrated hydrochloric acid (8 mL) was added to the distillate, and the resulting solution was evaporated to dryness under vacuum. The formed pyridinium hydrochloride was placed in 2-mL flask using a minimal amount of water (to dissolve the compound) for the quantitative collection of the formed hydrochloride, and excess of sodium hydroxide (1.5 g) was then added. The mixture was cooled down by liquid nitrogen during neutralization, and the reaction was deemed completed. The resulting mixture was distilled, and ^{15}N-Py was obtained as an aqueous solution (0.64 g) with concentration of about 25% (^{15}N isotopic purity is better than 60%), and the produced material was used in the subsequent NMR/MRI experiments. The total yield of pyridine was about 22%.

2.2.2 | Second (medium-scale optimized) procedure

Pyridine (60.00 mL, 744 mmol) and 2,4-dinitrochlorobenzene (25.4 g, 125 mmol) were placed in an oven-dried round bottom flask (1 L) supplied with a magnetic stir bar. The solids were dissolved in anhydrous methanol and left to stir at room temperature for 2 days under inert (argon) atmosphere. The flask was placed on a rotary evaporator to remove excess of unreacted pyridine, and anhydrous THF (300 mL) was added to the reaction mixture. White amorphous residue was formed on the bottom of the flask. THF was decanted carefully, leaving the residue on the bottom of the flask. Another portion of anhydrous THF (100 mL) was added rapidly, and the flask was rotated several times and left for several minutes before THF was carefully decanted from the residue. The THF wash was repeated five times. The flask was placed on a rotary evaporator to remove last traces of THF from the pyridine-Zincke salt. Anhydrous methanol (150 mL) was added, and the flask was flushed with argon and put aside.

To an oven-dried round bottom flask (5 L) supplied with a stir bar, $^{15}NH_4Cl$ (574 mmol, 31.26 g) and anhydrous methanol (3 L) were added. The solution was cooled to 0°C, and sodium methoxide methanolic solution (30 wt%, 516 mmol, 118 mL) was added dropwise. The methanolic solution of pyridine-Zincke salt (described above) was added dropwise to the flask. The resulting solution was left to stir under an inert atmosphere (argon) for 2 days. The supernatant solution was distilled, and 2M solution of hydrochloric acid (250 mL) in Et_2O was added to the distillate (pH ~ 2), and the resulting solution was evaporated to dryness under vacuum. The resulting crude pyridine hydrochloride was placed in a 100-mL flask, and an excess of solid sodium hydroxide (25 g) was added and the mixture was distilled. Molecular sieves (4 Å, 5.7 g, Fisher chemical, P/N M514-500) were added to the obtained ^{15}N-Py. A second distillation and drying by molecular sieves allowed the preparation of 3.3 g of ^{15}N-Py (yield, 33%; ^{15}N isotopic purity is greater than 81%) (Figure 2).

3 | PARAHYDROGEN PREPARATION, NMR, AND MRI EXPERIMENTS

Enrichment of parahydrogen (pH_2) spin isomer was performed with a Bruker parahydrogen generator that allows

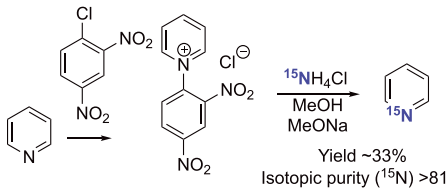

FIGURE 2 The overall scheme of ^{15}N-Py enrichment with ^{15}N (from $^{15}NH_4Cl$ source) via Zincke salt formation

filling of a 0.9-L tank with 7 atm of approximately 90% pH_2 in approximately 100 minutes.

For the observation of ^{15}N-enhanced resonances, the polarization transfer from pH_2-derived protons to ^{15}N nuclei of ^{15}N-Py (prepared via the first procedure described above) was realized via high-field SABRE (HF-SABRE) and SABRE-SHEATH approaches. Specifically, pH_2 gas was bubbled (flow rate 30 mL min^{-1}) through a 1/16 in (OD) Teflon capillary extended to the bottom of a 5-mm medium-wall NMR tube containing a SABRE catalyst solution and ^{15}N-Py (10mM of IrCl(COD)(IMes)) (IMes = 1,3-bis(2,4,6-trimethylphenyl)imidazol-2-ylidene[65,87]; COD = cyclooctadiene; note this catalyst precursor was synthesized in accord with a previously reported procedure[85]) in CD_3OD. pH_2 bubbling occurred in the magnetic shield for the SABRE-SHEATH approach. When the gas flow was halted, the sample was transferred to the high magnetic field, where ^{15}N NMR spectra were recorded. For the HF-SABRE method, pH_2 bubbling was performed at high magnetic field (7 T) of NMR spectrometer during the detection of ^{15}N resonances.

The MRI investigations were carried out with a 400-MHz Bruker scanner equipped with a $^{15}N/^{1}H$ 25-mm MRI probe. The standard EPI (echo-planar imaging) MRI pulse sequence was utilized with 32 × 32 matrix size, four averages, 11-millisecond echo time (TE), 75 × 75 mm^2 field of view (FOV), and approximately 4 seconds' total scan time. The MRI experiments were performed using a 10-mm outer dimeter NMR tube.

4 | RESULTS AND DISCUSSION

To the best of our knowledge, to date there has been only one method for the synthesis of ^{15}N-Py: the reaction of 2-ethoxy-3,4-dihydro-2*H*-pyran with ^{15}N-NH_4Cl in the presence of methylene blue (Figure 3).[83] The yield was reported as 55% when the equivalent ratio of pyran derivative and $^{15}NH_4Cl$ was used. In a similar manner, 4-methylpyridine was obtained from 2-ethoxy-4-methyl-3,4-dihydro-2*H*-pyran.[86] The main limitation of this synthetic approach is the use of substituted pyridine derivatives, which can be complex in the context of future SABRE biomedical applications.[5]

An alternative synthetic approach involves the formation of a Zincke salt[77] and is followed by reaction with $^{15}NH_4Cl$ (as a source of ^{15}N label) (Figure 4). To date, this approach has only been applied to the synthesis of ^{15}N-nicotinamide.[58,88,89] In the first step, the unlabeled pyridine derivative is reacted with dinitrochlorobenzene to form the Zincke salt (Figure 4). Next, $^{15}NH_4Cl$ is used (as a source of ^{15}N label) to enable heterocycle ring opening, and dinitroaniline is replaced by ^{15}N-labeled ammonia. After that, the cyclization proceeds, and the labeled ^{15}N-pyridine derivative is formed (Figure 4). The reactions shown in Figures 3 and 4 clearly indicate that preparation of ^{15}N-pyridine derivatives would become challenging using the method described in Whaley and Ott[83] (because a sophisticated precursor would be required), whereas the Zincke salt–based approach allows for straightforward ^{15}N-enrichment using a non-labeled biomolecule, e.g., nicotinamide (vitamin B3) shown in Figure 4.

The less-reactive Zincke salts such as l-*N*-(2,4-dinitrobenzene)pyridinium chloride have previously been employed to perform ring closure effectively and eliminate the dinitroaniline.[90] Therefore, we have employed and investigated this strategy for its potential of ^{15}N labeling of pyridine.

An initial quantity of *N*-(2,4-dinitrophenyl) pyridinium chloride was prepared by interaction of pyridine with 1-chloro-2,4-dinitrobenzene in acetone.[86] This salt was used in the reaction with a methanol solution of $^{15}NH_4Cl$ (Figure 2). Purification via filtration with charcoal and the distilling of all volatile compounds including ^{15}N-Py were performed under atmospheric pressure. We assumed that the slight decomposition of pyridine-Zincke salt back to the unlabeled pyridine during the synthesis and extraction could be responsible for the less-than-ideal isotopic purity at this stage (i.e., approximately 81% vs theoretical 98%). Next, the product was extracted in the form of solid pyridinium

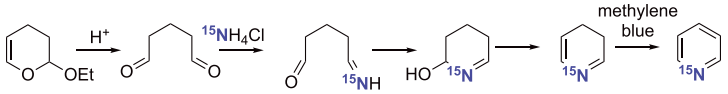

FIGURE 3 Reaction scheme from the previous report[83] of ^{15}N-pyridine synthesis

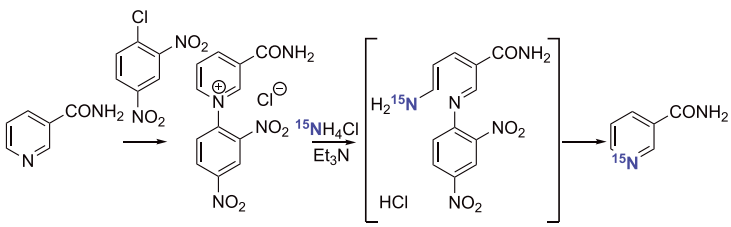

FIGURE 4 Reaction scheme and mechanism for the preparation of ^{15}N-nicotinamide via formation of a Zincke salt

hydrochloride, which is neutralized by NaOH, and distilled. The final product of ^{15}N-Py was formed as an aqueous solution with approximately 81% ^{15}N isotopic purity confirmed by mass spectrometry analysis (Figure 5). ^{1}H, ^{13}C, and ^{15}N NMR spectra are provided in Figures S1 to S3.

While this ^{15}N-labeling efficiency is lower than that reported for ^{15}N-nicotinamide (98%), it is relatively high and certainly useful for future biomedical applications of ^{15}N SABRE hyperpolarization. Of note, pyridine is one of the most studied molecules for the observation of hyperpolarized ^{1}H and ^{15}N NMR resonances via polarization transfer from parahydrogen via SABRE approaches, and as a result, this work would be also of interest to those working in the field of fundamental advances of SABRE hyperpolarization technology as well. Moreover, demonstration that the presented approach works for preparation of ^{15}N-Py (in addition to the previously reported ^{15}N-nicotinamide preparation[58]) opens the road for future ^{15}N-enrichment of more-complex pyridine derivatives using this relatively straightforward approach. The key synthetic results and their comparison with the method described in Whaley and Ott[83] are provided in Table 1.

Here, the feasibility of ^{15}N high-field (HF) SABRE was investigated in the context of an HP MRI application. In the case of HF-SABRE, pH_2 bubbling through a water-methanol solution of pyridine and homogeneous SABRE catalyst occurred directly inside the high field of a 300-MHz NMR spectrometer along with the recording of ^{15}N NMR spectra (Figure 6). Under these conditions, the ^{15}N signal enhancement of the free Py resonance is negligible (Figure 6B). The observable HP ^{15}N NMR signal of the bound ^{15}N-Py was detected only after 100 averages (approximately 50 s of total experimental time). The ^{15}N signal enhancement factor (ε_{15N}) of approximately 100-fold was estimated by comparison of the HP spectrum (Figure 6B) and a thermally polarized spectrum of a ^{15}N reference sample with known ^{15}N concentration and polarization (Figure 6A). ^{15}N SABRE-SHEATH approach (wherein pH_2 bubbling occurs at a micro-Tesla magnetic field created by the magnetic shield followed by fast sample transfer to the high magnetic field for analysis[56,57]) allowed detection of both free and catalyst-bounded ^{15}N-Py resonances (Figure 6C). As with the case of the HF-SABRE approach, the signal enhancement ε_{15N}

TABLE 1 Summary of ^{15}N pyridine syntheses using the method presented here and method employed in Whaley and Ott[83]

	Method from Whaley and Ott[83]	This Work Using Zincke Salt–based Method
Reaction yield	~55%	~33%
^{15}N isotopic purity	~98%	~81%
Straightforward applicability to preparation of substituted ^{15}N-pyridines	No	Yes

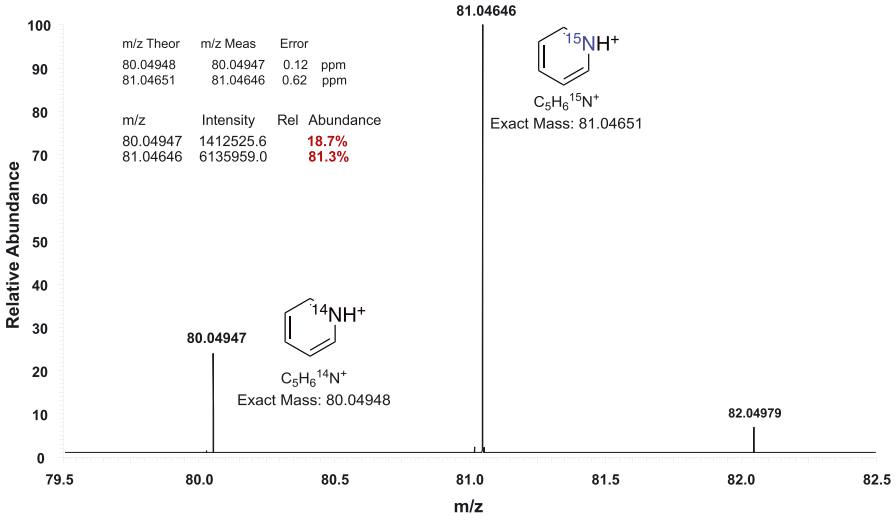

FIGURE 5 High-resolution mass spectrometry of the final product (^{15}N-Py) performed by direct liquid infusion using an Orbitrap mass spectrometer (Thermo-Finnigan, San Jose, California) equipped with an Ion-Max source housing and an atmospheric pressure chemical ionization (APCI) probe in positive ion mode at a resolving power of 60 000 (at m/z 400). Note the presence of the peak at approximately 82.05 due to contribution from ^{13}C natural abundance of approximately 1.1% (therefore, the probability of having one ^{13}C in any of the five carbon positions is greater than 5%)

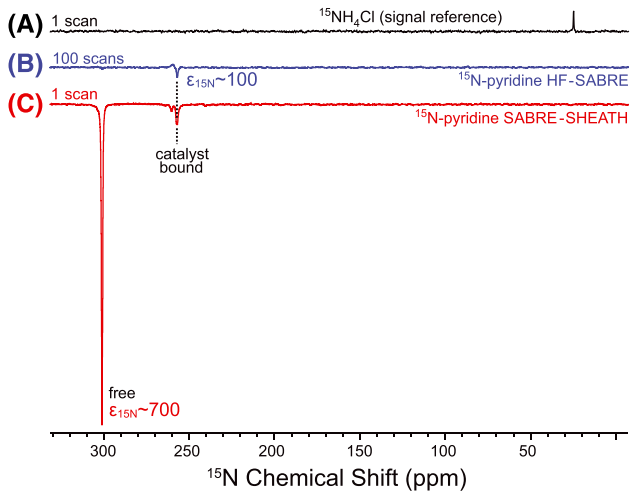

FIGURE 6 ^{15}N NMR spectra obtained for (A) ^{15}N signal reference of $^{15}NH_4Cl$ (37%) aqueous solution, (B) HF-SABRE, and (C) SABRE-SHEATH of HP ^{15}N resonances of ^{15}N-Py

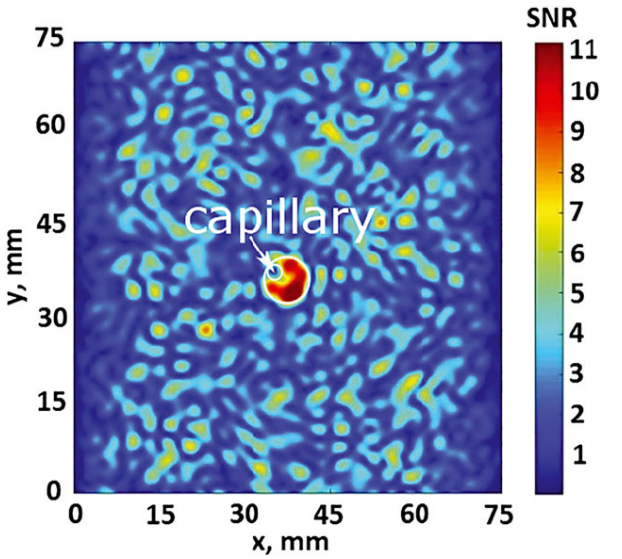

FIGURE 7 ^{15}N MRI image of high-field (HF) ^{15}N SABRE of HP ^{15}N-pyridine obtained using an EPI pulse sequence with 11- millisecond echo time (TE), 32 × 32 matrix size (2.4 × 2.4 mm^2 pixel size) over 75 × 75 mm^2 field of view (FOV), and four acquisitions (total experimental time was approximately 4 s)

(of about 700-fold) was estimated via comparison of the ^{15}N HP pyridine resonances with the ^{15}N signal reference provided by the thermal signal of $^{15}NH_4Cl$ (37%) aqueous solution (Figure 6A), in line with previous studies at such concentrations (ca. 100 mM).[56,57]

While ^{15}N MRI of SABRE-SHEATH has been demonstrated before,[57] ^{15}N MRI of HF-SABRE has not been investigated. Therefore, the HF-SABRE polarization approach was used to enable ^{15}N MRI of ^{15}N-Py. The EPI MRI pulse sequence was employed, and the corresponding ^{15}N 2D MRI image of the cross section of the 10-mm NMR tube is shown in Figure 7. The imaging spatial resolution was 2.4 × 2.4 mm^2, which is similar to previous resolution (2 × 2 mm^2) reported for ^{15}N SABRE-SHEATH imaging. However, we note that the HF-SABRE MRI image here was recorded at approximately 5-10 times lower concentration of the HP substrate (i.e., catalyst bound ^{15}N-Py) and significantly lower (by at least one order of magnitude) ^{15}N polarization value of the HP ^{15}N-Py. ^{15}N MRI with similar spatial resolution (despite nominally lower concentration and nuclear spin polarization) is possible, because ^{15}N polarization is continuously replenished by the HF-SABRE procedure.

The feasibility of HF-SABRE imaging is important in the context of potential biomedical applications as a facile approach for preparation of HP phantoms to optimize imaging protocols and studies. Moreover, SABRE-SHEATH primarily hyperpolarizes the free ^{15}N pool (Figure 6C), and therefore, MRI imaging of SABRE-SHEATH–hyperpolarized solutions reports on spatial distribution of the free pool of HP ^{15}N-Py. On the other hand, HF-SABRE enhances primarily catalyst-bound species (Figure 6B), and therefore, MRI imaging of HF-SABRE–hyperpolarized solutions provides visualization of the catalyst-bound HP ^{15}N-Py species. Moreover, since HF-SABRE hyperpolarization is quickly replenishable due to continuous pH_2 bubbling, the additional sensitivity boost due to continuous re-hyperpolarization is achieved, which is advantageous for catalysis visualization via MRI imaging.

5 | CONCLUSIONS

In summary, an efficient approach for ^{15}N labeling of pyridine is reported based on the formation of a Zincke salt intermediate. We demonstrated a relatively simple and cheap (1 g of $^{15}NH_4Cl$ costs less than $20, in 2017) synthetic approach for the ^{15}N-enriched pyridine synthesis, which can be used as a robust sample for both SABRE catalyst testing and MRI pulse sequence optimization and other applications. We envision that the relative simplicity and high labeling efficiency (>81%) and overall good yield (>33%) will be of use for future synthetic efforts of labeling of more complex pyridine derivatives in the context of SABRE hyperpolarization and bio-imaging applications. The presented approach is versatile, because it employs the exact non-enriched compound of interest as a precursor in non-^{15}N-labeled form. Therefore, complex pyridine-based compounds can be ^{15}N-enriched using

this approach. For example, we have recently reported on the synthesis of substituted ^{15}N-pyridine using the approach reported here for preparation of the corresponding Zincke salt.[91] The prepared ^{15}N-Py was employed for NMR signal hyperpolarization via the SABRE technique with signal enhancement of ^{15}N free resonance of approximately 700-fold via the SABRE-SHEATH approach and ^{15}N catalyst-bound resonance of approximately 100-fold via the HF-SABRE approach.

ACKNOWLEDGEMENTS

The Russian team thanks the Russian Science Foundation (grant 17-73-20030) for the support of ^{15}N pyridine testing via NMR and MRI. N.V.C. thanks Dr A.I. Taratayko for the useful discussions. This work was supported by National Science Foundation (NSF) under grants CHE-1416268 and CHE-1416432, NIH NIBIB 1R21EB018014, NIBIB 1R21EB020323, and NCI 1R21CA220137, DOD CDMRP BRP W81XWH-12-1-0159/BC112431, DOD PRMRP awards W81XWH-15-1-0271 and W81XWH-15-1-0272, and Exxon Mobil Knowledge Build.

CONFLICT OF INTEREST

The authors did not report any conflict of interest.

ORCID

Nikita V. Chukanov https://orcid.org/0000-0003-1246-8869
Larisa M. Kovtunova https://orcid.org/0000-0003-0922-6594
Valerii I. Bukhtiyarov https://orcid.org/0000-0003-4382-1207
Roman V. Shchepin https://orcid.org/0000-0001-9135-3036
Eduard Y. Chekmenev https://orcid.org/0000-0002-8745-8801
Boyd M. Goodson https://orcid.org/0000-0001-6079-5077
Kirill V. Kovtunov https://orcid.org/0000-0001-7577-9619
Igor V. Koptyug https://orcid.org/0000-0003-3480-7649

REFERENCES

1. Hiroaki H. *Expert Opinion Drug Discovery*. 2013;8:523.
2. Kurhanewicz J, Vigneron DB, Brindle K, et al. Analysis of cancer metabolism by imaging hyperpolarized nuclei: prospects for translation to clinical research. *Neoplasia*. 2011;13(2):81-97.
3. Clendinen CS, Stupp GS, Ajredini R, Lee-McMullen B, Beecher C, Edison AS. *Front Plant Sci*. 2015;6:611.
4. Theodorou V, Skobridis K, Alivertis D, Gerothanassis IP, Labelled J. Synthetic methodologies in organic chemistry involving incorporation of [^{17}O] and [^{18}O] isotopes. *Comp. Radiopharm.* 2014;57(8):481-508.
5. Nikolaou P, Goodson BM, Chekmenev EY. NMR hyperpolarization techniques for biomedicine. *Chem a Eur J*. 2015;21(8):3156-3166.
6. Goodson BM, Whiting N, Coffey AM, et al. *Emagres*. 2015;4:797.
7. Barskiy DA, Coffey AM, Nikolaou P, et al. NMR hyperpolarization techniques of gases. *Chem a Eur J*. 2017;23(4):725-751.
8. Ardenkjaer-Larsen J-H, Boebinger GS, Comment A, et al. Facing and overcoming sensitivity challenges in biomolecular NMR spectroscopy. *Angew Chem Int Ed*. 2015;54(32):9162-9185.
9. Nelson SJ, Kurhanewicz J, Vigneron DB, et al. 198ra108. *Sci Transl Med*. 2013;5.
10. Goodson BM. Nuclear magnetic resonance of laser-polarized noble gases in molecules, materials, and organisms. *J Magn Reson*. 2002;155(2):157-216.
11. Yen YF, Kohler SJ, Chen AP, et al. Imaging considerations for in vivo ^{13}C metabolic mapping using hyperpolarized ^{13}C-pyruvate. *Magn Reson Med*. 2009;62(1):1-10.
12. Sriram R, Kurhanewicz J, Vigneron DB. *eMagRes*. John Wiley & Sons, Ltd; 2014:311.
13. Kovtunov KV, Romanov AS, Salnikov OG, Barskiy DA, Chekmenev EY, Koptyug IV. *Tomography*. 2016;2:49.
14. Burueva DB, Romanov AS, Salnikov OG, et al. Extending the lifetime of hyperpolarized propane gas through reversible dissolution. *J Phys Chem C*. 2017;121(8):4481-4487.
15. Kovtunov KV, Truong ML, Barskiy DA, et al. Long-lived spin states for low-field hyperpolarized gas MRI. *Chem a Eur J*. 2014;20(45):14629-14632.
16. Kovtunov KV, Truong ML, Barskiy DA, et al. Propane-*d*6 heterogeneously hyperpolarized by parahydrogen. *J Phys Chem C*. 2014;118(48):28234-28243.
17. Barskiy DA, Salnikov OG, Romanov AS, et al. NMR Spin-Lock Induced Crossing (SLIC) dispersion and long-lived spin states of gaseous propane at low magnetic field (0.05 T). *J Magn Reson*. 2017;276:78-85.
18. Barskiy DA, Salnikov OG, Shchepin RV, et al. NMR SLIC sensing of hydrogenation reactions using parahydrogen in low magnetic fields. *J Phys Chem C*. 2016;120(51):29098-29106.
19. McCarney ER, Armstrong BD, Lingwood MD, Han S. Hyperpolarized water as an authentic magnetic resonance imaging contrast agent. *Proc Natl Acad Sci U S A*. 2007;104(6):1754-1759.
20. Coffey AM, Kovtunov KV, Barskiy D, et al. High-resolution low-field molecular magnetic resonance imaging of hyperpolarized liquids. *Anal Chem*. 2014;86(18):9042-9049.
21. Salnikov OG, Barskiy DA, Coffey AM, Kovtunov KV, Koptyug IV, Chekmenev EY. Efficient batch-mode parahydrogen-induced polarization of propane. *Chemphyschem*. 2016;17(21):3395-3398.
22. Zhang Y, Duan X, Soon PC, Sychrovský V, Canary JW, Jerschow A. Limits in proton nuclear singlet-state lifetimes measured with *para*-hydrogen-induced polarization. *Chemphyschem*. 2016;17(19):2967-2971.

23. Golman K, Zandt R i't, Thaning M. *Proc. Natl. Acad. Sci. U. S. A.* 2006;103:11270.

24. Day SE, Kettunen MI, Gallagher FA, et al. Detecting tumor response to treatment using hyperpolarized ^{13}C magnetic resonance imaging and spectroscopy. *Nat Med*. 2007;13(11): 1382-1387.

25. Golman K, Axelsson O, Johannesson H, Mansson S, Olofsson C, Petersson JS. Parahydrogen-induced polarization in imaging: subsecond ^{13}C angiography. *Magn Reson Med*. 2001;46(1):1-5.

26. Bhattacharya P, Chekmenev EY, Perman WH, et al. Towards hyperpolarized ^{13}C-succinate imaging of brain cancer. *J Magn Reson*. 2007;186(1):150-155.

27. Bhattacharya P, Chekmenev EY, Reynolds WF, et al. Parahydrogen-induced polarization (PHIP) hyperpolarized MR receptor imaging in vivo: a pilot study of ^{13}C imaging of atheroma in mice. *NMR Biomed*. 2011;24(8):1023-1028.

28. Coffey AM, Shchepin RV, Truong ML, Wilkens K, Pham W, Chekmenev EY. Open-source automated parahydrogen hyperpolarizer for molecular imaging using ^{13}C metabolic contrast agents. *Anal Chem*. 2016;88(16):8279-8288.

29. Coffey AM, Feldman MA, Shchepin RV, et al. High-resolution hyperpolarized in vivo metabolic ^{13}C spectroscopy at low magnetic field (48.7 mT) following murine tail-vein injection. *J Magn Reson*. 2017;281:246-252.

30. Durst M, Chiavazza E, Haase A, Aime S, Schwaiger M, Schulte RF. α-Trideuteromethyl[^{15}N]glutamine: a long-lived hyperpolarized perfusion marker. *Magn Reson Med*. 2016;76(6): 1900-1904.

31. Cudalbu C, Comment A, Kurdzesau F, et al. Feasibility of in vivo ^{15}N MRS detection of hyperpolarized ^{15}N labeled choline in rats. *Phys Chem Chem Phys*. 2010;12(22):5818-5823.

32. Gabellieri C, Reynolds S, Lavie A, Payne GS, Leach MO, Eykyn TR. Therapeutic target metabolism observed using hyperpolarized ^{15}N choline. *J Am Chem Soc*. 2008;130(14): 4598-4599.

33. Bales L, Kovtunov KV, Barskiy DA, et al. Aqueous, heterogeneous *para*-hydrogen-induced ^{15}N polarization. *J Phys Chem C*. 2017;121(28):15304-15309.

34. Kovtunov KV, Kovtunova LM, Gemeinhardt ME, et al. Heterogeneous microtesla SABRE enhancement of ^{15}N NMR signals. *Angew Chem Int Ed*. 2017;56(35):10433-10437.

35. Kovtunov KV, Barskiy DA, Salnikov OG, et al. Toward production of pure ^{13}C hyperpolarized metabolites using heterogeneous parahydrogen-induced polarization of ethyl[1-^{13}C]acetate. *RSC Adv*. 2016;6(74):69728-69732.

36. Kovtunov KV, Barskiy DA, Shchepin RV, et al. Production of pure aqueous ^{13}C-hyperpolarized acetate by heterogeneous parahydrogen-induced polarization. *Chem a Eur J*. 2016; 22(46):16446-16449.

37. Hata R, Nonaka H, Takakusagi Y, Ichikawa K, Sando S. Design of a hyperpolarized ^{15}N NMR probe that induces a large chemical-shift change upon binding of calcium ions. *Chem. Comm.* 2015;51(61):12290-12292.

38. Nonaka H, Hirano M, Imakura Y, Takakusagi Y, Ichikawa K, Sando S. Design of a ^{15}N molecular unit to achieve long retention of hyperpolarized spin state. *Sci Rep*. 2017;7(1):40104.

39. Sarkar R, Comment A, Vasos PR, et al. Proton NMR of ^{15}N-choline metabolites enhanced by dynamic nuclear polarization. *J Am Chem Soc*. 2009;131(44):16014-16015.

40. Theis T, Ortiz GX, Logan AWJ, et al. Direct and cost-efficient hyperpolarization of long-lived nuclear spin states on universal $^{15}N_2$-diazirine molecular tags. *Sci Adv*. 2016;2(3):e1501438.

41. Albers MJ, Bok R, Chen AP, et al. Hyperpolarized ^{13}C lactate, pyruvate, and alanine: noninvasive biomarkers for prostate cancer detection and grading. *Cancer Res*. 2008;68(20):8607-8615.

42. Larson PEZ, Hu S, Lustig M, et al. Fast dynamic 3D MR spectroscopic imaging with compressed sensing and multiband excitation pulses for hyperpolarized ^{13}C studies. *Magn Reson Med*. 2011;65(3):610-619.

43. Jiang W, Lumata L, Chen W, et al. Hyperpolarized ^{15}N-pyridine derivatives as pH-sensitive MRI agents. *Sci Rep*. 2015;5(1):9104.

44. Ardenkjaer-Larsen JH, Fridlund B, Gram A, et al. Increase in signal-to-noise ratio of >10,000 times in liquid-state NMR. *Proc Natl Acad Sci U S a*. 2003;100(18):10158-10163.

45. Reineri F, Viale A, Ellena S, et al. ^{15}N magnetic resonance hyperpolarization via the reaction of parahydrogen with ^{15}N-propargylcholine. *J Am Chem Soc*. 2012;134(27):11146-11152.

46. Carravetta M, Johannessen OG, Levitt MH. Beyond the T_1 limit: singlet nuclear spin states in low magnetic fields. *Phys Rev Lett*. 2004;92(15):153003.

47. Shchepin RV, Barskiy DA, Coffey AM, et al. ^{15}N hyperpolarization of imidazole-$^{15}N_2$ for magnetic resonance pH sensing via SABRE-SHEATH. *ACS Sensors*. 2016;1(6):640-644.

48. Adams RW, Aguilar JA, Atkinson KD, et al. Reversible interactions with *para*-hydrogen enhance NMR sensitivity by polarization transfer. *Science*. 2009;323(5922):1708-1711.

49. Adams RW, Duckett SB, Green RA, Williamson DC, Green GGR. A theoretical basis for spontaneous polarization transfer in non-hydrogenative parahydrogen-induced polarization. *J Chem Phys*. 2009;131(19):194505.

50. Kovtunov KV, Beck IE, Zhivonitko VV, Barskiy DA, Bukhtiyarov VI, Koptyug IV. Heterogeneous addition of H_2 to double and triple bonds over supported Pd catalysts: a parahydrogen-induced polarization technique study. *Phys Chem Chem Phys*. 2012;14(31):11008.

51. Kovtunov KV, Zhivonitko VV, Skovpin IV, Barskiy DA, Salnikov OG, Koptyug IV. Toward continuous production of catalyst-free hyperpolarized fluids based on biphasic and heterogeneous hydrogenations with parahydrogen. *J Phys Chem C*. 2013;117(44):22887-22893.

52. Barskiy DA, Shchepin RV, Coffey AM, et al. Over 20% ^{15}N hyperpolarization in under one minute for metronidazole, an antibiotic and hypoxia probe. *J Am Chem Soc*. 2016;138(26): 8080-8083.

53. Colell JFP, Logan AWJ, Zhou Z, et al. Generalizing, extending, and maximizing nitrogen-15 hyperpolarization induced by parahydrogen in reversible exchange. *J Phys Chem C*. 2017; 121(12):6626-6634.

54. Colell JFP, Emondts M, Logan AWJ, et al. Direct hyperpolarization of nitrogen-15 in aqueous media with parahydrogen in reversible exchange. *J Am Chem Soc*. 2017;139(23):7761-7767.
55. Logan AWJ, Theis T, Colell JFP, Warren WS, Malcolmson SJ. Hyperpolarization of nitrogen-15 Schiff bases by reversible exchange catalysis with *para*-hydrogen. *Chem a Eur J*. 2016; 22(31):10777-10781.
56. Theis T, Truong ML, Coffey AM, et al. Microtesla SABRE enables 10% nitrogen-15 nuclear spin polarization. *J Am Chem Soc*. 2015;137(4):1404-1407.
57. Truong ML, Theis T, Coffey AM, et al. ^{15}N hyperpolarization by reversible exchange using SABRE-SHEATH. *J Phys Chem C*. 2015;119(16):8786-8797.
58. Shchepin RV, Barskiy DA, Mikhaylov DM, Chekmenev EY. Efficient synthesis of nicotinamide-1-^{15}N for ultrafast NMR hyperpolarization using parahydrogen. *Bioconjug Chem*. 2016; 27(4):878-882.
59. Shchepin RV, Barskiy DA, Coffey AM, et al. Robust imidazole-$^{15}N_2$ synthesis for high-resolution low-field (0.05 T) ^{15}N hyperpolarized NMR spectroscopy. *ChemistrySelect*. 2017;2(16):4478-4483.
60. Shchepin RV, Chekmenev EY, Labelled J. Toward hyperpolarized molecular imaging of HIV: synthesis and longitudinal relaxation properties of ^{15}N-azidothymidine. *Comp. Radiopharm.* 2014;57(10):621-624.
61. Neumann KT, Lindhardt AT, Bang-Andersen B, Skrydstrup T, Labelled J. Synthesis and selective ^{2}H-, ^{13}C-, and ^{15}N-labeling of the Tau protein binder THK-523. *Comp. Radiopharm.* 2017;60(1):30-35.
62. Ardenkjaer-Larsen JH. On the present and future of dissolution-DNP. *J Magn Reson*. 2016;264:3-12.
63. Atkinson KD, Cowley MJ, Duckett SB, et al. *Para*-Hydrogen induced polarization without incorporation of *para*-hydrogen into the analyte. *Inorg Chem*. 2009;48(2):663-670.
64. Atkinson KD, Cowley MJ, Elliott PIP, et al. Spontaneous transfer of parahydrogen derived spin order to pyridine at low magnetic field. *J Am Chem Soc*. 2009;131(37):13362-13368.
65. Cowley MJ, Adams RW, Atkinson KD, et al. Iridium N-heterocyclic carbene complexes as efficient catalysts for magnetization transfer from *para*-hydrogen. *J Am Chem Soc*. 2011;133(16):6134-6137.
66. Shchepin RV, Truong ML, Theis T, et al. Hyperpolarization of "neat" liquids by NMR signal amplification by reversible exchange. *J. Phys. Chem. Lett.* 2015;6(10):1961-1967.
67. Mewis RE. Developments and advances concerning the hyperpolarisation technique SABRE. *Magn Reson Chem*. 2015;53(10):789-800.
68. Green RA, Adams RW, Duckett SB, Mewis RE, Williamson DC, Green GGR. The theory and practice of hyperpolarization in magnetic resonance using parahydrogen. *Prog. Nucl. Mag. Res. Spectrosc.* 2012;67:1-48.
69. Shchepin RV, Barskiy DA, Coffey AM, Goodson BM, Chekmenev EY. NMR signal amplification by reversible exchange of sulfur-heterocyclic compounds found in petroleum. *ChemistrySelect*. 2016;1(10):2552-2555.
70. Theis T, Truong M, Coffey AM, Chekmenev EY, Warren WS. LIGHT-SABRE enables efficient in-magnet catalytic hyperpolarization. *J Magn Reson*. 2014;248:23-26.
71. Pravdivtsev AN, Yurkovskaya AV, Zimmermann H, Vieth H-M, Ivanov KL. Transfer of SABRE-derived hyperpolarization to spin-1/2 heteronuclei. *RSC Adv*. 2015;5(78):63615-63623.
72. Zhivonitko VV, Skovpin IV, Koptyug IV. Strong ^{31}P nuclear spin hyperpolarization produced via reversible chemical interaction with parahydrogen. *Chem. Comm.* 2015;51(13):2506-2509.
73. Barskiy DA, Shchepin RV, Tanner CPN, et al. The absence of quadrupolar nuclei facilitates efficient ^{13}C hyperpolarization via reversible exchange with parahydrogen. *Chemphyschem*. 2017;18(12):1493-1498.
74. Zhou Z, Yu J, Colell JFP, et al. Long-lived $^{13}C_2$ nuclear spin states hyperpolarized by parahydrogen in reversible exchange at microtesla fields. *J Phys Chem Lett*. 2017;8(13):3008-3014.
75. Shchepin RV, Goodson BM, Theis T, Warren WS, Chekmenev EY. Toward hyperpolarized ^{19}F molecular imaging via reversible exchange with parahydrogen. *Chemphyschem*. 2017;18(15): 1961-1965.
76. Olaru AM, Burt A, Rayner PJ, et al. Using signal amplification by reversible exchange (SABRE) to hyperpolarise ^{119}Sn and ^{29}Si NMR nuclei. *Chem Comm*. 2016;52(100):14482-14485.
77. Zincke T, Heuser G, Möller W. I. Ueber Dinitrophenylpyridiniumchlorid und dessen Umwandlungsproducte. *Justus Liebigs Ann Chem*. 1904;333(2-3):296-345.
78. Barskiy DA, Kovtunov KV, Koptyug IV, et al. In situ and ex situ low-field NMR spectroscopy and MRI endowed by SABRE hyperpolarization. *Chemphyschem*. 2014;15(18):4100-4107.
79. Ivanov KL, Pravdivtsev AN, Yurkovskaya AV, Vieth H-M, Kaptein R. The role of level anti-crossings in nuclear spin hyperpolarization. *Prog Nucl Mag Res Spectrosc*. 2014;81:1-36.
80. Knecht S, Pravdivtsev AN, Hovener J-B, Yurkovskaya AV, Ivanov KL. Quantitative description of the SABRE process: rigorous consideration of spin dynamics and chemical exchange. *RSC Adv*. 2016;6(29):24470-24477.
81. Pravdivtsev AN, Yurkovskaya AV, Petrov PA, Vieth H-M, Ivanov KL. Analysis of the SABRE (signal amplification by reversible exchange) effect at high magnetic fields. *Appl Magn Reson*. 2016;47(7):711-725.
82. Truong ML, Shi F, He P, et al. *J Phys Chem B*. 2014;18:13882.
83. Whaley TW, Ott DG. *J. Labelled Comp*. 1974;10:283.
84. Hövener J-B, Pravdivtsev AN, Kidd B, et al. Parahydrogen-based hyperpolarization for biomedicine. *Angew Chem Int Ed*. 2018;57(35):11140-11162.
85. Barskiy DA, Kovtunov KV, Koptyug IV, et al. The feasibility of formation and kinetics of NMR signal amplification by reversible exchange (SABRE) at high magnetic field (9.4 T). *J Am Chem Soc*. 2014;136(9):3322-3325.
86. Okoh OA, Bisby RH, Lawrence CL, Rolph CE, Smith RB, Sulfur J. *Chem*. 2014;35:42.
87. Vazquez-Serrano LD, Owens BT, Buriak JM. The search for new hydrogenation catalyst motifs based on N-heterocyclic carbene ligands. *Inorg Chim Acta*. 2006;359(9):2786-2797.

88. Oppenheimer NJ, Matsunaga TO, Kam BL, Labelled J. Synthesis of ^{15}N-1 nicotinamide. A general, one step synthesis of ^{15}N labeled pyridine heterocycles. *Comp Radiopharm*. 1978;15(S1):191-196.
89. Burgos ES, Vetticatt MJ, Schramm VL. Recycling nicotinamide. The transition-state structure of human nicotinamide phosphoribosyltransferase. *J Am Chem Soc*. 2013;135(9):3485-3493.
90. Atkinson MR, Morton RK, Naylor R. 98. Synthesis of glycosylpyridinium compounds from glycosylamines and from glycosyl halides. *J Chem Soc*. 1965;610.
91. Chukanov NV, Salnikov OG, Shchepin RV, et al. ^{19}F hyperpolarization of ^{15}N-3-^{19}F-pyridine via signal amplification by reversible exchange. *J Phys Chem C*. 2018;122(40):23002-23010.

SUPPORTING INFORMATION

Additional supporting information may be found online in the Supporting Information section at the end of the article.

How to cite this article: Chukanov NV, Kidd BE, Kovtunova LM, et al. A versatile synthetic route to the preparation of ^{15}N heterocycles. *J Label Compd Radiopharm*. 2019;1–11. https://doi.org/10.1002/jlcr.3699

nature COMMUNICATIONS

ARTICLE

https://doi.org/10.1038/s41467-019-08298-8 OPEN

Unveiling coherently driven hyperpolarization dynamics in signal amplification by reversible exchange

Jacob R. Lindale[1], Shannon L. Eriksson[1], Christian P.N. Tanner[1], Zijian Zhou[1], Johannes F.P. Colell[1], Guannan Zhang[1], Junu Bae[1], Eduard Y. Chekmenev[2,3], Thomas Theis[1] & Warren S. Warren[4]

Signal amplification by reversible exchange (SABRE) is an efficient method to hyperpolarize spin-1/2 nuclei and affords signals that are orders of magnitude larger than those obtained by thermal spin polarization. Direct polarization transfer to heteronuclei such as ^{13}C or ^{15}N has been optimized at static microTesla fields or using coherence transfer at high field, and relies on steady state exchange with the polarization transfer catalyst dictated by chemical kinetics. Here we demonstrate that pulsing the excitation field induces complex coherent polarization transfer dynamics, but in fact pulsing with a roughly 1% duty cycle on resonance produces more magnetization than constantly being on resonance. We develop a Monte Carlo simulation approach to unravel the coherent polarization dynamics, show that existing SABRE approaches are quite inefficient in use of para-hydrogen order, and present improved sequences for efficient hyperpolarization.

[1] Department of Chemistry, Duke University, Durham, NC 27708, USA. [2] Department of Chemistry, Karmanos Cancer Institute (KCI), Wayne State University, Detroit, MI 48202, USA. [3] Russian Academy of Sciences, Leninskiy Prospekt 14, Moscow, Russia 119991. [4] Department of Physics, Chemistry, Biomedical Engineering, and Radiology, Duke University, Durham, NC 27708, USA. These authors contributed equally: Jacob R. Lindale, Shannon L. Eriksson. Correspondence and requests for materials should be addressed to W.S.W. (email: warren.warren@duke.edu)

While nuclear magnetic resonance (NMR) experiments boast a wealth of information, low thermal spin magnetization significantly limits sensitivity. Large magnetic fields increase the Zeeman interaction energy, thus inducing higher polarizations, but realistic field strengths still imply very small fractional magnetization near room temperature. Such issues may be circumvented by hyperpolarization methods, which afford significantly higher nuclear polarization and provide signals that are orders of magnitude larger than those achieved with thermal polarization. DNP[1–6], CIDNP[7–9], PHIP[10–17], and SABRE[18–32] are examples of such hyperpolarization modalities. Indeed, hyperpolarization techniques[33] are now having a significant impact on biomedical imaging[34–36].

Signal Amplification By Reversible Exchange (SABRE), which utilizes an iridium polarization transfer catalyst (PTC), is a convenient non-hydrogenative PHIP variant because it is inexpensive, only requires simple experimental hardware, and can be repeated many times without consuming substrate. In fact, unlike other hyperpolarization techniques, SABRE can be employed for continuous hyperpolarization of imaging agents[37]. Importantly, SABRE provides high levels of polarization (i.e., $P > 15\%$) in under a minute[31,32,38]. During the SABRE process, the PTC establishes scalar couplings between p-H_2 (which acts as a polarization source) and the target ligand. Under the right circumstances, these couplings convert hydrogen singlet order to flow into magnetization on the target ligands, including the very interesting case of direct transfer to heteronuclei such as ^{15}N. This flow of order is achieved by level anti-crossings at low (micro-Tesla) field (SABRE-SHEATH and later variants) or at high field in rotating frames created by very weak rf irradiation (LIGHT-SABRE and later variants)[19,21,24,25,30,39–42]. In either case, the system evolves under the given spin Hamiltonian until the PTC dissociates (either losing a ligand or losing p-H_2) and rebinding of unpolarized ligands from solution can create additional magnetization if the order in the hydrogen has not been depleted.

In typical heteronuclear experiments, the coupling between the bound parahydrogen atoms (which tends to preserve the singlet order), the couplings between those atoms and iridium-bound nitrogen in the PTC complex (which lets the order flow into nitrogen magnetization), and the width of the exchange-broadened resonance of the active complex are all very similar (10–30 Hz). This makes the SABRE process fundamentally incoherent, and impossible to model correctly by traditional approaches such as inserting relaxation into the density matrix. However, we demonstrate here that pulsing the field that generates hyperpolarization restores observable coherent hyperpolarization dynamics in both the low-field and high-field limits, providing a route to significantly boost hyperpolarized signals and efficiently consume singlet order. Furthermore, we develop and implement a Monte Carlo (MC) simulation approach to understand the coherent hyperpolarization dynamics. The MC simulations require fewer assumptions about the system and outperform current models[19,20] in the prediction of experimental data.

Results

Spin dynamics of SABRE. In the SABRE-SHEATH experiment, the spin Hamiltonian is given as the sum of the Zeeman interaction and the scalar coupling terms in the strong coupling limit like:

$$\hat{H}_{\mathrm{low-field}} = \omega_{iI}\sum_{i=1}^{n}\hat{I}_{z,i} + \omega_{iS}\sum_{i=1}^{n}\hat{S}_{z,i} + 2\pi\sum_{i\neq j}\mathcal{J}_{ij}\hat{I}_i\cdot\hat{I}_j + 2\pi\sum_{i\neq j}\mathcal{J}_{ij}\hat{S}_i\cdot\hat{S}_j + 2\pi\sum_{i\neq j}\mathcal{J}_{ij}\hat{I}_i\cdot\hat{S}_j \quad (1)$$

In this notation, ω_{iI} is the Larmor frequency of the hydrogen atoms (≈42 Hz at 1 μT), ω_{iS} is the Larmor frequency of the heteroatoms (≈4 Hz at 1 μT for ^{15}N), and J_{ij} is the scalar coupling between the spins i and j. In high-field hyperpolarization experiments (where here for simplicity we illustrate only irradiation at the heteronuclear frequency), the secular approximation is taken with the heteronuclear scalar couplings, truncating the spin product $\hat{I}_i\cdot\hat{S}_j$ to the z-terms, and an x-phase pulse is introduced in the form of

$$\hat{H}_{\mathrm{high-field}} = \sum_{i=1}^{n}\Omega_i\hat{S}_{z,i} + 2\pi\sum_{i\neq j}\mathcal{J}_{ij}\hat{I}_i\cdot\hat{I}_j + 2\pi\sum_{i\neq j}\mathcal{J}_{ij}\hat{I}_{i,z}\hat{S}_{j,z} + \omega_1\sum_{i=1}^{n}\hat{S}_{x,i} \quad (2)$$

where ω_1 is the nutation frequency of the pulse and Ω is the offset from resonance.

Once magnetic contact is established between the nuclei of the ligand and the parahydrogen singlet order via the PTC, the spin density $\hat{\rho}$ evolves coherently under the Liouville von Neumann (LvN) equation

$$\partial_t\hat{\rho}(t) = -i\left[\hat{H},\hat{\rho}(t)\right] \quad (3)$$

until the complex dissociates. Given the random distribution of PTC dissociation events, it would be easy to motivate dynamics that appear as coherent Rabi oscillations becoming pumped to saturation and converging to an average, reduced spin density[19]. While in certain limits, we have found this limit to be a valid description of the evolution of the SABRE dynamics, it is not the situation for a vast majority of the systems. Firstly, because J_{NH} is significantly large with respect to typical PTC lifetimes (20–50 ms), coherent evolution does not provide small perturbations to the overall dynamics, as would be required for such a perturbative, averaging method. In fact, all methods that utilize ensemble-averaged equations of motion will fail to correctly describe the dynamics in this exchange regime, as discretized dissociation events and subsequent evolution of the system will generate larger excursions from the average density matrix than would be allowed by conventional methods. For the same reasons, the superoperator models for SABRE, such as that by Knecht et al.[20], will also fail to correctly describe the hyperpolarization dynamics. However, by simply numerically simulating discrete dissociation events of individual PTCs in a Markov Chain Monte Carlo fashion and performing ensemble averaging of the resultant spin dynamics solution (see Suplementary Notes 1 and 4 for details), instead of the equation of motion, we arrive at a mathematically and physically fair model of the coherent hyperpolarization dynamics.

Coherent hyperpolarization dynamics. Using the form of the spin Hamiltonian presented in Eqs. 1 and 2, along with the computational method described above, we have constructed two SABRE experiments (Fig. 1) by which the coherent hyperpolarization dynamics may be studied and used to provide significant signal boosts over previously reported techniques. These are the (high field) Delayed Adiabatic Ramps Transfer Hyperpolarization (Fig. 1a), or DARTH-SABRE, and (low field) coherent SHEATH (Fig. 1b) experiments. Like other Spin Lock Induced Crossing (SLIC)-based methods for hyperpolarization[21,25], the DARTH-SABRE experiment only works for systems where the hydrides are chemically but not magnetically equivalent; we have chosen to test the DARTH-SABRE experiment using the canonical 4-spin AA'XX' $[Ir(H)_2(IMes)(^{15}N\text{-pyr})_3]^+$ SABRE system (Fig. 1a). The coherent SHEATH experiment does not have the same spin-topology restrictions that the DARTH-SABRE experiment does, and as such, we have chosen to polarize the 3-spin AA'X [Ir

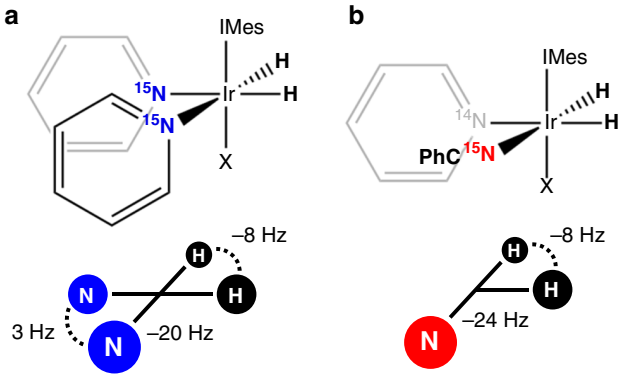

Fig. 1 Model SABRE systems. **a** DARTH-SABRE (4-spin AA'XX' system) and **b** coherent SHEATH (3-spin AA'X system) experiment. The magnetic structure of each system is shown below the chemical structure along with its homonuclear (dashed) and heteronuclear (solid) J-couplings

$(H)_2(IMes)(^{15}N\text{-}PhCN)(pyr)_2]^+$ (PhCN = benzonitrile) SABRE system (Fig. 1b).

In the DARTH-SABRE experiment, pulses that are slightly off resonance from the bound ^{15}N-pyridine spin are applied while ramping the pulse power from an initial value of ω_1=32 Hz with a rate of 42 Hz/s, directly hyperpolarizing z-magnetization (see Supplementary Note 3). This ramp induces hyperpolarized signals that are ~20% larger than if the pulse was a simple square pulse. For a fully enriched system like this, a 90_x ^1H-pulse (Fig. 2a) is used to refocus hydride singlet order into a state that would not destroy the necessary initial β-magnetization from thermal ligands if polarizing the T_N^{+1} state and vice versa, which gave an average of 2× larger signals than without the refocusing pulse (see Supplementary Note 3). Furthermore, the experimental data match the predicted DARTH dynamics with excellent agreement (Fig. 2c) with an AA'XX' spin system, exhibiting a strongly rising exchange baseline (the polarization to which the dynamics converge) to the dynamics and quite significantly damped coherent oscillations, due to the relatively short lifetime of the ^{15}N-pyridine complex (20 ms). While the enhancements shown here are modest, they become exponentially greater with shorter delay times, producing a maximum enhancement of ε = 1350 (Fig. 2e).

Similar to the DARTH-SABRE experiment, the coherent SHEATH experiment pulses a microTesla evolution field of ~0.6 μT to allow hyperpolarization transfer while interleaving storage fields that are approximately 100-fold greater than the evolution field (see Supplementary Note 2). This ensures no coherent evolution of the spin system during the delay. For the AA'X spin system used in these experiments, the data match the predicted SHEATH dynamics with exceptional accuracy (Fig. 2d) and result in an approximately 2.5-fold enhancement of signals that are coherently hyperpolarized over the exchange baseline, which is synonymous with the steady-state SABRE signal, and produces ^{15}N polarizations of ~4.5%. The data indicate that the natural-abundance pyridine co-ligand has no observable effect on the coherent component of the SABRE dynamics, most likely due to minimal coupling into the system by the small $^4J_{HH}$ couplings from the para-hydrogen derived hydrides to the ortho-proton on the pyridine. This is very important, as it means that the effect of binding a natural-abundance co-ligand, like pyridine in this complex, only affects chemical dynamics and thus is incorporated by simply changing the exchange rate. The ^{14}N nucleus in these experiments will not affect the dynamics of these experiments, as the quadrupolar relaxation of the C_1-symmetric complex is very fast (sub-millisecond).

The most significant difference in the DARTH and SHEATH dynamics is the exchange baseline, which is readily explained by the evolution of the singlet population (Fig. 2f) under these conditions and arises from the continual rebinding of unpolarized ligands after the previous species dissociates. The DARTH dynamics exhibit a significantly stronger exchange baseline as the initial consumption of the singlet order is consistently less by nearly a factor of 2 than the SHEATH dynamics, meaning that considerably more polarization may be generated by successively associating ligands. This effect arises as it is the secular term $(\hat{I}_{i,z}\hat{S}_{j,z})$ which drives the hyperpolarization dynamics, depreciating the magnitude of the state couplings with respect to a SHEATH Hamiltonian, where dynamics are driven by the non-secular $\hat{I}_i^{\pm}\hat{S}_j^{\mp}$ terms. Under the correct experimental conditions, significant population transfer may still be induced at high field while minimizing the singlet order consumption. The systems shown here exemplify two limits to SABRE dynamics, and, for instance, indicate that all SHEATH experiments should be performed with pulsed excitation but that hyperpolarization efficiency is generally greater for DARTH experiments under the correct conditions.

The systems and simulations shown in Fig. 2 all assume that the sample composition is either fully ^{15}N labeled (forming four spin-1/2 AA'XX' systems) or that the labeled ligand concentration is significantly greater than the unlabeled ligand concentration (forming the spin-1/2 AA'X systems). However, the simulations are readily extensible to the case where the target ligand is isotopically dilute and is exemplified by DARTH dynamics of such samples. In this case, we assume that most of the PTCs at time $t = 0$ do not contain polarizable (^{15}N) ligands, as ^{14}N-pyridine is significantly off-resonance from the DARTH pulse and will not generate hyperpolarization. However, the ^{14}N-pyridine must be included in the spin system as auxiliary nucleus, as the quadrupolar relaxation time T_Q in a C_{2v}-symmetic complex, like the tris-pyridine complex used in the DARTH experiments, is known to be longer[43] than free pyridine. The ^{14}N resonance of the $[Ir(H)_2(IMes)(^{14}N\text{-}pyr)_3]^+$ complex is considerably broader than that of the ^{15}N resonance, with $T_Q = 2.2$ ms, and provides a relaxation mechanism that makes the singlet order of the hydrides significantly less effective at long times. This is the simplest chemical example of a co-ligand which alters the coherent-component of the dynamics, highlighting the extensibility of the QMC simulations to study a rich variety of SABRE systems. When ^{15}N-ligands do bind, the dynamics are dominated by species with one bound, labeled ligand (forming four spin AA'XQ systems, where Q = ^{14}N-pyridine); and that when a polarized ligand dissociates, it is usually replaced with an unpolarizable ligand, hence the ^{15}N-magnetization does not evolve under a DARTH pulse. Depending on sample composition and dissociation rates of the various ligands, the average time where the catalyst is hyperpolarization inactive, here called $T_{inactive}$, is often important for the dynamics.

If $T_{inactive}$ is long with respect to the hydride exchange and the inter-pulse delay is short, the DARTH-SABRE experiment becomes quasi-CW, for which it is sufficient to simulate the system as if the PTCs only bind a hyperpolarization active ligand once (Fig. 3) as each active PTC will, on average, only see a single pulse and the probability of initializing at a time other than $t = 0$ is negligible. This effect changes when $T_{inactive}$ is shorter than the hydride exchange, in which case initialization must be allowed at any time during the dynamics (Fig. 3). The length of $T_{inactive}$ may be motivated from statistics and is taken to be $T_{inactive} = (k_{d,pyr}\,\zeta)^{-1}$, where ζ is the ^{15}N-enrichment.

When comparing the isotopically enriched samples to the natural abundance samples, the inclusion of a $T_{inactive} = 12$ s accounts for the deviation of the re-binding dynamics from the

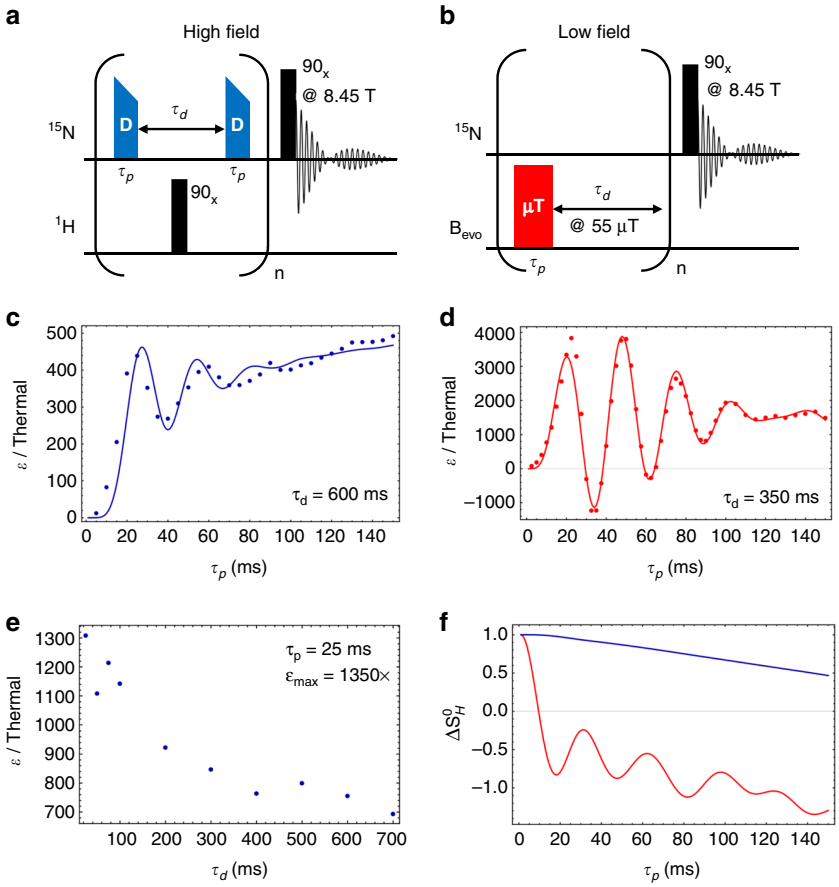

Fig. 2 Coherent hyperpolarization experiments. **a** DARTH_SABRE pulse sequence, where DARTH-pulses of length τ_p are given at intervals of τ_d for "n" repetitions and applied to the bound ^{15}N spin slightly off-resonance. The pulses adiabatically ramp towards the optimal matching condition to induce higher polarizations. **b** Coherent SHEATH pulse sequence, where analogous pulses are delivered to the sample at the optimal field condition, which is typically ≈0.5 μT, with inter-pulse delays using a ≈55 μT field to store magnetization. **c** Experimental DARTH-SABRE dynamics of an AA'XX' spin system using 50 mM ^{15}N-pyridine with an inter-pulse delay of τ_d=600 μs at 8.45 T. **d** Experimental coherent SHEATH dynamics of an AA'X spin system using 100 mM ^{15}N-benzonitrile with 33 mM pyridine and an inter-pulse delay of τ_d = 350 ms; detection was performed at 8.45 T. Data are shown fit to numerical QMC simulations using average PTC lifetimes of 20 ms (DARTH) and 50 ms (SHEATH). **e** Polarization as a function of the delay parameter for the DARTH-SABRE sequence using a 25 ms DARTH pulse, which corresponds to a π pulse. **f** Evolution of singlet population excess (DARTH AA'XX': S_H^0–T_H^0, blue line; SHEATH AA'X: S_H^0–T_H^-, red line) under the conditions used in the fit of the experimental data and normalized to the initial S_H^0 population

isotopically enriched sample (a lack of a significant exchange baseline), suggesting that sample composition is a critical factor to consider when deciding to run a pulsed experiment like DARTH-SABRE or a static-field experiment like SABRE-SHEATH. The highest overall enhancements are achieved in this fractionally labeled regime, and the highest relative polarizations are observed in the coherent dynamics regime (~20 ms DARTH-pulse). The re-binding effect may be recovered, as predicted from the simulations, by lengthening the delay time to 600 ms (Fig. 3). A 14% ^{15}N-enriched sample was prepared to mimic the binding dynamics of the natural abundance system but with greater signal-to-noise. For this system, $T_{inactive} = 350$ ms is sufficiently long for the experimentally observed window to reproduce the same effect while maintaining the condition that $T_{inactive} < k_{d,H2}^{-1}$. To confirm that this sample adequately reproduced the binding dynamics of the natural abundance system, the dynamics were monitored both with and without the ^{1}H-refocusing pulse, which confirmed that $T_{inactive}$ of the order of the lifetime of the hydrides as there was no additional enhancement observed.

SABRE is also very important for the hyperpolarization of both ^{1}H and ^{13}C, by which the mechanism is either direct polarization via *J*-couplings between the target nucleus and the *p*-H_2 derived hydrides or by spin-relay from a ^{15}N nucleus. As evolution in the QMC simulation is performed fully quantum mechanically, it is trivial to examine the hyperpolarization dynamics of these other nuclei and arbitrarily complex systems up to 15-spins may be studied. This size restriction only arises as this is the limit of the size of the Hamiltonian that can be exponentiated exactly in Hilbert space, which is how the QMC simulations are constructed. In either case, the construction of the simulation is (in effect) no different than as described above, with only alterations in the quantum part of the spin Hamiltonian to incorporate these nuclei and ensuring that all nuclei associated with one ligand dissociate simultaneously. These systems are often of greater complexity than the simple 3-spin and 4-spin systems shown previously. In fact, the simulation of the ortho-^{1}H line-shape on the ^{15}N-pyridine ring after a single 25 ms DARTH pulse requires the construction of an 8-spin AA'(XB_2)($X'B'_2$) system (Fig. 4). Instead of recording the polarization at each step, the density matrix of each dissociating pyridine was ensemble averaged using the QMC routine, which was then used to seed a simple pulse-acquire routine to generate the ^{1}H spectrum

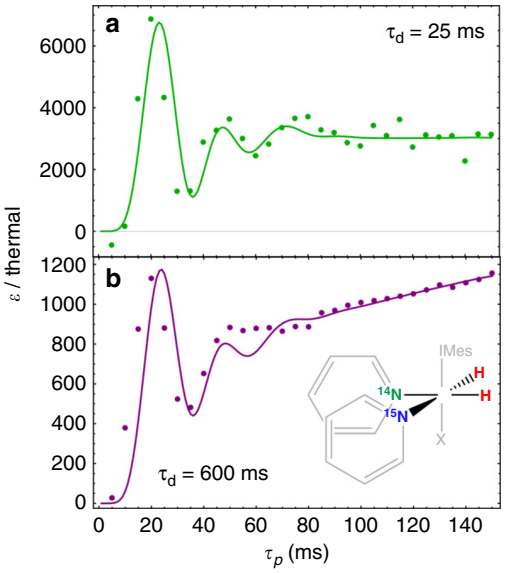

Fig. 3 Dynamics of isotopically dilute samples. Samples have final pyridine concentrations of 50 mM. **a** DARTH dynamics of natural abundance pyridine with delays $\tau_d = 25$ ms, making the dynamics quasi-CW. **b** DARTH dynamics of 15% labeled pyridine with delays $\tau_d = 600$ ms. Data are shown fit to numerical simulation with an average PTC lifetime of 20 ms

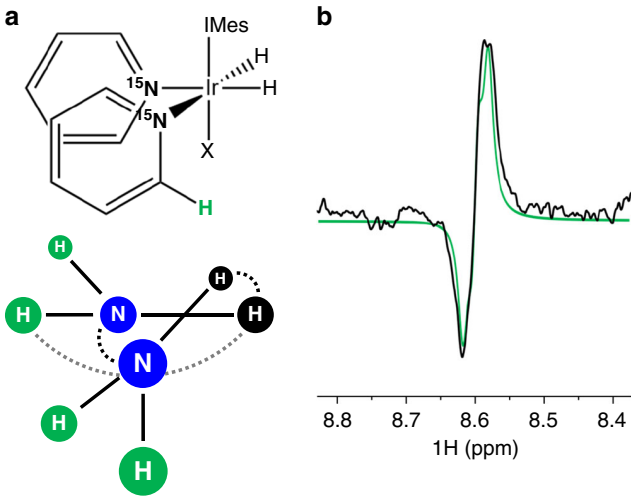

Fig. 4 Prediction of the ortho-^{1}H resonance lineshape after 25 ms DARTH pulse. **a** Chemical system and magnetic structure used in the simulation along with its dominant homonuclear (dashed, black) and heteronuclear (solid, black) J couplings, as well as the long-range $^4J_{HH}$ coupling (dashed, gray). **b** Experimental specrrum (black) along with fit (green) from QMC simulation

(Fig. 4b). As can be seen from Fig. 4, the theoretical result matches the experimental spectrum with excellent accuracy, emphasizing the robust nature of the QMC simulations.

SABRE chemical dynamics. In addition to providing critical insight into the hyperpolarization dynamics of SABRE, these coherent techniques may also yield critical information as to the chemical dynamics of the SABRE processes. This is exemplified here in to ways; firstly, we may utilize a DARTH-pulse to construct a DARTH-EXSY hybrid experiment to directly measure the hydride dissociation rate (Fig. 4) and we find it to be around 550 ms, more than 10 times the ligand exchange rate. The DARTH pulse generates a hyperpolarized triplet state on the hydrides, which exchanges off the complex during the delay time. By reducing the DARTH-SABRE sequence to a single pulse, one may directly measure the hydride rate of dissociation (Fig. 4b). Measuring the hydride kinetics like this concatenates the inherently second-order kinetics of the hydride exchange and makes it appear as only being first order, as there is distinguishability between the dissociating and associating species.

The pulsed SABRE-SHEATH experiments also provide opportunities to probe the chemical dynamics of the hyperpolarization process. For example, optimization of τ_d leads to the investigation of aspects of the chemical dynamics that evolve during the delay time. During τ_d, chemical exchange continues and fractionally recharges the singlet state on the hydrides. As apparent from Fig. 5c, τ_d is experimentally optimized at about 350 ms for experiments where the total length of the pulsing period was kept constant. Note that a sequence of 22 ms on resonance, followed by 2 s off resonance, then repeated many times (a 1% duty cycle) gives more

total signal than staying constantly on resonance. However, while keeping the experiment length constant is a reasonable practical comparison, it is much more instructive to look at the enhancement per pulse, which varies by a factor of 47 as the delay is changed (Fig. 5c). For very short times of τ_d, a single complex will experience multiple pulses at the evolution field before dissociation, and since the length was picked for optimal single-pulse excitation the signal is reduced; this effect would be expected to disappear with a higher dissociation rate. Figure 5C also shows that, beyond the ligand exchange rate, there is a second timescale to the delay dynamics, associated with the hydrogen exchange, giving a slowly rising component (at long times) of this data, characterizing the para-H_2 regeneration. Accordingly, observing the hyperpolarization dynamics as a function of the storage period τ_d contributes even more information about the dynamics of the entire system.

Discussion

We have shown that the DARTH-SABRE and coherent SHEATH experiments boast the ability to monitor the coherent hyperpolarization dynamics under the influence of chemical exchange. Accessing the coherent SABRE dynamics has shown the ability to bypass the damping of the hyperpolarized signal by the SABRE exchange dynamics in certain regimes, which is critical for ligands with exchange rates disparate from the period of their coherent evolution. Moreover, coherent SABRE hyperpolarization has proven to be an ideal model to study quantum systems that evolve under the influence of chemical exchange dynamics, which is readily extensible to many other complex systems, such as the 8-spin AA'(XB_2)(X'B'_2) system shown here. The implications of the above results are as follows: for a given proposed hyperpolarization substrate, the nuclear spin topology and chemical exchange rate of the ligand will have a considerable effect on the coherent polarization dynamics. The ability to study the coherent polarization dynamics at any field, in turn, allows for a more extensive set of spin topologies and system dynamics to be investigated, each providing a constraint in the design of an optimal hyperpolarization substrate.

Methods

Sample preparation and experiment details. Suitable volumes of a solution of pre-catalyst [Ir(IMes)(COD)Cl] (IMes = 1,3-bis(2,4,6-trimethylphenyl)imidazol-2-ylidene, COD = 1,5-cyclooctadiene) and diluted solutions of pyridine and/or labeled benzonitrile (in methanol-d_4) are combined to obtain samples 5 mM in pre-catalyst, 33 mM in pyridine and 100 mM in ^{15}N-benzonitrile for coherent

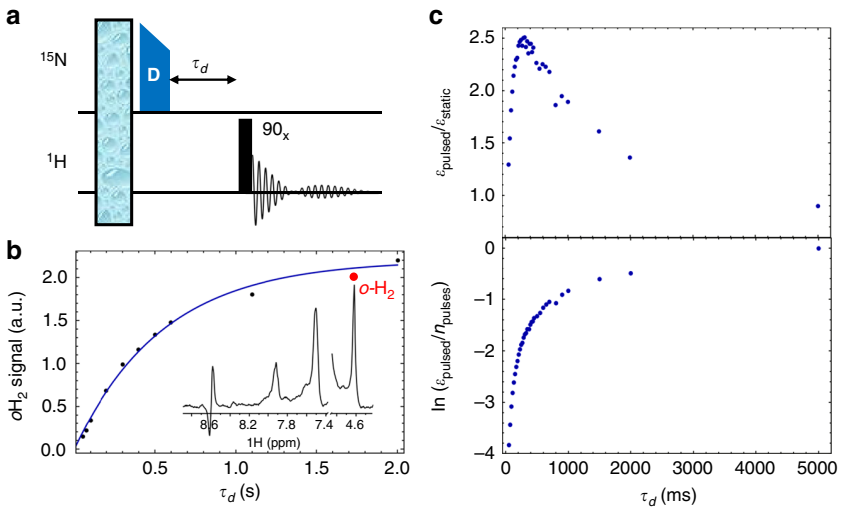

Fig. 5 Delay dynamics of coherent hyperpolarization experiment. **a** DARTH-EXSY pulse sequence, which uses a pre-saturation bubbling scheme to directly measure exchange of the hyperpolarized hydride. Thermal T_1 from inversion recovery is 888.4 ± 2.7 ms. **b** DARTH-EXSY signal on ortho-hydrogen weighted with T_1, yielding an average hydride lifetime of 547 ± 32 ms, making singlet order replentishment significantly slower than the ligand exchange. DARTH-EXSY spectrum (single shot, inset) with the signals of hyperpolarized ortho-hydrogen (red) indicated. **c** SHEATH delay dynamics show optimum total signal at $\tau_d = 350$ ms (top plot). Calculating the signal per pulse (bottom plot) also shows the effect of slow hydrogen replentishment with the gradually rising signal at long delay times

SHEATH experiments or samples 4.4 mM in pre-catalyst and 50 mM in pyridine (50 mM, 7 mM, or 0.18 mM in ^{15}N-pyridine). 500 µL of sample are transferred to a medium wall pressure NMR tube (Wilmad 524-PV-7) and transformed into the catalytically active species with a constant low flow of *para*-hydrogen (50 sccm/min, 45 min at 20 °C and 8 bar). Note that pyridine facilitates activation and acts as a coligand for the PTC complex. Absence of pyridine leads to extremely slow catalyst activation (~72 h at 20 °C) and significantly decreased substrate polarization if benzonitrile is used as a substrate. For all experiments, hyperpolarized signal is detected at 8.45 T.

Numeric SABRE simulation. For a given simulation length, a certain number of discrete dissociation events were sampled from a uniform probability distribution. Evolution between these timepoints is dictated only by the Magnus solution to the Liouville von Neumann equation. At the point of dissociation, the dissociation group is selectively traced out of the PTC spin density using tensor contraction in the spin product basis, at which point the singlet order on the parahydrogen is fractionally replenished and a new, unpolarized ligand is introduced to the system. This method maintains coherences between the spins that remain on the PTC. The simulations were averaged over 1600 iterations, which exhibits an error of approximately 1% with respect to a solution exhibiting errors of $O(10^{-7})$, which was taken at 100,000 iterations.

Data availability

All relevant data shown in the main text and the supplementary information are available from the authors upon request and are used in the example code in the supplementary information. Please contact jacob.lindale@duke.edu or warren.warren@duke.edu for access to the data shown here.

Received: 24 August 2018 Accepted: 21 December 2018
Published online: 23 January 2019

References

1. Abragam, A. & Goldman, M. Principles of dynamic nuclear-polarization. *Rep. Prog. Phys.* **41**, 395–467 (1978).
2. Barnes, A. B. et al. High-field dynamic nuclear polarization for solid and solution biological NMR. *Appl. Magn. Reson.* **34**, 237–263 (2008).
3. Bornet, A. et al. Boosting dissolution dynamic nuclear polarization by cross polarization. *J. Phys. Chem. Lett.* **4**, 111–114 (2013).
4. Jannin, S., Bornet, A., Colombo, S. & Bodenhausen, G. Low-temperature cross polarization in view of enhancing dissolution Dynamic Nuclear Polarization in NMR. *Chem. Phys. Lett.* **517**, 234–236 (2011).
5. Prisner, T. F. in *NMR of Biomolecules*. 419–431 (eds Ivano Bertini, Kathleen S. McGreevy, Giacomo Parigi) (Wiley-VCH Verlag GmbH & Co. KGaA, University of Florence, 2012).
6. Ardenkjaer-Larsen, J. H. et al. Increase in signal-to-noise ratio of >10,000 times in liquid-state NMR. *Proc. Natl Acad. Sci. USA* **100**, 10158–10163 (2003).
7. Goez, M. Photo-C. I. D. N. P. Spectroscopy. *Annu. Rep. NMR Spectro* **66**, 77–147 (2009).
8. Ivanov, K. L. et al. Transfer of CIDNP among coupled spins at low magnetic field. *Appl. Magn. Reson.* **30**, 513–534 (2006).
9. Vermeersch, G., Marko, J., Febvaygarot, N., Caplain, S. & Lablachecombier, A. Low-Field Photochemically Induced Dynamic Nuclear-Polarization (Photo-Cidnp) of Diazanaphthalenes. *J. Chem. Soc. Perk T* **2**, 2027–2030 (1984).
10. Atkinson, K. D. et al. Para-hydrogen induced polarization without incorporation of para-hydrogen into the analyte. *Inorg. Chem.* **48**, 663–670 (2009).
11. Bhattacharya, P. et al. Parahydrogen-induced polarization (PHIP) hyperpolarized MR receptor imaging in vivo: a pilot study of 13C imaging of atheroma in mice. *NMR Biomed.* **24**, 1023–1028 (2011).
12. Duckett, S. B. & Blazina, D. The study of inorganic systems by NMR spectroscopy in conjunction with parahydrogen-induced polarisation. *Eur. J. Inorg. Chem.* **2003**, 2901–2912 (2003).
13. Ivanov, K. L., Yurkovskaya, A. V. & Vieth, H. M. Parahydrogen induced polarization in scalar coupled systems: analytical solutions for spectral patterns and their field dependence. *Z. Phys. Chem.* **226**, 1315–1342 (2012).
14. Stevanato, G. AlternatingDelays Achieve Polarization Transfer (ADAPT) to heteronuclei in PHIP experiments. *J. Magn. Reson.* **274**, 148–162 (2017).
15. Bowers, C. R. & Weitekamp, D. P. Parahydrogen and synthesis allow dramatically enhanced nuclear alignment. *J. Am. Chem. Soc.* **109**, 5541–5542 (1987).
16. Bowers, C. R. & Weitekamp, D. P. Transformation of symmetrization order to nuclear-spin magnetization by chemical-reaction and nuclear-magnetic-resonance. *Phys. Rev. Lett.* **57**, 2645–2648 (1986).
17. Eisenschmid, T. C. et al. Para hydrogen induced polarization in hydrogenation reactions. *J. Am. Chem. Soc.* **109**, 8089–8091 (1987).
18. Barskiy, D. A. et al. In situ and ex situ low-field NMR spectroscopy and MRI endowed by SABRE hyperpolarization. *Chemphyschem* **15**, 4100–4107 (2014).
19. Colell, J. F. et al. Generalizing, extending, and maximizing nitrogen-15 hyperpolarization induced by parahydrogen in reversible exchange. *J. Phys. Chem. C.* **121**, 6626–6634 (2017).
20. Knecht, S., Pravdivtsev, A. N., Hövener, J.-B., Yurkovskaya, A. V. & Ivanov, K. L. Quantitative description of the SABRE process: rigorous consideration of spin dynamics and chemical exchange. *RSC Adv.* **6**, 24470–24477 (2016).
21. Pravdivtsev, A. N., Yurkovskaya, A. V., Vieth, H. M. & Ivanov, K. L. RF-SABRE: a way to continuous spin hyperpolarization at high magnetic fields. *J. Phys. Chem. B* **119**, 13619–13629 (2015).
22. Pravdivtsev, A. N., Yurkovskaya, A. V., Zimmermann, H., Vieth, H.-M. & Ivanov, K. L. Transfer of SABRE-derived hyperpolarization to spin-1/2 heteronuclei. *RSC Adv.* **5**, 63615–63623 (2015).

23. Pravdivtsev, A. N., Yurkovskaya, A. V., Zimmermann, H., Vieth, H.-M. & Ivanov, K. L. Enhancing NMR of insensitive nuclei by transfer of SABRE spin hyperpolarization. *Chem. Phys. Lett.* **661**, 77–82 (2016).
24. Theis, T. et al. Direct and cost-efficient hyperpolarization of long-lived nuclear spin states on universal (15)N2-diazirine molecular tags. *Sci. Adv.* **2**, e1501438 (2016).
25. Theis, T., Truong, M., Coffey, A. M., Chekmenev, E. Y. & Warren, W. S. LIGHT-SABRE enables efficient in-magnet catalytic hyperpolarization. *J. Magn. Reson.* **248**, 23–26 (2014).
26. Theis, T. et al. Microtesla SABRE Enables 10% Nitrogen-15 Nuclear Spin Polarization. *J. Am. Chem. Soc.* **137**, 1404–1407 (2015).
27. Adams, R. W. et al. Reversible interactions with para-hydrogen enhance NMR sensitivity by polarization transfer. *Science* **323**, 1708–1711 (2009).
28. Cowley, M. J. et al. Iridium N-heterocyclic carbene complexes as efficient catalysts for magnetization transfer from para-hydrogen. *J. Am. Chem. Soc.* **133**, 6134–6137 (2011).
29. Hovener, J. B. et al. Parahydrogen-based hyperpolarization for biomedicine. *Angew. Chem. Int. Ed. Engl.* **57**, 11140–11162 (2018).
30. Truong, M. L. et al. 15N hyperpolarization by reversible exchange using SABRE-SHEATH. *J. Phys. Chem. C.* **119**, 8786–8797 (2015).
31. Barskiy, D. A. et al. The absence of quadrupolar nuclei facilitates efficient (13) C hyperpolarization via reversible exchange with parahydrogen. *Chemphyschem* **18**, 1493–1498 (2017).
32. Barskiy, D. A. et al. Over 20%15N hyperpolarization in under one minute for metronidazole, an antibiotic and hypoxia probe. *J. Am. Chem. Soc.* **138**, 8080–8083 (2016).
33. Nikolaou, P., Goodson, B. M. & Chekmenev, E. Y. NMR hyperpolarization techniques for biomedicine. *Chem. Eur. J.* **21**, 3156–3166 (2015).
34. Kurhanewicz, J. et al. Analysis of cancer metabolism by imaging hyperpolarized nuclei: prospects for translation to clinical research. *Neoplasia* **13**, 81–97 (2011).
35. Nelson, S. J. et al. Metabolic imaging of patients with prostate cancer using hyperpolarized [1-(1)(3)C]pyruvate. *Sci. Transl. Med.* **5**, 198ra108 (2013).
36. Mugler, J. P. 3rd & Altes, T. A. Hyperpolarized 129Xe MRI of the Human Lung. *J. Magn. Reson.* **37**, 313–331 (2013).
37. Hovener, J. B. et al. A hyperpolarized equilibrium for magnetic resonance. *Nat. Commun.* **4**, 2946 (2013).
38. Rayner, P. J. et al. Delivering strong 1H nuclear hyperpolarization levels and long magnetic lifetimes through signal amplification by reversible exchange. *Proc. Natl Acad. Sci. USA* **114**, E3188–E3194 (2017).
39. Shchepin, R. V. et al. 15)N Hyperpolarization of Imidazole-(15)N2 for Magnetic Resonance pH Sensing via SABRE-SHEATH. *ACS Sens.* **1**, 640–644 (2016).
40. Pravdivtsev, A. N., Yurkovskaya, A. V., Lukzen, N. N., Ivanov, K. L. & Vieth, H. M. Highly Efficient Polarization of Spin-1/2 Insensitive NMR Nuclei by Adiabatic Passage through Level Anticrossings. *J. Phys. Chem. Lett.* **5**, 3421–3426 (2014).
41. Pravdivtsev, A. N., Yurkovskaya, A. V., Lukzen, N. N., Vieth, H. M. & Ivanov, K. L. Exploiting level anti-crossings (LACs) in the rotating frame for transferring spin hyperpolarization. *Phys. Chem. Chem. Phys.* **16**, 18707–18719 (2014).
42. Pravdivtsev, A. N., Yurkovskaya, A. V., Vieth, H. M. & Ivanov, K. L. Spin mixing at level anti-crossings in the rotating frame makes high-field SABRE feasible. *Phys. Chem. Chem. Phys.* **16**, 24672–24675 (2014).
43. Hsieh, Y., Rubenacker, G. V., Cheng, C. P. & Brown, T. L. Nitrogen-14 nuclear quadrupole resonance spectra of coordinated pyridine. *J. Am. Chem. Soc.* **99**, 1384–1389 (1977).

Acknowledgements

The authors thank the following funding sources: NSF CHE-1363008 and CHE-1665090. Research reported in this publication was also supported by the National Institute of Biomedical Imaging and Bioengineering of the NIH under R21EB025313. E.Y.C. additionally thanks the following funding sources: NSF CHE-1416268, NIH 1R21EB020323, and R21CA220137, DOD CDMRP W81XWH-12-1-0159/BC112431 and W81XWH-15-1-0271 awards. J.R.L. and T.T. thank Nathan J. Adamson (Duke University, Department of Chemistry) and Dr. Steven J. Malcolmson for the purification of the [Ir(IMes)(COD)] Cl pre-catalyst.

Author contributions

J.R.L. designed the DARTH-SABRE experiment, and with S.L.E. collected the experimental data. J.R.L. and W.S.W. conceived and constructed the Quantum Monte Carlo model. C.P.N.T. contributed to the QMC model and, along with Z.Z., J.F.P.C., and G.Z, assisted with experimental data collection. T.T. and E.Y.C. performed initial experiments with ramped pulses. J.R.L., T.T., and W.S.W. wrote the paper.

Additional information

Supplementary Information accompanies this paper at https://doi.org/10.1038/s41467-019-08298-8.

Competing interests: The authors declare no competing interests.

Journal peer review information: *Nature Communications* thanks the anonymous reviewers for their contribution to the peer review of this work. Peer reviewer reports are available.

THE JOURNAL OF PHYSICAL CHEMISTRY Letters

Cite This: J. Phys. Chem. Lett. 2019, 10, 4229−4236

Letter

pubs.acs.org/JPCL

Quasi-Resonance Fluorine-19 Signal Amplification by Reversible Exchange

Nuwandi M. Ariyasingha,[†] Jacob R. Lindale,[‡] Shannon L. Eriksson,[‡,§] Grayson P. Clark,[∥] Thomas Theis,[⊥] Roman V. Shchepin,[#] Nikita V. Chukanov,[▽,○] Kirill V. Kovtunov,[▽,○] Igor V. Koptyug,[▽,○] Warren S. Warren,[◆] and Eduard Y. Chekmenev*[,†,¶]

[†]Department of Chemistry, Integrative Biosciences (Ibio), Wayne State University, Karmanos Cancer Institute (KCI), Detroit, Michigan 48202, United States

[‡]Department of Chemistry, Duke University, Durham, North Carolina 27708, United States

[§]School of Medicine, Duke University, Durham, North Carolina 27708, United States

[∥]Department of Biomedical Engineering, Duke University, Durham, North Carolina 27708, United States

[⊥]Department of Chemistry, North Carolina State University, Raleigh, North Carolina 27695-8204, United States

[#]Department of Chemistry and Applied Biological Sciences, South Dakota School of Mines and Technology, Rapid City, South Dakota 57701, United States

[▽]International Tomography Center, SB RAS, 3A Institutskaya St., Novosibirsk 630090, Russia

[○]Novosibirsk State University, 2 Pirogova St., Novosibirsk 630090, Russia

[◆]Departments of Physics, Chemistry, Biomedical Engineering, and Radiology, Duke University, Durham, North Carolina 27708, United States

[¶]Russian Academy of Sciences, Leninskiy Prospekt 14, Moscow, 119991, Russia

Supporting Information

ABSTRACT: We report on an extension of the quasi-resonance (QUASR) pulse sequence used for signal amplification by reversible exchange (SABRE), showing that we may target distantly *J*-coupled ^{19}F-spins. Polarization transfer from the parahydrogen-derived hydrides to the ^{19}F nucleus is accomplished via weak five-bond *J*-couplings using a shaped QUASR radio frequency pulse at a 0.05 T magnetic field. The net result is the direct generation of hyperpolarized ^{19}F *z*-magnetization, derived from the parahydrogen singlet order. An accumulation of ^{19}F polarization on the free ligand is achieved with subsequent repetition of this pulse sequence. The hyperpolarized ^{19}F signal exhibits clear dependence on the pulse length, irradiation frequency, and delay time in a manner similar to that reported for ^{15}N QUASR-SABRE. Moreover, the hyperpolarized ^{19}F signals of 3-^{19}F-^{14}N-pyridine and 3-^{19}F-^{15}N-pyridine isotopologues are similar, suggesting that (i) polarization transfer via QUASR-SABRE is irrespective of the nitrogen isotopologue and (ii) the presence or absence of the spin-1/2 ^{15}N nucleus has no impact on the efficiency of QUASR-SABRE polarization transfer. Although optimization of polarization transfer efficiency to ^{19}F ($P_{^{19}F} \approx 0.1\%$) was not the goal of this study, we show that high-field SABRE can be efficient and broadly applicable for direct hyperpolarization of ^{19}F spins.

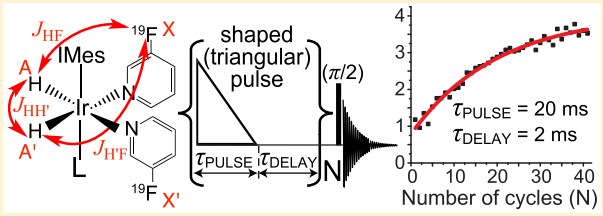

Hyperpolarization techniques increase nuclear spin polarization (*P*) by several orders of magnitude, enabling the corresponding gains in signals over that attainable via conventional NMR spectroscopy and MRI.[1−4] This revolutionary boost in detection sensitivity enables new applications such as detection of dilute biologically relevant molecules both in vitro[5−7] and in vivo.[8−12] A particularly exciting hyperpolarization technique is signal amplification by reversible exchange (SABRE), pioneered by Duckett and co-workers.[13−17] SABRE relies on simultaneous chemical exchange of parahydrogen (p-H_2) and substrate targeted for hyperpolarization (S) with an iridium polarization transfer catalyst (PTC), Figure 1a, during which the singlet order from the p-H_2-derived hydrides is allowed to transfer to the nuclear spins of the target substrates via the network of *J*-couplings. SABRE has gained popularity[18] because it is fast, efficient, and inexpensive relative to competing techniques. Polarization transfer is frequently accomplished in less than a minute with polarizations *P* sometimes exceeding 30%,[19−21] at a cost several orders of magnitude smaller than that of dissolution dynamic

Received: May 25, 2019
Accepted: July 10, 2019
Published: July 10, 2019

DOI: 10.1021/acs.jpclett.9b01505
J. Phys. Chem. Lett. 2019, 10, 4229−4236

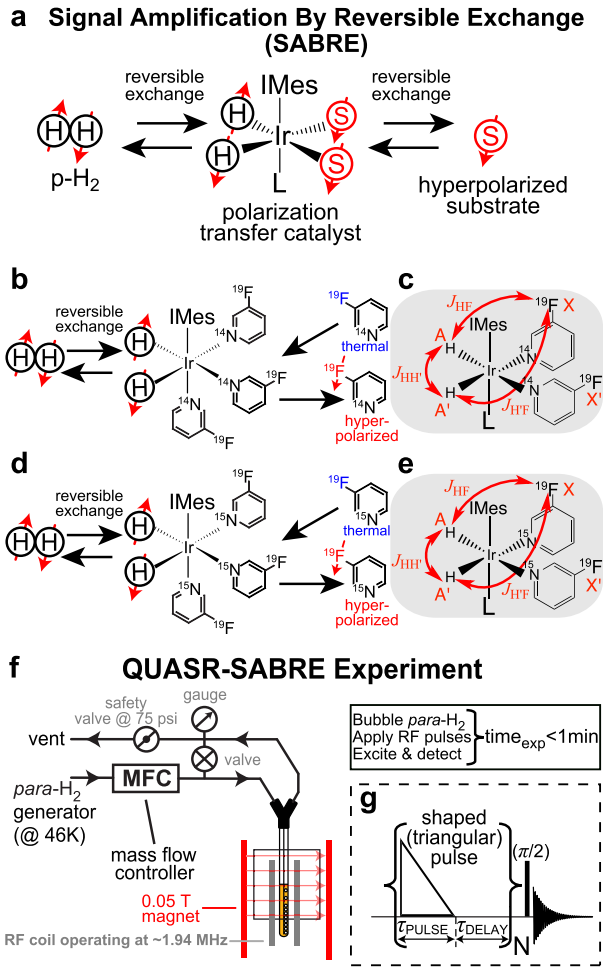

Figure 1. (a) Schematic of simultaneous chemical exchange of parahydrogen (p-H_2) and target substrate (S) on an activated IrIMes PTC in SABRE hyperpolarization process. (b) Schematic of SABRE chemical exchange with 3-^{19}F-pyridine as a substrate. (c) Spin system formed on the IrIMes catalyst with 3-^{19}F-pyridine as a substrate. (d) Schematic of SABRE chemical exchange with 3-^{19}F-^{15}N-pyridine as a substrate. (e) Spin system formed on the IrIMes catalyst with 3-^{19}F-^{15}N-pyridine as a substrate. Note the difference between the spin systems shown in panels c and e due to the presence of ^{14}N (natural abundance) and ^{15}N (isotopically enriched) nuclei. It is important to note that $^{5}J_{FH} \neq {}^{5}J_{FH'}$ in both panels c and e. (f) Schematic of the experimental setup for ^{19}F QUASR-SABRE experiment. (g) Overall schematic for quasi-resonance SABRE RF pulsing.

nuclear polarization (d-DNP), an alternative method of hyperpolarization.[4,22]

There are two major approaches for polarization transfer in SABRE. The first approach is conventional SABRE, which relies on coherently driven dynamics generated at a level anticrossing (LACs).[23,24] The LAC condition is achieved by matching a static magnetic field to the resonance frequency of the singlet to target magnetization transition, allowing flow of spin order through J-couplings of nuclear spins involved in the polarization transfer.[13] For the homonuclear case of conventional SABRE, as in polarization transfer from p-H_2-derived hydrides to the protons on the target substrate, the LAC condition is met at a magnetic field of a few millitesla and is determined by the chemical shift difference between p-H_2-derived hydrides and the target protons. For the heteronuclear case of conventional SABRE, broadly referring to polarization transfer from p-H_2-derived hydrides to the substrate's ^{13}C,[25] ^{15}N,[26] ^{31}P,[27] etc., the LAC condition is met at a magnetic field of a few microtesla,[26,28−30] determined by the difference in gyromagnetic ratios of the proton and target nucleus. The second approach to polarization transfer relies on application of radio frequency (RF) pulses, which are employed to create LAC conditions in an arbitrarily high magnetic field, e.g., the low-irradiation generation of high tesla-SABRE (LIGHT-SABRE) pulse sequence.[31] A number of other approaches have been demonstrated over the years, such as RF-SABRE,[32] spin-lock induced crossing-SABRE (SLIC-SABRE),[33] delayed adiabatic ramps transfer hyperpolarization-SABRE (DARTH-SABRE),[34] and others.[35,36] One key strength of the RF-based approach, which has remained largely unrealized, is the potential to perform SABRE at a wide range of magnetic fields. For example, one can use low-field, and potentially portable, electromagnets; high-resolution NMR spectrometers; or MRI scanners. The RF-based approaches have primarily focused on SABRE of ^{15}N spins for two reasons: First, the dipolar relaxation of ^{15}N magnetization is significantly longer and there is great potential for extremely long-lived ($T_s \approx 20$ min) $^{15}N_2$ singlet states.[37−43] Second, isotopic enrichment of ^{15}N heterocycles[44−46] and other molecular carriers that efficiently bind iridium is relatively simple.[45,47]

SABRE hyperpolarization of ^{19}F spins is particularly attractive, because the ^{19}F spin has the second highest detection sensitivity among stable nuclei with a gyromagnetic ratio ($\gamma_{^{19}F}$) of $0.93{\cdot}\gamma_{^{1}H}$, and approximately $9{\cdot}\gamma_{^{15}N}$. Moreover, unlike ^{15}N and ^{13}C, ^{19}F is nearly 100% naturally abundant, obviating the need for isotopic enrichment needed for ^{15}N- and ^{13}C-labeled targets. While ^{19}F is found in more than 20% of drugs,[48,49] it has a negligible biological presence, making its spectroscopic and imaging detection relatively background-free compared to that of proton spins. This allows the potential for broad applications for the theranostic imaging and studies of drug interactions. To the best of our knowledge, there have been five previous reports on SABRE hyperpolarization of ^{19}F using spontaneous polarization transfer and no reported efforts using an RF-based SABRE approach.[13,50−53] In this work, we employ a recently developed QUASi-Resonance SABRE[54] (QUASR-SABRE) experiment, relying on SLIC pulses,[55] for feasibility studies of RF-based hyperpolarization of ^{19}F spins five bonds removed from the p-H_2-derived hydrides.

For this study, we have used two compounds as SABRE substrates: 3-^{19}F-pyridine (196665, Sigma-Aldrich) and recently synthesized 3-^{19}F-^{15}N-pyridine,[51] seen in panels b and d of Figure 1, respectively. Panels c and e of Figure 1 show the network of J-couplings formed during the temporary association of p-H_2 and the corresponding target substrates with an activated precatalyst [Ir(IMes)(COD)Cl] (IMes = 1,3-bis(2,4,6-trimethylphenyl)imidazol-2-ylidene, COD = 1,5-cyclooctadiene).[17] A solution of 100 mM substrates (3-^{19}F-pyridine or 3-^{19}F-^{15}N-pyridine) and 5 mM IrIMes[17] catalyst was prepared in methanol-d_4 and activated for at least 30 min with pH_2 flow of 20 standard cubic centimeters (sccm) . Approximately 87% pH_2 was directed into a medium-walled 5 mm NMR tube setup at a flow rate of ∼70 sccm while the QUASR-SABRE pulse sequence was applied (Figure 1g).

We have employed three different ^{19}F hyperpolarization approaches: (i) QUASR-SABRE; (ii) in situ SABRE, the

DOI: 10.1021/acs.jpclett.9b01505
J. Phys. Chem. Lett. 2019, 10, 4229−4236

process of hyperpolarization by applying a 90-degree hard pulse during p-H_2 bubbling at the spectrometer field (0.05 T); and (iii) conventional SABRE at 6 mT.[13,55] The QUASR-SABRE study of 3-^{19}F-pyridine and 3-^{19}F-^{15}N-pyridine was performed using a 0.05 T NMR spectrometer under similar experimental conditions[54] but with the spectrometer operating at the ^{19}F Larmor frequency (1.94 MHz). The shaped pulse was applied with a maximum ω_1 = 1.24 kHz and a ramp down to ω_1 = 0 Hz for τ_{PULSE}, followed by a subsequent inter-pulse delay τ_{DELAY} (Figure 1f). Given significant nonlinearities in the low-power range of the radio frequency (RF) amplifier, the actual applied pulse can be closely approximated with a truncated double-Gaussian pulse of the form

$$s(t) = \frac{1}{2}(a_1 e^{-t^2/\tau_{PULSE}^2\cdot\sigma_1} + a_2 e^{-t^2/\tau_{PULSE}^2\cdot\sigma_2}) \left(1 - \tanh\left(\frac{t}{\tau_{PULSE}\cdot\delta} - a_3\right)\right) \quad (1)$$

The values for each of the variables in eq 1 are given in the Supporting Information. This QUASR-SABRE pulse sequence has the potential to be applied without modifications dependent on molecular parameters, like the magnitude of the J-couplings or chemical shifts. The large pulse power and ramped pulse shape make hyperpolarization insensitive to the frequency offset despite pumping the LAC far from the optimal resonance condition. The process of pulsing and delay was repeated N times before irradiating the sample with a hard 90-pulse similar to previous work,[54] and the free induction decay was detected (Figure 1g).

Recently, a quantum Monte Carlo (QMC) simulation approach to SABRE dynamics was introduced,[38] which demonstrated the ability to predict coherent hyperpolarization dynamics for pulsed SABRE experiments with high accuracy. However, this method would have a prohibitive computational cost in the limit where there is a significant degree of coupling between each pulse, like the case here, as the entire pulse-train must be simulated. So long as the time-step of the simulation is much smaller than the lifetime of the SABRE complex τ_{PTC}, the coherent hyperpolarization dynamics are well-approximated by

$$\partial_t\hat{\rho} = -i[\hat{H}, \hat{\rho}] - \frac{\hat{M}\hat{\rho}}{\tau_{PTC}} \quad (2)$$

where $\hat{M}$ is the same operator to control exchange as used in the QMC simulation. The approximation made by eq 2 has the distinct advantage that it has a simple numerical solution that does not require iteration, making the simulation incredibly fast. This makes the explicit calculation of the effects of entire pulse sequences tractable, as opposed to approximating the dynamics as being identical and additive under each pulse, as done previously. In the simulations shown here, we have used a 10 μs step size and have approximated the $\tau_{PTC} \approx 25$ ms. We note that this spin system is at the upper computational limit for Liouville space; however, it is far from the 15-spin limit of the Hilbert-space methods utilized here.

Specifically, we have constructed this system to include the parahydrogen-derived hydrides, the long-range ^{19}F nuclei, and ortho-protons on pyridine, as it is assumed that all other couplings are either small or will not significantly affect the ^{19}F hyperpolarization dynamics. This forms a six-spin AA′(BX)-(B′X′) system with the Hamiltonian:

$$\hat{H}(t) = \sum_i \Delta\omega_i\hat{I}_{iz} + \Delta\omega_F(\hat{S}_{4z} + \hat{S}_{6z}) + 2\pi\left[J_{HH}\hat{I}_1\cdot\hat{I}_2 + J_{HH'}(\hat{I}_{1z}\hat{I}_{3z} + \hat{I}_{2z}\hat{I}_{5z}) + J_{HF}(\hat{I}_{1z}\hat{S}_{4z} + \hat{I}_{2z}\hat{S}_{6z}) + J_{H'F}(\hat{I}_{3z}\hat{S}_{4z} + \hat{I}_{5z}\hat{S}_{6z})\right] + \omega_{1F}(t)(\hat{S}_{4x} + \hat{S}_{6x}) \quad (3)$$

The $J_{HH'}$ term is the coupling between the hydrides on the ortho-proton, J_{HF} the long-range $^5J_{HF}$ coupling, $J_{H'F}$ the ortho-proton to ^{19}F ^3J-coupling, and $\omega_{1F}(t)$ the time-dependent pulse shape in the case of the QUASR-SABRE pulse sequence.

The ^{19}F QUASR-SABRE spectra of 3-^{19}F-pyridine and 3-^{19}F-^{15}N-pyridine are shown in panels a and b of Figure 2, respectively, exhibiting $\varepsilon^{19}_F \approx 6700$ ($P_F \approx 0.10\%$) and $\varepsilon^{19}_F \approx 7100$ ($P_F \approx 0.11\%$), respectively. Conventional SABRE yielded an $\varepsilon_F \approx 17\,800$ ($P_F \approx 0.26\%$) for 3-^{19}F-^{15}N-pyridine, shown in Figure 2f, which is highly surprising as there are no resonance conditions at 6 mT that lead to hyperpolarized fluorine magnetization. The resonance condition for ^{19}F hyperpolariza-

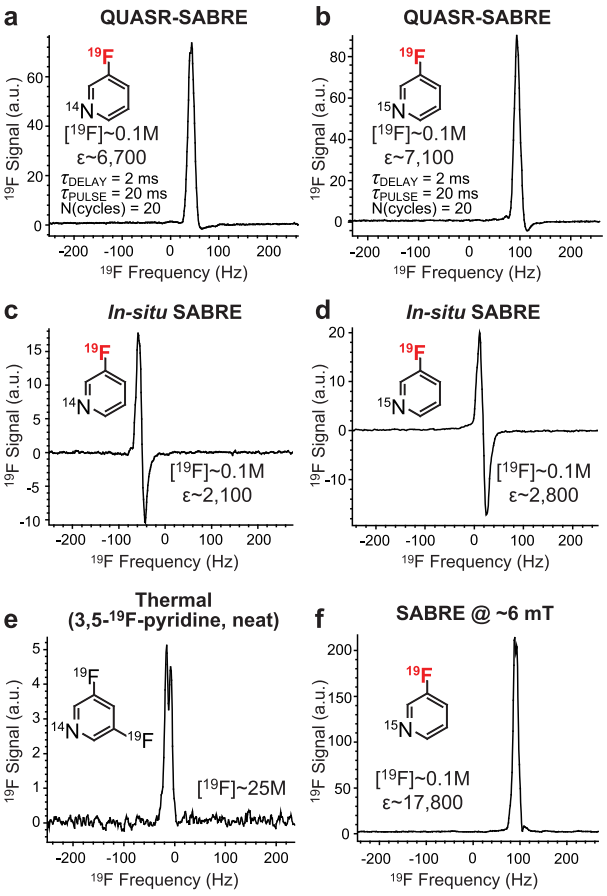

Figure 2. ^{19}F spectra of QUASR-SABRE hyperpolarized 3-^{19}F-pyridine (a) and of QUASR-SABRE hyperpolarized 3-^{19}F-^{15}N-pyridine (b). ^{19}F in situ SABRE spectra of hyperpolarized 3-^{19}F-pyridine (c) and 3-^{19}F-^{15}N-pyridine (d). Note that although the signals are hyperpolarized, the NMR lines are antiphase, which may not be suitable for some MRI sequences. ^{19}F spectrum of thermally polarized signal reference neat 3,5-^{19}F-pyridine (e). ^{19}F spectrum of 3-^{19}F-^{15}N-pyridine hyperpolarized via conventional SABRE at ~6 mT (f). All NMR spectra were acquired using a single scan.

DOI: 10.1021/acs.jpclett.9b01505
J. Phys. Chem. Lett. 2019, 10, 4229−4236

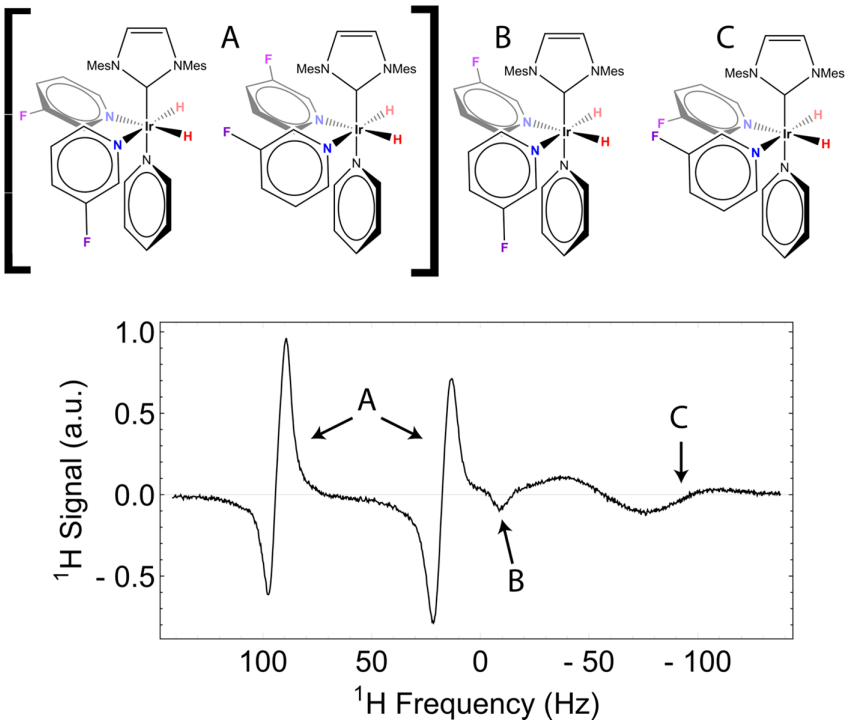

Figure 3. (top) Conformers of the activated PTC with associated ligands and hydrides inducing different chemical environments for the associated hydrides. (bottom) ^{1}H spectrum at 1 T with 45° tip angle demonstrating four distinct hydride species coming from three inequivalent conformers with two pairs of equivalent hydrides (B and C) and one pair of inequivalent hydrides (A).

tion is instead at approximately ±3.2 μT. This suggests that the resulting ^{19}F-signal arises from cross relaxation from the ortho-^{1}H on the pyridinyl ring.[51] Spectra acquired with either QUASR-SABRE or conventional SABRE exhibit in-phase resonances in contrast to the in situ SABRE spectra of the corresponding compounds (Figure 2c,d), which exhibit antiphase spin order. This antiphase spin order arises as, in the absence of a radiofrequency pulse, there is still an allowed transition between the $S_H T^0_{H'F} \rightarrow T^0_H S_{H'F}$ states, for which the $S_{H'F}$ order rapidly decays into $\hat{I}_{H'z}\hat{S}_{Fz}$ because of the ∼120 kHz frequency difference between the ^{1}H and ^{19}F nuclei at this field. Conversely, off-resonance SLIC excitation is known to generate solely in-phase $\hat{S}_z$ order, as will any hyperpolarized signal derived from cross relaxation from the ortho-^{1}H. Note that the frequency shift observed in all the spectra shown in Figure 2 is a result of the magnetic field drift due to the temperature fluctuations of the B_0 magnet occurring during the spectral acquisition process.

The spectra shown in Figure 2a,b suggest that the observed signals are the result of direct polarization transfer from the *p*-H_2-derived hydrides to ^{19}F nuclei driven by QUASR-SABRE. This is because the observed spectra have in-phase signatures, versus the antiphase signatures expected from in situ hyperpolarization (Figure 2c,d), and no ortho-^{1}H magnetization is generated at this field to afford cross relaxation. Moreover, we do not expect the spin-1/2 relayed mechanism through $^2J_{NH}$ to be the dominant pathway for hyperpolarization transfer, because there is little difference in the SABRE spectra of 3-^{19}F-pyridine and 3-^{19}F-^{15}N-pyridine.[21,56]

The enhancement values were computed as described previously[54] by taking the product of the ratio of the ^{19}F concentrations of the species of interest (C_{REF}/C_{HP}), i.e., ^{19}F, present in the thermally polarized reference compound (C_{REF}, neat 3,5-^{19}F-pyridine; Figure 2e) and the HP substrate compound (C_{HP}), with the integrated signal intensity ratio of the HP substrate and the thermal signal reference compound (S_{HP}/S_{REF}) multiplied by a factor of 1.85 (which is the ratio of the cross-sectional areas of the thermal signal reference to the hyperpolarized arrangements as implemented by the experimental setup) as discussed in detail elsewhere.[57] Nuclear spin polarization P was computed by multiplying $\varepsilon_{^{19}F}$ by equilibrium ^{19}F polarization at 0.05 T and 300 K (ca. 1.5×10^{-5}%).

3-^{19}F-Pyridine presents an interesting chemical system, as the complex may take on four possible conformations upon association of two 3-^{19}F-pyridine ligands as seen in Figure 3. When the fluorine substituents are both positioned between the pyridine rings, the complex is highly unstable because of the proximity of two highly electronegative groups. The hydrides in this conformer are therefore short-lived and yield the broad peak labeled "C" in Figure 3. When the fluorine substituents are both positioned in the periphery, the complex is stable and yields a longer-lived hydride species producing the peak labeled "B". The two conformers with one central and one peripheral fluorine substituent are degenerate and are not destabilized by proximity of the fluorine substituents. Because the meta-substituted pyridine is asymmetric, this final conformation induces a chemical inequivalence between the hydrides producing two antisymmetric peaks labeled "A" separated by 1.77 ppm. This chemical shift difference prevents LIGHT-SABRE[31] hyperpolarization at high field. However, using a lower field (50 mT) as in QUASR-SABRE allows collapse of these disparate hydride resonance frequencies onto a single peak of accidental equivalence.

DOI: 10.1021/acs.jpclett.9b01505
J. Phys. Chem. Lett. 2019, 10, 4229−4236

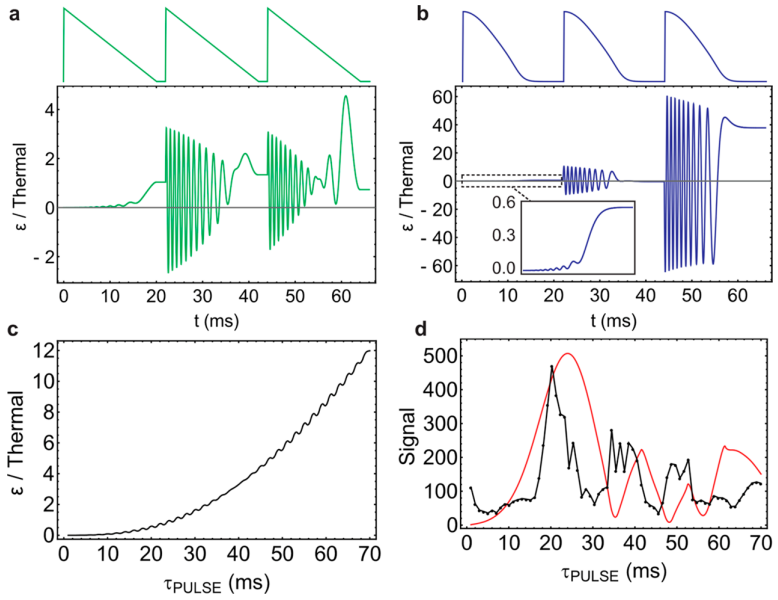

Figure 4. ^{19}F QUASR-SABRE of 3-^{19}F-pyridine. Coherent hyperpolarization dynamics during a triangular pulse (a) and the nonlinear pulse approximation used in these experiments (b). The dynamics predicted during a single pulse (c) vary greatly from those predicted from the explicit calculation of the entire pulse sequence (d), which is shown in red overlaying the experimental (0.05 T) data in black (the black solid lines are added to guide the eye).

The QUASR-SABRE pulse sequence was applied in a regime where there is extreme coherent coupling between each consecutive QUASR pulse, which arises when the delay is much shorter than the lifetime of the species (typically ∼25 ms). In such a regime, the dynamics generated by the pulse sequence are far from intuitive. Given that the ortho-protons of the pyridine are ∼100 Hz offset in resonance from the parahydrogen-derived hydrides, this spin system effectively reduces to an AA′XX′ spin system, for which the SABRE dynamics have been characterized extensively.[35] During the first pulse, very little hyperpolarized signal is generated until the pulse power approaches the LAC condition, given by $\omega_{1F}/2\pi = {}^{2}J_{HH}$. Given the short 2 ms interpulse delay, the beginning of each subsequent QUASR pulse induces large coherent oscillations at the, albeit time-dependent, nutation frequency. The relatively large signal produced with a (20 ms QUASR-pulse +2 ms delay)$_{30}$ train corresponds to when the coherent oscillations halt coincident with an effective $(2n + 1)\pi$-pulse in the hyperpolarization dynamics, giving the largest deviation from equilibrium. The optimal 2 ms delay was surprising, given that other pulsed techniques[34] find the optimal interpulse delay at times on the order of 100 ms. However, given that the QUASR-pulse power is so off-resonance from the SLIC matching condition, only a small amount of polarization may be generated from each pulse; thus, not requiring significant parahydrogen exchange, the interpulse delay can be largely decreased to afford larger signals in this experiment. Interestingly, the maximum observed in Figure 4c is recovered only when the nonlinearities in the pulse shape are reintroduced into the simulation.

It is important to note that the QUASR-SABRE signals are approximately 2.6-fold smaller than the signal obtained by conventional SABRE (Figure 2). This is well understood as the ramifications of various experimental details. First, because the rapid coherent oscillations induced by the QUASR-pulse will average under exchange toward the center of these oscillations, the hyperpolarization generated by each pulse is significantly damped. Also, the large nutation frequency allows for simultaneous irradiation of the free ^{19}F-species, thus dramatically attenuating the signal to 52% of the generated hyperpolarization (see the Supporting Information for details). Given that $^{5}J_{HF}$ = 0.34 Hz,[58] only small perturbations can be made to the system, leading to very slow oscillations on the order of seconds, with very weak pulses, on the order of a few hertz in amplitude, as detailed by conventional SLIC theory.[31,59] Despite the experimental limitations of the complex polarization dynamics, our key finding of the feasibility of QUASR-SABRE polarization of ^{19}F is extended by the insensitivity of the hyperpolarized ^{19}F signal to the frequency offset (Figure 5a), showing that even with a ∼300 Hz offset significant polarization may be achieved. Naturally, the hyperpolarized ^{19}F signal increases with N pumping cycles, demonstrating a clear polarization build-up (Figure 5b) in a manner consistent with SABRE.[31,54] Note the positive value at

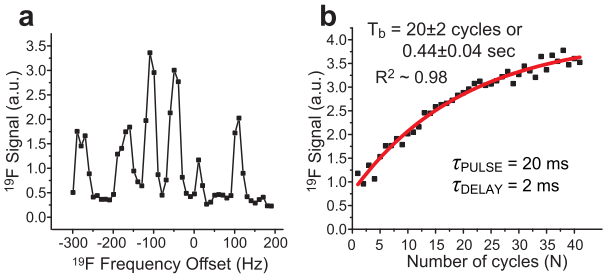

Figure 5. ^{19}F QUASR-SABRE of 3-^{19}F-pyridine. Hyperpolarized 3-^{19}F-pyridine signal dependence on the SLIC-pulse frequency offset (a) and number of pumping cycles (N) demonstrating the build-up of ^{19}F polarization with the monoexponential build-up (red curve) constant of 0.44 ± 0.04 s (b). All data were acquired at 0.05 T magnetic field, and the black solid lines are added to guide the eye.

DOI: 10.1021/acs.jpclett.9b01505
J. Phys. Chem. Lett. 2019, 10, 4229−4236

$N = 0$ is likely due to residual polarization build-up due to in situ SABRE.

We have shown that fluorine hyperpolarization can be generated directly through five chemical bonds with the QUASR-SABRE experiment, which is significantly further than with nearly all other reported approaches for SABRE. The ^{19}F polarization levels achieved by the QUASR-SABRE approach here are relatively low (ca. 0.1%), although fundamentally significantly higher polarization levels should be achievable, i.e. potentially significantly exceeding 10%, and it is important to discuss the areas of potential improvement of the QUASR-SABRE approach. First and foremost, the applications of RF pulses need to be better synchronized with/tailored to the exchange processes, and issues with nonlinear polarization dynamics (which significantly decreased the attainable polarization level in this study, see the Supporting Information for details) may potentially improve the polarization transfer efficiency by several folds. Second, the use of higher and more homogeneous magnetic fields may render the opportunity to more selectively excite catalyst-bound ^{19}F resonance, while having less destructive effect on ^{19}F resonances of free species. Third, the design of more advanced shapes of the RF pulse with optimized RF power may also significantly boost the efficiency of the QUASR-SABRE approach. Moreover, the additional improvement in operation conditions, such as increasing pH_2 pressure, parahydrogen fraction, and pH_2 flow rate, will likely also improve the overall level of ^{19}F polarization. Although biomedical applications such as ^{19}F-based in vivo tracking, spectroscopy, or imaging will be challenging to perform with the relatively low polarization level of ^{19}F polarization, future improvements (as described above) may likely enable such applications in a manner similar to that of biomedical applications of ^{13}C HP contrast agents. We hope the pioneering results reported here can be improved and that higher levels of ^{19}F polarization can be obtained through future work across a wide range of compounds such as ^{19}F-containing drugs with suitable *N*-heterocyclic motifs (e.g., 5-fluorouracil, celecoxib, sitagliptin, fluconazole, etc.). We note that not any ^{19}F-containing molecule can be readily hyperpolarized via SABRE in general and the QUASR-SABRE approach in particular, because of the requirement of chemical exchange of ^{19}F-containing molecules on a suitable time scale (0.001−0.1 s). While currently the SABRE hyperpolarization approach has been broadly applied to N-containing heterocycles, the chemistry of SABRE-amenable biomolecular motifs is rapidly growing because of new chemistries of exchange, which has recently made S-heterocycles[60] and keto-carboxylic acids[61] amenable to SABRE hyperpolarization. As the SABRE hyperpolarization technique continues to rapidly develop, we expect more biomolecular structures (including drugs) to be amenable to QUASR-SABRE hyperpolarization. Spectroscopy of ^{19}F-hyperpolarized drugs is attractive because the lack of background signal and greater chemical shift dispersion of ^{19}F compared to that of ^{1}H allow for specific characterization with little to no background interference. Moreover, RF-based hyperpolarization approaches offer many practical advantages compared to low-field methods as the sample does not need to be shuttled between the matching field and the detector field, therefore enabling signal averaging and multidimensional HP NMR spectroscopy.[62]

■ ASSOCIATED CONTENT

Supporting Information

The Supporting Information is available free of charge on the ACS Publications website at DOI: 10.1021/acs.jpclett.9b01505.

^{19}F QUASR-SABRE simulation description; Mathematica code (PDF)

■ AUTHOR INFORMATION

Corresponding Author

*E-mail: chekmenev@wayne.edu.

ORCID

Thomas Theis: 0000-0001-6779-9978
Kirill V. Kovtunov: 0000-0001-7577-9619
Igor V. Koptyug: 0000-0003-3480-7649
Warren S. Warren: 0000-0001-8458-2076
Eduard Y. Chekmenev: 0000-0002-8745-8801

Notes

The authors declare no competing financial interest.

■ ACKNOWLEDGMENTS

This work was supported by NSF under Grants CHE-1836308 and CHE-1665090. Research reported in this publication was also supported by the National Institute of Biomedical Imaging and Bioengineering of the NIH under R21EB025313, and 1R21EB020323; by National Cancer Institute under 1R21CA220137; and by DOD CDMRP under BRP W81XWH-12-1-0159/BC112431 and under W81XWH-15-1-0271. Russian team thanks grants from RFBR (17-54-33037, 18-43-543023, 19-43-540004) and Higher Education of the RF (AAAA-A16-116121510087-5).

■ REFERENCES

(1) Goodson, B. M.; Whiting, N.; Coffey, A. M.; Nikolaou, P.; Shi, F.; Gust, B. M.; Gemeinhardt, M. E.; Shchepin, R. V.; Skinner, J. G.; Birchall, J. R.; et al. Hyperpolarization Methods for MRS. *Emagres* **2015**, *4*, 797−810.

(2) Nikolaou, P.; Goodson, B. M.; Chekmenev, E. Y. NMR Hyperpolarization Techniques for Biomedicine. *Chem. - Eur. J.* **2015**, *21*, 3156−3166.

(3) Kovtunov, K. V.; Pokochueva, E. V.; Salnikov, O. G.; Cousin, S.; Kurzbach, D.; Vuichoud, B.; Jannin, S.; Chekmenev, E. Y.; Goodson, B. M.; Barskiy, D. A.; et al. Hyperpolarized NMR: D-DNP, PHIP, and SABRE. *Chem. - Asian J.* **2018**, *13*, 1857−1871.

(4) Ardenkjaer-Larsen, J. H.; Fridlund, B.; Gram, A.; Hansson, G.; Hansson, L.; Lerche, M. H.; Servin, R.; Thaning, M.; Golman, K. Increase in Signal-to-Noise Ratio of > 10,000 Times in Liquid-State NMR. *Proc. Natl. Acad. Sci. U. S. A.* **2003**, *100*, 10158−10163.

(5) Eshuis, N.; van Weerdenburg, B. J. A.; Feiters, M. C.; Rutjes, F. P. J. T.; Wijmenga, S. S.; Tessari, M. Quantitative Trace Analysis of Complex Mixtures Using SABRE Hyperpolarization. *Angew. Chem., Int. Ed.* **2015**, *54*, 1481−1484.

(6) Reile, I.; Aspers, R. L. E. G.; Tyburn, J.-M.; Kempf, J. G.; Feiters, M. C.; Rutjes, F. P. J. T.; Tessari, M. Dosy Analysis of Micromolar Analytes: Resolving Dilute Mixtures by SABRE Hyperpolarization. *Angew. Chem., Int. Ed.* **2017**, *56*, 9174−9177.

(7) Barskiy, D. A.; Coffey, A. M.; Nikolaou, P.; Mikhaylov, D. M.; Goodson, B. M.; Branca, R. T.; Lu, G. J.; Shapiro, M. G.; Telkki, V.-V.; Zhivonitko, V. V.; et al. NMR Hyperpolarization Techniques of Gases. *Chem. - Eur. J.* **2017**, *23*, 725−751.

(8) Kurhanewicz, J.; Vigneron, D. B.; Brindle, K.; Chekmenev, E. Y.; Comment, A.; Cunningham, C. H.; DeBerardinis, R. J.; Green, G. G.; Leach, M. O.; Rajan, S. S.; et al. Analysis of Cancer Metabolism by

DOI: 10.1021/acs.jpclett.9b01505
J. Phys. Chem. Lett. 2019, 10, 4229−4236

Imaging Hyperpolarized Nuclei: Prospects for Translation to Clinical Research. *Neoplasia* **2011**, *13*, 81−97.
(9) Nelson, S. J.; Kurhanewicz, J.; Vigneron, D. B.; Larson, P. E. Z.; Harzstark, A. L.; Ferrone, M.; van Criekinge, M.; Chang, J. W.; Bok, R.; Park, I.; et al. Metabolic Imaging of Patients with Prostate Cancer Using Hyperpolarized 1-C-13 Pyruvate. *Sci. Transl. Med.* **2013**, *5*, 198ra108.
(10) Hövener, J.-B.; Pravdivtsev, A. N.; Kidd, B.; Bowers, C. R.; Glöggler, S.; Kovtunov, K. V.; Plaumann, M.; Katz-Brull, R.; Buckenmaier, K.; Jerschow, A.; et al. Parahydrogen-Based Hyperpolarization for Biomedicine. *Angew. Chem., Int. Ed.* **2018**, *57*, 11140−11162.
(11) Golman, K.; in 't Zandt, R.; Thaning, M. Real-Time Metabolic Imaging. *Proc. Natl. Acad. Sci. U. S. A.* **2006**, *103*, 11270−11275.
(12) Day, S. E.; Kettunen, M. I.; Gallagher, F. A.; Hu, D. E.; Lerche, M.; Wolber, J.; Golman, K.; Ardenkjaer-Larsen, J. H.; Brindle, K. M. Detecting Tumor Response to Treatment Using Hyperpolarized C-13 Magnetic Resonance Imaging and Spectroscopy. *Nat. Med.* **2007**, *13*, 1382−1387.
(13) Adams, R. W.; Aguilar, J. A.; Atkinson, K. D.; Cowley, M. J.; Elliott, P. I. P.; Duckett, S. B.; Green, G. G. R.; Khazal, I. G.; Lopez-Serrano, J.; Williamson, D. C. Reversible Interactions with Para-Hydrogen Enhance NMR Sensitivity by Polarization Transfer. *Science* **2009**, *323*, 1708−1711.
(14) Adams, R. W.; Duckett, S. B.; Green, R. A.; Williamson, D. C.; Green, G. G. R. A Theoretical Basis for Spontaneous Polarization Transfer in Non-Hydrogenative Parahydrogen-Induced Polarization. *J. Chem. Phys.* **2009**, *131*, 194505.
(15) Atkinson, K. D.; Cowley, M. J.; Elliott, P. I. P.; Duckett, S. B.; Green, G. G. R.; Lopez-Serrano, J.; Whitwood, A. C. Spontaneous Transfer of Parahydrogen Derived Spin Order to Pyridine at Low Magnetic Field. *J. Am. Chem. Soc.* **2009**, *131*, 13362−13368.
(16) Balu, A. M.; Duckett, S. B.; Luque, R. Para-Hydrogen Induced Polarisation Effects in Liquid Phase Hydrogenations Catalysed by Supported Metal Nanoparticles. *Dalton Trans* **2009**, 5074−5076.
(17) Cowley, M. J.; Adams, R. W.; Atkinson, K. D.; Cockett, M. C. R.; Duckett, S. B.; Green, G. G. R.; Lohman, J. A. B.; Kerssebaum, R.; Kilgour, D.; Mewis, R. E. Iridium N-Heterocyclic Carbene Complexes as Efficient Catalysts for Magnetization Transfer from Para-Hydrogen. *J. Am. Chem. Soc.* **2011**, *133*, 6134−6137.
(18) Colell, J. F. P.; Logan, A. W. J.; Zhou, Z.; Shchepin, R. V.; Barskiy, D. A.; Ortiz, G. X.; Wang, Q.; Malcolmson, S. J.; Chekmenev, E. Y.; Warren, W. S.; et al. Generalizing, Extending, and Maximizing Nitrogen-15 Hyperpolarization Induced by Parahydrogen in Reversible Exchange. *J. Phys. Chem. C* **2017**, *121*, 6626−6634.
(19) Rayner, P. J.; Burns, M. J.; Olaru, A. M.; Norcott, P.; Fekete, M.; Green, G. G. R.; Highton, L. A. R.; Mewis, R. E.; Duckett, S. B. Delivering Strong ^{1}H Nuclear Hyperpolarization Levels and Long Magnetic Lifetimes through Signal Amplification by Reversible Exchange. *Proc. Natl. Acad. Sci. U. S. A.* **2017**, *114*, E3188−E3194.
(20) Kidd, B. E.; Gesiorski, J. L.; Gemeinhardt, M. E.; Shchepin, R. V.; Kovtunov, K. V.; Koptyug, I. V.; Chekmenev, E. Y.; Goodson, B. M. Facile Removal of Homogeneous SABRE Catalysts for Purifying Hyperpolarized Metronidazole, a Potential Hypoxia Sensor. *J. Phys. Chem. C* **2018**, *122*, 16848−16852.
(21) Barskiy, D. A.; Shchepin, R. V.; Coffey, A. M.; Theis, T.; Warren, W. S.; Goodson, B. M.; Chekmenev, E. Y. Over 20% ^{15}N Hyperpolarization in under One Minute for Metronidazole, an Antibiotic and Hypoxia Probe. *J. Am. Chem. Soc.* **2016**, *138*, 8080−8083.
(22) Ardenkjaer-Larsen, J. H. On the Present and Future of Dissolution-DNP. *J. Magn. Reson.* **2016**, *264*, 3−12.
(23) Pravdivtsev, A. N.; Yurkovskaya, A. V.; Vieth, H.-M.; Ivanov, K. L.; Kaptein, R. Level Anti-Crossings Are a Key Factor for Understanding Para-Hydrogen-Induced Hyperpolarization in SABRE Experiments. *ChemPhysChem* **2013**, *14*, 3327−3331.
(24) Ivanov, K. L.; Pravdivtsev, A. N.; Yurkovskaya, A. V.; Vieth, H.-M.; Kaptein, R. The Role of Level Anti-Crossings in Nuclear Spin Hyperpolarization. *Prog. Nucl. Magn. Reson. Spectrosc.* **2014**, *81*, 1−36.
(25) Barskiy, D. A.; Shchepin, R. V.; Tanner, C. P. N.; Colell, J. F. P.; Goodson, B. M.; Theis, T.; Warren, W. S.; Chekmenev, E. Y. The Absence of Quadrupolar Nuclei Facilitates Efficient ^{13}C Hyperpolarization Via Reversible Exchange with Parahydrogen. *ChemPhysChem* **2017**, *18*, 1493−1498.
(26) Theis, T.; Truong, M. L.; Coffey, A. M.; Shchepin, R. V.; Waddell, K. W.; Shi, F.; Goodson, B. M.; Warren, W. S.; Chekmenev, E. Y. Microtesla SABRE Enables 10% Nitrogen-15 Nuclear Spin Polarization. *J. Am. Chem. Soc.* **2015**, *137*, 1404−1407.
(27) Zhivonitko, V. V.; Skovpin, I. V.; Koptyug, I. V. Strong ^{31}P Nuclear Spin Hyperpolarization Produced Via Reversible Chemical Interaction with Parahydrogen. *Chem. Commun.* **2015**, *51*, 2506−2509.
(28) Shchepin, R. V.; Truong, M. L.; Theis, T.; Coffey, A. M.; Shi, F.; Waddell, K. W.; Warren, W. S.; Goodson, B. M.; Chekmenev, E. Y. Hyperpolarization of "Neat" Liquids by NMR Signal Amplification by Reversible Exchange. *J. Phys. Chem. Lett.* **2015**, *6*, 1961−1967.
(29) Truong, M. L.; Theis, T.; Coffey, A. M.; Shchepin, R. V.; Waddell, K. W.; Shi, F.; Goodson, B. M.; Warren, W. S.; Chekmenev, E. Y. ^{15}N Hyperpolarization by Reversible Exchange Using SABRE-SHEATH. *J. Phys. Chem. C* **2015**, *119*, 8786−8797.
(30) Kiryutin, A. S.; Yurkovskaya, A. V.; Zimmermann, H.; Vieth, H.-M.; Ivanov, K. L. Complete Magnetic Field Dependence of SABRE-Derived Polarization. *Magn. Reson. Chem.* **2018**, *56*, 651−662.
(31) Theis, T.; Truong, M.; Coffey, A. M.; Chekmenev, E. Y.; Warren, W. S. LIGHT-SABRE Enables Efficient in-Magnet Catalytic Hyperpolarization. *J. Magn. Reson.* **2014**, *248*, 23−26.
(32) Pravdivtsev, A. N.; Yurkovskaya, A. V.; Vieth, H.-M.; Ivanov, K. L. RF-SABRE: A Way to Continuous Spin Hyperpolarization at High Magnetic Fields. *J. Phys. Chem. B* **2015**, *119*, 13619−13629.
(33) Pravdivtsev, A. N.; Skovpin, I. V.; Svyatova, A. I.; Chukanov, N. V.; Kovtunova, L. M.; Bukhtiyarov, V. I.; Chekmenev, E. Y.; Kovtunov, K. V.; Koptyug, I. V.; Hövener, J.-B. Chemical Exchange Reaction Effect on Polarization Transfer Efficiency in SLIC-SABRE. *J. Phys. Chem. A* **2018**, *122*, 9107−9114.
(34) Lindale, J. R.; Eriksson, S. L.; Tanner, C. P. N.; Zhou, Z.; Colell, J. F. P.; Zhang, G.; Bae, J.; Chekmenev, E. Y.; Theis, T.; Warren, W. S. Unveiling Coherently driven Hyperpolarization Dynamics in Signal Amplification by Reversible Exchange. *Nat. Commun.* **2019**, *10*, 395.
(35) Pravdivtsev, A. N.; Yurkovskaya, A. V.; Zimmermann, H.; Vieth, H.-M.; Ivanov, K. L. Transfer of SABRE-Derived Hyperpolarization to Spin-1/2 Heteronuclei. *RSC Adv.* **2015**, *5*, 63615−63623.
(36) Roy, S. S.; Stevanato, G.; Rayner, P. J.; Duckett, S. B. Direct Enhancement of Nitrogen-15 Targets at High-Field by Fast ADAPT-SABRE. *J. Magn. Reson.* **2017**, *285*, 55−60.
(37) Shchepin, R. V.; Jaigirdar, L.; Chekmenev, E. Y. Spin-Lattice Relaxation of Hyperpolarized Metronidazole in Signal Amplification by Reversible Exchange in Micro-Tesla Fields. *J. Phys. Chem. C* **2018**, *122*, 4984−4996.
(38) Theis, T.; Ortiz, G. X.; Logan, A. W. J.; Claytor, K. E.; Feng, Y.; Huhn, W. P.; Blum, V.; Malcolmson, S. J.; Chekmenev, E. Y.; Wang, Q.; et al. Direct and Cost-Efficient Hyperpolarization of Long-Lived Nuclear Spin States on Universal $^{15}N_2$-Diazirine Molecular Tags. *Sci. Adv.* **2016**, *2*, e1501438.
(39) Nonaka, H.; Hata, R.; Doura, T.; Nishihara, T.; Kumagai, K.; Akakabe, M.; Tsuda, M.; Ichikawa, K.; Sando, S. A Platform for Designing Hyperpolarized Magnetic Resonance Chemical Probes. *Nat. Commun.* **2013**, *4*, 2411.
(40) Bales, L.; Kovtunov, K. V.; Barskiy, D. A.; Shchepin, R. V.; Coffey, A. M.; Kovtunova, L. M.; Bukhtiyarov, A. V.; Feldman, M. A.; Bukhtiyarov, V. I.; Chekmenev, E. Y.; et al. Aqueous, Heterogeneous Parahydrogen-Induced ^{15}N Polarization. *J. Phys. Chem. C* **2017**, *121*, 15304−15309.
(41) McCormick, J.; Korchak, S.; Mamone, S.; Ertas, Y. N.; Liu, Z.; Verlinsky, L.; Wagner, S.; Glöggler, S.; Bouchard, L.-S. More Than 12% Polarization and 20 minute Lifetime of ^{15}N in a Choline

DOI: 10.1021/acs.jpclett.9b01505
J. Phys. Chem. Lett. 2019, 10, 4229−4236

Derivative Utilizing Parahydrogen and a Rhodium Nanocatalyst in Water. *Angew. Chem., Int. Ed.* **2018**, *57*, 10692−10696.
(42) Zhang, G.; Colell, J. F. P.; Glachet, T.; Lindale, J. R.; Reboul, V.; Theis, T.; Warren, W. S. Terminal Diazirines Enable Reverse Polarization Transfer from $^{15}N_2$ Singlets. *Angew. Chem., Int. Ed.* **2019**, DOI: 10.1002/anie.201904026.
(43) Shchepin, R. V.; Birchall, J. R.; Chukanov, N. V.; Kovtunov, K. V.; Koptyug, I. V.; Theis, T.; Warren, W. S.; Gelovani, J. G.; Goodson, B. M.; Shokouhi, S.; et al. Hyperpolarizing Concentrated Metronidazole $^{15}NO_2$ Group over Six Chemical Bonds with More Than 15% Polarization and 20 minute Lifetime. *Chem. - Eur. J.* **2019**, *25*, 8829−8836.
(44) Chukanov, N. V.; Kidd, B. M.; Kovtunova, L. M.; Bukhtiyarov, V. I.; Shchepin, R. V.; Chekmenev, E. Y.; Goodson, B. M.; Kovtunov, K. V.; Koptyug, I. V. A Versatile Synthetic Route to the Preparation of ^{15}N Heterocycles. *J. Labelled Compd. Radiopharm.* **2019**, DOI: 10.1002/jlcr.3699.
(45) Shchepin, R. V.; Barskiy, D. A.; Mikhaylov, D. M.; Chekmenev, E. Y. Efficient Synthesis of Nicotinamide-1-^{15}N for Ultrafast NMR Hyperpolarization Using Parahydrogen. *Bioconjugate Chem.* **2016**, *27*, 878−882.
(46) Shchepin, R. V.; Barskiy, D. A.; Coffey, A. M.; Feldman, M. A.; Kovtunova, L. M.; Bukhtiyarov, V. I.; Kovtunov, K. V.; Goodson, B. M.; Koptyug, I. V.; Chekmenev, E. Y. Robust Imidazole-$^{15}N_2$ Synthesis for High-Resolution Low-Field (0.05 T) ^{15}N hyperpolarized NMR Spectroscopy. *ChemistrySelect* **2017**, *2*, 4478−4483.
(47) Shen, K.; Logan, A. W. J.; Colell, J. F. P.; Bae, J.; Ortiz, G. X., Jr.; Theis, T.; Warren, W. S.; Malcolmson, S. J.; Wang, Q. Diazirines as Potential Molecular Imaging Tags: Probing the Requirements for Efficient and Long-Lived SABRE-Induced Hyperpolarization. *Angew. Chem., Int. Ed.* **2017**, *56*, 12112−12116.
(48) Wang, J.; Sánchez-Roselló, M.; Aceña, J. L.; del Pozo, C.; Sorochinsky, A. E.; Fustero, S.; Soloshonok, V. A.; Liu, H. Fluorine in Pharmaceutical Industry: Fluorine-Containing Drugs Introduced to the Market in the Last Decade (2001−2011). *Chem. Rev.* **2014**, *114*, 2432−2506.
(49) Ojima, I. *Fluorine in Medicinal Chemistry and Chemical Biology*; Wiley-Backwell, 2009.
(50) Shchepin, R. V.; Goodson, B. M.; Theis, T.; Warren, W. S.; Chekmenev, E. Y. Toward Hyperpolarized ^{19}F Molecular Imaging Via Reversible Exchange with Parahydrogen. *ChemPhysChem* **2017**, *18*, 1961−1965.
(51) Chukanov, N. V.; Salnikov, O. G.; Shchepin, R. V.; Svyatova, A.; Kovtunov, K. V.; Koptyug, I. V.; Chekmenev, E. Y. ^{19}F Hyperpolarization of ^{15}N-3-^{19}F-Pyridine Via Signal Amplification by Reversible Exchange. *J. Phys. Chem. C* **2018**, *122*, 23002−23010.
(52) Buckenmaier, K.; Rudolph, M.; Back, C.; Misztal, T.; Bommerich, U.; Fehling, P.; Koelle, D.; Kleiner, R.; Mayer, H. A.; Scheffler, K.; et al. SQUID-Based Detection of Ultra-Low-Field Multinuclear NMR of Substances Hyperpolarized Using Signal Amplification by Reversible Exchange. *Sci. Rep.* **2017**, *7*, 13431.
(53) Olaru, A. M.; Robertson, T. B. R.; Lewis, J. S.; Antony, A.; Iali, W.; Mewis, R. E.; Duckett, S. B. Extending the Scope of ^{19}F Hyperpolarization through Signal Amplification by Reversible Exchange in MRI and NMR Spectroscopy. *ChemistryOpen* **2018**, *7*, 97−105.
(54) Theis, T.; Ariyasingha, N. M.; Shchepin, R. V.; Lindale, J. R.; Warren, W. S.; Chekmenev, E. Y. Quasi-Resonance Signal Amplification by Reversible Exchange. *J. Phys. Chem. Lett.* **2018**, *9*, 6136−6142.
(55) DeVience, S. J.; Walsworth, R. L.; Rosen, M. S. Preparation of Nuclear Spin Singlet States Using Spin-Lock Induced Crossing. *Phys. Rev. Lett.* **2013**, *111*, 173002.
(56) Shchepin, R. V.; Jaigirdar, L.; Theis, T.; Warren, W. S.; Goodson, B. M.; Chekmenev, E. Y. Spin Relays Enable Efficient Long-Range Heteronuclear Signal Amplification by Reversible Exchange. *J. Phys. Chem. C* **2017**, *121*, 28425−28434.
(57) Truong, M. L.; Shi, F.; He, P.; Yuan, B.; Plunkett, K. N.; Coffey, A. M.; Shchepin, R. V.; Barskiy, D. A.; Kovtunov, K. V.; Koptyug, I. V.; et al. Irreversible Catalyst Activation Enables Hyperpolarization and Water Solubility for NMR Signal Amplification by Reversible Exchange. *J. Phys. Chem. B* **2014**, *18*, 13882−13889.
(58) Eshuis, N.; Aspers, R. L. E. G.; van Weerdenburg, B. J. A.; Feiters, M. C.; Rutjes, F. P. J. T.; Wijmenga, S. S.; Tessari, M. Determination of Long-Range Scalar $^1H-^1H$ Coupling Constants Responsible for Polarization Transfer in SABRE. *J. Magn. Reson.* **2016**, *265*, 59−66.
(59) Theis, T.; Feng, Y.; Wu, T.; Warren, W. S. Composite and Shaped Pulses for Efficient and Robust Pumping of Disconnected Eigenstates in Magnetic Resonance. *J. Chem. Phys.* **2014**, *140*, 014201.
(60) Shchepin, R. V.; Barskiy, D. A.; Coffey, A. M.; Goodson, B. M.; Chekmenev, E. Y. NMR Signal Amplification by Reversible Exchange of Sulfur-Heterocyclic Compounds Found in Petroleum. *ChemistrySelect* **2016**, *1*, 2552−2555.
(61) Iali, W.; Roy, S. S.; Tickner, B. J.; Ahwal, F.; Kennerley, A. J.; Duckett, S. B. Hyperpolarising Pyruvate through Signal Amplification by Reversible Exchange (SABRE). *Angew. Chem., Int. Ed.* **2019**, DOI: 10.1002/anie.201905483.
(62) Eshuis, N.; Aspers, R. L. E. G.; van Weerdenburg, B. J. A.; Feiters, M. C.; Rutjes, F. P. J. T.; Wijmenga, S. S.; Tessari, M. 2D NMR Trace Analysis by Continuous Hyperpolarization at High Magnetic Field. *Angew. Chem., Int. Ed.* **2015**, *54*, 14527−14530.

DOI: 10.1021/acs.jpclett.9b01505
J. Phys. Chem. Lett. 2019, 10, 4229−4236

Hyperpolarized Propane: Clinical-scale Production of Long Lived Spin States, Condensation, and Imaging

Oleg G. Salnikov,[1,2] Nuwandi M Ariyasingha,[3] Panayiotis Nikolaou,[4] Boyd M. Goodson,[5] Kirill V. Kovtunov,[1,2] Igor V. Koptyug, [1,2] and Eduard Y. Chekmenev[3,6]

[1]International Tomography Center, SB RAS, [2]Novosibirsk State University, Novosibirsk, 630090, Russia
[3]Department of Chemistry, Integrative Biosciences (Ibio), Wayne State University, Karmanos Cancer Institute (KCI), Detroit, MI 48202, USA
[4]Vanderbilt University Institute of Imaging Science (VUIIS), Department of Radiology, Nashville, TN 37232 USA
[5]Department of Chemistry and Biochemistry and Materials Technology Center, Southern Illinois University, Carbondale, IL 62901, USA
[6]Russian Academy of Sciences, Moscow, 119991, Russia

Purpose: Biomedical applications demand a sufficiently long lifetime of hyperpolarized (HP) compounds. The decay of the HP state is typically governed by the process of spin-lattice relaxation characterized by the T_1 constant. Because ^{129}Xe and ^{3}He have significantly greater T_1 values than that of protons, the development of inhalable HP contrast agents has primarily employed these heteronuclei. This approach has a significant translational challenge, because conventional clinical MRI scanners can only image protons, and therefore the ^{129}Xe contrast agent requires highly specialized hardware and software, which are available only to a limited number of research sites around the globe. The unique properties of the long-lived spin states (LLSSs) recently explored by Levitt and others allow preparing HP states with the exponential decay constant T_{LLSS}, which can significantly exceed the T_1 constant. As a result of this fundamental breakthrough, the interest in the use of HP protons sites have been rekindled, because the lifetime of HP state can be sufficiently long, and such HP states can be readily imaged on conventional clinical MRI scanners. HP propane gas can be readily prepared through the process of parahydrogen-induced polarization (PHIP) via parahydrogen (pH_2) addition to propylene or cyclopropane over supported metal catalysts.

Methods: We have developed a clinical-scale propane polarizer prototype device for reacting propylene with pH_2 gases over a heterogeneous (HET) catalyst to produce HP propane gas. The core of the polarizer is comprised of ¼ in. OD copper tubing filled with ~12 g of copper beads and a small quantity (60-280 mg) of 1 wt% Rh/TiO_2 catalyst. This type of Rh/TiO_2 catalyst was tested in previous (small-scale) studies. The Cu particles provide a significantly more efficient dissipation of heat generated during the highly exothermic chemical reaction.

Results and Discussion: (i) Here we show that more than 0.3 liters of hyperpolarized propane gas can be produced in 2 seconds. This production rate is more than an order of magnitude greater than that demonstrated previously. The reported production rate is comparable to that employed for in-human MRI using HP noble gas (e.g. ^{129}Xe) produced via Spin Exchange Optical Pumping (SEOP). We show that high polarization values can be retained despite the significant increase in the production rate of hyperpolarized propane. The enhanced signals of produced hyperpolarized propane gas were revealed by stopped-flow MRI visualization at 4.7 T (Figure 1). **(ii)** At 0.05 T, the parahydrogen-induced overpopulation of a HP propane LLSS decays exponentially with a time constant (T_{LLSS}) approximately 3-fold longer than the corresponding T_1 values. Both T_{LLSS} and T_1 exhibit linear increases with propane pressure in the range from 1 atm (the most biomedically relevant condition for pulmonary MRI) to 5 atm. The T_{LLSS} value of HP propane gas at 1 atm is ~3 s. **(iii)** Deuteration of the hydrogenation substrate yields hyperpolarized propane-d_6 gas with T_{LLSS} values approximately 20% shorter than those of hyperpolarized propane gas, indicating that deuteration does not benefit the lifetime of the LLSS HP state. **(iv)** The use of buffering gas during parahydrogen addition results in: (a) no significant changes in T_1 values; (b) a reduction of T_{LLSS} values; yet (c) an increase of the polarization levels of HP propane gas with a propane concentration decrease. **(v)** Moreover, we demonstrate the feasibility of HP propane cryo-collection (which can be potentially useful for preparing larger amounts of concentrated HP propane, when a buffering gas is employed), and T_{LLSS} of liquefied HP propane exceeds 14.7 seconds, which is greater than the T_{LLSS} value of HP propane gas at any pressure studied. **(vi)** Finally, we have explored the utility of partial Spin-Lock Induced Crossing (SLIC) RF pulses for converting the overpopulated LLSS into observable ^{1}H nuclear magnetization. We find that the bulk of the overpopulated LLSS is retained even when the optimal or near-optimal values of SLIC pulse duration are employed, and the overpopulated LLSS of propane is also relatively immune to strong RF pulses—thereby indicating that the LLSS may be suitable as a spin-polarization reservoir in the context of NMR/MRI applications. The presented findings may be useful for improving levels of polarization of HP propane produced by HET-PHIP; increasing the lifetime of the HP state during preparation and delivery; and developing efficient approaches for ultrafast MRI imaging of HP propane in the context of biomedical applications of HP propane gas, including its potential use as an inhalable contrast agent. **(vii)** The polarization enhancement values recorded in such manner for the H_A proton were nearly unchanged (ε_{HA} ranging from 950 to 1150, Figure 1) over the range of reactor temperatures studied (between 20 °C to 140 °C). This trend is important for two reasons. First of all, it indicates that a robust catalyst performance for hyperpolarization of propane gas can indeed be obtained over a wide range of temperatures with effectively ~100% chemical conversion. Second, the highest levels of polarization enhancement were observed at 40-60 °C, suggesting that reactor temperatures near that of the human body (ca. 40 °C) can be readily employed without sacrificing polarization efficiency.

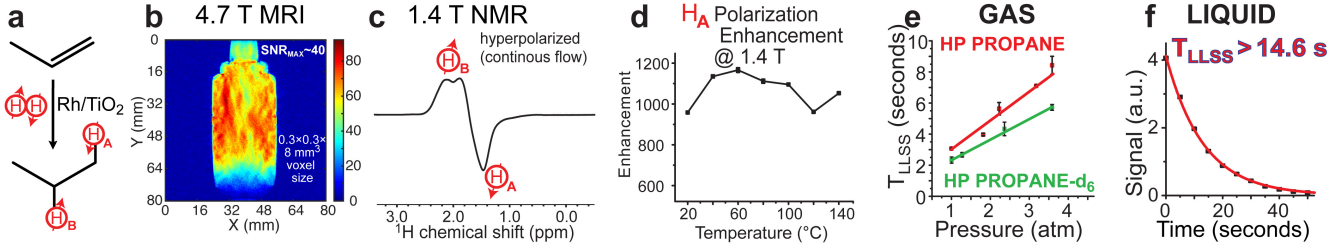

Figure 1. a) Schematic of pairwise parahydrogen addition to propylene via heterogeneous (HET) parahydrogen induced polarization (PHIP); b) 2D MRI image of HP propane phantom at 4.7 T; c) NMR spectrum of HP propane gas at 1.4 T; d) temperature dependence of H_B polarization enhancement at 1.4 T; e) pressure dependence of T_{LLSS} of HP propane and HP propane-d_6 gas; f) Signal decay of the overpopulated LLSS of liquid propane at ~0.05 T.

Conclusion: The presented findings bode well for future *in vivo* use of HP propane gas.

Acknowledgements: This work was supported by NSF under grants CHE-1836308 and CHE-1416432, NIH 1R21EB020323, DOD CDMRP W81XWH-15-1-0271 W81XWH-15-1-0272, and RFBR 17-54-33037_OHKO_a. O.G.S. and K.V.K. thank the Russian Science Foundation (grant #17-73-20030).

References: (**1**) Kovtunov, K. V., et al. *Chem. Eur. J.* **2014,** *20*, 11636–11639. (**2**) Kovtunov, K. V., et al. *J. Phys. Chem. C* **2014,** *118*, 28234–28243. (**3**) Kovtunov, K. V., et al. *Chem. Eur. J.* **2014,** *20*, 14629–14632. (**4**) Kovtunov, K. V., et al. *Top. Curr. Chem.* **2013,** *338*, 123-180. (**5**) Burueva, D. B., et al. *J. Phys. Chem. C* **2017,** *121*, 4481–4487. (**6**) Barskiy, D. A., et al. *J. Magn. Reson.* **2017,** *276*, 78-85. (**7**) Kovtunov, K. V., et al. *Chem. Asian J.* **2018,** *13*, 1857-1871. (**8**) Barskiy, D. A., et al. *Chem. Eur. J.* **2017,** *23*, 725–751. (**9**) Hövener, J.-B., et al. *Angew. Chem. Int. Ed.* **2018,** *57*, 11140-11162. (**10**) Bouchard, L. S., et al. *Angew. Chem. Int. Ed.* **2007,** *46*, 4064-4068. (**11**) Koptyug, I. V., et al. *J. Am. Chem. Soc.* **2007,** *129*, 5580-5586. (**12**) Bouchard, L. S., et al. *Science* **2008,** *319*, 442-445. (**13**) Salnikov, O. G., et al. *ChemPhysChem* **2018,** *19*, 2621-2626. (14) Barskiy, D. A., et al. *J. Phys. Chem. C* **2017,** *121*, 10038–10046. (**15**) Salnikov, O. G., et al. *ChemPhysChem* **2016,** *17*, 3395–3398.

New Developments in ^{129}Xe and ^{131}Xe Hyperpolarization via Clinical-Scale Stopped-Flow Spin-Exchange Optical Pumping

Boyd Goodson
Department of Chemistry and Biochemistry, Southern Illinois University, Carbondale, IL 62901

In spin exchange optical pumping (SEOP), circularly polarized laser light is used to generate highly non-equilibrium nuclear spin population distributions in noble gases; such hyperpolarized (HP) noble gases have been utilized in a number of applications over the years, from pulmonary imaging to tests of fundamental physics. At first glance, SEOP appears to be a relatively simple two-step process: first, the electron spins of an alkali metal vapor (typically Rb or Cs) are prepared in an electronically spin-polarized ground state via depletion pumping by the applied laser light; in the second step, the electron spin polarization is spontaneously transferred to noble gas nuclei via Fermi contact interactions during gas-phase collisions. Long nuclear spin relaxation times allow the nuclear spin polarization to accumulate over time, rendering the noble gas hyperpolarized. Underlying SEOP's apparent simplicity are a number of rich and complex phenomena that present both challenges and opportunities for efforts to maximize the production of HP gases for applications. One aspect concerns the technological approaches for preparing HP gases via SEOP. Here, we are concerned with stopped-flow SEOP (SF SEOP), where gas loading, optical pumping, decantation, and cell re-loading are carried out in subsequent steps (typically with Xe-rich mixtures). Although continuous-flow (CF SEOP) devices have understandably dominated clinical-scale production of HP 129Xe (I=1/2), SF SEOP devices can be cheaper and simpler to build, operate, and automate (in part because of the lack of need for cryo-collecting the HP Xe over time).

Results from three different bodies of work will be discussed: First, our ongoing efforts to develop a third-generation SF SEOP polarizer with be described, including aspects of device design (with topics including choice of laser technology), operation, and performance, as well as comparison with our first- and second-generation devices offering near-unity 129Xe polarization at ~1 L/hr production rates. Second, we report a long-standing effort to perform accurate simulations of SF SEOP in the high-laser-flux / high-xenon-density regimes; these simulations quantitatively reproduce most of the previous experimental observations in these regimes, and provide insight both into underlying phenomena and improvements in future polarizer design. Lastly, we report on our efforts to polarize the other xenon isotope with high natural abundance but also non-zero spin: 131Xe. The quadrupolar nature of this isotope presents significant challenges for SEOP, given that the spin-relaxation time constants are typically less than 1 minute. While it is possible that 131Xe could provide an alternative contrast for pulmonary imaging, a key motivation for the work is for the creation of polarized nuclear targets for polarized neutron scattering experiments to test fundamental symmetries (CPT violation). Use of enriched 131Xe and low-field in situ HP 131Xe NMR enabled optimization of various experimental parameters and measurement of 131Xe polarization dynamics, and the demonstration of record high 131Xe polarizations (several percent) at these densities (~0.4 atm).

New Approaches in SABRE: Cleavable Metabolic / pH-Sensing "Double Agents", and Preparation of Purified Agents via Heterogeneous Catalysis and Catalyst Immobilization

B.M. Goodson[a]

[a]*Southern Illinois University, Carbondale, IL USA; E-mail: bgoodson@chem.siu.edu*

PURPOSE: The parahydrogen-based technique dubbed SABRE (for Signal Amplification By Reversible Exchange [1]) is a hyperpolarization approach of growing interest because it is low cost, can be performed quickly and easily, and does not require major instrumentation. Moreover, SABRE does not require irreversible chemical alteration of the substrate (unlike "traditional" parahydrogen-induced polarization or PHIP). However, SABRE must overcome a number of challenges if it is to find more general use in many possible applications, including within biomedical and clinical realms. Our collaborative efforts (as well as those of many others) are working to improve the achievable polarization, broaden SABRE's applicability to different classes of substrates, and develop approaches for removing and recycling the organometallic catalysts that are needed to enable SABRE (but otherwise represent unwanted contaminants of the resulting hyperpolarized agents).

METHODS / RESULTS / DISCUSSION: First, to broaden SABRE applicability we are investigating cleavable "double agents" [2] comprised of one moiety that reversibly binds SABRE catalysts and a payload moiety (in analogy to recent PHIP/'side-arm' results [3]). In one example, following SABRE hyperpolarization (facilitated by spin relay [4] within a micro-Tesla field [5]) and rapid hydrolysis, two hyperpolarized (HP) species are created—a pH-sensing agent and a metabolic agent (e.g. ^{15}N-imidazole and ^{13}C-acetic acid). Hyperpolarization is transferred from hydrides to catalyst-bound 15N during para-H2 bubbling within a magnetic shield. Coupling between the imidazole ring nitrogens then allows relay of spin order to other heteronuclei (including 'distant' 13C spins), resulting in signal enhancement that is retained upon hydrolytic cleavage at 0.3 T 'storage field'. 13C and 15N enhancements of ~263 and ~493, respectively, are achieved in the intact substrate prior to cleavage, with T1's of ~52 s for 13C and ~149 s for 15N resonances at 0.3 T. Hydrolytic cleavage takes place on a time scale much faster than the time required to transfer the sample to the magnet. 13C and 15N enhancements of ~140 and ~180, respectively, are attained in free acetic acid/acetate and imidazole, respectively, with an estimated T1 of ~14 s for 13C at 0.3 T. The large dispersive signal from bound substrate (despite low concentration) suggests that a significant fraction of spin order is not yet transferred to the free substrate, suggesting considerable room for improvement. Attempts to re-hyperpolarize 13C spins after cleavage were not successful, supporting the need for the spin-relay.

Towards the creation of catalyst-free HP agents, we are pursuing both heterogeneous catalysts [6] and catalyst-immobilization strategies [7], and obtained ^{15}N polarizations of the potential hypoxia sensor metronidazole [8] of ~34% [7]. Immobilization of the standard and most-potent (IrIMes) homogeneous SABRE catalyst uses the following experimental procedure: following SABRE (or SABRE-SHEATH) enhancement, commercial S-functionalized microbeads are rapidly added to the sample. In an experiment involving S-functionalized beads were added to a solution of 20 mM hyperpolarized metronizadole and 1 mM IrIMes SABRE catalyst in D4-methanol, the method uses inexpensive, commercially available microparticles, and it is sufficiently rapid (<<T1) to maintaining 15N polarization of up to ~83% of the initial value). 15N polarization of up to ~83% of the initial value). Using S-functionalized microbeads was much more effective than using unfunctionalized silica beads of the same size distribution. Successful removal of homogeneous catalyst from solution under these conditions was confirmed by the absence of SABRE after particle addition and ICPMS.

CONCLUSIONS AND ACKNOLWEDGEMENTS: Spin relays allow SABRE hyperpolarization of "distant" heteronuclear spins, enabling the creation of HP "double agents", here comprised of the pH sensor imidazole and acetate, of relevance to GBM. Rapid hydrolytic cleavage gives rise to both free agents without compromising the hyperpolarized state. The catalyst / substrate separation strategies use commercially available particles and are sufficiently rapid to maintain much of the initial hyperpolarization. Taken together, these results opening a door to a host of new compounds being hyperpolarized via SABRE, yet free of catalysts, for use in a wide range of envisioned biomedical applications. Funding support: NSF CHE-1416268 & CHE-1416432, NIH 1R21EB020323 & R21CA220137, DOD W81XWH-12-1-0159/BC112431, W81XWH-15-1-0271 & W81XWH-15-1-0272.

REFERENCES: [1] R. W. Adams, *et al*., *Science*, 323, 1708-1711 (2009); [2] B. Kidd, J. Mashni, *et al*., Chem.-Eur. J. 24, 10641–10645 (2018); [3] F. Reineri, T. Boi, S. Aime, *Nat. Commun*. 6, 5858 (2015); [4] R. Shchepin, L. Jaigirdar, *et al*., *J. Phys. Chem. C* 121, 28425-28434 (2017); [5] T. Theis, M. L. Truong, *et al*., *J. Am. Chem. Soc.*, 137, 1404-1407 (2015); [6] K. V. Kovtunov, *et al*., *Angew. Chem. Int. Ed.* 56, 10433–10437 (2017); [7] B. Kidd, J. Gesiorski, *et al.*, J. Phys. Chem. C. 122, 16848−16852 (2018); [8] D. A. Barskiy, *et al.*, *J. Am. Chem. Soc.*138, 8080–8083 (2016).

Parahydrogen Derived Polarization for Metabolic Imaging

Eduard Y. Chekmenev

Department of Chemistry, Karmanos Cancer Institute (KCI), Integrative Biosciences (Ibio), Wayne State University, Detroit, MI, USA
Russian Academy of Sciences, Leninskiy Prospekt 14, Moscow, Russia

Parahydrogen Induced Polarization (PHIP) relies on the pairwise parahydrogen (pH_2) addition. We have employed PHIP technique for pH_2 pairwise addition to propylene and cyclopropane to produce hyperpolarized (HP) propane gas using our automated clinical-scale propane hyperpolarizer. Propylene substrate reacts with pH_2 on heterogeneous catalyst yielding catalyst-free HP propane with 100% chemical conversion. We show that up to 1% proton polarization can be achieved for producing ~0.3 standard liters of propane (clinically relevant dose) in approximately 2 seconds. The corresponding high-resolution gas-phase images of stopped HP propane gas are shown in **Fig. 1**. The pairwise pH_2 addition creates long-lived spin states (LLSS) in propane spin system with T_{LLSS} exceeding 13 seconds in the gas phase and exceeding 15 seconds in the liquefied state at magnetic fields below 0.4 T. This 'hidden' singlet state of HP propane can be revealed by transferring the sample to the high magnetic field (ALTADENA experiment) or by polarization transfer from the singlet to magnetization using RF pulse sequences (a.k.a. S2M). Partial spin-lock induced crossing (SLIC) pulse sequence can be employed to transform a fraction of HP propane LLSS into observable magnetization. This RF excitation approach offers numerous advantages: (i) it is selective to singlet state of HP propane compared to z-magnetization of background tissue protons; (ii) requires ultra-low RF irradiation power; (iii) the produced by SLIC magnetization is aligned in x-y plane and can be readily used for ultra-fast ecoplanar imaging readout producing no or little background signal from surrounding tissues. All-in-all, HP propane can be potentially employed as an inhalable contrast agent for functional pulmonary MRI with this sensing approach on 0.35 T FDA-approved clinical MRI scanners. Moreover, unlike HP Xe or HP ^{129}Xe (which are not FDA-approved as of 09/2018), FDA affirmed that propane is generally recognized as safe (GRAS) for the use in foods (as a propellant, etc.) without limitations (see Title 21, volume 3 for details). As a result, we envision fast clinical translation due to (i) established history of propane use and regulation, and (ii) HP propane detection on clinical MRI scanners.

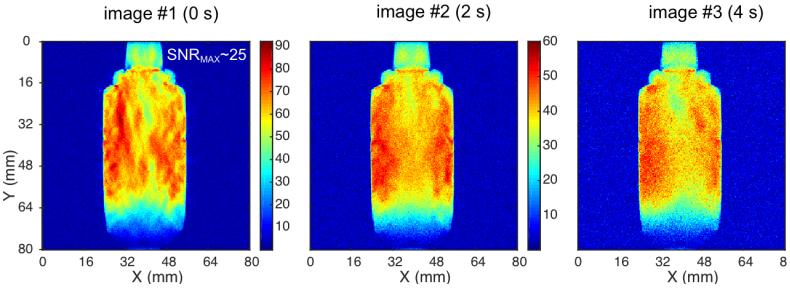

Figure 1. Coronal 2D MRI of ~0.15 standard liters of HP propane gas in a ~56 mL collection container after production of ~0.3-liter batch in ~2 seconds. These 2D slices were acquired on a 4.7 T MRI with the following imaging parameters: 2D GRE images were acquired every ~2 sec, 256×256 matrix with TR ~ 7 ms, slice thickness = 8 mm. Field of view = 80×80 mm^2, pixel size (spatial resolution) = 0.3×0.3 mm^2.

Signal Amplification By Reversible Exchange (SABRE) relies on chemical or exchange reactions pH_2 and to-be-hyperpolarized substrate. A variant of SABRE, SABRE in SHield Enables Alignment Transfer to Heteronuclei (SHEATH), was introduced for efficient hyperpolarization of heteronuclei (^{15}N, ^{13}C, ^{19}F, etc.) in micro-Tesla static magnetic fields. High level of ^{15}N polarization was demonstrated for metronidazole: P_{15N} ~24% at 0.1 M concentration, and P_{15N} ~34% at 0.02 M with 85% pH_2, **Fig. 2a**. The studies of nuclear spin relaxation revealed that T_1 values are generally very short (few seconds) in micro-Tesla field regime most likely due to paramagnetic IrIMes catalyst. However, ^{15}N T_1 values are significantly longer in the milli-Tesla magnetic field range (>3 minutes), and RF-based polarization transfer methods can have an advantage over SABRE-SHEATH: for example, we show that quasi-resonance (QUASR) SABRE (a variant of LIGHT-SABRE) can more than double P_{15N} in metronidazole-$^{15}N_2$-$^{13}C_2$. Metronidazole is FDA-approved antibiotic, and it can be potentially employed for hypoxia sensing using HP MRSI in a manner similar to that using ^{18}FMISO PET imaging.

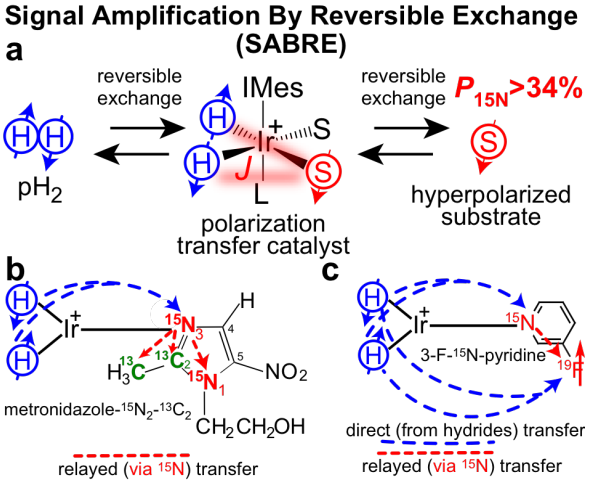

Figure 2. (**a**) the schematics of SABRE hyperpolarization technique; (**b**) spin-relayed SABRE-SHEATH polarization transfer in metronidazole-$^{15}N_2$-$^{13}C_2$ to remove ^{15}N and ^{13}C sites; (**c**) SABRE-SHEATH polarization transfer to remote ^{19}F sites in 3-F-^{15}N-pyridine.

We have recently demonstrated that SABRE-SHEATH can be employed for spin-relayed hyperpolarization transfer to remote ^{15}N and ^{13}C sites over 4 chemical bonds away from pH_2-derived hydride protons, **Fig. 2b**. Furthermore, the recent studies of 3-F-^{14}N-pyridine and 3-F-^{15}N-pyridine isotopomers revealed that SABRE-SHEATH from pH_2-derived hydrides to ^{19}F site (5 chemical bonds from pH_2-derived hydrides) is accomplished via direct mechanism rather than spin-relay mechanism, **Fig. 2c**. These results are additionally substantiated by QUASR-SABRE studies in 3-F-^{14}N-pyridine and 3-F-^{15}N-pyridines. Taken together, efficient SABRE hyperpolarization of heteronuclei (^{15}N, ^{13}C, ^{19}F, etc.) can be accomplished over 4-5 (and potentially even more) chemicals bonds from pH_2-derived hydrides, which are the source of SABRE hyperpolarization, therefore significantly expanding the reach of SABRE hyperpolarization technique.

Abstract ID : **77**

New developments in production of proton-hyperpolarized propane gas for MRI

Content

Hyperpolarization allows one to increase the NMR sensitivity by several orders of magnitude. The main drivers behind the development of hyperpolarization techniques are their biomedical applications. For example, the inhalation of hyperpolarized noble gases, such as 129Xe and 3He, enables functional imaging of lung diseases. However, highly specialized 129Xe and 3He MR equipment and software is required which is not available on conventional clinical MRI scanners. Therefore, 1H-hyperpolarized gases, e.g. propane, represent a promising alternative. Hyperpolarization of propane can be accomplished by pairwise addition of parahydrogen to propylene over heterogeneous catalyst.

Here, we present our recent results on hyperpolarization of propane gas. We developed propane polarizer that enables production of hyperpolarized propane on a clinical scale (production rate >0.3 L just in 2 s, that is more than an order of magnitude greater than that demonstrated previously). Importantly, high polarization levels (~1%) can be retained despite the increase in production rate, allowing stopped-flow slice-selective high-resolution 2D MRI visualization. It was demonstrated that at ~0.05 T magnetic field hyperpolarized propane occurs as a long-lived spin state, which lifetime TLLS is ~3 times greater than T1. The use of buffering gases leads to the increase of propane polarization despite slight TLLS decrease. Cryocollection of hyperpolarized propane, which can be employed for buffering gas separation, increases TLLS up to 14.7 s in the liquid state, which is higher than that of gaseous hyperpolarized propane at any pressure studied. We also explored feasibility of propane hyperpolarization via hydrogenation of cyclopropane with parahydrogen. 1H polarization up to 2.4% was obtained, that is several times greater than that obtained with propylene as a precursor. The resulting NMR signal enhancement was sufficient for 2D MRI despite relatively low chemical conversion of cyclopropane substrate.

This work was supported by Russian Science Foundation (grant #17-73-20030) and DOD CDMRP W81XWH-15-1-0271.

Student stipend

No

Primary author(s) : Dr SALNIKOV, Oleg G. (International Tomography Center SB RAS and Novosibirsk State University); Dr KOVTUNOV, Kirill V. (International Tomography Center SB RAS); ARIYASINGHA, Nuwandi M. (Wayne State University); Dr NIKOLAOU, Panayiotis (Vanderbilt University Institute of Imaging Science); Prof. CHEKMENEV, Eduard Y. (Wayne State University); Prof. KOPTYUG, Igor V. (International Tomography Center SB RAS)

Presenter(s) : Dr SALNIKOV, Oleg G. (International Tomography Center SB RAS and Novosibirsk State University)

Track Classification : Hyp - Hyperpolarization techniques

Contribution Type : Talk

Towards Synthesis of a Family of Novel Cleavable "Double Agents" for SABRE Hyperpolarization

Miranda N. Limbach,[1] Max E. Gemeinhardt,[1] Thomas R. Gebhardt,[1] Ishani Senanayake,[1] Jamil A. Mashni,[1] Bryce E. Kidd,[1] Eduard Y. Chekmenev,[2] Yuqing Hou,[1] and Boyd M. Goodson[1]

1.) Department of Chemistry and Biochemistry, Southern Illinois University, Carbondale, Illinois 62901
2.) Department of Chemistry, Wayne State University, Karmanos Cancer Institute (KCI), Detroit, Michigan 48202 (United States) and Russian Academy of Sciences, Leninskiy Prospekt 14, 119991 Moscow (Russia)

Low detection sensitivity makes it challenging for MRI to image all but the most concentrated species in the body; however, enabling the study of low-concentration species would be highly desirable, e.g. to map and quantify metabolic biomarkers of disease states. Hyperpolarization[1]—the creation of highly non-equilibrium nuclear spin population distributions—promises to enable such studies by increasing the MR detection sensitivity by orders of magnitude. A number of molecules have attracted interest as potential hyperpolarized (HP) agents, particularly those involved in metabolic cycles and/or known to undergo selective uptake exhibit disease-specific reactivity. For example, spin-labeled derivatives of selected carboxylic acids can provide enhanced MR signals from metabolites *in vivo* (e.g. Krebs cycle intermediates[2,3]), and have been a primary target of hyperpolarization via dissolution dynamic nuclear polarization (d-DNP).[4]

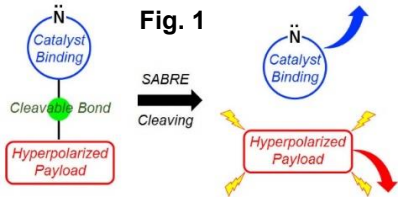

Fig. 1

An alternative type of hyperpolarization is parahydrogen-induced polarization (PHIP).[5] Such parahydrogen-based approaches are of increasing interest because they are inexpensive, rapid (working in seconds), relatively easy to perform, and don't require major instrumentation. In "traditional" PHIP,[6] an unsaturated precursor is catalytically hydrogenated with parahydrogen (*para*-H_2); in the more recent variant SABRE[7] (signal amplification by reversible exchange) the catalyst merely brings the substrate and *para*-H_2 together in a transient complex, and spin order is transferred spontaneously via the scalar coupling network, *without* requiring permanent chemical change to the substrate. SABRE does not consume a precursor to achieve hyperpolarization—greatly facilitating optimization, and removing the need to consider the degree of reaction completion. A disadvantage of *both* approaches is that only a limited range of substrates has been amenable; "traditional" PHIP requires unsaturated precursors, and SABRE has generally required a sp^1 or sp^2 hybridized atom to reversibly bind to the Ir-based catalyst (as is found, e.g., in N-heterocycles) to achieve efficient and direct hyperpolarization.

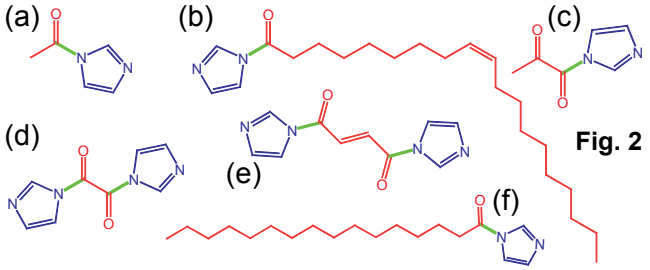

Fig. 2

One recent way to combat this problem has been to allow SABRE hyperpolarization to be 'relayed' from an ancillary substance (that reversibly binds the catalyst) to the target substrate via hydrogen exchange in an aprotic solvent.[8] As an alternative approach (inspired by the side-arm approach demonstrated for "traditional PHIP"[9]), we have been investigating the creation of agents comprised of a Ir-catalyst-binding moiety and a "payload" moiety; in this approach, the intact agent is hyperpolarized via SABRE, then cleaved to produce the desired hyperpolarized agent or agents (**Fig. 1**). More specifically, we have been investigating the use of imidazole rings as the catalyst-binding agent, as cleavage would produce not only the HP metabolic agent, but also a biologically compatible molecule with a chemical shift that is highly sensitive to pH[10] (thereby comprising a "double agent").[11] Our first success has been with 1–^{13}C-$^{15}N_2$-acetylimidazole (**Fig. 2a**); we recently demonstrated that ^{15}N labeling the imidazole ring enables SABRE hyperpolarization to be spin-relayed[12] to the distal ^{13}C carbonyl site.[11] Moreover, rapid base-catalyzed hydrolysis produced separate hyperpolarized $^{15}N_2$-imidazole (pH sensor) and ^{13}C-acetate/acetic acid[11] (metabolic sensor, of interest for imaging glioblastoma multiforme[13-15]).

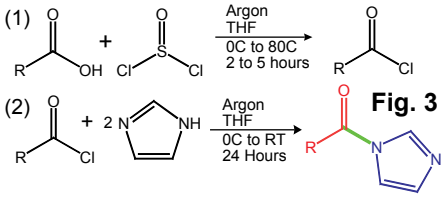

Fig. 3

We are currently working to expand on this approach by developing syntheses of a family of compounds capable of undergoing SABRE hyperpolarization and hydrolytic cleavage (**Fig. 2**); the general approach is outlined in **Fig. 3**. The one-pot syntheses begin by reacting a chosen carboxylic acid (including ^{13}C-labeled variants) with an effective chlorinating agent under inert conditions. Imidazole (^{15}N-labeled previously[16]) is then added to the chlorinated derivative to replace the chloride leaving group on the carboxyl and to form a hydrochloride salt. Tetrahydrofuran is a favored solvent because the salt biproduct is not soluble and can be easily filtered out. The filtrate can then be rotovapped to yield the product. Derivatives in **Figs. 2(a) & (c)** are of interest as metabolic sensors. Diimidazole variants (as in **Figs. 2(d)&(e)**) may give rise to long-lived singlet (^{13}C-^{13}C) states. Long-chain fatty-acid derivatives (e.g. **Figs. 2(c)&(f)**) may enable studies of spin chains and limitations of spin-relay. Efforts to synthesize these and others (in both labeled and naturally abundant variants) will be reported, along with ongoing SABRE hyperpolarization efforts.

Acknowledgements: This work was funded by of NSF CHE-1416432 & CHE-1836308, NIH 1R21EB020323 & 1R21CA220137, DOD CDMRP W81XWH-12-1-0159/BC112431, W81XWH-15-1-0271 & W81XWH-15-1-0272, and SIUC MTC & OSPA. Y.H. acknowledges support from the Meyers Institute.
References: [1] Nikolaou *et al.*, *Chem. Eur. J.* 2015, *21*, 3156; [2] Kurhanewicz, et al., *Neoplasia* 2011, 13, 81; [3] Nelson, *et al., Sci. Transl. Med* 2013, 5, 198ra108; [4] Ardenkjaer-Larsen, *et al., PNAS* 2003, 100, 10158; [5] Hovener, *et al.*, *Angew. Chem. Int. Ed.* 2018; [6] Bowers *et al.*, *J. Am. Chem. Soc.* 1987, *109*, 5541; Adams, *et al.*, *Science* 2009, *323*, 1708; [8] Iali, *et al., Sci. Adv*. 2018, 4, eaao6250; [9] Reineri *et al.*, *Nat Commun* 2015, *6*, 5858; [10] Shchepin, *et al., ACS Sens.* 2016, 1, 640; [11] Kidd *et al., Chem. Eur. J.* 2018; [12] Shchepin, *et al. JPCC* 2017, 121, 28425; [13] Mashimo, *et al.*, *Cell* 2014, *159*, 1603; [14] Bastiaansen *et al.*, *Biochim. Biophys. Acta* 2013, *1830*, 4171; [15] Mishkovsky *et al.*, *J. Cereb. Blood Flow Metab.* 2012, *32*, 2108.

Developing Hyperpolarized ^{131}Xe as a Potential Target for Neutron Optics Searches for Time-Reversal Invariance Violation

Liana Bales[1], Dustin Basler[1], Kierstyn Albin[1], Saiful Islam[1],
Michael J. Barlow[2], Eduard Y. Chekmenev[3] and Boyd M. Goodson[1]

[1]Department of Chemistry & Biochemistry, Southern Illinois University, Carbondale, IL; [2]School of Medicine, University of Nottingham, Queens Medical Centre, Nottingham, UK; [3]Wayne State University & Karmanos Cancer Institute (KCI), Detroit, MI, United States

The Standard Model of physics ostensibly appears complete; however, considerable empirical evidence remains unexplained, including the presence of dark matter and energy. Another mystery of present interest is the gross asymmetry in the apparent amount of matter versus antimatter in the universe. Explanation of these and other phenomena will require the discovery of new physics beyond the Standard Model of particles and interactions. Observations and characterization of any new sources of time-reversal invariance violation (TRIV) should be fertile ground for such discoveries.[1] Correspondingly, the NOPTREX collaboration[2] is working to develop a sensitive 'null-test' for TRIV in the transmission of polarized neutrons passing through polarized targets of heavy nuclei that have neutron resonances that exhibit large parity-odd asymmetries. One of the most promising targets is ^{131}Xe. However, the need for a large spin polarization poses a major challenge.

We are investigating the viability of using (stopped-flow) spin exchange optical pumping (SEOP)[3] for creating sufficiently hyperpolarized ^{131}Xe for the envisioned neutron optics studies. Whereas ^{129}Xe (I=1/2) can be routinely hyperpolarized via stopped-flow SEOP to achieve near-unity levels,[4] ^{131}Xe (I=3/2) has a strong nuclear electric quadrupole moment, giving rise to much faster T_1 relaxation (dominated by self-relaxation). The binary collision pathway[5] is 3.95x10^{-2} amg^{-1}·s-1 (giving a T_1 of only ~25 s at ~1 atm of Xe, whereas T_1 can be hours for ^{129}Xe); furthermore, Xe-^{131}Xe van der Waals complexes and wall collisions can give even shorter relaxation times.[6] Arguably the most successful effort to date to polarize larger ^{131}Xe quantities directly via SEOP has been by Meersmann et al.[6]; for ~72 cc cells containing ~0.1 bar of naturally abundant Xe, ^{131}Xe polarizations of ≤2.2% were reported after separation from Rb. While the polarization was likely higher before transfer, large improvements in ^{131}Xe magnetization are needed for the envisioned neutron experiments to be viable.

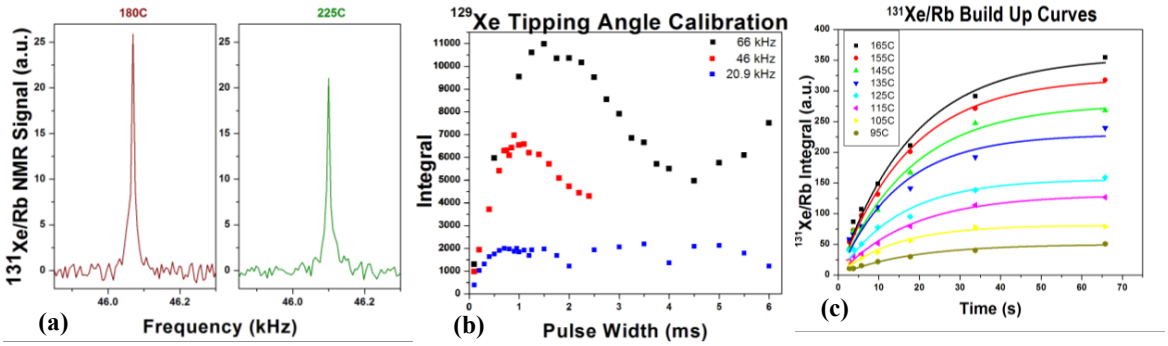

Fig. 1 (a). Single-scan ^{131}Xe NMR at 46 kHz, using 155 W laser power and at 180°C & 225 °C; **(b).** ^{129}Xe Tipping Angle Calibration Curves at 20.9 kHz, 46 kHz, & 66 kHz using ~70 W laser power. **(c).** ^{131}Xe NMR at 46 kHz using ~70 W power (6-scan averages), showing ^{131}Xe polarization dynamics as a function of temperature.

We are working to optimize the polarization of ^{131}Xe during stopped-flow SEOP at higher Xe densities and (initially) moderate scales (~100 cc), as a function of gas partial pressures, AM choice (Rb vs. Cs), temperature, and resonant laser power—including a 180 W spectrally narrowed QPC Ultra500 laser and a rented ultra-narrow OptiGrate laser. 84%-enriched ^{131}Xe is now enabling single-shot *in situ* NMR detection with good SNR (**Fig. 1a**). Determining absolute P_{131Xe} is challenging; we recently reported data from a somewhat indirect, 2-step process involving three different nuclei (^{1}H, ^{129}Xe, & ^{131}Xe) detected at two different frequencies (66 & 20 kHz).[7] An estimated P_{131Xe}~3.5% at 0.4 bar, which would constitute improvements (*cf.* Ref. [6]) of ~1.5-fold and >20-fold in for P_{131Xe} and number of HP ^{131}Xe spins, respectively. In addition to more laser power, we are augmenting our apparatus to provide a more direct way of calibrating P_{131Xe} where all three spins (^{1}H, ^{129}Xe, ^{131}Xe) can all be acquired at the same three frequencies (20.9 kHz, 46 kHz, and 66 kHz), requiring pulse-tipping calibrations for each of these nuclei at these frequencies (e.g. **Fig. 1b**). In addition to determining absolute ^{131}Xe polarizations with high precision and accuracy, ongoing work includes studies of polarization dynamics by collecting build-up curves for both ^{129}Xe and ^{131}Xe (e.g. **Fig. 1c**) over a wide range of temperatures, laser centroid offsets, and laser powers with the more powerful QPC-Ultra500 laser, which (along with optically detected electron spin resonance) will hopefully allow fundamental constants governing ^{131}Xe SEOP—and optimal conditions—to be determined, thereby permitting us to extrapolate our results to what would be needed for the envisioned neutron optics experiments.

Acknowledgements: Funding: DoD (W81XWH-12-1-0159/BC112431, W81XWH-15-1-0271 & W81XWH-15-1-0272).

References: [1]Bowman & Gudkov, *PRC*, **90**, 065503, 2014***;*** [2]Curole & Snow, APS April 2017, C6.003 [3]Walker & Happer *Rev. Mod. Phys.* **69**, 629, 1997; [4]Nikolaou et al., *PNAS,* **110**, 14150, 2013; [5]Brinkmann, et al., *Helv. Phys. Acta*, **35**, 431, 1962; [6]Stupic, et al., *JMR*, 208, **58**, 2011; [7]Molway et al. ENC 2018.

^{85}Rb / ^{133}Cs Optically Detected Electron Spin Resonance in "Hybrid" Spin-Exchange Optical Pumping Cells in Clinically Relevant Regimes

Justin Porter[1], Dustin Basler[1], Joseph W. Plummer[2], Graeme Russell[2], Bryce E. Kidd[1], Eduard Y. Chekmenev[3], Michael J. Barlow[2], and Boyd M. Goodson[1]

[1]Department of Chemistry & Biochemistry, Southern Illinois University, Carbondale, IL, United States; [2]School of Medicine, University of Nottingham, Queens Medical Centre, Nottingham, UK; [33]Wayne State University & Karmanos Cancer Institute (KCI), Detroit, MI, United States

Optically detected electron spin resonance (ODESR) is a method for obtaining a direct measure of the electron spin polarization (P_{AM}) of alkali metal vapor atoms.[1-6] However, such direct measurement of P_{AM} can be challenging, particularly under conditions of high Xe densities and high resonant laser fluxes. For example, the ESR lifetime is limited by collisions with gas species—particularly xenon—as well as high laser power.[4] Correspondingly, the high-[Xe], high-[hν] conditions for clinical-scale stopped-flow[7-8] spin-exchange optical pumping (SEOP)[9] present a challenge for resolving the fine structure of ESR lines and subsequent P_{AM} measurement. Moreover, background electromagnetic fields present in laboratory environments can lead to interference issues, presenting additional challenges. Thus, the purpose of the present work is to explore ODESR under these demanding conditions and evaluate its potential for probing various phenomena underlying SEOP in such regimes.

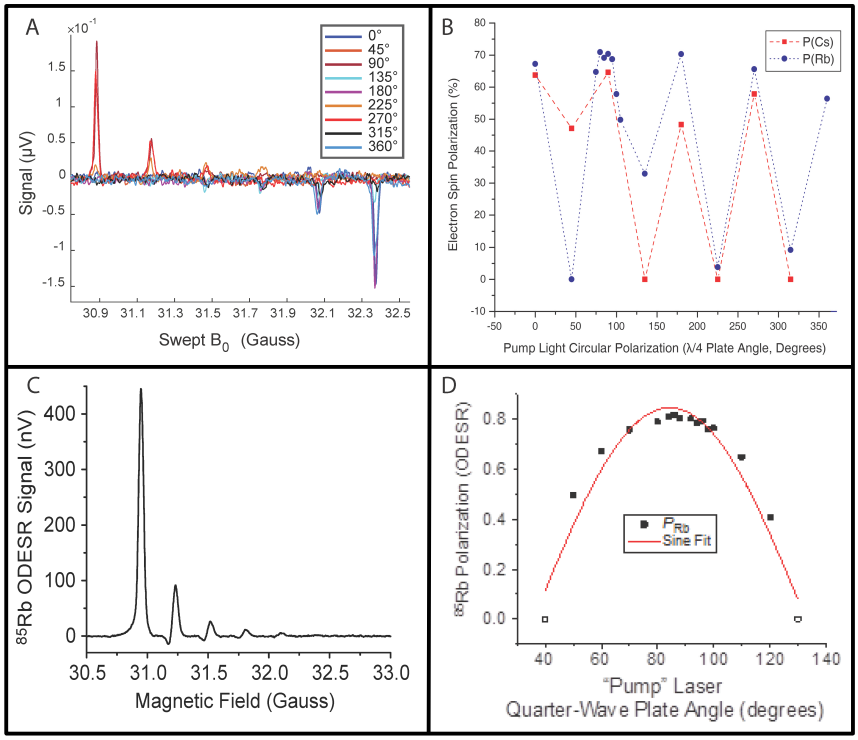

Fig. 1A. ESR as a function of pump light circular polarization for Cs pumped / Rb probed Cs/Rb hybrid cell. **B.** Rough comparison of Cs and Rb electron spin polarization as a function of pump light circular polarization for Cs pumped, Cs/Rb hybrid cell. **C.** ODESR of Rb pumped / Rb probed Cs/Rb hybrid cell signal averaged over 176 scans. Polarization of 78%. **D.** P_{Rb} measurement at various λ/4 plate angle settings, well-reproduced by sinusoidal fit in Rb pumped / Rb probed Cs/Rb hybrid cell.

In our recent work,[9] ODESR signals were successfully detected from ^{85}Rb and ^{133}Cs within clinical-scale SEOP cells and were studied as functions of cell temperature, xenon, light polarization, and probe laser power. To perform these experiments, we have constructed an ODESR system comprised of a SEOP setup (using a high-power laser and 3D-printed clinical-scale oven and cell[8]), a waveform generator (WFG) that ramps the main magnetic field, a second WFG (with output broadcast through an RF coil), a probe laser, and a photodiode whose output is connect to an RF lockin that records ODESR signals. Our approach has now been extended to the more complex case of "hybrid" Cs/Rb cells. We find that, under low-pressure (300 torr N_2) gas mixtures, hyperfine ODESR lines from both metals can be well resolved (e.g. **Fig. 1A**), allowing metal-metal spin-exchange to be studied. For example, "combination" experiments can be performed where one metal is optically pumped, but the other metal is optically probed. Using this approach, we find that the Rb/Cs metal vapors undergo efficient spin exchange to yield comparably high electron spin polarization values (**Fig. 1B**). The system is sufficiently stable for long-time averaging with ~1 nV baselines (**Fig. 1C**). Moreover, given the absence of a low-noise linear amplifier, the ODESR signal is actually detected using the output from the waveform generator itself; given that we cannot saturate the lines with RF power, we are experimenting with using systematic variation of the pump light CP (**Fig. 1D**) in order to enable extrapolalation of P_{AM} values of ODESR spectra obtained at high-[Xe] conditions to those of what would be obtained with perfect CP light. More generally, these efforts should allow measurement of various parameters of SEOP (e.g. Xe/Rb and Xe/Cs spin-destruction rates)—giving insight into the relative utility of Cs vs. Rb vs. hybrids for SEOP hyperpolarization of xenon. Finally, ODESR should allow comparison with / validation of bulk PRb estimates made using an indirect Beer's law / magnetic-field-cycling approach[7,8]).

Acknowledgements: We thank several members of the SEOP community over the years for their help and advice, including Geoff Schrank, Brian Saam, Thad Walker, and Tom Gentile, as well as former SIUC students Nick Whiting and Kaili Ranta. This work was funded in part by DoD (W81XWH-12-1-0159/BC112431, W81XWH-15-1-0271, & W81XWH-15-1-0272).

References: [1]Young et al., *APL*, **70**, 3081, 1997; [2]Levron et al., *APL* **73**, 2666, 1998; [3]Appelt et al., *APL* **75**, 427, 1999; [4]Appelt et al., *PRA* **59**, 2078, 1999; [5]Chann et al., *PRA* **66**, 032703, 2002; [6]Baranga et al., *PRA* **58**, 1412, 1998; [7]Nikolaou, et al., *PNAS*, **110**, 14150, 2013; [8]Nikolaou, et al., *JACS*, **136**, 1636, 2014; [9]Kidd et al., ENC 2018.

Efficient Spin-Relayed Heteronuclear Long-Range Signal Amplification by Reversible Exchange

Roman Shchepin,[2] Jonathan Birchall,[1] Nikita Chukanov,[3,4] Kirill Kovtunov,[3,4] Igor Koptyug,[3,4] Thomas Theis,[5] Warren Warren,[6] Juri Gelovani,[1] Boyd Goodson,[7] Matthew Rosen,[8] Yi-Fen Yen,[8] Wellington Pham,[2] Eduard Chekmenev[1,9]

[1]Department of Chemistry, Ibio, Karmanos Cancer Institute, Wayne State University, Detroit, MI 48202, USA
[2]Vanderbilt University Institute of Imaging Science (VUIIS), Department of Radiology, Nashville, TN 37232 USA
[3]International Tomography Center, SB RAS, [4]Novosibirsk State University, Novosibirsk, 630090, Russia
[5]Department of Chemistry, North Carolina State University, Raleigh, NC, 27695, USA
[6]Department of Chemistry, Duke University, Durham, NC 27708, USA
[7]Department of Chemistry and Biochemistry, Southern Illinois University, Carbondale, Illinois 62901, USA
[8]Massachusetts General Hospital/Athinoula A. Martinos Center for Biomedical Imaging, Boston, MA 02129, USA
[9]Russian Academy of Sciences, Moscow, 119991, Russia

NMR hyperpolarization techniques transiently increase nuclear spin polarization (P) by several orders of magnitude. This significant P increase enables metabolic magnetic resonance spectroscopy (MRS) and MRS imaging (MRSI) after a bolus injection of a hyperpolarized (HP) compound to detect abnormal metabolism in cancer and other diseases. The ^{13}C isotope has been widely employed in a number of biomolecules, most notably in 1-^{13}C-pyruvate. However, this approach has a number of shortcomings. First, the lifetime of HP states (governed by the spin-lattice constant of exponential decay) is relatively short, with T_1 on the order of 1 min. As a result, only a limited number of metabolic pathways have been amenable to MRSI, because sufficient levels of nuclear spin polarization must persist until detection. Here, we employed the Signal Amplification by Reversible Exchange in SHield Enables Alignment Transfer to Heteronuclei (SABRE-SHEATH) hyperpolarization technique (1,4), which relies on performing simultaneous chemical exchange of parahydrogen (pH_2) and to-be-hyperpolarized biomolecules (without altering their structure) within the ligand sphere of a catalyst within micro-Tesla (μT) magnetic fields (Figure 1). SABRE-SHEATH has been shown to produce ^{15}N HP states with up to P≥30% in under one minute although these high polarization levels have been previously obtained at relatively low concentration of ^{15}N spins (7,8). Unlike other hyperpolarization techniques, SABRE-SHEATH requires relatively simple and inexpensive hardware (1,4). Although to date ^{15}N hyperpolarization of several biomolecules has been shown via SABRE-SHEATH, which indeed opens up a range of potential contrast agents, nearly all previous reports have been focused on hyperpolarization of ^{15}N sites that directly interact with the Ir catalytic center of the Ir-IMes polarization transfer catalyst, i.e. the catalyst typically used in most SABRE experiments. The direct polarization transfer from pH_2-derived hydrides to these ^{15}N sites is efficient (i.e. fast and yielding high P_{15N}), because the two-bond ^1H-^{15}N spin-spin couplings are relatively strong (e.g. 10-20 Hz) and sufficiently different from each other as to render the exchangeable catalyst binding sites magnetically inequivalent from one another (1). Although direct SABRE-SHEATH of remote spin-½ sites over ≥3 chemical bonds is inefficient in general (8), a network of J-coupled spin-½ nuclei can transmit polarization at least several chemical bonds away from pH_2-derived hydrides (2,3,5,6). Here, we show that uniformly ^{15}N-labeled metronidazole-$^{15}N_3$ (MNZ-$^{15}N_3$) can be efficiently hyperpolarized via the SABRE-SHEATH approach with P_{15N} >16% for each of the three ^{15}N sites using 87% pH_2, i.e. pH_2-derived hyperpolarization can be efficiently transmitted over six chemical bonds via a network of two-bond spin-spin couplings (Figure 1). In less than a minute of parahydrogen bubbling at ~0.4 μT, a high level of nuclear spin polarization P_{15N} of ~16% is achieved on all three ^{15}N sites of metronidazole-$^{15}N_3$ at up to ~41 mM concentration. At 1.4 T, the HP state of the $^{15}NO_2$ group persists for tens of minutes (T_1~10 min). Metronidazole is an FDA-approved antibiotic, and it can be safely administered orally and intravenously in large (multi-gram) doses. We envision a potential use of this contrast agent for hypoxia sensing (the focus of our future studies) in a manner similar to that of ^{18}F-fluoromisonidazole (FMISO) and other nitro-group containing radiotracers via Positron Emission Tomography (PET). The results presented here (P_{15N} ~ 16% at ≥98% ^{15}N enrichment, T_1 ~ 10 min, fast polarization, and straightforward isotopic enrichment) bode well for such envisioned cellular and *in vivo* experiments.

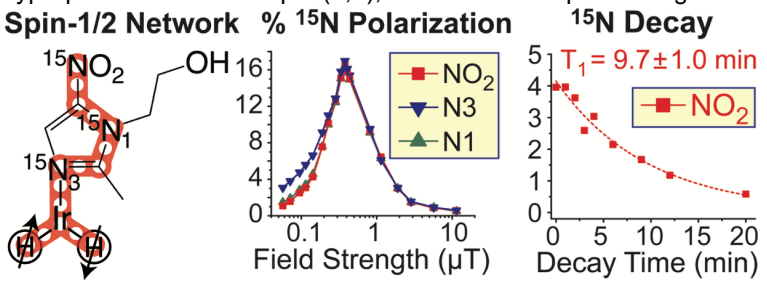

Figure 1. (**left**) the path (in red color) of chemical bonds over which the network of I=1/2 spin relays is established in metronidazole-$^{15}N_3$ (MNZ) undergoing SABRE hyperpolarization; (**right**) the decay curve of the HP $^{15}NO_2$ group in MNZ antibiotic.

ACKNOWLEDGMENTS: NSF CHE-1836308 and CHE-1416432, DOD CDMRP W81XWH-12-1-0159/BC112431, W81XWH-15-1-0271 and W81XWH-15-1-0271, NIH R21CA220137 and R01CA16700, the Russian Science Foundation (grant #17-73-20030), Russian Ministry of Science and Higher Education (project 0267-2019-0004).

REFERENCES: (**1**) Theis, T., et al. *J. Am. Chem. Soc.* **2015,** *137*, 1404. (**2**) Shchepin, R. V., et al. Y. *J. Phys. Chem. C* **2017,** *121*, 28425. (**3**) Shchepin, R. V., et al. *J. Phys. Chem. C* **2018,** *122*, 4984. (**4**) Hövener, J.-B., et al. *Angew. Chem. Int. Ed.* **2018,** *57*, 11140. (**5**) Shchepin, R. V., et al. *under review*. (**6**) Kidd, B., et al. *Chem. Eur. J.* **2018,** *24*, 10641. (**7**) Kidd, B. E., et al. *J. Phys. Chem. C* **2018,** *122*, 16848. (**8**) Barskiy, D. A., et al. *J. Am. Chem. Soc.* **2016,** *138*, 8080–8083.